

AD-A089 008

BELL HELICOPTER TEXTRON FORT WORTH TX

F/G 1 3

VALIDATION OF THE ROTORCRAFT FLIGHT SIMULATION PROGRAM (CB1) US--ETC(U)

JUL 80 J R VAN GAASBEEK

DAAJ02-77-C-0003

UNCLASSIFIED

BHT-699-099-006

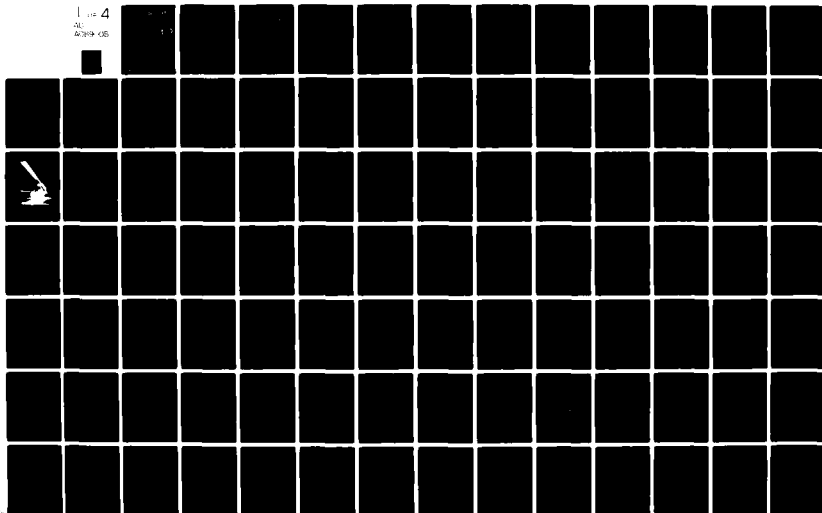
USAAVRADCOM-TR-80-D-4

NL

1 of 4

AL

6/29/80



USAAVRADCOM-TR-80-D-4

**LEVEL**



12

**VALIDATION OF THE ROTORCRAFT FLIGHT SIMULATION  
PROGRAM (C81) USING OPERATIONAL LOADS SURVEY  
FLIGHT TEST DATA**

**AD A089008**

James R. Van Gaasbeek  
Bell Helicopter Textron  
P.O. Box 482  
Fort Worth, Texas 76101

**DTIC**  
**ELECTE**  
SEP 11 1980  
**S** **D**  
C

July 1980

Final Report for Period November 1976 - November 1979

Approved for public release;  
distribution unlimited.

Prepared for

**APPLIED TECHNOLOGY LABORATORY**

**U. S. ARMY RESEARCH AND TECHNOLOGY LABORATORIES (AVRADCOM)**

Fort Eustis, Va. 23604

DDC FILE COPY

80 9 10 012

## APPLIED TECHNOLOGY LABORATORY POSITION STATEMENT

This report documents an effort to apply the Rotorcraft Flight Simulation, Computer Program C81, to model several test points from the Operational Loads Survey Flight Test Program for an AH-1G helicopter. The principal parameters investigated were aircraft controls, attitude, and performance, and main rotor aerodynamic loads, bending moments and accelerations.

The C81 used for this investigation is designated version AGAJ77. The immediately preceding version in the public domain is designated version AGAJ76. AGAJ77 differs from AGAJ76 in the following respects: an improved autopilot, more comprehensive elastic rotor analysis, an improved engine/governor model, an improved wake analysis, and enhanced output capabilities. While most of these improvements were successfully installed in the computer software, extensive difficulties were experienced in the implementation of the elastic rotor refinements. While the other improvements may make the AGAJ77 version preferable for many types of studies, AGAJ76 is recommended for the examination of rotor dynamics and loads. In using either program, some evaluation of the program's applicability to the problem under investigation through correlation with existing data is a judicious first step.

The results of this study provide an accurate assessment of the capabilities of the Rotorcraft Flight Simulation (Version AGAJ77) in modelling teetering rotor aircraft performance and loads. A useful evaluation of the Operational Loads Survey Flight Test Program is also included and should be reviewed by those planning major test programs.

The Project Engineer for this contract was Mr. Edward E. Austin, Aeromechanics Technical Area, Aeronautical Technology Division.

### DISCLAIMERS

The findings in this report are not to be construed as an official Department of the Army position unless so designated by other authorized documents.

When Government drawings, specifications, or other data are used for any purpose other than in connection with a definitely related Government procurement operation, the United States Government thereby incurs no responsibility nor any obligation whatsoever; and the fact that the Government may have formulated, furnished, or in any way supplied the said drawings, specifications, or other data is not to be regarded by implication or otherwise as in any manner licensing the holder or any other person or corporation, or conveying any rights or permission, to manufacture, use, or sell any patented invention that may in any way be related thereto.

Trade names cited in this report do not constitute an official endorsement or approval of the use of such commercial hardware or software.

### DISPOSITION INSTRUCTIONS

Destroy this report when no longer needed. Do not return it to the originator.

Unclassified

SECURITY CLASSIFICATION OF THIS PAGE (When Data Entered)

REPORT DOCUMENTATION PAGE		READ INSTRUCTIONS BEFORE COMPLETING FORM	
1. REPORT NUMBER USAAVRADCOM TR-80-D-4	2. GOVT ACCESSION NO. AD-A089	3. RECIPIENT'S CATALOG NUMBER 0089	
4. TITLE (and Subtitle) VALIDATION OF THE ROTORCRAFT FLIGHT SIMULATION PROGRAM (C81) USING OPERA- TIONAL LOADS SURVEY FLIGHT TEST DATA		5. TYPE OF REPORT, PERIOD COVERED Final report, November 1976 - November 1979	
6. AUTHOR(s) James R. Van Gaasbeek		7. CONTRACT OR GRANT NUMBER(s) DAAJ02-77-C-0003	
8. PERFORMING ORGANIZATION NAME AND ADDRESS Bell Helicopter Textron P. O. Box 482 Fort Worth, Texas 76101		9. PROGRAM ELEMENT, PROJECT, TASK AREA & WORK UNIT NUMBERS 62209A 1L262209AH76 00/179 EK	
11. CONTROLLING OFFICE NAME AND ADDRESS Applied Technology Laboratory, U.S. Army Research and Technology Laboratories (AVRADCOM) Fort Eustis, Virginia 23604		12. REPORT DATE July 1980	
14. MONITORING AGENCY NAME & ADDRESS (if different from Controlling Office) 335		13. NUMBER OF PAGES 332	
		15. SECURITY CLASS. (of this report) Unclassified	
		15a. DECLASSIFICATION/DOWNGRADING SCHEDULE	
16. DISTRIBUTION STATEMENT (of this Report)  Approved for public release; distribution unlimited.			
17. DISTRIBUTION STATEMENT (of the abstract entered in Block 20, if different from Report)			
18. SUPPLEMENTARY NOTES			
19. KEY WORDS (Continue on reverse side if necessary and identify by block number) Digital Simulation      Helicopter Dynamics Rotorcraft Simulation      Maneuvers Operational Loads Survey      Flight Test Data Helicopter Aerodynamics      Flight Test Instrumentation			
20. ABSTRACT (Continue on reverse side if necessary and identify by block number) The Rotorcraft Flight Simulation Program C81 has been used to simulate several test points from the Operational Loads Survey Flight Test Program for an AH-1G helicopter in order to demonstrate program capabilities. The results of those simulations are summarized in this report. Measured and computed performance characteristics and main rotor bending moments and accelerations are compared for steady-state and maneuvering flight (continued)			

DD FORM 1 JAN 73 1473 EDITION OF 1 NOV 65 IS OBSOLETE

Unclassified  
SECURITY CLASSIFICATION OF THIS PAGE (When Data Entered)

054200

72



Unclassified

SECURITY CLASSIFICATION OF THIS PAGE(When Data Entered)

20. conditions. Computed main rotor aerodynamic quantities are compared with test data, in contour-plot form, for level flight conditions.

This report also contains a brief description of the flight test program, a detailed description of the creation of the input decks used for the simulations, and a discussion of possible improvements for future test programs.

SECURITY CLASSIFICATION OF THIS PAGE(When Data Entered)

## PREFACE

The analysis described in this report was performed under Contract DAAJ02-77-C-0003 awarded in 1976 by the Eustis Directorate of the U.S. Army Air Mobility Research and Development Laboratory (USAAMRDL).\*

Technical program direction was provided by Mr. E. E. Austin of USARTL. Principal Bell Helicopter personnel associated with the simulation portion of this contract were Messrs. James R. Van Gaasbeek, John J. Corrigan and Harry F. Anderson.

Accession For	
NTIS GFA&I	<input checked="checked" type="checkbox"/>
DDC TAB	<input type="checkbox"/>
Unannounced	<input type="checkbox"/>
Justification	
By	
Distribution/	
Availability Codes	
Dist	Avail and/or special
A	

\*Redesignated Applied Technology Laboratory, U.S. Army Research and Technology Laboratories (AVRADCOM), effective 1 September 1977.

## TABLE OF CONTENTS

	<u>Page</u>
PREFACE.....	3
LIST OF ILLUSTRATIONS.....	8
LIST OF TABLES.....	17
1. INTRODUCTION.....	19
1.1 PREVIOUS FLIGHT SIMULATION PROGRAM CORRELATION EFFORTS.....	19
1.2 MODIFICATIONS TO PROGRAM C81.....	21
2. THE OPERATIONAL LOADS SURVEY TEST PROGRAM, DATA RETRIEVAL AND REDUCTION.....	24
2.1 THE OPERATIONAL LOADS SURVEY FLIGHT TEST PROGRAM.....	24
2.2 SELECTION OF FLIGHT TEST CONDITIONS.....	25
2.3 TEST DATA RETRIEVAL AND REDUCTION.....	27
3. DATA DECK PREPARATION.....	43
3.1 PROGRAM LOGIC GROUP.....	43
3.2 ROTOR AERODYNAMIC TABLES.....	47
3.3 MAIN ROTOR GROUP.....	55
3.4 MAIN ROTOR ELASTIC BLADE DATA GROUP.....	66
3.5 TAIL ROTOR GROUP.....	80
3.6 TAIL ROTOR ELASTIC BLADE DATA GROUP.....	81
3.7 ROTOR AERODYNAMIC GROUP.....	81
3.8 ROTOR INDUCED VELOCITY DISTRIBUTION TABLES GROUP.....	83
3.9 ROTOR WAKE AT AERODYNAMIC SURFACES TABLE GROUP.....	85
3.10 FUSELAGE GROUP.....	85
3.11 LANDING GEAR GROUP.....	89
3.12 WING GROUP.....	90
3.13 STABILIZING SURFACE NUMBER 1 GROUP.....	94
3.14 STABILIZING SURFACE NUMBER 2 GROUP.....	94
3.15 STABILIZING SURFACE NUMBER 3 GROUP.....	97
3.16 JET GROUP.....	98
3.17 EXTERNAL STORE/AERODYNAMIC BRAKE GROUP.....	98
3.18 ROTOR CONTROLS GROUP.....	98
3.19 ENGINE-GOVERNOR GROUP.....	101
3.20 ITERATION LOGIC GROUP.....	103
3.21 FLIGHT CONSTANTS GROUP.....	105

# TABLE OF CONTENTS    (Continued)

	<u>Page</u>
4.    C81 NUMERICAL SOLUTION METHODS.....	107
4.1    ROTOR MODELS.....	107
4.2    C81 TRIM METHODS.....	107
4.3    C81 MANEUVER METHODS.....	112
4.4    C81 ROTOR-INDUCED VELOCITY MODELS.....	113
5.    PERFORMANCE COMPARISONS.....	117
5.1    AIRCRAFT ATTITUDES.....	117
5.2    CONTROL POSITIONS AND ANGLES.....	122
5.3    MAIN ROTOR HUB FLAPPING ANGLES.....	134
5.4    HORSEPOWER COMPARISONS.....	137
5.5    MAIN ROTOR AERODYNAMIC ENVIRONMENT.....	146
6.    MAIN ROTOR LOADS AND ACCELERATIONS.....	178
6.1    CALCULATION OF ROTOR RESPONSE OUTPUTS IN C81.....	178
6.2    MAIN ROTOR PITCH LINK LOADS.....	181
6.3    MAIN ROTOR BEAM BENDING MOMENTS.....	189
6.4    MAIN ROTOR CHORD BENDING MOMENTS.....	198
6.5    MAIN ROTOR TORSIONAL BENDING MOMENTS.....	210
6.6    MAIN ROTOR BEAM ACCELERATIONS.....	220
6.7    MAIN ROTOR CHORD ACCELERATIONS.....	232
7.    MANEUVER SIMULATION.....	241
7.1    MANEUVER SIMULATION TECHNIQUE.....	241
7.2    PERFORMANCE COMPARISONS.....	248
7.3    COMPARISON OF MAIN ROTOR LOADS AND ACCELERATIONS.....	285
8.    REVIEW OF THE OLS FLIGHT TEST PROGRAM.....	304
8.1    INSTRUMENTATION.....	304
8.2    DETERMINATION OF TEST AIRCRAFT PHYSICAL CHARACTERISTICS.....	306
8.3    TYPES OF TESTING PERFORMED.....	307
8.4    DATA STORAGE METHODS.....	307
8.5    REPORTING METHODS.....	308
8.6    PILOT TECHNIQUE AND TEST METHODOLOGY.....	308
8.7    SUMMARY.....	309

TABLE OF CONTENTS (Concluded)

	<u>Page</u>
9. CONCLUSIONS AND RECOMMENDATIONS.....	310
9.1 OLS TEST PROGRAM CONCLUSIONS.....	310
9.2 RECOMMENDATIONS FOR THE OLS AND FUTURE TEST PROGRAMS.....	310
9.3 CONCLUSIONS WITH RESPECT TO THE C81 SIMULATIONS.....	311
9.4 RECOMMENDATIONS FOR FUTURE MODIFICATIONS TO C81.....	312
10. REFERENCES.....	314
APPENDIX A - CONTOUR PLOTS OF MAIN ROTOR AERODYNAMIC QUANTITIES DERIVED FROM MEASURED DATA FOR FOUR LEVEL FLIGHT TEST CONDITIONS.....	318

## LIST OF ILLUSTRATIONS

<u>Figure</u>		<u>Page</u>
1	Operational Loads Survey Test Vehicle.....	26
2	OLS Airspeed Calibration Chart, Boom System.....	35
3	Stagnation Point Location Calibration Curves.....	42
4	OLS Program Logic Group.....	44
5	Aerodynamic Table for BHT 540 Airfoil Section....	48
6	Aerodynamic Table for NACA 001 Airfoil Section...	51
7	OLS Main Rotor Group.....	56
8	Simplified AH-1G Basic Lines Drawing.....	57
9	AH-1G OLS Main Rotor Hub.....	61
10	OLS Pylon Inputs, Full Rotor Mass.....	65
11	OLS Main Rotor Elastic Blade Data Group.....	67
12	Inputs to the Rotor Frequency Program DNAM05 for the OLS Main Rotor.....	71
13	Comparison of Measured and DNAM05-Computed Main Rotor Natural Frequencies.....	77
14	OLS Tail Rotor Group.....	79
15	OLS Rotor Aerodynamic Subgroup Group.....	82
16	Inputs to the Rotor Wake Program AR9101 for Flight 35A, Counters 610 Through 615.....	84
17	OLS Fuselage Group (Flight 35A Configuration)....	86
18	OLS Wing Group.....	91
19	OLS Stabilizing Surface Number 1 Group.....	95
20	OLS Stabilizing Surface Number 2 Group.....	96
21	OLS External Stores/Aerodynamic Brake Group.....	96

LIST OF ILLUSTRATIONS (Continued)

<u>Figure</u>		<u>Page</u>
22	OLS Controls Group.....	100
23	OLS Engine Group.....	102
24	OLS Iteration Logic Group.....	104
25	Comparison of Measured and Computed Aircraft Pitch Attitude and Angle of Attack in Level Flight.....	118
26	Comparison of Measured and Computed Aircraft Roll Attitude and Sideslip Angle in Level Flight.....	119
27	Measured Hub Feathering Time Histories for Counters 610, 615, 635, 675 and 1078.....	124
28	Comparison of Measured and Computed Collective Pitch Angle and Stick Position.....	127
29	Comparison of Measured and Computed Longitudinal Cyclic Pitch Angle and Stick Position.....	130
30	Comparison of Measured and Computed Lateral Cyclic Pitch Angle and Stick Position.....	132
31	Comparison of Measured and Computed Pedal Position.....	133
32	Measured Hub Flapping Angle Time Histories for Counters 610, 615, 635, 675 and 1078.....	135
33	Comparison of Measured and Computed Hub Flapping Angles.....	138
34	Comparison of Measured and Computed Horsepower...	140
35	Comparison of Main Rotor Normal Force Coefficient Contour Plots Generated from Flight Test and C81 Data for Flight 35A, Counter 611 (8319 Pounds Gross Weight, Aft CG, Clean Wing, 66 KTAS).....	148

# LIST OF ILLUSTRATIONS (Continued)

<u>Figure</u>		<u>Page</u>
36	Comparison of Main Rotor Pitching Moment Coefficient Contour Plots Generated from Flight Test and C81 Data for Flight 35A, Counter 611 (8319 Pounds Gross Weight, Aft CG, Clean Wing, 66 KTAS).....	154
37	Comparison of Main Rotor Angle-of-Attack Contour Plots Generated from Flight Test and C81 Data for Flight 35A, Counter 611 (8319 Pounds Gross Weight, Aft CG, Clean Wing, 66 KTAS).....	159
38	Comparison of Main Rotor Normal Force Coefficient Contour Plots Generated from Flight Test and C81 Data for Flight 35A, Counter 610 (8319 Pounds Gross Weight, Aft CG, Clean Wing, 142 KTAS).....	164
39	Comparison of Main Rotor Pitching Moment Coefficient Contour Plots Generated from Flight Test and C81 Data for Flight 35A, Counter 610 (8319 Pounds Gross Weight, Aft CG, Clean Wing, 142 KTAS).....	169
40	Comparison of Main Rotor Angle-of-Attack Contour Plots Generated from Flight Test and C81 Data for Flight 35A, Counter 610 (8319 Pounds Gross Weight, Aft CG, Clean Wing, 142 KTAS).....	174
41	Comparison of Measured and Computed Main Rotor Pitch Link Loads in Forward Flight.....	182
42	Comparison of Measured and Computed Main Rotor Pitch Link Load Waveforms for Counter 611 (8319 Pounds Gross Weight, Aft CG, Clean Wing, 66 KTAS).....	188
43	Comparison of Measured and Computed Main Rotor Beam Bending Moments for Counter 615 (8319 Pounds Gross Weight, Aft CG, Clean Wing, 129 KTAS).....	190



# LIST OF ILLUSTRATIONS (Continued)

<u>Figure</u>		<u>Page</u>
44	Comparison of Measured and Computed Main Rotor Beam Bending Moment Waveforms at Station 37.5 for Counter 615 (8319 Pounds Gross Weight, Aft CG, Clean Wing, 129 KTAS).....	193
45	Comparison of Measured and Computed Main Rotor Beam Bending Moments for Counter 610 (8319 Pounds Gross Weight, Aft CG, Clean Wing, 142 KTAS).....	196
46	Comparison of Measured and Computed Main Rotor Chord Bending Moments for Counter 615 (8319 Pounds Gross Weight, Aft CG, Clean Wing, 129 KTAS).....	199
47	Comparison of Measured and Computed Main Rotor Chord Bending Moment Waveforms at Station 81.5 for Counter 615 (8319 Pounds Gross Weight, Aft CG, Clean Wing, 129 KTAS).....	203
48	Comparison of Measured and Computed Main Rotor Chord Bending Moments for Counter 610 (8319 Pounds Gross Weight, Aft CG, Clean Wing, 142 KTAS).....	206
49	Comparison of Measured and Computed Main Rotor Chord Bending Moments for Counter 635 (9069 Pounds Gross Weight, Mid CG, Hog Configuration, 136 KTAS).....	208
50	Comparison of Measured and Computed Main Rotor Torsional Bending Moments for Counter 615 (8319 Pounds Gross Weight, Aft CG, Clean Wing, 129 KTAS).....	211
51	Comparison of Measured Steady Torsional Bending Moment Radial Distribution with Distributions Computed by the AGAJ7714 and AGAJ7625 Versions of C81 for Counter 615 (8319 Pounds Gross Weight, Aft CG, Clean Wing, 129 KTAS).....	214

# LIST OF ILLUSTRATIONS (Continued)

<u>Figure</u>		<u>Page</u>
52	Comparison of Measured and Computed Main Rotor Torsional Bending Moment Waveforms at Station 81.5 for Counter 615 (8319 Pounds Gross Weight, Aft CG, Clean Wing, 129 KTAS).....	215
53	Comparison of Measured and Computed Main Rotor Torsional Bending Moments for Counter 610 (8319 Pounds Gross Weight, Aft CG, Clean Wing, 142 KTAS).....	218
54	Comparison of Measured and Computed Main Rotor Beamwise Accelerations for Counter 611 (8319 Pounds Gross Weight, Aft CG, Clean Wing, 66 KTAS).....	221
55	Comparison of Measured and Computed Main Rotor Beamwise Acceleration Waveforms at Station 132 for Counter 615 (8319 Pounds Gross Weight, Aft CG, Clean Wing, 129 KTAS).....	227
56	Comparison of Measured and Computed Main Rotor Beamwise Accelerations for Counter 610 (8319 Pounds Gross Weight, Aft CG, Clean Wing, 142 KTAS).....	228
57	Comparison of Measured and Computed Main Rotor Chordwise Accelerations for Counter 611 (8319 Pounds Gross Weight, Aft CG, Clean Wing, 66 KTAS).....	234
58	Comparison of Measured and Computed Main Rotor Chordwise Acceleration Waveforms at Station 37.5 for Counter 611 (8319 Pounds Gross Weight, Aft CG, Clean Wing, 66 KTAS).....	236
59	Comparison of Measured and Computed Main Rotor Chordwise Accelerations for Counter 610 (8319 Pounds Gross Weight, Aft CG, Clean Wing, 142 KTAS).....	239
60	Flight Constants Group Inputs for Maneuver Simulations.....	243
61	Maneuver Specification Inputs for the Simulation of the Maneuvers of Flight 32A.....	244

# LIST OF ILLUSTRATIONS (Continued)

<u>Figure</u>		<u>Page</u>
62	Comparison of Measured and Computed Airframe Roll Rate Time Histories for the Right Rolling Pullout Maneuver of Counter 561.....	249
63	Comparison of Measured and Computed Airframe Pitch Rate Time Histories for the Right Rolling Pullout Maneuver of Counter 561.....	251
64	Comparison of Measured and Computed Airframe Yaw Rate Time Histories for the Right Rolling Pullout Maneuver of Counter 561.....	252
65	Comparison of Measured and Computed Airframe Roll Rate Time Histories for the Symmetric Pullup Maneuver of Counter 562.....	253
66	Comparison of Measured and Computed Airframe Pitch Rate Time Histories for the Symmetric Pullup Maneuver of Counter 562.....	254
67	Comparison of Measured and Computed Airframe Yaw Rate Time Histories for the Symmetric Pullup Maneuver of Counter 562.....	255
68	Comparison of Measured and Computed Normal Load Factor Time Histories for the Right Rolling Pullout Maneuver of Counter 561.....	256
69	Comparison of Measured and Computed Normal Load Factor Time Histories for the Symmetric Pullup Maneuver of Counter 562.....	260
70	Comparison of Measured and Computed Airframe Roll Attitude Time Histories for the Right Rolling Pullout Maneuver of Counter 561.....	262
71	Comparison of Measured and Computed Airframe Pitch Attitude Time Histories for the Right Rolling Pullout Maneuver of Counter 561.....	263
72	Comparison of Measured and Computed Airframe Yaw Attitude Time Histories for the Right Rolling Pullout Maneuver of Counter 561.....	264
73	Comparison of Measured and Computed Airframe Roll Attitude Time Histories for the Symmetric Pullup Maneuver of Counter 562.....	266

# LIST OF ILLUSTRATIONS (Continued)

<u>Figure</u>		<u>Page</u>
74	Comparison of Measured and Computed Airframe Pitch Attitude Time Histories for the Symmetric Pullup Maneuver of Counter 562.....	267
75	Comparison of Measured and Computed Airframe Yaw Attitude Time Histories for the Symmetric Pullup Maneuver of Counter 562.....	268
76	Comparison of Measured and Computed Airspeed/ Boom Angle of Attack Time Histories for the Right Rolling Pullout Maneuver of Counter 561.....	269
77	Comparison of Measured and Computed Airspeed/ Boom Sideslip Angle Time History for the Right Rolling Pullout Maneuver of Counter 561.....	270
78	Comparison of Measured and Computed Airspeed/ Boom Angle of Attack Time Histories for the Symmetric Pullup Maneuver of Counter 562.....	272
79	Comparison of Measured and Computed Airspeed/ Boom Sideslip Angle Time Histories for the Symmetric Pullup Maneuver of Counter 562.....	273
80	Comparison of Measured and Computed Main Rotor Torque Time Histories for the Right Rolling Pullout Maneuver of Counter 561.....	274
81	Comparison of Measured and Computed Tail Rotor Torque Time Histories for the Right Rolling Pullout Maneuver of Counter 561.....	275
82	Comparison of Measured and Computed Engine RPM Time Histories for the Right Rolling Pullout Maneuver of Counter 561.....	276
83	Comparison of Measured and Computed Main Rotor Torque Time Histories for the Symmetric Pullup Maneuver of Counter 562.....	279
84	Comparison of Measured and Computed Tail Rotor Torque Time Histories for the Symmetric Pullup Maneuver of Counter 562.....	281
85	Comparison of Measured and Computed Engine RPM Time Histories for the Symmetric Pullup Maneuver of Counter 562.....	282

LIST OF ILLUSTRATIONS (Continued)

<u>Figure</u>		<u>Page</u>
86	Comparison of Measured and Computed Main Rotor Hub Flapping Time Histories for the Right Rolling Pullout Maneuver of Counter 561.....	283
87	Comparison of Measured and Computed Main Rotor Hub Flapping Time Histories for the Symmetric Pullup Maneuver of Counter 562.....	284
88	Comparison of Measured and Computed Main Rotor Pitch Link Load Time Histories for the Right Rolling Pullout Maneuver of Counter 561.....	286
89	Comparison of Measured and Computed Main Rotor Pitch Link Load Time Histories for the Symmetric Pullup Maneuver of Counter 562.....	288
90	Comparison of Measured and Computed Main Rotor Beam Bending Moment (Station 37.5) Time Histories for the Right Rolling Pullout Maneuver of Counter 561.....	290
91	Comparison of Measured and Computed Main Rotor Beam Bending Moment (Station 37.5) Time Histories for the Symmetric Pullup Maneuver of Counter 562....	292
92	Comparison of Measured and Computed Main Rotor Chord Bending Moment (Station 132.0) Time Histories for the Right Rolling Pullout Maneuver of Counter 561.....	293
93	Comparison of Measured and Computed Main Rotor Chord Bending Moment (Station 132.0) Time Histories for the Symmetric Pullup Maneuver of Counter 562.....	294
94	Comparison of Measured and Computed Main Rotor Torsional Moment (Station 184.8) Time Histories for the Right Rolling Pullout Maneuver of Counter 561.....	296
95	Comparison of Measured and Computed Main Rotor Torsional Moment (Station 184.8) Time Histories for the Symmetric Pullup Maneuver of Counter 562....	297

LIST OF ILLUSTRATIONS (Concluded)

<u>Figure</u>		<u>Page</u>
96	Comparison of Measured and Computed Main Rotor Beam Acceleration (Station 132.0) Time Histories for the Right Rolling Pullout Maneuver of Counter 561.....	299
97	Comparison of Measured and Computed Main Rotor Beam Acceleration (Station 155.8) Time Histories for the Symmetric Pullup Maneuver of Counter 562....	300
98	Comparison of Measured and Computed Main Rotor Chord Acceleration (Station 81.5) Time Histories for the Right Rolling Pullout Maneuver of Counter 561.....	302
99	Comparison of Measured and Computed Main Rotor Chord Acceleration (Station 37.5) Time Histories for the Symmetric Pullup Maneuver of Counter 562....	303

## LIST OF TABLES

<u>Table</u>	<u>Page</u>
1    DEFINITION OF FLIGHT CONDITIONS SELECTED FOR DATA ANALYSIS.....	28
2    AVAILABILITY OF PERFORMANCE DATA FOR TEST POINTS SELECTED AND DATA REDUCTION METHODS USED.....	32
3    AVAILABILITY OF MAIN ROTOR BENDING MOMENT AND PITCH LINK LOAD DATA FOR TEST POINTS SELECTED AND DATA REDUCTION METHODS USED.....	36
4    AVAILABILITY OF MAIN ROTOR ACCELERATION DATA FOR TEST POINTS SELECTED AND DATA REDUCTION METHODS USED.....	39
5    COMPARISON OF MEASURED AND NASTRAN-COMPUTED FREQUENCIES FOR THE FIRST FOUR ELASTIC FUSELAGE MODES - AH-1G WITH OLS ROTOR, LIGHT GROSS WEIGHT, AFT CENTER OF GRAVITY CONFIGURATION.....	64
6    AIRCRAFT MASS PROPERTIES FOR FUSELAGE GROUP.....	88
7    ESSENTIAL FLIGHT CONSTANTS GROUP INPUTS.....	106
8    TEN INDEPENDENT VARIABLES AND TEN CONSTRAINT QUANTITIES IN A NORMAL QUASI-STATIC TRIM.....	109
9    ABSOLUTE VALUE OF NET UNBALANCED FORCES AND MOMENTS, AND CORRESPONDING ACCELERATIONS, AFTER TIME-VARIANT TRIM FOR COUNTER 610 (8319 POUNDS, AFT CG, CLEAN WING, 142 KTAS) USING THE INTERNAL INDUCED VELOCITY DISTRIBUTION.....	111
10    COMPARISON OF MEASURED AND COMPUTED AIRCRAFT ATTITUDES FOR COUNTERS 635, 675 AND 1093.....	120
11    COMPARISON OF MEASURED AND COMPUTED CONTROL POSITIONS AND ANGLES FOR COUNTERS 635, 675 AND 1093.....	128
12    COMPARISON OF MEASURED AND COMPUTED HUB FLAPPING ANGLES FOR COUNTERS 635, 675 AND 1093....	139
13    COMPARISON OF MEASURED AND COMPUTED HORSEPOWER REQUIRED FOR COUNTERS 635, 675 AND 1093.....	143

LIST OF TABLES (Concluded)

<u>Table</u>		<u>Page</u>
14	EXAMPLE OF CALCULATION OF STEADY PITCH LINK LOAD FOR C81 SIMULATION OF COUNTER 614 (8319 POUND GROSS WEIGHT, AFT CG, CLEAN WING, 116 KTAS).....	184
15	COMPARISON OF MEASURED AND COMPUTED PITCH LINK AXIAL FORCE AMPLITUDES FOR COUNTERS 635, 675 AND 1093.....	187



## 1. INTRODUCTION

The Operational Loads Survey (OLS), a comprehensive flight test program, was conducted by Bell Helicopter Textron under contract to the U.S. Army using an extensively instrumented AH-1G helicopter. The test program was designed to record the rotor aerodynamic environment, and rotor, control system, and airframe response and loads over the operational spectrum of the aircraft. The goals of the current study, which was initiated shortly after completion of the test program, were to modify the Rotorcraft Flight Simulation Program C81 and to simulate several test points from the Operational Loads Survey and to compare the computed and experimental data. The necessity for such correlation efforts and the modifications made to C81 are briefly discussed in this section of the report. The OLS test program, the flight conditions selected, and the data reduction techniques are discussed in Section 2; the creation of the input decks for the C81 simulations is discussed in Section 3. The rotor models, trim and maneuver integration techniques, and rotor-induced velocity models used in the simulations are described in Section 4. The results of the level flight simulations are given in Sections 5 and 6, with the results of the maneuver simulations being presented in Section 7. The OLS test program and data acquisition, storage and retrieval techniques were examined to determine if they provide a suitable data base for verification of flight simulation programs. The results of that study are given in Section 8. Conclusions and recommendations for the total effort are given in Section 9.

### 1.1 PREVIOUS FLIGHT SIMULATION PROGRAM CORRELATION EFFORTS

The use of large-scale, sophisticated digital computer simulations in all phases of the rotorcraft design cycle has become widespread throughout the industry in the past decade. Manufacturers, government agencies and universities have a selection of such programs to use in designing, evaluating, and researching helicopter phenomena. Most of these programs are limited in scope, in that they may treat only certain types of rotors, or they may concentrate on rotor aerodynamics in the absence of rotor dynamics, or they analyze only the rotor, disregarding the airframe.

Certain programs, such as REXOR<sup>1</sup>, Normal Modes<sup>2</sup>, and the Rotorcraft Flight Simulation Program C81<sup>3</sup>, are more general-purpose in nature and of more universal applicability. As these programs have been developed and the level of sophistication of their analysis has increased, selection of the appropriate program to use for a particular problem and assessment of the accuracy of the program have become difficult tasks.

A comparison of several rotor analysis programs was coordinated by Ormiston<sup>4</sup> in 1974. Each program was used to compute performance data and rotor loads for the same hypothetical articulated rotor at three advance ratios. Although the programs were in substantial agreement in the performance analysis, the loads computed varied widely due to differences in the engineering analyses, or to the implementation of these analyses. No test data were available to determine the absolute accuracy of any of the predictions.

Three separate studies designed to determine the adequacy and accuracy of the Rotorcraft Flight Simulation Program C81 have been performed under contract to the U.S. Army. Freeman and Bennett<sup>5</sup> simulated the wind tunnel test of a scale model articulated rotor, with the test data made available for

---

<sup>1</sup>Anderson, W. D., Conner, F., Kretsinger, P., and Reaser, J. S., REXOR ROTORCRAFT SIMULATION, VOLUME I, ENGINEERING DOCUMENTATION, Lockheed California Co., USAAMRDL TR-76-28A, U.S. Army Air Mobility Research and Development Laboratory, Fort Eustis, Virginia, July 1976, AD A028314.

<sup>2</sup>Bergquist, R. R., and Thomas, G. C., TECHNICAL MANUAL, NORMAL MODES ROTOR AEROELASTIC ANALYSIS COMPUTER PROGRAM, unpublished report, U.S. Army Air Mobility Research and Development Laboratory, Fort Eustis, Virginia.

<sup>3</sup>Van Gaasbeek, J. R., McLarty, T. T., and Hsieh, P. Y., ROTORCRAFT FLIGHT SIMULATION, COMPUTER PROGRAM C81, Bell Helicopter Textron, USARTL TR 77-54A, -54B, and -54C, Applied Technology Laboratory, U.S. Army Research and Technology Laboratories, Fort Eustis, Virginia, October 1979.

<sup>4</sup>Ormiston, R. A., COMPARISON OF SEVERAL METHODS FOR PREDICTING LOADS ON A HYPOTHETICAL HELICOPTER ROTOR, Journal of the American Helicopter Society, 19, No. 4, October 1974.

<sup>5</sup>Freeman, F. D., and Bennett, R. L., APPLICATION OF ROTORCRAFT FLIGHT SIMULATION PROGRAM (C81) TO PREDICT ROTOR PERFORMANCE AND BENDING MOMENTS FOR A MODEL FOUR-BLADED ARTICULATED ROTOR SYSTEM, Bell Helicopter Textron, USAAMRDL TR 74-70, U.S. Army Air Mobility Research and Development Laboratory, Fort Eustis, Virginia, November 1974, AD A004015.

comparison after the computer runs were completed. Briczinski<sup>6</sup> simulated both the H-53 and S-67 helicopters and compared the calculated data with available test data, while Staley<sup>7</sup> compared calculated and test data for a BO-105. Several deficiencies in C81 were identified by Briczinski and all analysts found the program to use a large amount of computer time. Many of the problems encountered during these three studies were addressed by Bell Helicopter Textron in work performed under two contracts with the U.S. Army.

## 1.2 MODIFICATIONS TO PROGRAM C81

As part of a larger contracted effort, McLarty<sup>8</sup> modified the Rotorcraft Flight Simulation Program C81 to eliminate three of the problems identified in the previous studies (References 5, 6 and 7.) Investigation has shown that a large amount of run time was being absorbed by the 20-segment tail rotor. Since most users are generally interested in the details of the trim and response of only one rotor, the program was modified to allow either rotor to be analyzed with as few as three segments. This allowed a reduction in the time required to analyze a tail rotor by as much as 85 percent. The second major problem, noted by both Briczinski<sup>6</sup> and Freeman and Bennett<sup>5</sup>, was that the requirement for equal segment lengths caused an inaccurate representation of the hub region of an articulated rotor, unless the rotor hinge offsets were 5 or 10 percent. Accordingly, the program was also modified to permit unequal rotor segmentation. Lastly, the Rotor Frequency Program DN9100 was modified to punch out blade bending moment coefficients for input to C81 with the rotor mode shapes, instead of computing the bending moment coefficients in C81.

<sup>6</sup>Briczinski, S. J., VALIDATION OF THE ROTORCRAFT FLIGHT SIMULATION PROGRAM (C81) FOR ARTICULATED ROTOR HELICOPTERS THROUGH CORRELATION WITH FLIGHT DATA, Sikorsky Aircraft Div., United Technologies Corp., USAAMRDL TR 76-4, U.S. Army Air Mobility Research and Development Laboratory, Fort Eustis, Virginia, May 1976, AD A025934.

<sup>7</sup>Staley, J. A., VALIDATION OF ROTORCRAFT FLIGHT SIMULATION PROGRAM THROUGH CORRELATION WITH FLIGHT DATA FOR SOFT-IN-PLANE HINGELESS ROTORS, Boeing Vertol Co., USAAMRDL TR 75-50, U.S. Army Air Mobility Research and Development Laboratory, Fort Eustis, Virginia, January 1976, AD A021176.

<sup>8</sup>McLarty, T. T., Van Gaasbeek, J. R., and Hsieh, P. Y., ROTORCRAFT FLIGHT SIMULATION WITH COUPLED ROTOR AEROELASTIC STABILITY ANALYSIS, Bell Helicopter Textron, USAAMRDL TR 76-41A, -41B, and -41C, U.S. Army Air Mobility Research and Development Laboratory, Fort Eustis, Virginia, May 1977, AD A042462, A042908, and A042907.

Under the current contract, the program has been modified to further improve the rotor dynamic representation, to include a simple dynamic engine representation, and to simplify the use of the program. The first goal was accomplished by including the effects of undersling, precone, inplane offset and prelag of the feathering axis in DN9100 (renamed DNAM05), with complementary modifications made to C81. The second goal, a simple dynamic engine model, was achieved by implementing a first-order differential equation for the horsepower-available equation, patterned after the model in the hybrid-computer version of C81. The resulting time lag improves the simulation of rotor rpm variations during maneuvers.

The remaining modifications were implemented to satisfy the third goal, ease of use. The first such modification provides the user with a numerical filter to enhance the numerical stability of the trim procedure and to improve the program's ability to simulate a user-specified maneuver. The second modification permits the user to use the maneuver time-history postprocessing analyses after a time-variant trim, thereby eliminating many forms of external postprocessing required with previous versions of C81.

Experience with C81 has shown that difficulties were encountered while trying to trim an elastic rotor in extreme flight conditions when the torsional degree of freedom was included in the rotor elastic mode shapes. The problem was partially overcome when a numerical damper was included in the time-variant trim procedure, but a torsion-induced numerical instability in the thrust-induced velocity iteration loop still hampered trim. (This procedure is invoked when the built-in induced velocity model is used.) This continuing problem has been addressed by numerically filtering the thrust in the loop, thereby introducing a lag in the change of induced velocity due to an azimuthal change in instantaneous thrust.

The digital filter was also used to solve another problem that had frequently hampered the simulation of time-varying maneuvers with elastic, two-bladed rotors. The maneuver autopilot, available in earlier versions of the program, allowed the analyst to stipulate a desired normal-load-factor time history (the g-tracker option) or to use the autopilot to hold one or more aircraft Euler angles constant. The autopilot operated on the instantaneous aircraft response and was usually unable to track a desired normal-load-factor time history for a symmetric pullup for rotorcraft with an elastic two-bladed rotor. A significant improvement was gained by using a filtered value of  $\dot{W}$  in the equation for the required pitch rate,

$$q_{\text{required}} = [(NLF_{\text{desired}} - \cos\theta \cos\phi)g + \dot{W} + PV]/U \quad (1)$$

This equation is derived from the Z-force Euler equation of motion (Reference 9). A filter frequency of main rotor one-per-rev has been found to give the best results. The maneuver autopilot was also modified to allow the user to specify desired time histories for rotorcraft pitch rate, roll rate, yaw rate or rate-of-climb.

Required data postprocessing has been greatly reduced by four additional modifications to the program. The maneuver data postprocessing package, GDAJ07, has been modified to allow the user to access several options after time-variant trim. With this modification, the user can plot rotor mode-shape participation factors after trim to assure himself that the rotor is, in fact, trimmed. In addition, blade-element accelerations have been added to the list of variables that can be plotted after trim or maneuver, expanding that list from approximately 1500 to almost 2400 variables.

The third modification added a rotor contour plot option to the program, allowing the user to plot up to 39 different rotor variables in polar form, enhancing visualization of the rotor operating condition and response. Finally, the flight path stability analysis (STAB) was modified to output the numerators of up to 21 rotorcraft transfer functions, instead of the three previously available. A detailed description of the analysis incorporated in the AGAJ77 version of C81, a user's guide and a programmer's guide are provided in Reference 3.

---

<sup>9</sup>Etkin, G., DYNAMICS OF FLIGHT, John Wiley and Sons, Inc., New York, 1959, page 116.

## 2. THE OPERATIONAL LOADS SURVEY FLIGHT TEST PROGRAM, DATA RETRIEVAL AND REDUCTION

The primary goal of this study was to compare C81-computed performance, rotor loads, and vibration data with that measured during the Operational Loads Survey test flight in order to determine the program's capabilities and accuracy. To that end, nine OLS level flight conditions and two high-g maneuvers were selected and data were retrieved and reduced. The test program under which the data was acquired, the criteria under which the test points were chosen, and the data retrieved and reduced are discussed in this section.

### 2.1 THE OPERATIONAL LOADS SURVEY FLIGHT TEST PROGRAM

An AH-1G helicopter was bailed to Bell Helicopter by the Army for the Operational Loads Survey flight test program. The weapons were removed from the turret and the armor plate was removed from the cockpit and engine compartment. A 28-track FM tape recorder was installed in the ammunition bay and a telemetry transmitter was placed in the tailboom. A boom was placed on the nose of the aircraft to support sideslip, angle-of-attack and airspeed instrumentation. Accelerometers and strain gages were installed throughout the aircraft to measure rigid-body flight path motion, vibrations, and bending moments. The tail rotor was also instrumented to measure flight loads.

New blades were manufactured for the main rotor in order to accommodate the extensive instrumentation installed in a fiberglass sleeve attached to the exterior of the blades. The mid-span and tip weights were reduced to retune the blades with the additional mass and stiffness of the sleeve. Strain gages and accelerometers were installed on one blade to measure beam and chord bending moments at eight blade stations, torsional moments at four blade stations, and beam and chord accelerations at eight blade stations.

Absolute pressure transducers were arrayed chordwise on both the upper and lower surface of the other blade at five radial stations in order to record the pressure distribution. Bell Helicopter-developed Boundary Layer Buttons, used to measure flow angles, were also installed. The instrumentation wiring was installed and the 0.125-inch-thick fiberglass sleeves were attached to the blades, with removable formed-aluminum cuffs at the five stations with pressure transducers to allow access to the instrumentation. Hot-wire anemometers were then applied to the leading edge at the same five blade stations.

The fiberglass sleeve added 0.25 inch to the standard airfoil thickness and increased the blade chord from 27.0 to 28.625 inches. The thickness-to-chord ratio was increased from 0.0933 to 0.09677. A 10-inch chord model of the airfoil was constructed with pressure transducers and hot wires to determine the aerodynamic characteristics of the new airfoil and to calibrate the stagnation point location with angle of attack. Unfortunately, the model was not tested due to funding limitations.

A standard AH-1G hub was instrumented to measure beam, chord and torsional bending moments and accelerations, and feathering and flapping. Power supplies and multiplexors were placed in a housing that was installed on the trunnion blocks so that it flapped and rotated with the rotor. The multiplexed signals were sent to the tape recorder and telemetry equipment through a slip ring assembly at the center of the multiplexor housing.

The modified aircraft, with protective gloves placed over the blade pressure taps to keep the orifices clear, is shown in Figure 1. A detailed description of the aircraft modifications and instrumentation is given in Reference 10.

The aircraft was flown in several gross weight and center-of-gravity combinations, both with and without wing stores. The test program consisted of hover, level flight speed sweeps to  $V_H$ , autorotations, symmetric and rolling pull ups, and NOE maneuvers. For some tests, noise measurements were recorded simultaneously in order to determine the rotor aerodynamic phenomena that correspond to measured acoustic signatures. The analog flight test tapes have been digitized and the data recorded on 175 digital tapes. In combination with the reports describing the aircraft, calibration curves, and pilot cards, these tapes constitute an enormous library of consistent, well-documented test data, ideally suited for further investigation of helicopter flight phenomena and verification of rotorcraft simulation programs. Data extraction, manipulation and reduction are facilitated by a series of computer programs that can tabulate or plot the data on suitable scales.

## 2.2 SELECTION OF FLIGHT TEST CONDITIONS

The flight test conditions for correlation were chosen to provide data for a series of steady-flight test points from hover to maximum level flight airspeed ( $V_H$ ) in one gross

<sup>10</sup> Shockey, G. A., Cox, C. R., and Williamson, J. W., AH-1G HELICOPTER AERODYNAMIC AND STRUCTURAL LOADS SURVEY, USAAMRDL TR 76-39, Bell Helicopter Textron, U.S. Army Air Mobility Research and Development Laboratory, Fort Eustis, Virginia, February 1977, AD A036910.



Figure 1. Operational Loads Survey Test Vehicle.



weight and center-of-gravity configuration. Three additional steady-state test points were chosen to yield data at  $V_H$  for other gross weight and center-of-gravity configurations. The symmetric pull-up and rolling pullout with the highest normal load factors were selected for the maneuver cases. The flight number and counter number of each of the test points selected, as well as a definition of the aircraft configuration and flight condition, are listed in Table 1.

Hover cases were flown only for the light gross weight, middle center-of-gravity configuration. The hover flights were all flown in a 10-knot south wind (according to the pilot card), with the aircraft hovering stationary relative to the ground. Counter 1078, in which the aircraft was flown heading into the wind, was chosen as the hover case.

Ideally, other light gross weight, middle center-of-gravity cases would have been chosen for the level-flight speed sweep data comparisons. Unfortunately, several channels designated for main rotor blade loads data were reassigned for recording acoustics data for these cases (Flight 43), so the light gross weight, aft center-of-gravity test points of Flight 35A were chosen. These counters (611, 612, 614, 615, and 610) provide a more complete set of bending moment data. The remaining three  $V_H$  level-flight test points (Counters 635, 675 and 1093) were chosen to provide the maximum rotor loads data for several different configurations.

## 2.3 TEST DATA RETRIEVAL AND REDUCTION

Over 350 data items were recorded simultaneously by an on-board FM tape recorder system throughout the OLS flight test program. This capacity was exceeded by data requirements during the acoustics portion of the tests, so data from the aircraft-mounted microphones were recorded on bands previously dedicated to recording some blade bending moment data. All data were digitized, at sample rates selected to retain important high-frequency information, and stored on tape for future data reduction. Aircraft performance and main rotor bending moments, accelerations and aerodynamic data for the eleven flight test conditions of Table 1 were extracted from the digital tapes, processed, and reduced.

### 2.3.1 Effects of Recording System and Filters on Test Data

The OLS test data have been processed through several electronic devices between the sensing of the data value and the output of reduced data in an engineer-useable form. Each of the electronic devices has individual frequency response characteristics that can modify the signal. In effect, the

TABLE 1. DEFINITION OF FLIGHT CONDITIONS  
SELECTED FOR DATA ANALYSIS

Flight Counter	Gross Weight (lb)	Center-of-Gravity Location*	True Airspeed (knots)	Flight Condition
45B 1078	8289	Mid,Clean	10**	OGE Hover
35A 611	8319	Aft,Clean	66	0.5 $V_H$ SL***
35A 612	8319	Aft,Clean	85	0.6 $V_H$ SL
35A 614	8319	Aft,Clean	116	0.8 $V_H$ SL
35A 615	8319	Aft,Clean	129	0.9 $V_H$ SL
35A 610	8319	Aft,Clean	142	$V_H$ SL
36A 635	9069	Mid,Hog <sup>t</sup>	136	$V_H$ SL
37A 675	9068	Aft,Hog <sup>t</sup>	138	$V_H$ SL
45C 1093	8300	Fwd,Clean	145	$V_H$ SL
32A 562	8289	Mid,Clean	134 (entry)	1.75g Symmetric Pullup
32A 561	8289	Mid,Clean	134 (entry)	2.0g Left Rolling Pullout

\*Aft = Aft CG Mid = Middle CG Fwd = Forward CG

\*\*Counter 1078 was hover with respect to the ground; the aircraft was at a heading of 180° with a 10-knot south wind reported on the pilot card.

\*\*\*SL = Straight and level steady-state flight.

<sup>t</sup> The hog configuration has 4 simulated XM-159 rocket pods attached to the wings.

data are filtered to some extent by each component in the data acquisition and reduction cycle. The effects of this filtering at each stage of the process must be considered in interpreting the data.

#### 2.3.1.1 Filtering During Data Acquisition

There are three types of filtering implicitly involved in the data acquisition process. The particular instrument being used to measure a physical quantity has an individual frequency response that automatically filters very high frequency data out of the signal that the instrument produces. Additionally, the instrument may not have a uniform transfer function within its operating frequency range. This would introduce amplitude or phase distortion in the signal output from the device.

The signal-conditioning and multiplexing electronics can introduce amplitude and phase distortion to the signal generated by the sensor. The signal conditioners used in this test program had a flat frequency response to at least three kilohertz. The frequency-division multiplexing causes no distortion of the signal.

The FM tape recorder electronics, and the tape itself, also have distinct frequency response characteristics, and amplitude and phase distortion can be introduced at this stage of the data acquisition procedure.

No systematic study of the transfer functions of the whole instrumentation and recording system appears in any of the flight test documentation. However, the overall frequency response of each of the sixteen bands is known. Bands one through six have no amplitude or phase distortion to at least 50 hertz, bands seven through thirteen have an overall transfer function that is flat to at least 200 hertz, and signals recorded on bands fourteen through sixteen are good to 400 hertz.

#### 2.3.1.2 Filtering During Digitization

Filtering also occurs during the digitization of the data recorded on the FM tapes during flight test. A seven-pole Butterworth filter was used to filter the data as it was read from the analog tape. This particular filter has a flat amplitude transfer function out to frequencies near the break frequency, a one-half decibel drop in amplitude at the break

frequency, and the amplitude transfer function decreases at 42 decibels per decade thereafter. The filter used for data on bands one through six had a break frequency of 50 hertz, the filter used for the data on bands seven through thirteen had a break frequency of 200 hertz and the data on bands fourteen through sixteen were filtered at 400 hertz.

The Butterworth filter causes a phase shift in the data that is linear with frequency, to frequencies that are at least one-half the filter break frequency. This constitutes a constant time lag over that frequency range. This group time delay is known and is accounted for in the DATAMAP processing program, but was not accounted for in earlier data reduction routines.

Aliasing might also have occurred during the digitization procedure. Given a digitization sample rate at a frequency of  $\omega_{SR}$  samples per second, a signal at a frequency  $(\omega_{SR})/2 + \Delta\omega$  would be aliased into the digital signal at a frequency of  $(\omega_{SR})/2 - \Delta\omega$ . The digitization sample rate was at a frequency of more than 10 times the filter frequency used for a particular band during the digitization. Since the seven-pole Butterworth filter has a steep rolloff after the break frequency, the signal at the digitization frequency would have had negligible amplitude, ensuring that aliasing did not occur in the digitized data.

#### 2.3.1.3 Frequency Content of the Digitized Data

Performance data were recorded primarily on bands one through six, with a few performance data items recorded on bands seven through thirteen and on bands fourteen through sixteen (see Table B.6, Reference 10). Main rotor pitch link axial force was recorded on track 1, band 6, and track 11, band 5; the remaining main rotor bending moment data items were recorded on bands seven through thirteen and fourteen through sixteen. Rotor accelerations and pressure tap data were all recorded on bands seven through thirteen and fourteen through sixteen. As a result of these recorder band assignments, the digitized data have suffered no phase or amplitude distortion up to frequencies of at least 25 hertz, with the main rotor moments, accelerations and pressure data being unaffected up to 100 hertz.

The main rotor was operated at 324 RPM for the test conditions investigated in this study. At that rotational speed, 25 hertz is slightly greater than 4.6 per rev. Therefore, the five-per-rev component of most of the digitized performance and main rotor pitch link load data has a slightly different group time delay from the lower frequency components. All main rotor moment, acceleration, and aerodynamic data on the digital

tapes are unaffected by filtering through frequencies as large as main rotor five-per-rev, the highest frequency of interest in this investigation.

#### 2.3.1.4 Filtering During Data Reduction

Two additional forms of filtering can take place during the data reduction process. Some data reduction programs, such as DATAMAP,<sup>11</sup> used for portions of the data analysis in this study, do not work directly from the digital tapes. Instead, data are transferred from the digital tapes to a disk-resident master file. An additional digitization procedure takes place in the transfer step, in that a skip factor can be introduced, whereby only every  $n^{\text{th}}$  data point available on the digital tape is transferred to the master file. Therefore, the data on the master file have effective sample rates equal to the original digitization rate divided by the skip factor. Almost all data processed in this manner had an effective sample rate of at least 512 samples per second, ensuring negligible distortion due to aliasing at frequencies equal to, or less than, main rotor five-per-rev. Due to the record length, and the fact that DATAMAP can only process a maximum of 4096 data points simultaneously, some of the maneuver data were transferred at an effective rate of 256 samples per second. These data still have minimal distortion due to aliasing at 64 hertz, and negligible aliasing effects at 32 hertz, which is in excess of main rotor 5-per-rev.

A digital filter is also built into the data reduction programs. DATAMAP, for example, contains a bi-directional Chebyshev filter. The analyst selects a frequency and number of poles for the filter (usually four). The filter processes the signal in both the forward and reverse directions and then processes the separate results to eliminate phase distortion. The filter frequency used in all the data reduction runs was greater than, or equal to, 50 hertz, ensuring negligible amplitude distortion at frequencies equal to, or below, main rotor 5-per-rev.

#### 2.3.2 Performance Data

The performance data extracted for the selected counters are listed in Table 2, with the method of data reduction denoted. Almost all performance data items are available for all counters of interest.

<sup>11</sup>Philbrick, R. B., and Eubanks, A. L., OPERATIONAL LOADS SURVEY - DATA MANAGEMENT SYSTEM, VOLUMES I AND II, Bell Helicopter Textron, USARTL TR 78-52A, -52B, Applied Technology Laboratory, U.S. Army Research and Technology Laboratories, Fort Eustis, Virginia, 1979, AD A065129 and A065270.

TABLE 2. AVAILABILITY OF PERFORMANCE DATA FOR TEST POINTS  
SELECTED AND DATA REDUCTION METHODS USED.

Item	Item Code	Counter									
		1078	611	612	614	615	610	635	675	1093	561 562
Collective Stick	D023	H	H	H	H	H	H	H	H	H	T T
Long. Cyclic Stick	D021	H	H	H	H	H	H	H	H	H	T T
Lateral Cyclic Stick	D022	H	H	H	H	H	H	H	H	H	T T
Pedal	D024	H	H	H	H	H	H	H	H	H	T T
M/R Hub Feathering	D111	H	H	H	H	H	H	H	H	H	M M
M/R Hub Flapping	D110	H	H	H	H	H	H	H	H	H	E E
Yaw Attitude	D011	H	H	H	H	H	H	H	H	H	T T
Pitch Attitude	D010	H	H	H	H	H	H	H	H	H	T T
Roll Attitude	D009	H	H	H	H	H	H	H	H	H	T T
Yaw Rate	V014	-	-	-	-	-	-	-	-	-	T T
Pitch Rate	V013	-	-	-	-	-	-	-	-	-	T T
Roll Rate	V012	-	-	-	-	-	-	-	-	-	T T
Boom Sideslip	D007	M	H	H	H	H	H	H	H	M	T T
Boom Angle of Attack	D008	M	H	H	H	H	H	H	H	M	T T
Boom Static Pressure	P030	M	H	H	H	H	H	H	H	M	-

TABLE 2. (Concluded)

Item	Item Code	Counter										
		1078	611	612	614	615	610	635	675	1093	561	562
Boom Airspeed	P002	H	H	H	H	H	H	H	H	H	E	E
Outside Air Temp	T004	H	H	H	H	H	H	H	H	H	-	-
CG Load Factor	A005	-	-	-	-	-	-	-	-	-	T	T
Engine N2	R511	M	H	H	H	H	H	H	H	M	T	T
Engine Torque Pressure	P506	H	H	H	H	H	H	H	H	H	T	E
M/R Mast Torque	M107	M	H	H	H	H	H	H	H	M	T	E
T/R Mast Torque	M207	M	H	H	H	H	H	H	H	M	E	E

Symbols

- E - Envelope plot only  
 H - Harmonic analysis performed on the test data  
 M - Test data missing  
 T - Time-history plots created

The sine and cosine one-per-rev components of the measured hub flapping angle can be directly compared with the hub flapping angles computed by C81, while the measured steady and one-per-rev feathering angles can be compared with those computed by C81. The measured feathering angle is referenced to zero radius, as is that in C81, but the algebraic sign of the one-per-rev components must be reversed to account for a difference in the flight test and analytical sign conventions.

The yaw angle measured during the flight tests is not an Euler angle, as the yaw gyro is uncaged at the beginning of each record. Therefore, it is only a measure of the yaw deviation during the record.

The boom airspeed is measured in knots-squared. The square-root of the mean value of this data item is indicated airspeed that is converted to calibrated airspeed using the chart given in Figure 2. The calibrated airspeed is divided by the square-root of the density ratio (determined from the pressure altitude and OAT on the pilot card) to yield true airspeed, in knots.

Engine horsepower output is determined from the recorded engine torque pressure reading using the calibration coefficient of 23.16 horsepower/psi. The steady component of the measured rotor mast torques is used, with the rpm measured for that rotor, to compute the horsepower required for that rotor.

Envelope plots, as used for presenting some of the maneuver data, result from plotting only the minimum and maximum values of the data, versus time, and connecting those points with lines. Such plots give the band containing the data.

### 2.3.3 Main Rotor Blade Bending Moment, Pitch Link Load and Acceleration Data

The beam and chord bending moments and accelerations are measured in a coordinate system aligned with the local blade section chord. Inboard of the feathering bearings, this is the inplane-out-of-plane coordinate system. Outboard of the bearings, the coordinate system has been rotated through the total local geometric pitch angle.

The bending moment data recorded and the methods of data reduction are given in Table 3.

Many of the bending moment channels became nonfunctional between Counter 675 and Counter 1078, although the chord bending moment data at Station 155.8 is available only for Counter 1093 (among those examined). The torsional bending moment data



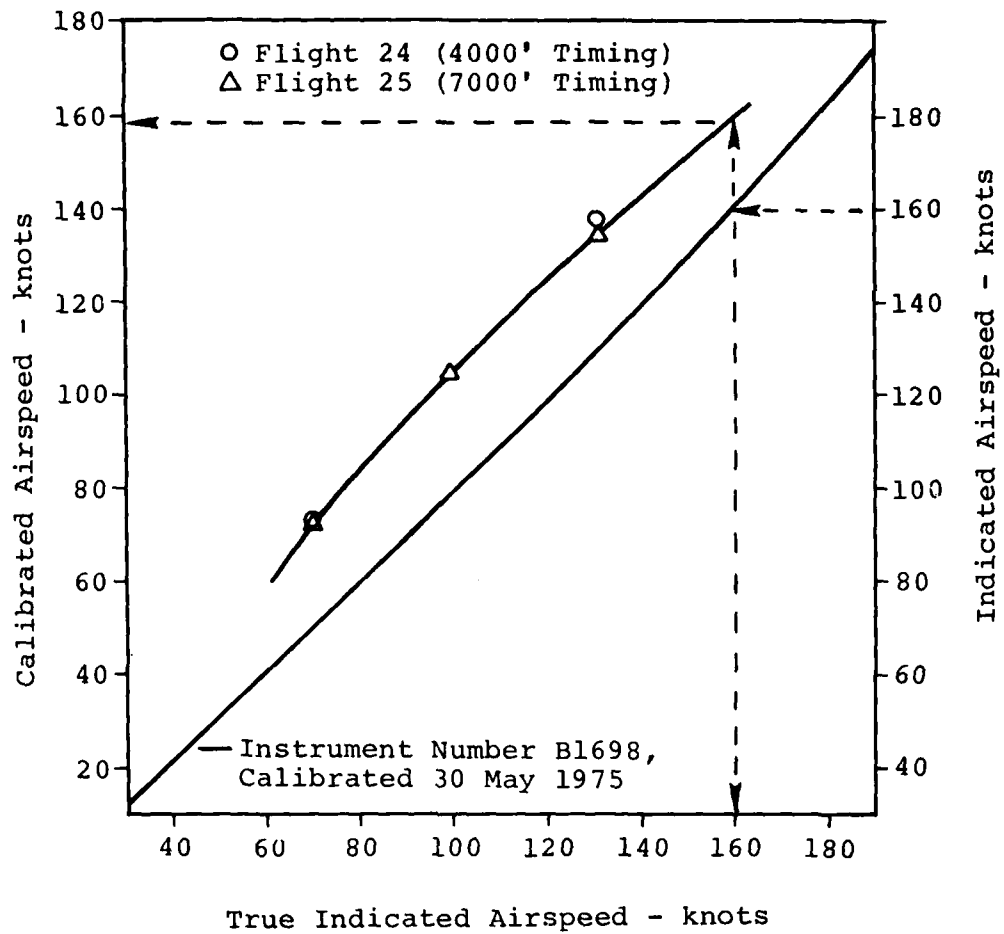


Figure 2. OLS Airspeed Calibration Chart, Boom System.

TABLE 3. AVAILABILITY OF MAIN ROTOR BENDING MOMENT AND PITCH LINK LOAD DATA FOR TEST POINTS SELECTED AND DATA REDUCTION METHODS USED.

Item	Item Code	1078	611	612	614	615	610	Counter				
								635	675	1093	558	562
Beam, Sta	6.0	B112	M	B	B	B	B	B	B	M	E	E
	11.5	B114	M	B	B	B	B	B	B	M	E	E
	37.5	B118	B	B	B	B	B	B	B	B	E	E
	60.0	B120	M	B	B	B	B	B	B	M	E	E
	81.5	B126	M	B	B	B	B	B	B	M	E	E
	103.0	B128	B	B	B	B	B	B	B	B	E	E
	132.0	B122	M	B	B	B	B	B	B	M	E	E
	155.8	B130	B	B	B	B	B	B	B	B	E	E
	184.8	B132	B	B	B	B	B	B	B	B	E	E
	212.3	B124	B	B	B	B	B	B	B	B	E	E
	238.1	B134	B	B	B	B	B	B	B	B	E	E
	6.0	B113	B	B	B	B	B	B	B	B	E	E
	11.5	B115	M	B	B	B	B	B	B	M	E	E
Chord, Sta	60.0	B121	M	B	B	B	B	B	B	M	E	E
	81.5	B127	B	B	B	B	B	B	B	M*	E	E

TABLE 3. (Concluded)

Item	Item Code	Counter									
		1078	611	612	614	615	610	635	675	1093	561 562
	103.0	B129	B	B	B	B	B	B	B	B	E E
	132.0	B123	M	B	B	B	B	B	B	M	E E
	155.8	B136	M	M	M	M	M	M	M	B	M M
	184.8	B133	B	B	B	B	B	B	B	B	E E
	212.3	B125	B	B	B	B	B	B	B	B	E E
Torsion, Sta	6.0	M906	M	M	M	M	M	M	M	M	M M
	81.5	M150	M	B	B	B	B	B	B	M	E E
	132.0	M935	B	B	B	B	B	B	B	B	E E
	184.8	M936	B	B	B	B	B	B	B	B	E E
	238.1	M937	B	B	B	B	B	B	B	B	E E
Red Pitch Link Axial Force		F103	M	B	B	B	B	B	B	M	E E
		F104	B	B	B	B	B	B	B	B	E E
White Pitch Link Axial Force											

Symbols

B - Harmonic analysis performed on the test data and envelope plots created.

E - Envelope plots only

M - Test data missing

\*There are data stored for this strain gage, but they are unreliable.

for Station 6.0 are missing for all counters, but being inboard of the feathering bearing, the absence of this data item is a small loss.

Axial force data for only the white pitch link are available for counters 1078 and 1093, while data for both pitch links are available for all other test points of interest.

All rotor acceleration data (Table 4) are available for the selected counters, with three exceptions. The accelerations are measured relative to inertial space.

Longitudinal, lateral and vertical absolute accelerations were measured at the top of the mast, and the data were extracted for all counters of interest, except counter 635, for which the data were missing. Time-history plots were created for these quantities for all the test points and these data were harmonically analyzed for the level flight conditions.

#### 2.3.4 Main Rotor Aerodynamic Data

Absolute pressure transducers were installed in a chordwise array on both the upper and lower surfaces at five radial stations on one main rotor blade. Data from several of the pressure transducers are missing for some counters. The absence of these data can be compensated for in most cases by interpolation, but the leading edge upper surface pressure tap at 60 percent radius was not functional for any of the selected counters. Since this pressure transducer is located in the region of the leading edge suction peak, with its attendant large gradients, the data cannot be accurately extrapolated. Therefore, no pressure data were reduced for the 60-percent radial station.

Pressure data at the four remaining radial stations, airspeed and temperature data were extracted from the digital tapes and processed by the Operational Loads Survey Data Management System (Reference 11). The DMS was then used to integrate the data to compute the normal force ( $C_N$ ), chord force ( $C_C$ ) and pitching moment ( $C_M$ ) coefficients and create contour plots of these aerodynamic quantities.

Hot wire anemometers were located around the leading edge of the blade at five radial stations. The hot-wire installation at 95 percent radius was nonfunctional throughout the test. The resistance of each wire is a function of its temperature, which is dependent on the velocity of the air passing over it. The wire will be hottest when the stagnation point passes over the wire, causing its resistance to increase and a small spike to appear in the signal from that wire. By plotting the

TABLE 4. AVAILABILITY OF MAIN ROTOR ACCELERATION DATA FOR TEST POINTS  
SELECTED AND DATA REDUCTION METHODS USED.

Item	Item Code	1078	611	612	614	615	Counter						
							610	635	675	1093	561	562	
Beam, Sta	3.5	A889	B	B	B	B	B	B	B	B	B	E	E
	11.0	A890	B	B	B	B	B	B	B	B	B	E	E
	16.0	A901	B	B	B	B	B	B	B	B	B	E	E
	37.5	A902	B	B	B	B	B	B	B	B	B	E	E
	60.0	A938	M	B	B	B	B	B	B	B	M	E	E
	103.0	A940	B	B	B	B	B	B	B	B	B	E	E
	132.0	A950	B	B	B	B	B	B	B	B	B	E	M
	155.8	A951	B	B	B	B	B	B	B	B	B	E	E
	184.8	A952	B	B	B	B	B	B	B	B	B	E	E
	238.1	A953	B	B	B	B	B	B	B	B	B	E	E
Chord, Sta	3.5	A905	B	B	B	B	B	B	B	B	B	E	E
	37.5	A900	B	B	B	B	B	B	B	B	B	E	E
	60.0	A955	B	B	B	B	B	B	B	B	B	E	E
	81.5	A956	B	B	B	B	B	B	B	B	B	E	E
	103.0	A967	B	B	B	B	B	B	B	B	B	E	E

TABLE 4. (Concluded)

Item	Item Code	Counter									
		1078	611	612	614	615	610	635	675	1093	561 562
	132.0 A968	B	B	B	B	B	B	B	B	B	E E
	155.8 A969	B	B	B	B	B	B	B	B	B	E E
	184.8 A970	B	B	B	B	B	B	B	B	B	E E
	238.1 A971	B	B	B	B	B	B	B	B	B	E E
	263.0 A972	B	B	B	B	B	B	B	B	B	E E

Symbols

B - Harmonic analysis performed on the test data and envelope plots created.

E - Envelope plots only

M - Test data missing

signal versus azimuth, the analyst can determine the blade azimuth at which the stagnation point crosses each wire, and then plot the stagnation point location versus azimuth.

A scale model of the OLS airfoil had been built to calibrate stagnation point location with angle of attack, but the wind tunnel test was not conducted. In the absence of an experimental calibration, the government supplied a set of calibration curves computed with a two-dimensional airfoil program<sup>12</sup> (Figure 3). These curves and the Mach number time history at each radial station were used to convert the stagnation point time history to an angle-of-attack time history. Finally, the angle-of-attack time histories were converted into main rotor contour plots.

---

<sup>12</sup>Smetana, F. O., Summey, D. C., Smith, N. S., and Carden, R. K., LIGHT AIRCRAFT LIFT, DRAG AND MOMENT PREDICTION, A REVIEW AND ANALYSIS, CR 2523, National Aeronautics and Space Administration, Washington, D. C., 1975.

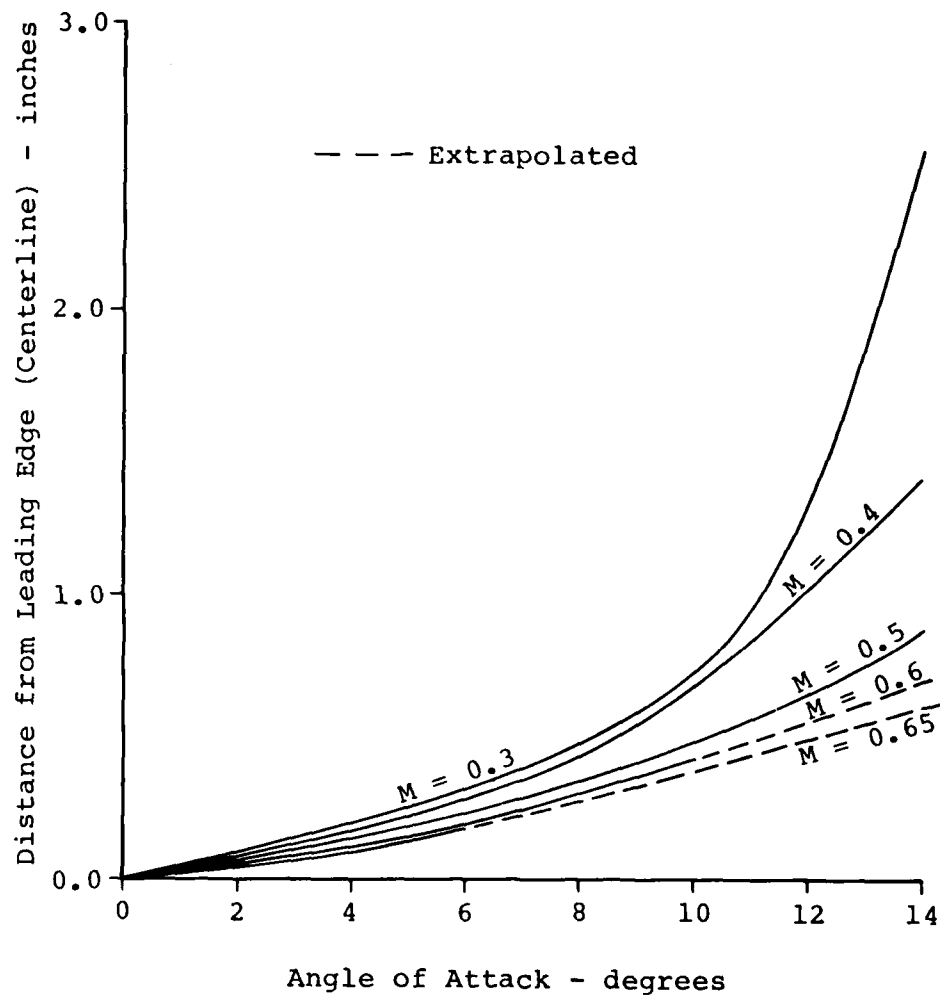


Figure 3. Stagnation Point Location Calibration Curves.



### 3. DATA DECK PREPARATION

Once a physical system has been analyzed, and the analysis coded for simulation, the quality of the results is directly dependent upon the quality of the data used as inputs to the simulation. The Rotorcraft Flight Simulation Program C81 can have up to 120 inputs just to control the type of analysis performed; it can have over 60,000 inputs to describe the aircraft geometry and the aerodynamics for a trim or a trim plus flightpath stability run. A complete sensitivity analysis has yet to be performed on C81, but many of the inputs have a very strong bearing on the results, while others have a very small effect on the outcome of the simulation.

As part of the effort described in this report, the investigators have endeavored to document the input data deck describing the AH-1G with the instrumented rotor. The method of assembling the deck, the source of the inputs, and the assumptions made in estimating those inputs not directly measurable are described below, in the order in which the data are input. It should be noted that a production AH-1G deck existed as a starting point, and that approximately 250 man-hours were expended in the acquisition and documentation of the data deck. Staley (Reference 7) has indicated that the first time he assembled a C81 data deck (to represent an MBB/Vertol BO-105), the process required approximately 400 manhours.

The OLS deck described here was assembled in less time only due to the experience of the users and the existence of an AH-1G deck.

#### 3.1 PROGRAM LOGIC GROUP

The inputs in the Program Logic Group were selected to give the desired input, analytical and output options (see Sections 2.3 and 3.3 of Volume II of Reference 3). The inputs are listed in Figure 4.

##### CARD 11

IPL(1) was zero, since a full aircraft was being modeled.

IPL(2) was set to 2 because an airfoil table was being used for each rotor, but the wing and stabilizing surface aerodynamics were being represented by equations.

IPL(3) was zero, since both rotors were included in the model.



The main rotor was modeled with 20 unequal segments, so IPL(4) was set to -20. The tail rotor was modeled with five equal segments (IPL(5) = 5). This has been found to improve the aerodynamic representation over that obtained with the standard three segments when the correct hub extent and built-in tip-loss factor are retained in the Tail Rotor Group.

The OLS main rotor was modeled as inelastic (IPL(6) = 0) for initial performance runs and with nine elastic mode shapes (IPL(6) = 9) for the blade loads and acceleration analysis. The tail rotor was modeled as inelastic (IPL(7) = 0).

Both rotor pylons were modeled as inelastic, so IPL(9) and IPL(10) were set to zero for all cases.

Separate rotor airfoil aerodynamic subgroups were used for the rotors, so IPL(11) = 2.

A Rotor-Induced Velocity Distribution table was used for the main rotor during some of the analysis. IPL(12) was set to 1 for those cases.

Rotor Wake Tables and Harmonic Blade Shakers were not used, so IPL(13) = IPL(14) = 0.

#### CARD 12

The Wing Group and Stabilizing Surface #1 Group (vertical stabilizer) were input without control linkage inputs, so IPL(15) and IPL(16) were input as -1. The elevator is connected to the longitudinal cyclic. Stabilizer Surface #2 and #3 Groups, which represent the right and left horizontal stabilizers were input with control linkages, so IPL(17) and IPL(18) were input as 1. A fourth stabilizing surface was not required to model the OLS aircraft, so IPL(19) was set to 0.

Some of the OLS aircraft configurations simulated had four external stores. IPL(21) was set to 4 for those cases.

The remainder of the inputs on CARD 12 and all of those on CARD 13 were set to 0.

#### CARD 14

The flight condition indicator, IPL(43), was set to 0 because unaccelerated trims were being simulated. IPL(44) was set to 1 so that the roll angle was held constant at the input value for each trim, except for the 10 KTAS case. Yaw angle was held constant for that case, with IPL(44) = 0.

A partial derivative matrix was computed every fifth iteration (IPL(45) = 0 or 5), as this has been found to give a reasonable balance between rapid convergence and reduced run time.

The first Rotor Aerodynamic Subgroup was used for the main rotor aerodynamics (IPL(46) = 1) and the second subgroup was used for the tail rotor aerodynamics (IPL(47) = 2).

Neither unsteady aerodynamics option was invoked during the analysis, so IPL(48) was set to 0.

The quasi-static trim (IPL(49) = IPL(50) = 0) procedure was used for both rotors except when the main rotor was modeled with elastic modes. In the latter case, IPL(49) was set to 1.

It was found to be unnecessary to decouple and rebalance either rotor during the trim procedure, so both IPL(51) and IPL(52) were set to zero.

IPL(53) was set to 1 whenever the time-varient trim was activated so that blade element accelerations were computed for the elastic rotor.

The inputs on the remainder of CARD 14 and all the inputs on CARD 15 were set to zero.

#### CARD 16

IPL(71) was set to 0 for the initial trim in each sweep and set to 2 for subsequent trims in the run in order to suppress additional, unnecessary, printout of the inputs.

IPL(72) was set to 1 in order to have trim iteration data printed out. In the event that a case fails to trim, the trim iteration data facilitates locating the cause of the problem.

IPL(73) was set to 1 to have the optional trim page printed for the main rotor.

IPL(74) through IPL(78) were set to zero, as the output options controlled by these inputs were not desired.

IPL(79) was set to 1 for many of the trim cases so that main rotor contour plots would be generated.

The inputs on the remainder of CARD 16 and all the inputs on CARD 17 were set to zero, as none of the options controlled by those inputs were required for the OLS correlation study.

### 3.2 ROTOR AERODYNAMIC TABLES

The input format for the Rotor Aerodynamic Tables is given in Sections 2.4 and 3.4 of Volume II of Reference 3. The tables used in this analysis are listed in Figures 5 and 6.

Separate tables were used to provide the steady-state aerodynamic coefficients for the main and tail rotors. No aerodynamic data are available for the OLS main rotor airfoil; but due to its similarity to the production AH-1G airfoil (BHT-developed 540 airfoil), the table for that airfoil was used (See Figure 5). The data in that table are based on a wind tunnel test, with standard corrections applied to  $C_{l_{\max}}$  and  $C_{D_0}$ . (The wind tunnel test was documented in a BHT memo, which is not available in the public domain. The exact corrections have not been documented.)

The test data were also smoothed to account for data scatter and asymmetries. Since high angle-of-attack and high Mach number test data were not available for the 540 airfoil, data for these conditions for a NACA 0012 were taken from Reference 13. The two sets of data were joined together with a smooth transition.

A production AH-1G tail rotor was used during the OLS tests. This rotor has a NACA 0015 airfoil, and the table listed in Figure 6 provides the aerodynamic coefficients for this airfoil. The data table was constructed using the data in Reference 14 and extending the Mach number range using Reference 15. No pitching moment coefficients were prepared for inclusion in this table.

<sup>13</sup>Critzos, C. C., Heyson, H. H., and Boswinkel, R. W., Jr., AERODYNAMIC CHARACTERISTICS OF NACA 0012 AIRFOIL SECTION AT ANGLES OF ATTACK from 0° to 180°, NACA TN 3361, National Advisory Council for Aeronautics, Washington, D. C., 1955.

<sup>14</sup>Shivers, J. P., and Carpenter P. J., EFFECTS OF COMPRESSIBILITY ON ROTOR HOVERING PERFORMANCE AND SYNTHESIZED BLADE-SECTION CHARACTERISTICS DERIVED FROM MEASURED ROTOR PERFORMANCE OF BLADES HAVING NACA 0015 AIRFOIL TIP SECTIONS, NACA TN 4356, National Advisory Council for Aeronautics, Washington, D. C., 1958.

<sup>15</sup>Graham, D. J., Nitzberg, G. E., and Olson, N., A SYSTEMATIC INVESTIGATION OF PRESSURE DISTRIBUTIONS AT HIGH SPEEDS OVER FIVE REPRESENTATIVE NACA LOW-DRAG AND CONVENTIONAL AIRFOIL SECTIONS, NACA TR-832, National Advisory Council for Aeronautics, Washington, D.C., 1949.

SUPER 540 EXT'D SUPER 540 EXT'D CLCD DATA TABLES USED

ALPHA/MACH	0.0	0.1	0.2	0.3	0.4	0.5	0.6	0.7	0.8	0.9	1.0	1.1	1.2	1.3	1.4	1.5	1.6	1.7	1.8	1.9	2.0	2.1	2.2	2.3	2.4	2.5	2.6	2.7	2.8	2.9	3.0	3.1	3.2	3.3	3.4	3.5	3.6	3.7	3.8	3.9	4.0	4.1	4.2	4.3	4.4	4.5	4.6	4.7	4.8	4.9	5.0	5.1	5.2	5.3	5.4	5.5	5.6	5.7	5.8	5.9	6.0	6.1	6.2	6.3	6.4	6.5	6.6	6.7	6.8	6.9	7.0	7.1	7.2	7.3	7.4	7.5	7.6	7.7	7.8	7.9	8.0	8.1	8.2	8.3	8.4	8.5	8.6	8.7	8.8	8.9	9.0	9.1	9.2	9.3	9.4	9.5	9.6	9.7	9.8	9.9	10.0	10.1	10.2	10.3	10.4	10.5	10.6	10.7	10.8	10.9	11.0	11.1	11.2	11.3	11.4	11.5	11.6	11.7	11.8	11.9	12.0	12.1	12.2	12.3	12.4	12.5	12.6	12.7	12.8	12.9	13.0	13.1	13.2	13.3	13.4	13.5	13.6	13.7	13.8	13.9	14.0	14.1	14.2	14.3	14.4	14.5	14.6	14.7	14.8	14.9	15.0	15.1	15.2	15.3	15.4	15.5	15.6	15.7	15.8	15.9	16.0	16.1	16.2	16.3	16.4	16.5	16.6	16.7	16.8	16.9	17.0	17.1	17.2	17.3	17.4	17.5	17.6	17.7	17.8	17.9	18.0	18.1	18.2	18.3	18.4	18.5	18.6	18.7	18.8	18.9	19.0	19.1	19.2	19.3	19.4	19.5	19.6	19.7	19.8	19.9	20.0	20.1	20.2	20.3	20.4	20.5	20.6	20.7	20.8	20.9	21.0	21.1	21.2	21.3	21.4	21.5	21.6	21.7	21.8	21.9	22.0	22.1	22.2	22.3	22.4	22.5	22.6	22.7	22.8	22.9	23.0	23.1	23.2	23.3	23.4	23.5	23.6	23.7	23.8	23.9	24.0	24.1	24.2	24.3	24.4	24.5	24.6	24.7	24.8	24.9	25.0	25.1	25.2	25.3	25.4	25.5	25.6	25.7	25.8	25.9	26.0	26.1	26.2	26.3	26.4	26.5	26.6	26.7	26.8	26.9	27.0	27.1	27.2	27.3	27.4	27.5	27.6	27.7	27.8	27.9	28.0	28.1	28.2	28.3	28.4	28.5	28.6	28.7	28.8	28.9	29.0	29.1	29.2	29.3	29.4	29.5	29.6	29.7	29.8	29.9	30.0	30.1	30.2	30.3	30.4	30.5	30.6	30.7	30.8	30.9	31.0	31.1	31.2	31.3	31.4	31.5	31.6	31.7	31.8	31.9	32.0	32.1	32.2	32.3	32.4	32.5	32.6	32.7	32.8	32.9	33.0	33.1	33.2	33.3	33.4	33.5	33.6	33.7	33.8	33.9	34.0	34.1	34.2	34.3	34.4	34.5	34.6	34.7	34.8	34.9	35.0	35.1	35.2	35.3	35.4	35.5	35.6	35.7	35.8	35.9	36.0	36.1	36.2	36.3	36.4	36.5	36.6	36.7	36.8	36.9	37.0	37.1	37.2	37.3	37.4	37.5	37.6	37.7	37.8	37.9	38.0	38.1	38.2	38.3	38.4	38.5	38.6	38.7	38.8	38.9	39.0	39.1	39.2	39.3	39.4	39.5	39.6	39.7	39.8	39.9	40.0	40.1	40.2	40.3	40.4	40.5	40.6	40.7	40.8	40.9	41.0	41.1	41.2	41.3	41.4	41.5	41.6	41.7	41.8	41.9	42.0	42.1	42.2	42.3	42.4	42.5	42.6	42.7	42.8	42.9	43.0	43.1	43.2	43.3	43.4	43.5	43.6	43.7	43.8	43.9	44.0	44.1	44.2	44.3	44.4	44.5	44.6	44.7	44.8	44.9	45.0	45.1	45.2	45.3	45.4	45.5	45.6	45.7	45.8	45.9	46.0	46.1	46.2	46.3	46.4	46.5	46.6	46.7	46.8	46.9	47.0	47.1	47.2	47.3	47.4	47.5	47.6	47.7	47.8	47.9	48.0	48.1	48.2	48.3	48.4	48.5	48.6	48.7	48.8	48.9	49.0	49.1	49.2	49.3	49.4	49.5	49.6	49.7	49.8	49.9	50.0	50.1	50.2	50.3	50.4	50.5	50.6	50.7	50.8	50.9	51.0	51.1	51.2	51.3	51.4	51.5	51.6	51.7	51.8	51.9	52.0	52.1	52.2	52.3	52.4	52.5	52.6	52.7	52.8	52.9	53.0	53.1	53.2	53.3	53.4	53.5	53.6	53.7	53.8	53.9	54.0	54.1	54.2	54.3	54.4	54.5	54.6	54.7	54.8	54.9	55.0	55.1	55.2	55.3	55.4	55.5	55.6	55.7	55.8	55.9	56.0	56.1	56.2	56.3	56.4	56.5	56.6	56.7	56.8	56.9	57.0	57.1	57.2	57.3	57.4	57.5	57.6	57.7	57.8	57.9	58.0	58.1	58.2	58.3	58.4	58.5	58.6	58.7	58.8	58.9	59.0	59.1	59.2	59.3	59.4	59.5	59.6	59.7	59.8	59.9	60.0	60.1	60.2	60.3	60.4	60.5	60.6	60.7	60.8	60.9	61.0	61.1	61.2	61.3	61.4	61.5	61.6	61.7	61.8	61.9	62.0	62.1	62.2	62.3	62.4	62.5	62.6	62.7	62.8	62.9	63.0	63.1	63.2	63.3	63.4	63.5	63.6	63.7	63.8	63.9	64.0	64.1	64.2	64.3	64.4	64.5	64.6	64.7	64.8	64.9	65.0	65.1	65.2	65.3	65.4	65.5	65.6	65.7	65.8	65.9	66.0	66.1	66.2	66.3	66.4	66.5	66.6	66.7	66.8	66.9	67.0	67.1	67.2	67.3	67.4	67.5	67.6	67.7	67.8	67.9	68.0	68.1	68.2	68.3	68.4	68.5	68.6	68.7	68.8	68.9	69.0	69.1	69.2	69.3	69.4	69.5	69.6	69.7	69.8	69.9	70.0	70.1	70.2	70.3	70.4	70.5	70.6	70.7	70.8	70.9	71.0	71.1	71.2	71.3	71.4	71.5	71.6	71.7	71.8	71.9	72.0	72.1	72.2	72.3	72.4	72.5	72.6	72.7	72.8	72.9	73.0	73.1	73.2	73.3	73.4	73.5	73.6	73.7	73.8	73.9	74.0	74.1	74.2	74.3	74.4	74.5	74.6	74.7	74.8	74.9	75.0	75.1	75.2	75.3	75.4	75.5	75.6	75.7	75.8	75.9	76.0	76.1	76.2	76.3	76.4	76.5	76.6	76.7	76.8	76.9	77.0	77.1	77.2	77.3	77.4	77.5	77.6	77.7	77.8	77.9	78.0	78.1	78.2	78.3	78.4	78.5	78.6	78.7	78.8	78.9	79.0	79.1	79.2	79.3	79.4	79.5	79.6	79.7	79.8	79.9	80.0	80.1	80.2	80.3	80.4	80.5	80.6	80.7	80.8	80.9	81.0	81.1	81.2	81.3	81.4	81.5	81.6	81.7	81.8	81.9	82.0	82.1	82.2	82.3	82.4	82.5	82.6	82.7	82.8	82.9	83.0	83.1	83.2	83.3	83.4	83.5	83.6	83.7	83.8	83.9	84.0	84.1	84.2	84.3	84.4	84.5	84.6	84.7	84.8	84.9	85.0	85.1	85.2	85.3	85.4	85.5	85.6	85.7	85.8	85.9	86.0	86.1	86.2	86.3	86.4	86.5	86.6	86.7	86.8	86.9	87.0	87.1	87.2	87.3	87.4	87.5	87.6	87.7	87.8	87.9	88.0	88.1	88.2	88.3	88.4	88.5	88.6	88.7	88.8	88.9	89.0	89.1	89.2	89.3	89.4	89.5	89.6	89.7	89.8	89.9	90.0	90.1	90.2	90.3	90.4	90.5	90.6	90.7	90.8	90.9	91.0	91.1	91.2	91.3	91.4	91.5	91.6	91.7	91.8	91.9	92.0	92.1	92.2	92.3	92.4	92.5	92.6	92.7	92.8	92.9	93.0	93.1	93.2	93.3	93.4	93.5	93.6	93.7	93.8	93.9	94.0	94.1	94.2	94.3	94.4	94.5	94.6	94.7	94.8	94.9	95.0	95.1	95.2	95.3	95.4	95.5	95.6	95.7	95.8	95.9	96.0	96.1	96.2	96.3	96.4	96.5	96.6	96.7	96.8	96.9	97.0	97.1	97.2	97.3	97.4	97.5	97.6	97.7	97.8	97.9	98.0	98.1	98.2	98.3	98.4	98.5	98.6	98.7	98.8	98.9	99.0	99.1	99.2	99.3	99.4	99.5	99.6	99.7	99.8	99.9	100.0
------------	-----	-----	-----	-----	-----	-----	-----	-----	-----	-----	-----	-----	-----	-----	-----	-----	-----	-----	-----	-----	-----	-----	-----	-----	-----	-----	-----	-----	-----	-----	-----	-----	-----	-----	-----	-----	-----	-----	-----	-----	-----	-----	-----	-----	-----	-----	-----	-----	-----	-----	-----	-----	-----	-----	-----	-----	-----	-----	-----	-----	-----	-----	-----	-----	-----	-----	-----	-----	-----	-----	-----	-----	-----	-----	-----	-----	-----	-----	-----	-----	-----	-----	-----	-----	-----	-----	-----	-----	-----	-----	-----	-----	-----	-----	-----	-----	-----	-----	-----	-----	------	------	------	------	------	------	------	------	------	------	------	------	------	------	------	------	------	------	------	------	------	------	------	------	------	------	------	------	------	------	------	------	------	------	------	------	------	------	------	------	------	------	------	------	------	------	------	------	------	------	------	------	------	------	------	------	------	------	------	------	------	------	------	------	------	------	------	------	------	------	------	------	------	------	------	------	------	------	------	------	------	------	------	------	------	------	------	------	------	------	------	------	------	------	------	------	------	------	------	------	------	------	------	------	------	------	------	------	------	------	------	------	------	------	------	------	------	------	------	------	------	------	------	------	------	------	------	------	------	------	------	------	------	------	------	------	------	------	------	------	------	------	------	------	------	------	------	------	------	------	------	------	------	------	------	------	------	------	------	------	------	------	------	------	------	------	------	------	------	------	------	------	------	------	------	------	------	------	------	------	------	------	------	------	------	------	------	------	------	------	------	------	------	------	------	------	------	------	------	------	------	------	------	------	------	------	------	------	------	------	------	------	------	------	------	------	------	------	------	------	------	------	------	------	------	------	------	------	------	------	------	------	------	------	------	------	------	------	------	------	------	------	------	------	------	------	------	------	------	------	------	------	------	------	------	------	------	------	------	------	------	------	------	------	------	------	------	------	------	------	------	------	------	------	------	------	------	------	------	------	------	------	------	------	------	------	------	------	------	------	------	------	------	------	------	------	------	------	------	------	------	------	------	------	------	------	------	------	------	------	------	------	------	------	------	------	------	------	------	------	------	------	------	------	------	------	------	------	------	------	------	------	------	------	------	------	------	------	------	------	------	------	------	------	------	------	------	------	------	------	------	------	------	------	------	------	------	------	------	------	------	------	------	------	------	------	------	------	------	------	------	------	------	------	------	------	------	------	------	------	------	------	------	------	------	------	------	------	------	------	------	------	------	------	------	------	------	------	------	------	------	------	------	------	------	------	------	------	------	------	------	------	------	------	------	------	------	------	------	------	------	------	------	------	------	------	------	------	------	------	------	------	------	------	------	------	------	------	------	------	------	------	------	------	------	------	------	------	------	------	------	------	------	------	------	------	------	------	------	------	------	------	------	------	------	------	------	------	------	------	------	------	------	------	------	------	------	------	------	------	------	------	------	------	------	------	------	------	------	------	------	------	------	------	------	------	------	------	------	------	------	------	------	------	------	------	------	------	------	------	------	------	------	------	------	------	------	------	------	------	------	------	------	------	------	------	------	------	------	------	------	------	------	------	------	------	------	------	------	------	------	------	------	------	------	------	------	------	------	------	------	------	------	------	------	------	------	------	------	------	------	------	------	------	------	------	------	------	------	------	------	------	------	------	------	------	------	------	------	------	------	------	------	------	------	------	------	------	------	------	------	------	------	------	------	------	------	------	------	------	------	------	------	------	------	------	------	------	------	------	------	------	------	------	------	------	------	------	------	------	------	------	------	------	------	------	------	------	------	------	------	------	------	------	------	------	------	------	------	------	------	------	------	------	------	------	------	------	------	------	------	------	------	------	------	------	------	------	------	------	------	------	------	------	------	------	------	------	------	------	------	------	------	------	------	------	------	------	------	------	------	------	------	------	------	------	------	------	------	------	------	------	------	------	------	------	------	------	------	------	------	------	------	------	------	------	------	------	------	------	------	------	------	------	------	------	------	------	------	------	------	------	------	------	------	------	------	------	------	------	------	------	------	------	------	------	------	------	------	------	------	------	------	------	------	------	------	------	------	------	------	------	------	------	------	------	------	------	------	------	------	------	------	------	------	------	------	------	------	------	------	------	------	------	------	------	------	------	------	------	------	------	------	------	------	------	------	------	------	------	------	------	------	------	------	------	------	------	------	------	------	------	------	------	------	------	------	------	------	------	------	------	------	------	------	------	------	------	------	------	------	------	------	------	------	------	------	------	------	------	------	------	------	------	------	------	------	------	------	------	------	------	------	------	------	------	------	------	------	------	------	------	------	------	------	------	------	------	------	------	------	------	------	------	------	------	------	------	------	------	------	------	------	------	------	------	------	------	------	------	------	------	------	------	------	------	------	------	------	------	------	------	------	------	------	------	------	------	------	------	-------

Figure 5. Aerodynamic Table for Bell 540 Airfoil Section.

[illegible]

**Figure 5. Continued.**

SUPER 540 EXT'D SUPER 540 EXT'D CLCD DATA TABLES USED

ALPHA/MACH	0.20000	0.30000	0.40000	0.50000	0.60000	0.70000	0.75000	0.80000	0.90000
-180+00000	0.0	0.0	0.0	0.0	0.0	0.0	0.0	0.0	0.0
-170+00000	0.0	0.0	0.0	0.0	0.0	0.0	0.0	0.0	0.0
-160+00000	0.0	0.0	0.0	0.0	0.0	0.0	0.0	0.0	0.0
-150+00000	0.0	0.0	0.0	0.0	0.0	0.0	0.0	0.0	0.0
-140+00000	0.0	0.0	0.0	0.0	0.0	0.0	0.0	0.0	0.0
-130+00000	0.0	0.0	0.0	0.0	0.0	0.0	0.0	0.0	0.0
-120+00000	0.0	0.0	0.0	0.0	0.0	0.0	0.0	0.0	0.0
-110+00000	0.0	0.0	0.0	0.0	0.0	0.0	0.0	0.0	0.0
-100+00000	0.0	0.0	0.0	0.0	0.0	0.0	0.0	0.0	0.0
-90+00000	0.0	0.0	0.0	0.0	0.0	0.0	0.0	0.0	0.0
-80+00000	0.0	0.0	0.0	0.0	0.0	0.0	0.0	0.0	0.0
-70+00000	0.0	0.0	0.0	0.0	0.0	0.0	0.0	0.0	0.0
-60+00000	0.0	0.0	0.0	0.0	0.0	0.0	0.0	0.0	0.0
-50+00000	0.0	0.0	0.0	0.0	0.0	0.0	0.0	0.0	0.0
-40+00000	0.0	0.0	0.0	0.0	0.0	0.0	0.0	0.0	0.0
-30+00000	0.0	0.0	0.0	0.0	0.0	0.0	0.0	0.0	0.0
-20+00000	0.0	0.0	0.0	0.0	0.0	0.0	0.0	0.0	0.0
-10+00000	0.0	0.0	0.0	0.0	0.0	0.0	0.0	0.0	0.0
0+00000	0.0	0.0	0.0	0.0	0.0	0.0	0.0	0.0	0.0
10+00000	0.0	0.0	0.0	0.0	0.0	0.0	0.0	0.0	0.0
20+00000	0.0	0.0	0.0	0.0	0.0	0.0	0.0	0.0	0.0
30+00000	0.0	0.0	0.0	0.0	0.0	0.0	0.0	0.0	0.0
40+00000	0.0	0.0	0.0	0.0	0.0	0.0	0.0	0.0	0.0
50+00000	0.0	0.0	0.0	0.0	0.0	0.0	0.0	0.0	0.0
60+00000	0.0	0.0	0.0	0.0	0.0	0.0	0.0	0.0	0.0
70+00000	0.0	0.0	0.0	0.0	0.0	0.0	0.0	0.0	0.0
80+00000	0.0	0.0	0.0	0.0	0.0	0.0	0.0	0.0	0.0
90+00000	0.0	0.0	0.0	0.0	0.0	0.0	0.0	0.0	0.0
100+00000	0.0	0.0	0.0	0.0	0.0	0.0	0.0	0.0	0.0
110+00000	0.0	0.0	0.0	0.0	0.0	0.0	0.0	0.0	0.0
120+00000	0.0	0.0	0.0	0.0	0.0	0.0	0.0	0.0	0.0
130+00000	0.0	0.0	0.0	0.0	0.0	0.0	0.0	0.0	0.0
140+00000	0.0	0.0	0.0	0.0	0.0	0.0	0.0	0.0	0.0
150+00000	0.0	0.0	0.0	0.0	0.0	0.0	0.0	0.0	0.0
160+00000	0.0	0.0	0.0	0.0	0.0	0.0	0.0	0.0	0.0
170+00000	0.0	0.0	0.0	0.0	0.0	0.0	0.0	0.0	0.0
180+00000	0.0	0.0	0.0	0.0	0.0	0.0	0.0	0.0	0.0

Figure 5. Concluded.



Figure 6. Aerodynamic Table for NACA 0015 Airfoil Section.





CCCC DATA TABLES USED

CM

NACA D013

1.000000  
0.000000  
0.00

0.00  
0.00  
0.00

ALPHA/PI  
-1.000000  
1.000000

Figure 6. Concluded.

### 3.3 MAIN ROTOR GROUP

The input format for the Main Rotor Group is described in Sections 2.5 and 3.5 of Volume II of Reference 3. The inputs for this group are listed in Figure 7.

Main rotor hub and blade inputs were taken, in part, from the following drawings:

- AH-1G Basic Lines Data (Figure 8)
- 540-011-001 Blade Assembly
- 540-011-101 Hub and Blade Assembly
- 540-011-102 Trunnion
- 540-011-147 Pitch Horn Assembly
- 540-011-154 Grip Assembly
- 299-328-001 Blade Assembly Advanced Instrumentation
- 540 Main Rotor

(The production AH-1G main rotor is designated as the Model 540, or 540, rotor system).

#### CARD 31

There are two main rotor blades (XMR(1)), and the undersling (XMR(2) = 4.5) was determined from the -101 drawing.

The input for the aerodynamic reference center was 101.0 so that CARDS 3K through 3M would be read to give the radial distribution of the aerodynamic reference center.

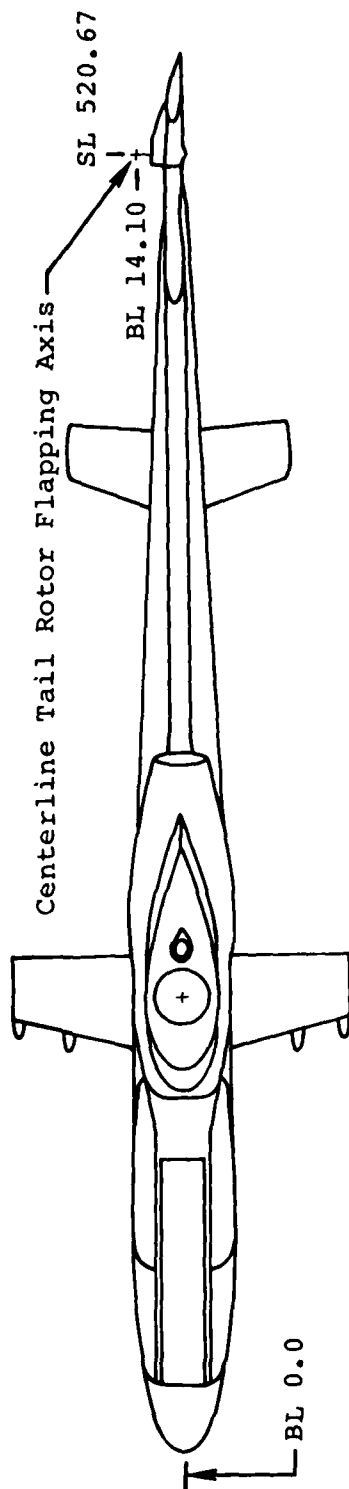
The radius (XMR(4) = 22.0) was determined from the -101 drawing.

The chord was input as zero because the radial chord distribution was to be input on CARDS 3N through 3P.

The linear,  $-10^\circ$ , twist distribution was determined from the -001 blade drawing. The flapping stop location (XMR(7) = 12.0) was determined from the -101 drawing.

MINKTULSN		VAN GAASDEEK AN-16 MAIN ROTOR GROUP 209 ROTOR WITH OLS INS'YR.		(05-02-74)		MAIN ROTOR GROUP		-10-00000		-01		12-00000	
2-0000000	4-000000	101-0000	22-00000	0	135-000	0	0	0	0	0	0	0	0
200-0000	0	132-700	47-00001	0	1000000	0	0	0	0	0	0	0	0
1-000000	0	180-9-00	0	0	0	0	0	0	0	0	0	0	0
2-070000	0	0	1-100000	0	0	0	0	0	0	0	0	0	0
0	0	-9-067000	14-10000	0	0	0	0	0	0	0	0	0	0
0	0	0	0	0	0	0	0	0	0	0	0	0	0
0	0	0	0	0	0	0	0	0	0	0	0	0	0
5-000000	0	0	0	0	0	0	0	0	0	0	0	0	0
6-000000	20-07300	37-00000	52-00000	0	0	0	0	0	0	0	0	0	0
103-0000	118-0000	132-0000	143-2000	0	0	0	0	0	0	0	0	0	0
1-08-0000	212-3000	224-0000	238-1000	0	0	0	0	0	0	0	0	0	0
0	0	0	0	0	0	0	0	0	0	0	0	0	0
-02012500	-02012500	-02012500	-02012500	0	0	0	0	0	0	0	0	0	0
-02012500	-02012500	-02012500	-02012500	0	0	0	0	0	0	0	0	0	0
14-00000	19-00001	6-200000	27-00000	0	0	0	0	0	0	0	0	0	0
2-0-02500	26-02500	26-02500	28-02500	0	0	0	0	0	0	0	0	0	0
26-02500	26-02500	28-02500	28-02500	0	0	0	0	0	0	0	0	0	0

Figure 7. OLS Main Rotor Group.



SCALE 0.015" = 1.0"

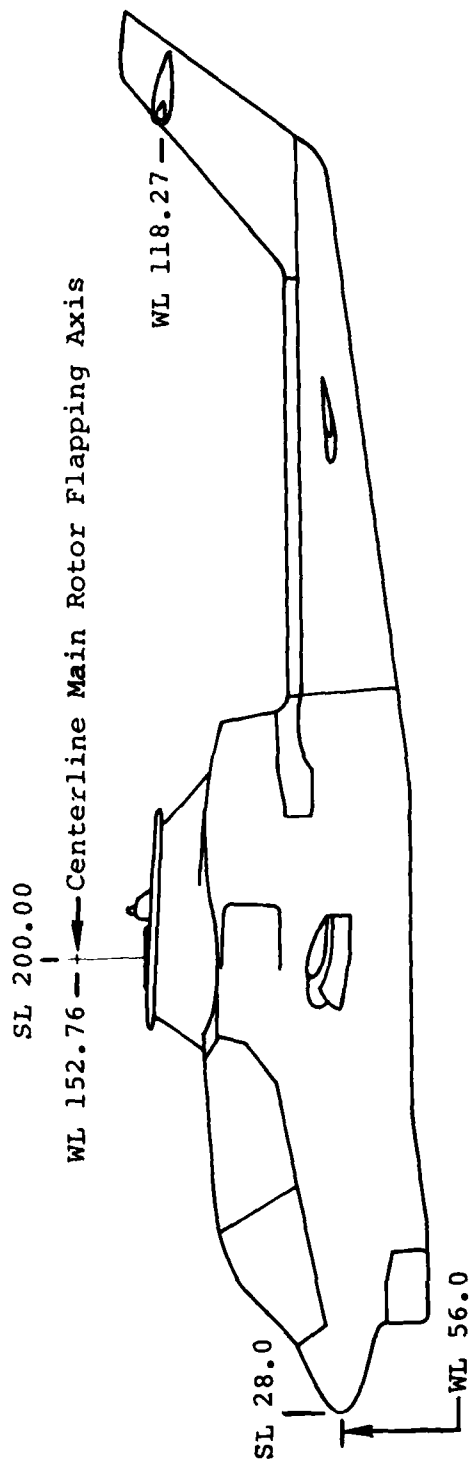


Figure 8. Simplified AH-1G Basic Lines Data Drawing.

### CARD 32

Since the mast is fixed with respect to the aircraft, the location of the main rotor teetering pin, as given on the AH-1G Basic Lines Drawing, was taken as the mast pivot point (XMR(8), XMR(9) and XMR(10)).

The blade weight and inertia inputs were computed by the Rotor Frequency Program DNAM05 (see Section 3.4 of this report). These two inputs (XMR(11) and XMR(12)) are the weight and flapping inertia of the blade, and that portion of the hub associated with the blade, that is outboard of the flapping hinge. For the OLS teetering rotor, these inputs are one-half the total weight and flapping inertia of the rotor. These two inputs were included in the deck whether or not elastic mode shapes were used to represent the rotor. If mode shapes were used, both of these inputs were ignored in the analysis, as C81 used the mass distribution input with the mode shapes.

The nominal main rotor and engine operating speeds are known to be 324 and 6600, respectively, yielding a rotor-to-engine gear ratio (XMR(13)) of 0.0491.

No rotor pitch-lag coupling ratio (XMR(14)) was input, as it would have a negligible effect for this teetering rotor in the quasi-static trim. The effect was included automatically in the elastic mode shapes when they were used.

### CARD 33

The rotor-to-swashplate angle ratio (XMR(15)) was input as 1.0 because all the effects of angled pitch links, scissor arms, and differences in swashplate and pitch horn radii were included in the control rigging in the Controls Group. The flapping stop spring rate, XMR(17), was determined by a static analysis of the mast, as described in Reference 16. (There is no separate flapping stop assembly on the AH-1G main rotor. Excessive down-flapping is restrained by contact between the lower inside portion of the central hole in the yoke assembly and the mast.)

There was no flapping spring on the OLS rotor, so XMR(18) was input as 0.0.

<sup>16</sup>Dooley, L. W., and Van Gaasbeek, J. R., FLAPPING LOAD PREDICTION AND NONLINEAR HUB SPRING DESIGN-INTERIM REPORT OF TASKS I AND II, Technical Report 699-099-091, Bell Helicopter Textron, Fort Worth, Texas, 1978, page 13.



The reduced rotor frequency for the UNSAN unsteady aerodynamics option (XMR(19)) was input as 1.0, even though this option was not invoked. (Unity is usually chosen for this input, as the predominant pitch motion of the blade is at one-per-rev due to control motion.)

The input for the lead-lag damper was zero because the OLS main rotor was a stiff inplane rotor, lacking a lag hinge and damper.

The hub extent, XMR(21), was set equal to the radius of the main rotor blade retention bolt, as determined from the -001 and -154 drawings.

#### CARD 34

The precone angle, XMR(22), was determined from the -101 drawing.

The pitch-change axis location, XMR(23), was input as zero, even though the quarter-chord of the sleeved section is not on the pitch-change axis. The effect of this offset on the steady-state aerodynamics is accounted for in the aerodynamic reference point offset distribution on CARDS 3K through 3M. The value input for XMR(23) is used only in the Theodorsen portion of the BUNS unsteady aerodynamics option, which was not invoked.

XMR(24) was input as 0.0 since the production AH-1G main rotor hub, which was unmodified for the OLS test program, has no pitch-flap coupling.

The drag coefficient for the hub, XMR(25), was estimated to be that of a two-dimensional ellipse of the same thickness ratio as the grip. The ellipse drag coefficient was taken from Reference 17, using a Reynolds number computed at the bolt-hole radius in hover on a standard day ( $6 \times 10^5$ ).

The OLS rotor had no lead-lag spring, and the tip vortex effect option was not activated; therefore both XMR(26) and XMR(27) were set to 0.0.

#### CARD 35

The OLS rotor had a square tip, so XMR(29) was input as zero, and XMR(30) was also input as zero to activate the internal tip-loss factor calculation.

---

<sup>17</sup>McCormick, B. W., AERODYNAMICS OF V/STOL FLIGHT, Academic Press, New York, 1967, page 33.

The pitch link moment arm, XMR(31), was determined from the -147 drawing.

The distance to the pitch-horn attachment point, XMR(32), was set to 14.1, which is the radius of the inboard feathering bearing. (The AH-1G main rotor hub geometry is shown in Figure 9.) The input to C81 must be consistent with the hub geometry inputs to DNAM05 (to be discussed in Section 3.4) to ensure that the coordinate transformation between the inplane-out-of-plane and beam-chord coordinate systems (discussed in Section 6.1.2) is performed at the correct radial station.

The downwash factor at the fuselage center-of-pressure was estimated using a simple method to be described in the discussion of the inputs to the Wing Group (Section 3.12.1 of this report). This method indicated that the downwash at the fuselage cp was zero except at very low speeds. The input was 2.0 between hover and 10 knots.

The pitch-cone coupling ratio, XMR(35), was computed to be -0.68 from the first coning mode calculated by DNAM05 (see Section 8.1.1.2 of Volume I of Reference 3). This input is used when the main rotor is modelled as inelastic. The input is ignored when elastic modes are input for the main rotor.

#### CARD 36

The main rotor nacelle weight was included in the overall weight of the aircraft, so XMR(36) through XMR(40) were set to 0.0.

The main rotor differential nacelle flat plate drag area was estimated to be due to two components. The first component consisted of the equivalent flat plate drag area of the rotating control components between the top of the sail (the cowling enclosing the transmission and engine) and the hub. This component of the drag was estimated to be equal to the drag of the two-dimensional cylinder swept by the pitch links at a Reynold's number for that cylinder at the maximum forward flight speed,  $R_e = 5 \times 10^5$ . This cylinder has a drag coefficient of 0.33 (Reference 17, page 33) and a frontal area of 3.0 square feet, yielding an equivalent flat plate drag area of 1.0 square foot. The equivalent flat plate drag area of the multiplexor box was the second component of the nacelle drag. The multiplexor box was a cylinder, so the drag coefficient of a cylinder at the Reynolds number at maximum forward flight airspeed was multiplied by the frontal area to yield an additional 1.0 square foot of flat plate drag area. Therefore, the nacelle flat plate drag, XMR(40), was input as 2.0 square feet.

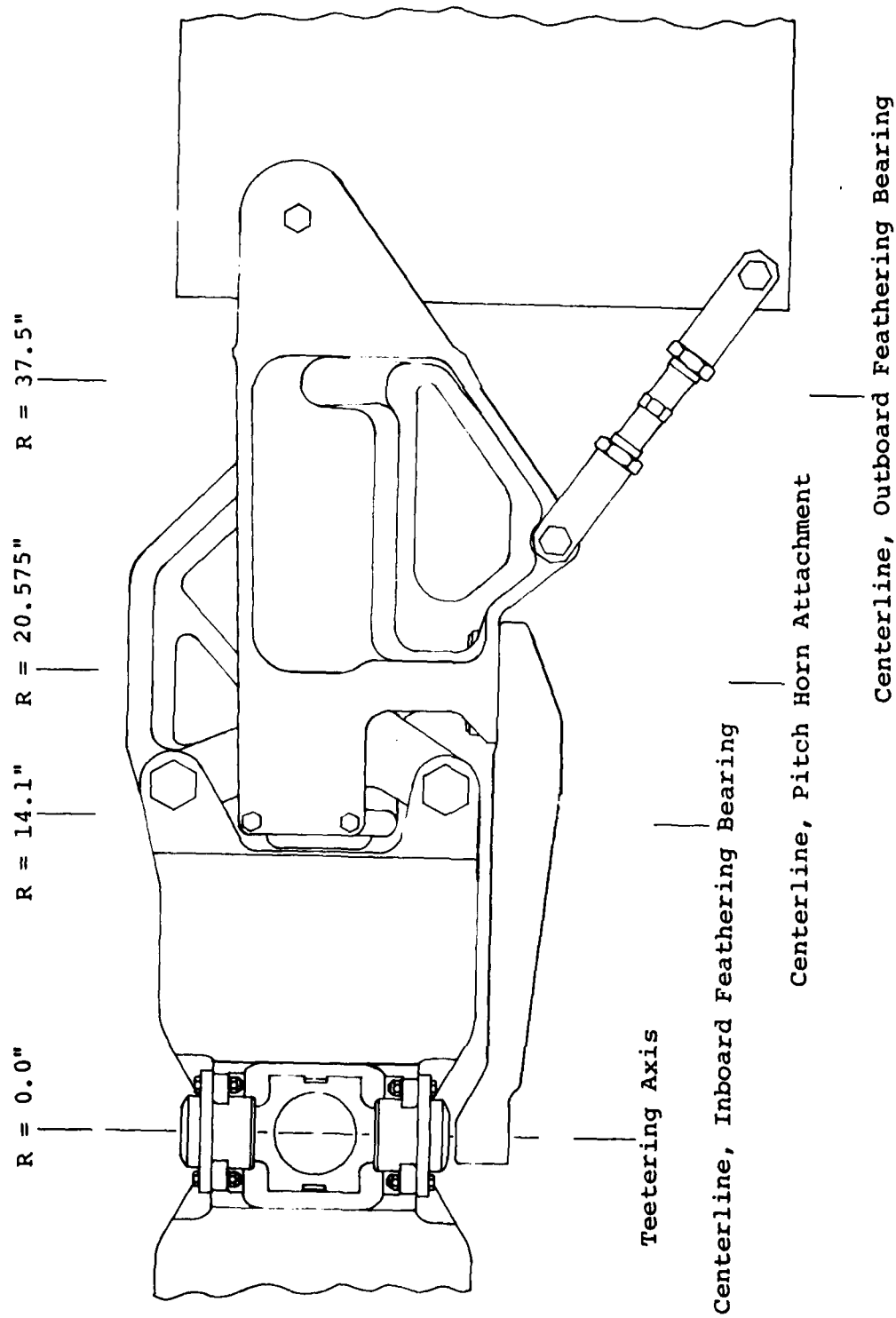


Figure 9. AH-1G OLS Main Rotor Hub.

The center of pressure of the nacelle drag was estimated to be half way between the top of the sail and the hub, so this distance was input for XMR(41).

The OLS main rotor first mass moment, XMR(42), was computed by DNAM05.

#### CARD 37

The AH-1G used in the test program had no control phasing or mast tilt, so XMR(43) through XMR(45) were input as zero.

The mast length, XMR(46), was also input as zero because the mast pivot point was located at the teetering pin.

The OLS main rotor did not have a nonlinear flapping spring, so XMR(47) through XMR(49) were set to 0.0.

#### CARD 38

The main rotor one-per-rev frequency, 5.4 hertz, was chosen as the filter frequency, as this would yield the maximum two-per-rev attenuation with the minimum of one-per-rev phase lag.

The remainder of the inputs on CARD 38 were set to 0.0 because the OLS rotor had no prelag and the precon starts at zero radius, as determined from the -101 drawing.

#### CARDS 39, 3A and 3B

Several considerations were involved in selecting the main rotor radius distribution. The primary consideration was to include the radii at which the blade instrumentation was located. In addition, previous experience had shown that segment lengths should be larger than two percent of the rotor radius, and less than ten percent. The shorter segments should be in the regions where the blade undergoes large elastic curvature.

#### CARDS 3C through 3J

A detailed NASTRAN model of the AH-1G helicopter had been prepared under an Army contract<sup>18</sup>. This model was modified to

<sup>18</sup>Cronkhite, J. D., Berry, V. L., and Brunken, J. E., A NASTRAN VIBRATION MODEL OF THE AH-1G HELICOPTER AIRFRAME, TR 74-045, U.S. Army Rock Island Arsenal, Rock Island, Illinois, 1974.

have a mass distribution approximately that of the OLS aircraft in its Flight 35A configuration. The gross weight and center-of-gravity stationline computed by NASTRAN were 8319 pounds and 199.5, while the flight-test engineer estimated these quantities to be 8319 pounds and 200.6 for the actual ship.

The frequencies computed for the first four elastic airframe modes were compared with the measured frequencies (taken from Reference 19) in Table 5. As can be seen, the pylon frequencies are underpredicted while the fuselage frequencies are computed in close agreement with those measured in shake test. The most likely cause for the discrepancy in the pylon frequencies is the inability to properly model the nonlinear Lord mounts used to attach the transmission to the airframe.

The NASTRAN-generated pylon frequencies and mode shapes, as listed in Figure 10, were used in initial simulations, but convergent trims were achieved only for a few cases. Since the pylon frequencies were not computed correctly and the shake-test data did not provide sufficient information to determine the pylon inputs experimentally, the pylon model was not used for any further simulation runs.

#### CARDS 3K through 3M

The airfoil lift and drag forces act through a given point on the section chordline called the aerodynamic reference point. The aerodynamic moment about this point depends solely on the value of  $C_M$  and is independent of the lift and drag forces.

The production 540 airfoil table, CLCD5474 (Section 3.2) was constructed using the section quarter-chord as the aerodynamic reference point.

The production 540 rotor was designed so that the section quarter chord and the pitch change axis were coincident. Therefore, inboard of the radius at which the sleeve starts (83 inches), the aerodynamic reference center offset was zero. The application of the sleeve extended the leading edge of the airfoil 0.125 inch and the trailing edge 1.5 inches, thereby shifting the aerodynamic reference center (quarter-chord) aft 0.28125 inch, which was the input outboard of radial station 83.

<sup>19</sup>White, J. A., MODEL AH-1G AIRFRAME AND CONTROL SYSTEM  
GROUND VIBRATION TEST RESULTS, Technical Report 299-099-819,  
Bell Helicopter Company, Fort Worth, Texas, 1976.

TABLE 5. COMPARISON OF MEASURED AND NASTRAN-COMPUTED  
FREQUENCIES FOR THE FIRST FOUR ELASTIC FUSELAGE  
MODES - AH-1G WITH OLS ROTOR, LIGHT GROSS  
WEIGHT, AFT CENTER-OF-GRAVITY CONFIGURATION.

MEASURED FREQUENCY, Hz											
RESPONSE COORDINATE		90-DEG GEAR				ENG REAR		T.R. MAST		NASTRAN- COMPUTED FREQUENCY, Hz	
		NOSE VERTICAL		BOX VERT		SLING VERT		VERT			
HUB FORCE	DIRECTION	VERT	LAT	LONG	LONGITUDINAL	LONGITUDINAL	LONGITUDINAL	LONG			
	MAGNITUDE	MAX	MAX	MAX	MAX	MAX	MAX	MAX			

Mode Shape  
Identification

2	Pylon Longitudinal	-	-	3.8	4.1	4.1	4.2	2.91
3	Pylon Lateral	-	5.0	-	-	-	-	3.84
4	1st Fuselage Lateral	-	6.9	-	-	-	-	7.24
5	1st Fuselage Vertical	7.9	-	8.6	8.8	8.3	8.4	8.07

The test data were extracted from Table VIII of Reference 19.

Figure 10. OLS Pylon Inputs, Full Rotor Mass.

### CARDS 3N through 3P

The chord at each radial station was determined from the Hub and Blade Assembly Drawing, 540-011-101, and the OLS Blade Drawing, 299-328-001.

### 3.4 MAIN ROTOR ELASTIC BLADE DATA GROUP

The Main Rotor Elastic Blade Data Group input format is given in Sections 2.6 and 3.6 of Volume II of Reference 3, and the inputs to this group are listed in Figure 11. Reference is also made to Section 7.1 of Volume II of Reference 3, which contains the User's Instructions for the Rotor Frequency Program DNAM05. The inputs to this auxiliary program for the OLS main rotor are listed in Figure 12.

Inputs to earlier versions of the Rotor Frequency program had been determined for the Model 540 rotor and continuously refined as the program and the physical description of the rotor improved.

The Model 540 inputs for the DF1758 version of the program were published in Reference 20. For the current study, the latest version of the inputs were modified to account for the change in midspan and tip tuning weights and the addition of the fiberglass sleeve. The structural properties of the sleeve were computed, using BHT Program CBCR02,<sup>21</sup> as

Sleeve Center-of-Gravity Location	10.96 Inches from Leading Edge
$\Delta \text{weight/inch}$	0.1678 lb/in.
$\Delta \rho I_{xx}$	0.00036 in.-lb-sec <sup>2</sup> /in.
$\Delta \rho I_{yy}$	0.035 in.-lb-sec <sup>2</sup> /in.
$\Delta EI_B$	$8.45 \times 10^6$ lb-in. <sup>2</sup>
$\Delta EI_C$	$579.9 \times 10^6$ lb-in. <sup>2</sup>

<sup>20</sup>Van Gaasbeek, J. R., AN INVESTIGATION OF HIGH-G MANEUVERS OF THE AH-1G HELICOPTER, USAAMRDL TR 75-18, Bell Helicopter Textron, U.S. Army Air Mobility Research and Development Laboratory, Eustis Directorate, Fort Eustis, Virginia, April 1975, AD A012234.

<sup>21</sup>Tisdale, P. R., COMPUTER PROGRAMS FOR ROTOR LOADS AND STRESS ANALYSIS, Technical Report 299-099-749, Bell Helicopter Company, Fort Worth, Texas, 1975, pages 4.1 through 4.13.



MAIN ROTOR AERELASTIC BLADE DISTRIBUTIONS AND DATA									
BLADE STATION NUMBER		HEIGHT (LB/IN)	BEAMWISE INERTIA (IN-LB-SEC <sup>2</sup> /IN)	CHORDWISE INERTIA (IN-LB-SEC <sup>2</sup> /IN)	BEAMWISE LG OFFSET (IN)	CHORDWISE LG OFFSET (IN)			
1	0.00	5.3702	0.0001	0.0090	0.00	0.00	0.00	0.00	0.00
2	20.57	5.7138	0.0090	0.1149	0.00	0.00	0.00	0.00	0.00
3	37.50	6.1672	0.0098	0.2190	0.00	0.00	0.00	0.00	0.00
4	52.80	6.6217	0.0121	0.3183	0.00	0.00	0.00	0.00	0.00
5	66.00	7.0750	0.0117	0.4189	0.00	0.00	0.00	0.00	0.00
6	77.00	7.5280	0.0017	0.4693	0.00	0.00	0.00	0.00	0.00
7	92.40	7.9810	0.0017	0.4693	0.00	0.00	0.00	0.00	0.00
8	103.00	8.4340	0.0017	0.4693	0.00	0.00	0.00	0.00	0.00
9	118.80	8.8870	0.0018	0.4693	0.00	0.00	0.00	0.00	0.00
10	132.00	9.3400	0.0018	0.4693	0.00	0.00	0.00	0.00	0.00
11	145.20	9.7930	0.0018	0.4693	0.00	0.00	0.00	0.00	0.00
12	155.80	10.2460	0.0024	0.4693	0.00	0.00	0.00	0.00	0.00
13	171.60	10.6990	0.0024	0.4693	0.00	0.00	0.00	0.00	0.00
14	184.80	11.1520	0.0014	0.4693	0.00	0.00	0.00	0.00	0.00
15	198.00	11.6050	0.0014	0.4693	0.00	0.00	0.00	0.00	0.00
16	212.40	12.0580	0.0015	0.4693	0.00	0.00	0.00	0.00	0.00
17	224.40	12.5110	0.0015	0.4693	0.00	0.00	0.00	0.00	0.00
18	238.10	12.9640	0.0018	0.4693	0.00	0.00	0.00	0.00	0.00
19	250.80	13.4170	0.0027	0.4693	0.00	0.00	0.00	0.00	0.00
20	264.00	13.8700	0.0027	0.4693	0.00	0.00	0.00	0.00	0.00
TOTAL BLADE WEIGHT = 488.14 LB									
FLAPPING INERTIA/BLADE = 1503.44 SLUG-FT <sup>2</sup> /RAD									
BLADE TIP WEIGHT = 0.0 LB									
BLADE STATION NUMBER		RADIUS	OUT-OF-PLANE DISPLACEMENT	TORSIONAL	OUT-OF-PLANE BENDING MOMENT COEFFICIENT	IMPLANE TORSIONAL	IMPLANE BENDING MOMENT COEFFICIENT	IMPLANE TORSIONAL	IMPLANE BENDING MOMENT COEFFICIENT
0	0.00	0.00	-0.0000	-0.01117	0.00	-0.0000	0.00	-0.0000	0.00
1	0.00	0.00	-0.0027	-0.00982	10.49	-0.0000	10.49	-0.0000	10.49
2	20.57	0.00	-0.0027	-0.00982	10.49	-0.0000	10.49	-0.0000	10.49
3	37.50	0.00	-0.0027	-0.00982	10.49	-0.0000	10.49	-0.0000	10.49
4	52.80	0.00	-0.0027	-0.00982	10.49	-0.0000	10.49	-0.0000	10.49
5	66.00	0.00	-0.0027	-0.00982	10.49	-0.0000	10.49	-0.0000	10.49
6	77.00	0.00	-0.0027	-0.00982	10.49	-0.0000	10.49	-0.0000	10.49
7	92.40	0.00	-0.0027	-0.00982	10.49	-0.0000	10.49	-0.0000	10.49
8	103.00	0.00	-0.0027	-0.00982	10.49	-0.0000	10.49	-0.0000	10.49
9	118.80	0.00	-0.0027	-0.00982	10.49	-0.0000	10.49	-0.0000	10.49
10	132.00	0.00	-0.0027	-0.00982	10.49	-0.0000	10.49	-0.0000	10.49
11	145.20	0.00	-0.0027	-0.00982	10.49	-0.0000	10.49	-0.0000	10.49
12	155.80	0.00	-0.0027	-0.00982	10.49	-0.0000	10.49	-0.0000	10.49
13	171.60	0.00	-0.0027	-0.00982	10.49	-0.0000	10.49	-0.0000	10.49
14	184.80	0.00	-0.0027	-0.00982	10.49	-0.0000	10.49	-0.0000	10.49
15	198.00	0.00	-0.0027	-0.00982	10.49	-0.0000	10.49	-0.0000	10.49
16	212.40	0.00	-0.0027	-0.00982	10.49	-0.0000	10.49	-0.0000	10.49
17	224.40	0.00	-0.0027	-0.00982	10.49	-0.0000	10.49	-0.0000	10.49
18	238.10	0.00	-0.0027	-0.00982	10.49	-0.0000	10.49	-0.0000	10.49
19	250.80	0.00	-0.0027	-0.00982	10.49	-0.0000	10.49	-0.0000	10.49
20	264.00	0.00	-0.0027	-0.00982	10.49	-0.0000	10.49	-0.0000	10.49

Figure 11. OLS Main Rotor Elastic Blade Data Group.

MODE 3	BLADE NUMBER	STATION	DISPLACEMENT		TORSIONAL	BENDING MOMENT COEFFICIENT		TORSIONAL
			OUT-OF-PLANE	IN-PLANE		OUT-OF-PLANE	IN-PLANE	
	0	0.0	0.0011	0.2116	0.0044	0.0	-175567.0	207.0
	1	0.0	-0.0011	0.2116	0.0044	-0.0077	-162325.0	207.0
	2	20.57	-0.0264	0.2020	70.5220	-0.0077	-162325.0	207.0
	3	37.50	-0.3065	0.1609	79.7210	-0.0077	-149601.0	241.79
	4	52.60	-0.4537	0.1075	83.2022	229450.0	-134356.0	263.11
	5	66.00	-0.5672	0.0527	86.1894	220255.0	-127607.0	243.84
	6	81.50	-0.6718	-0.0127	89.6236	149000.0	-114613.0	213.90
	7	97.50	-0.7760	-0.0571	92.4923	179500.0	-105500.0	218.80
	8	103.00	-0.7360	-0.0571	92.4923	179500.0	-105500.0	186.00
	9	118.60	-0.7169	-0.1552	98.6336	4307.0	-6233.0	166.77
	10	132.00	-0.6632	-0.2001	102.0923	2131.0	-71591.0	166.77
	11	145.20	-0.5782	-0.2425	105.2356	1250.0	-60564.0	151.11
	12	158.60	-0.4789	-0.2745	107.6866	1150.0	-54912.0	137.48
	13	175.60	-0.3785	-0.3051	110.1372	644.0	-3763.0	121.71
	14	184.60	-0.3597	-0.3297	113.2172	113.2172	-2146.0	100.79
	15	198.00	-0.2461	-0.3966	115.1137	-1532.0	-2146.0	100.79
	16	212.30	0.2226	-0.4411	116.9251	-3376.0	-14390.0	762.10
	17	224.40	0.3921	-0.4775	118.1693	-3335.0	-8856.0	610.90
	18	238.10	0.5784	-0.5198	119.5222	-3259.0	-4136.0	450.00
	19	250.60	0.7784	-0.5655	120.0000	-2071.0	-1268.0	269.00
	20	264.00	0.9800	-0.6055	120.0000	-2440.0	-735.0	92.81

MODE 4	BLADE NUMBER	STATION	DISPLACEMENT		TORSIONAL	BENDING MOMENT COEFFICIENT		TORSIONAL
			OUT-OF-PLANE	IN-PLANE		OUT-OF-PLANE	IN-PLANE	
	0	0.0	0.0016	0.0419	-0.0115	0.0	-2626.0	-113.0
	1	0.0	-0.0016	0.0419	-0.0115	0.0	-2626.0	-113.0
	2	20.57	-0.1504	0.0384	-14.0464	4550.0	-5193.0	-350.0
	3	37.50	-0.2414	0.0273	-15.5569	16924.0	-47080.0	-367.0
	4	52.60	-0.3215	0.0077	-16.2922	18650.0	-4332.0	-341.0
	5	66.00	-0.3841	-0.0117	-16.9015	16792.0	-3874.0	-323.0
	6	81.50	-0.4419	-0.0325	-17.4594	15139.0	-3525.0	-307.0
	7	97.50	-0.4919	-0.0590	-18.0538	14210.0	-2768.0	-287.0
	8	103.00	-0.4930	-0.0762	-19.7575	13261.0	-2377.0	-268.0
	9	118.60	-0.5060	-0.0885	-20.6523	12495.0	-19915.0	-238.0
	10	132.00	-0.4982	-0.0984	-21.5933	12051.0	-16877.0	-208.0
	11	145.20	-0.4694	-0.1042	-22.3851	10387.0	-1236.0	-182.0
	12	158.60	-0.4301	-0.1086	-23.4323	9455.0	-641.0	-157.0
	13	175.60	-0.3841	-0.1046	-25.1013	8324.0	-3780.0	-123.0
	14	184.60	-0.3269	-0.0962	-25.8065	6402.0	-2104.0	-112.0
	15	198.00	0.1050	-0.0894	-26.2839	3956.0	-804.0	-74.0
	16	212.30	0.2902	-0.0730	-26.6846	1568.0	-167.0	-42.0
	17	224.40	0.5217	-0.0537	-27.0797	1054.0	6.5	-29.0
	18	238.10	0.7784	-0.0337	-27.0797	1054.0	6.5	-29.0
	19	250.60	1.0000	-0.0337	-27.0797	1054.0	6.5	-29.0
	20	264.00	1.0000	-0.0337	-27.0797	1054.0	6.5	-29.0

MODE 5	BLADE NUMBER	STATION	DISPLACEMENT		TORSIONAL	BENDING MOMENT COEFFICIENT		TORSIONAL
			OUT-OF-PLANE	IN-PLANE		OUT-OF-PLANE	IN-PLANE	
	0	0.0	0.0018	-0.0236	-0.0008	0.0	89348.0	175.0
	1	0.0	-0.0018	-0.0236	-0.0008	0.0	89348.0	175.0
	2	20.57	0.2755	-0.0195	1.9223	-6030.0	85912.0	-43.0
	3	37.50	0.3985	-0.0102	-2.2671	-74151.0	85912.0	-235.0
	4	52.60	0.4756	0.0095	-1.6942	-66384.0	81306.0	567.0
	5	66.00	0.4899	0.0188	-0.9647	-50901.0	78374.0	954.0
	6	81.50	0.5109	0.0134	0.3293	-36991.0	74669.0	731.0
	7	97.50	0.5273	0.0082	2.1092	-27606.0	62899.0	719.0
	8	103.00	0.1703	-0.0141	3.0951	-51304.0	57874.0	747.0
	9	118.60	-0.0623	-0.0405	3.9515	-6210.0	51810.0	755.0
	10	132.00	-0.2652	-0.0613	5.7191	840.0	43759.0	694.0
	11	145.20	-0.4524	-0.0771	7.5055	6571.0	40951.0	623.0
	12	158.60	-0.5761	-0.0934	8.8911	18190.0	3773.0	546.0
	13	175.60	-0.6483	-0.1108	10.4777	18190.0	2164.0	415.0
	14	184.60	-0.6983	-0.0411	12.6917	20770.0	2164.0	344.0
	15	198.00	-0.6126	-0.0281	13.4269	19836.0	15191.0	344.0
	16	212.30	-0.4059	0.0241	13.4269	16276.0	10065.0	373.0
	17	224.40	-0.1471	0.0794	13.4269	9609.0	4980.0	325.0
	18	238.10	0.2569	0.1506	14.4030	3885.0	1596.0	214.0
	19	250.60	0.5217	0.2460	14.4030	-80.0	388.0	64.0
	20	264.00	1.0000	0.2460	14.4030	-80.0	388.0	64.0

Figure 11. Continued.

MODE 6	BLADE STATION NUMBER	RADIUS	DISPLACEMENT		TORSIONAL	BENDING MOMENT COEFFICIENT	
			OUT-OF-PLANE	IN-PLANE		OUT-OF-PLANE	IN-PLANE
	0	0.0	0.0000	0.0000	0.0000	0.0000	0.0000
	1	6.00	-0.0018	-0.0005	-0.0337	-0.0018	-0.0005
	2	20.57	0.0041	-0.0016	-0.0334	0.0041	-0.0016
	3	37.50	0.0100	-0.0024	-1.7771	0.0100	-0.0024
	4	52.80	0.0163	-0.0029	-1.8537	0.0163	-0.0029
	5	66.00	0.0208	-0.0032	-1.8918	0.0208	-0.0032
	6	81.50	0.0252	-0.0037	-1.9203	0.0252	-0.0037
	7	95.40	0.0315	-0.0028	-1.9510	0.0315	-0.0028
	8	103.00	0.3529	-0.0026	-1.9839	0.3529	-0.0026
	9	118.80	0.4149	-0.0021	-2.0330	0.4149	-0.0021
	10	132.00	0.4668	-0.0018	-2.0786	0.4668	-0.0018
	11	145.00	0.5187	-0.0016	-2.1225	0.5187	-0.0016
	12	155.60	0.5507	-0.0010	-2.1528	0.5507	-0.0010
	13	171.60	0.6234	-0.0009	-2.1942	0.6234	-0.0009
	14	184.80	0.6762	-0.0000	-2.2203	0.6762	-0.0000
	15	198.00	0.7293	0.0005	-2.2474	0.7293	0.0005
	16	212.30	0.7812	0.0011	-2.2679	0.7812	0.0011
	17	226.10	0.8326	0.0017	-2.2871	0.8326	0.0017
	18	239.10	0.8822	0.0023	-2.3051	0.8822	0.0023
	19	250.80	0.9451	0.0023	-2.3272	0.9451	0.0023
	20	264.00	1.0000	0.0037	-2.3731	1.0000	0.0037
MODE 7	BLADE STATION NUMBER	RADIUS	DISPLACEMENT		TORSIONAL	BENDING MOMENT COEFFICIENT	
			OUT-OF-PLANE	IN-PLANE		OUT-OF-PLANE	IN-PLANE
	0	0.0	-0.0000	-0.0000	0.0000	-0.0000	-0.0000
	1	6.00	-0.0047	-0.0168	-0.1163	-0.0047	-0.0168
	2	20.57	-0.0187	-0.0573	-0.6346	-0.0187	-0.0573
	3	37.50	-0.0402	-0.0994	-0.9282	-0.0402	-0.0994
	4	52.80	-0.0581	-0.1321	-1.1635	-0.0581	-0.1321
	5	66.00	-0.0710	-0.1543	-1.3573	-0.0710	-0.1543
	6	81.50	-0.0806	-0.1726	-1.5060	-0.0806	-0.1726
	7	95.40	-0.0858	-0.1692	-1.5744	-0.0858	-0.1692
	8	103.00	-0.0894	-0.1555	-1.6567	-0.0894	-0.1555
	9	118.80	-0.0810	-0.1366	-1.7476	-0.0810	-0.1366
	10	132.00	-0.0737	-0.1116	-1.8455	-0.0737	-0.1116
	11	145.00	-0.0672	-0.0868	-1.9492	-0.0672	-0.0868
	12	155.60	-0.0624	-0.0668	-2.0582	-0.0624	-0.0668
	13	171.60	-0.0587	-0.0498	-2.1726	-0.0587	-0.0498
	14	184.80	-0.0557	0.0098	-2.2932	-0.0557	0.0098
	15	198.00	0.0337	0.0291	-2.4198	0.0337	0.0291
	16	212.30	0.2495	0.0729	-2.5532	0.2495	0.0729
	17	226.10	0.4457	0.1106	-2.6937	0.4457	0.1106
	18	239.10	0.6135	0.1411	-2.8412	0.6135	0.1411
	19	250.80	0.8234	0.1911	-3.0050	0.8234	0.1911
	20	264.00	1.0000	0.2295	-3.1866	1.0000	0.2295
MODE 8	BLADE STATION NUMBER	RADIUS	DISPLACEMENT		TORSIONAL	BENDING MOMENT COEFFICIENT	
			OUT-OF-PLANE	IN-PLANE		OUT-OF-PLANE	IN-PLANE
	0	0.0	0.0000	0.0000	0.0000	0.0000	0.0000
	1	6.00	-0.0046	-0.0062	-0.0000	-0.0046	-0.0062
	2	20.57	-0.0080	-0.0212	-0.0000	-0.0080	-0.0212
	3	37.50	-0.0164	-0.0392	-1.46321	-0.0164	-0.0392
	4	52.80	-0.0253	-0.0551	-1.70180	-0.0253	-0.0551
	5	66.00	-0.0373	-0.0675	-1.80434	-0.0373	-0.0675
	6	81.50	-0.0494	-0.0653	-1.89279	-0.0494	-0.0653
	7	95.40	-0.0604	-0.0653	-1.96553	-0.0604	-0.0653
	8	103.00	-0.0440	-0.0897	-2.02425	-0.0440	-0.0897
	9	118.80	-0.0519	-0.0925	-2.07155	-0.0519	-0.0925
	10	132.00	-0.0528	-0.0913	-2.10248	-0.0528	-0.0913
	11	145.00	-0.0509	-0.0860	-2.12749	-0.0509	-0.0860
	12	155.60	-0.0465	-0.0765	-2.14613	-0.0465	-0.0765
	13	171.60	-0.0393	-0.0615	-2.15815	-0.0393	-0.0615
	14	184.80	-0.2938	-0.0414	-2.16245	-0.2938	-0.0414
	15	198.00	-0.0153	0.0160	-2.16000	-0.0153	0.0160
	16	212.30	0.0439	0.0170	-3.12964	0.0439	0.0170
	17	226.10	0.2386	0.0486	-3.20470	0.2386	0.0486
	18	239.10	0.4851	0.0824	-3.24457	0.4851	0.0824
	19	250.80	0.7327	0.1259	-3.26451	0.7327	0.1259
	20	264.00	1.0000	0.1659	-3.26216	1.0000	0.1659

Figure 11. Continued

70

Figure 11. Concluded.

PAGE 1 JMT PROGRAM DNAM05 - COMPILED 03/20/79 09/10/79  
NATURAL BLADE MODES 540279

26 SEG OLS MR PRECONE AND UNDERSLING HSOFT = -17.2

SEG	SEGMENT LENGTH (IN)	RADIUS AT OUTBD END (IN)	WT/IN (LBF/IN)	EL10**(-6) (LBF*IN**2)	BEAM CHORD	TWIST AT OUTBD END (DEG)	CENTER OF GRAVITY OFFSETS (IN)	CF AT INSU END (LBF/RPM**2)
1	3.50	8.280	344.90	5003.10	0.0	0.0	0.0	1.21491
2	2.50	1.264	8.37	4262.10	0.0	0.0	0.0	1.21331
3	3.00	3.196	8.27	4143.10	0.0	0.0	0.0	1.21168
4	3.10	7.822	340.50	8492.10	0.0	0.0	0.0	1.20569
5	6.47	6.936	202.60	1750.00	-0.5341	0.0	0.0	1.19222
6	13.18	6.241	800.00	1463.60	-1.2784	0.0	0.120	1.15511
7	3.75	5.908	800.00	450.58	-1.4205	0.0	3.610	1.10512
8	3.50	7.164	407.69	8232.00	-2.0000	0.0	2.302	1.07998
9	11.80	4.127	89.50	4240.00	-2.2727	0.0	1.300	1.03706
10	17.20	0.952	89.50	4240.00	-2.5000	0.0	0.900	0.99544
11	6.00	0.775	61.75	4065.00	-3.0871	0.0	0.900	0.96814
12	15.50	0.858	55.00	4150.00	-3.5000	0.0	1.770	0.94343
13	10.90	0.830	53.30	4290.00	-3.9015	0.0	1.710	0.91955
14	10.60	0.869	49.66	4079.00	-4.5000	0.0	2.385	0.88653
15	15.80	0.762	44.50	3820.00	-5.0000	0.0	1.450	0.84643
16	13.20	0.726	40.10	3600.00	-5.5000	0.0	1.340	0.80464
17	13.20	0.875	40.00	3390.00	-5.9015	0.0	0.850	0.77078
18	10.60	1.048	40.83	3255.00	-6.5000	0.0	0.571	0.71192
19	15.80	1.062	41.00	2910.00	-7.0000	0.0	-0.550	0.63554
20	13.20	1.039	39.60	2650.00	-7.5000	0.0	0.010	0.56282
21	14.30	1.260	39.50	2650.00	-8.0417	0.0	-1.017	0.47306
22	12.10	1.186	42.00	2650.00	-8.5000	0.0	-1.870	0.37614
23	13.70	1.266	42.40	2655.00	-9.0189	0.0	-1.129	0.27522
24	12.70	1.189	38.40	2660.00	-9.5000	0.0	-1.970	0.16560
25	13.20	1.160	38.40	2690.00	-10.0000	0.0	-0.430	0.05736
26						0.0	0.0	

4 HUB SEGMENTS  
GIMBALED HUB TYPE  
2.0 BLADES  
28.63 INCH CHORD

ROTOR RPM	ROTOR PITCH (DEG)	ROOT COLLECTIVE PITCH (DEG)	FREQUENCY SWEEP PARAMETERS (CPM)	TORSO (EQ. DRIVE TRAIN SPRING RATE)/BLADE	VMAS (EQ. PYLON MASS)/BLADE, VERTICALLY	PMAS (EQ. PYLON MASS)/BLADE, IN PLANE	VSOFT (EQ. PYLON VERTICAL RESTRAINT)	HSOFT (EQ. PYLON IN PLANE RESTRAINT)	RDOFT (FLAPPING RESTRAINT AT R=0)/BLADE
290.00	32.400	8.50	0.0	0.0	0.0	0.0	0.0	-17.2	0.0
350.00	15.00	29.00	0.0	0.0	0.0	0.0	0.0	0.0	0.0
INITIAL INCREMENT	8.750	29.00	0.0	0.0	0.0	0.0	0.0	0.0	0.0
FINAL	350.00	29.00	0.0	0.0	0.0	0.0	0.0	0.0	0.0

504.298 LBM/BLADE  
110.787 SLUG-FT\*\*2/BLADE  
1499.704 SLUG-FT\*\*2/BLADE  
5.078

Figure 12. Inputs to the Rotor Frequency Program  
DNAM05 for the OLS Main Rotor.

PAGE 2      BMT PROGRAM DNAM05 - COMPILED 03/20/79      09/10/79  
                                  NATURAL BLADE MODES      540279

26 DEG JLS MR    PRECUNE AND UNDERSLING HSOFT = -17.2

CK                    CONTRL SYSTEM SPRING RATE    396000.0    IN-LBF/RAD  
 PHUFF                CONTRL SYSTEM DAMPING RATIO    6.000    IN  
                          PITCH HURN ATTACHMENT RADIAL    14.100    IN  
 PARM                PITCH HURN MOMENT ARM    -9.250    IN  
 PLSTA                PITCH LINK RADIAL STATION    0.0    IN

FMUFF                FLAPPING HINGE RADIAL STATION    0.0    IN  
 FLPSM                FLAPPING SPRING RATE    0.0    FT-LBF/DEG  
 FMAGL                FLAPPING HINGE SKEW ANGLE    0.0    DEG  
 CHUFF                LAG HINGE RADIAL STATION    0.0    IN  
 SPRLG                LAG SPRING RATE    0.0    FT-LBF/DEG  
 ALPHA1                LAG HINGE SKEW ANGLE FOR    0.0    DEG  
                          FLAP-LAG COUPLING    0.0    DEG  
 ALPHA3                LAG HINGE SKEW ANGLE FOR    0.0    DEG  
                          PITCH-LAG COUPLING

RPCUNE                RADIUS WHERE PRECUNE STARTS    0.0    IN  
 PRECON                PRECUNE ANGLE    2.750    DEG  
 VUPCA                VERT OFFSET OF PCA AT R=RPCUNE    -4.500    IN  
 RPLAG                RADIUS WHERE PHELAG STARTS    0.0    IN  
 HUPCA                PHELAG ANGLE    0.0    DEG  
                          HURIZ OFFSET OF PCA AT R=RPLAG    0.0    IN

RBCS                RADIUS WHERE BLADE COORDINATE    0.0    IN  
 BCUNE                SYSTEM STARTS    0.0    IN  
 VBRS                BLADE CUNING ANGLE RELATIVE TO    0.0    DEG  
                          PCA AT 0 DEG COLLECTIVE PITCH  
 BUTS#P                VERT OFFSET OF BLADE SYSTEM    0.0    IN  
                          FROM PCA AT 0 DEG COLLECTIVE  
 HURS                BLADE SWEEP ANGLE RELATIVE TO    0.0    DEG  
                          PCA AT 0 DEG COLLECTIVE  
                          HURIZ OFFSET OF BLADE SYSTEM    0.0    IN  
                          FROM PCA AT 0 DEG COLLECTIVE

EFFECTIVE BLADE CG    -0.159    IN FWD FROM PCA  
 EFFECTIVE (BLADE PLUS HUR) CG    -0.159    IN FWD FROM PCA  
 CLAMPED TORSIONAL FREQUENCY    15.3341    HERTZ  
 TORSIONAL INERTIA ABOUT PCA    42.662    IN-LB-SEC\*\*2

SPECIAL OPTIONS INVOKED:  
 TORSION OPTION IS ON  
 UNEQUAL SEGMENTS ARE USED

Figure 12. Continued.

PAGE	3	BMT PROGRAM UNAM05 - COMPILED 03/20/79	09/10/79
		NATURAL BLADE MODES	540279
	26 SEG OLS MR	PRECONC AND UNDERSLING HSOFT = -17.2	
	IBB	BEAM RADIUS OF	CHORD RADIUS OF
	IN-LB-SEC**2/IN	GYRATION - INCH	GYRATION - INCH
1	0.000100	0.06d3	1.794
2	0.000100	0.1732	4.550
3	0.000100	0.1100	2.888
4	0.089800	2.1919	2.725
5	0.089800	4.2367	2.781
6	0.089800	2.3579	2.931
7	0.089800	2.4235	1.790
8	0.035600	1.3857	3.067
9	0.006400	0.7741	4.758
10	0.002400	0.9470	6.929
11	0.002400	0.9870	6.929
12	0.001700	0.9206	7.699
13	0.001700	0.8750	8.134
14	0.001700	0.8864	8.195
15	0.001500	0.8946	8.310
16	0.001500	0.8426	8.295
17	0.001500	0.8318	8.334
18	0.001500	0.7863	7.518
19	0.002400	0.9190	7.168
20	0.002400	0.9345	6.851
21	0.001400	0.7216	6.565
22	0.001200	0.6066	6.204
23	0.001300	0.6508	5.835
24	0.001500	0.6766	6.117
25	0.001800	0.7648	6.142
26	0.002700	0.9484	6.827

Figure 12. Continued.

09/10/79  
540279

PAGE 4 BHT PROGRAM DNAMOS - COMPILED 03/20/79  
NATURAL BLADE MODES

26 SEG OLS MR PRECONE AND UNDERSLING HSOFT = -17.2

SEG	G (LBF-IN**2) (E-6)	SHEAR CENTER OFFSET (IN) BEAM CHORD	NEUTRAL AXIS OFFSET (IN) BEAM CHORD
1	36.000	0.0	0.0
2	36.000	0.0	0.0
3	36.000	0.0	0.0
4	36.000	0.0	0.0
5	36.000	0.0	0.0
6	36.000	0.0	0.0
7	37.850	0.0	0.0
8	67.000	0.0	0.0
9	84.600	0.0	0.773
10	74.000	0.0	1.050
11	74.000	0.0	0.560
12	61.700	0.0	0.560
13	55.200	0.0	0.730
14	50.000	0.0	1.200
15	44.200	0.0	1.160
16	38.100	0.0	1.000
17	34.500	0.0	0.750
18	33.800	0.0	0.530
19	33.800	0.0	0.290
20	33.800	0.0	-0.168
21	33.800	0.0	-0.450
22	33.800	0.0	-0.690
23	33.800	0.0	-0.627
24	33.800	0.0	-0.850
25	33.800	0.0	-1.149
26	33.800	0.0	-2.510
			-2.520

FEATHERING BEARING HAS BEEN PUT IN SEGMENT 4

Figure 12. Concluded.



The sleeve properties were incorporated into the 540 properties, resulting in the inputs given in Figure 12.

PHOFF was taken to be 14.1 inches, as it was assumed that the shears and moments in the pitch link are reacted at the inner feathering bearing (See Figure 9). In fact, a dual load path exists between the inner and outer feathering bearings (14.1 to 37.5-inch radius) and the load distribution in this region cannot be precisely defined.

Twenty-six segments of unequal length were used to model the rotor in DNAM05, with several short segments in the hub region to properly model the rapid radial changes in properties. Mode shape data were punched for the twenty radii corresponding to those used in the Main Rotor Group.

The frequencies computed by DNAM05 are dependent upon the pylon impedances used in the analysis. For the generation of the frequency plots for the OLS rotor, the pylon was modeled as rigid vertically (as the AH-1G pylon has essentially no vertical freedom), and a representative value was chosen for the inplane pylon impedance. In this manner, the inplane frequency and mode shapes computed by the program are for the rotor mounted on the airframe.

The computation of rotor response in C81 can be approached in two ways: the analyst can use rotor modes generated with representative pylon impedances directly, or rotor modes can be generated for an infinitely rigid pylon in DNAM05 (HSOFT = 0.0), and pylon modes can be input to C81, with the coupling being accounted for in the simulation. Due to the lack of adequate or accurate experimental or analytical pylon mode shape data, an inplane pylon impedance was used to generate rotor mode shapes in DNAM05 for all the simulations.

Previous studies of the AH-1G rotor had shown that an inplane pylon impedance (HSOFT) of -34.4 resulted in accurate computation of the first inplane cyclic mode. The latest version of the Rotor Frequency Program uses an impedance-per-blade, whereas earlier versions used an impedance-per-rotor. Therefore, -17.2 was used to generate the main rotor mode shapes. The AH-1G main rotor pylon is rigidly attached to the aircraft vertically, so VSOFTE was input as zero.

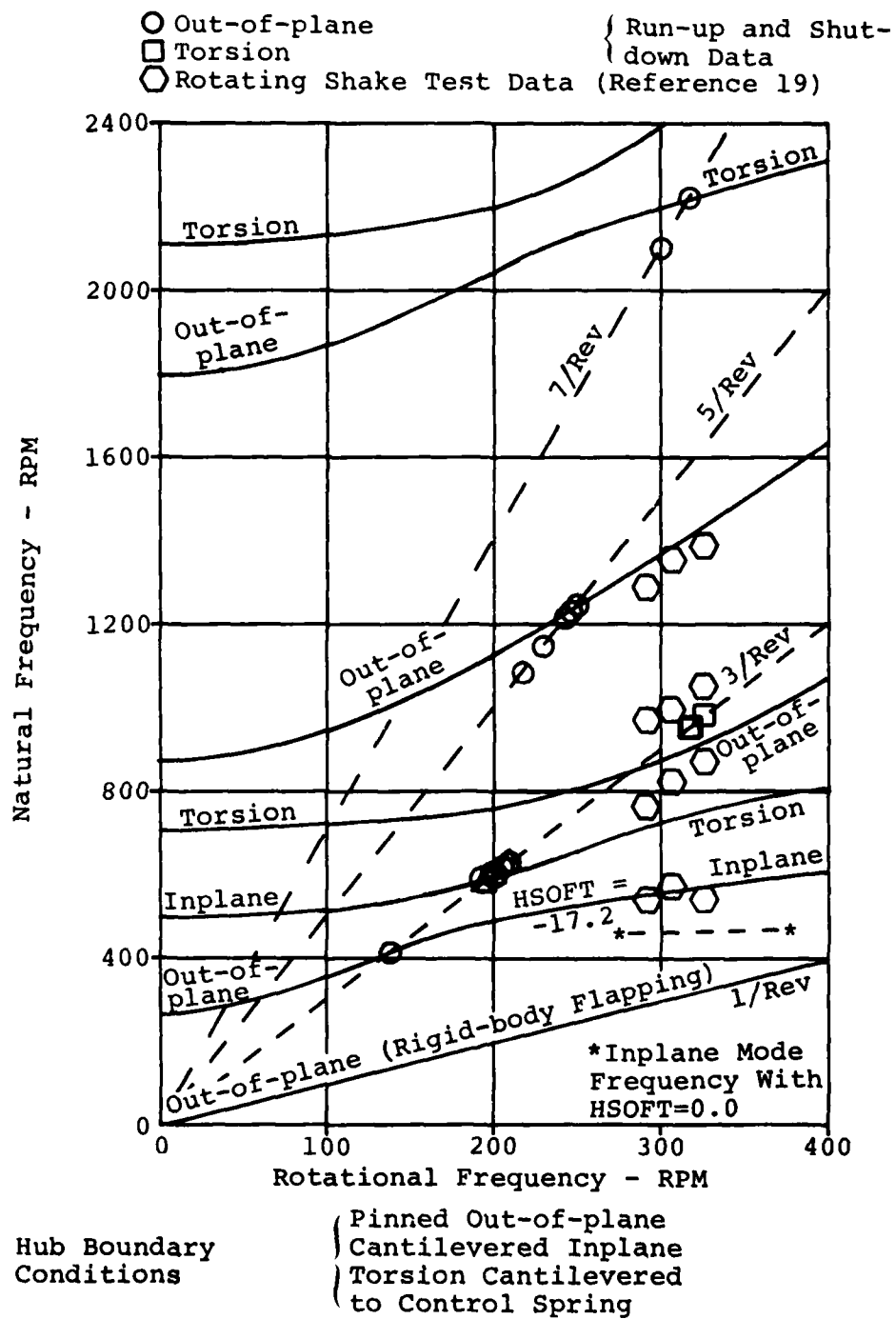
The control system spring rate was measured during the aircraft shake test, and reported in Reference 19. The control system damping has been measured to be as high as 20 percent in unreported tests, but the 6 percent value used in DNAM05 was estimated to be a representative value.

A comparison of measured and computed frequencies is given in Figure 13. (The predicted frequencies are for coupled modes, so the mode type changes with rpm in some cases.) The frequencies measured during ground run-up, shut-down and rotating shake test are also plotted in the figure. The computed and measured frequencies agree quite favorably, except for the cyclic torsion and "S-ing" modes. (The "S-ing" mode is the first elastic cyclic out-of-plane mode, and is usually placed below three-per-rev.) The computed modes are in reverse position compared with the measured modes, i.e., the computed torsion mode is at a lower frequency than the "S-ing" mode, and both are at lower frequencies than the measured frequencies. These two modes both exhibit a high-degree of beam-torsion coupling, and are important to the proper calculation of the rotor response and loads. The discrepancy in the identification of these two modes is significant, as is the computation of frequencies lower than those measured, because the three-per-rev response of the two modes will be substantially affected.

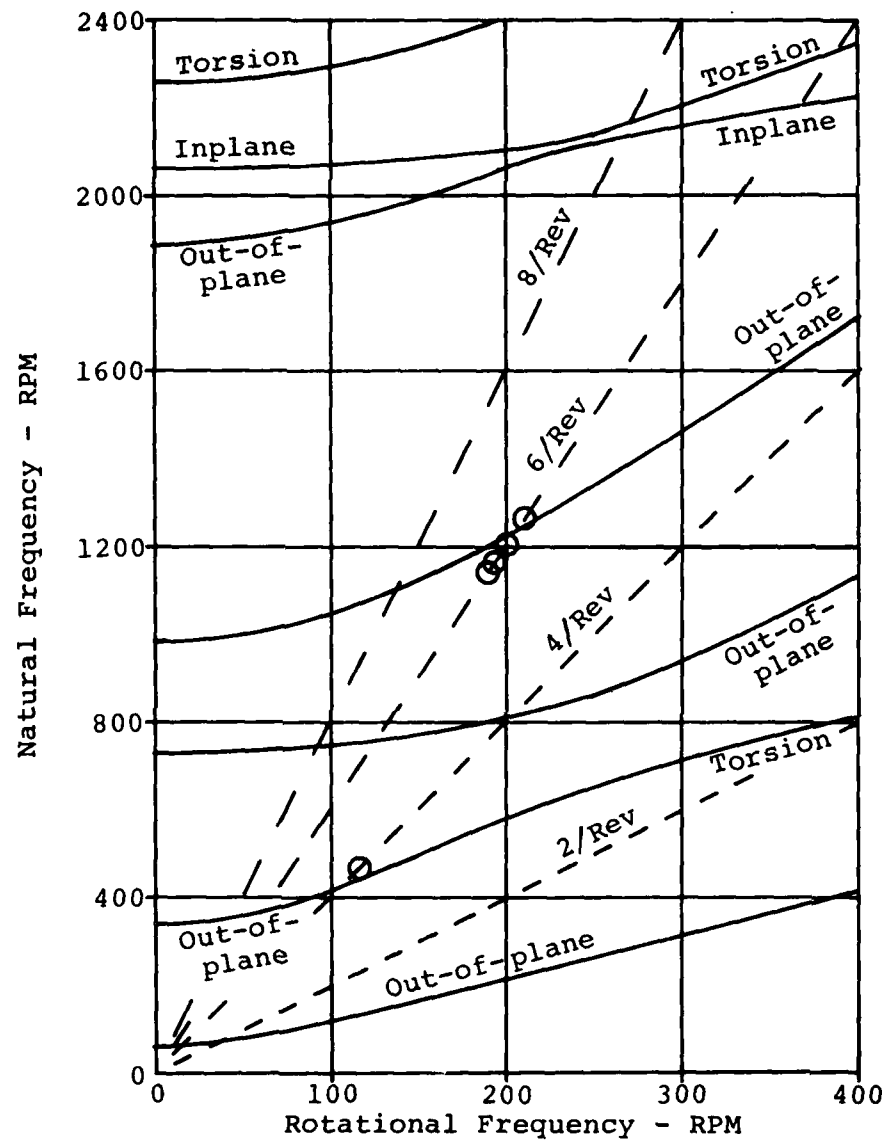
The analysis incorporated in DNAM05 and the coding of that analysis have been examined in detail for errors that might be the cause of the "S-ing"-torsion mode discrepancy. No errors were found, and DNAM05 has been successfully identifying the cyclic torsion and "S-ing" mode frequencies for other two-bladed teetering rotors. The inputs were also reexamined in detail, and no errors were located.

The instrumented blade was cantilevered at the bolt holes (radial station 41.0) in a fixture and subjected to a shake test. The reported experimental torsional frequency for the clamped blade was 20.0 hertz (Reference 10, page 22). The DNAM05 deck of Figure 12 was modified by removing the first eight segments, setting XNIN to 18, PHOFF to 1.0 and CK to 999999999. Additionally, 41.0 was subtracted from all the radii. A rigid hub type was used, JHUB was set to zero, and the program run for zero rpm and zero collective, yielding a first torsional frequency of 21.25 hertz. This is slightly higher than the measured frequency, but the test stand could not be perfectly rigid. This result indicates that the cause of the "S-ing"-torsion mode discrepancy will most likely be found to be in the hub model.

The first five cyclic and first four collective modes were used in the C81 simulations.



○ Out-of-Plane Run-up and Shut-down Data



Hub Boundary Conditions

- ( Cantilevered Out-of-plane
- ( Pinned Inplane
- ( Torsion Cantilevered to Control Spring

b) Collective Modes (Respond only at Even Harmonics).

Figure 13. Concluded.

### 3.5 TAIL ROTOR GROUP

The input format for the Tail Rotor Group is given in Sections 2.7 and 3.7 of Volume II of Reference 3. The inputs to this group are listed in Figure 14. The following drawings were used to determine the inputs for this group:

AH-1G Basic Lines Data (Figure 8)  
204-011-702-17 T/R Blade Assembly  
204-011-728-15 T/R Grip Assembly  
205-011-703-3 T/R Static Stop  
204-011-722-5 T/R Yoke Assembly  
204-011-801-11 T/R Hub Assembly

Only inputs that were determined by methods other than those discussed in Section 3.3 will be discussed.

The aerodynamic reference center was assumed to be on the pitch-change-axis, so XTR(3) was set to zero. A constant chord, equal to the blade chord, was input as XTR(5).

Blade weight, inertia and first mass moment were taken from a DNAM05 run for the production AH-1G tail rotor.

A flapping stop spring rate of 10,000 ft-lb/deg was assumed to reflect the rigid stops and stiff pylon.

The drag coefficient for the hub was based on a chord-to-thickness ratio of 1.33 for a Reynold's number, at the bolt hole, of 200,000. The drag coefficient was obtained from data in Reference 22.

The sidewash coefficient, XTR(28), was assumed to be 0.2.

The tail rotor analysis in C81 assumes that this rotor turns in a left-handed sense. The lateral mast tilt was input as  $-90^\circ$  (i.e., to the left), to yield counterclockwise rotation when viewed from the right side of the aircraft, even though the tail rotor was on the right-hand side of the aircraft, as shown in Reference 10.

<sup>22</sup>Hoerner, Signard, FLUID DYNAMIC DRAG, published by the author, Brick Town, New Jersey, 1965.



### 3.6 TAIL ROTOR ELASTIC BLADE DATA GROUP

The tail rotor was modeled as inelastic, so no mode shape data were input in this group.

### 3.7 ROTOR AERODYNAMIC GROUP

The input format for the Rotor Aerodynamic Group is given in Sections 2.9 and 3.9 of Volume II of Reference 3. The inputs to this group are listed in Figure 15.

The first five data cards are the Rotor Aerodynamic Subgroup for the main rotor, while the second five data cards are the Rotor Aerodynamic Subgroup for the tail rotor. Only the inputs required to supplement the airfoil data tables are included.

The drag divergence Mach number, YRR(1,1), was determined as described in Dommasch<sup>23</sup> for the Mach numbers at which

$$\frac{dC_{D_o}}{dM} = 0.1 \quad (2)$$

The Mach number for the lower boundary of the supersonic region, YRR(2,1), was calculated as described in Section 3.9.2 of Volume II of Reference 3.

The maximum  $C_l$  at  $M = 0$ , YRR(3,1),  $C_{l_{max}}$  in reverse flow, YRR(7,1), and  $C_{l_\alpha}$  at  $M = 0$ , YRR(8,1), were taken directly from the plots of the airfoil data tables.

The coefficients of  $M$  in the  $C_{l_{max}}$  (YRR(4,1), YRR(5,1) and YRR(6,1)) and the  $C_{l_\alpha}$  equations were determined from a third order curve fit of  $C_{l_{max}}$  versus Mach number and  $C_{l_\alpha}$  versus Mach number. The thickness-to-chord ratio was computed from the blade drawing, 299-328-001.

<sup>23</sup>Dommasch, D. P., Sherby, S. S., and Connally, T. F., AIRPLANE AERODYNAMICS, Fourth Edition, Pitman Publishing Corporation, New York, 1967.

ACMU0LS1		VAN GAASBEEK AM-1G M/M IN GROUP ONE, T/M IN GROUP TWO (OLS CORRELATION)		(05-03-79)	
		HTH AERODYNAMIC GROUP			
•7000000	1.110000	1.232300	•2904000	-2.307400	•0000000
•1000000	•11029000	•3546000	•2449000	•0	•0
•0	•0	•9710002E-01	1.0000000	•0	1.0000000
•0	•0	•0	•0	•0	•0
•0	1.242000	1.491600	•0 263000	•0 3000000E-02	•0
•7500000	•11907000	•8779000	•8683000	•0 107000	•0
•0	•0	•1000000	2.0000000	•0 2000000	•0
•0	•0	•0	•0	•0	•0
•0	•0	•0	•0	•0	•0

Figure 15. OLS Rotor Aerodynamic Subgroup Group.



The coefficient of the yaw angle in the Mach number equation and the exponent in the Mach number equation for yawed flow (YRR(20,1) and YRR(21,1)) are recommended values and are discussed in Section 3.4 of Volume I of Reference 3.

The zero lift line orientation determined by YRR(29,1), YRR(30,1) and YRR(31,1) is constant with Mach number.

Comparisons between test data and the results of initial runs (made to check the data deck) showed that the computed power required was lower than that measured in flight. The difference between the measured and computed power was roughly proportional to velocity-squared, indicating that the rotor drag coefficients were too low. The value of  $C_{D_o}$  in the basic

production airfoil table, CLCD5474, is 0.0068, which is low compared to the values (with standard roughness) for a NACA 0009 ( $C_{D_o} = 0.0091$ ) and an NACA 0012 ( $C_{D_o} = 0.0098$ ) (Reference

24). When similar power-required discrepancies had been experienced with simulations of a regular AH-1G, a  $\Delta C_D$  (YRR(34,1)) of 0.003 was found to produce better agreement. (The  $\Delta C_D$  input to C81 is added to the entire drag table.)

The remaining five cards in the Rotor Aerodynamic group are used for the tail rotor aerodynamic calculations and refer to the second airfoil data table, CLCD0015. The necessary inputs for this group were obtained in a manner identical to that described above for the main rotor.

### 3.8 ROTOR INDUCED VELOCITY DISTRIBUTION TABLES GROUP

The input format for the Rotor Induced Velocity Distribution Tables Group is described in Sections 2.10 and 3.10 of Volume II of Reference 3. Due to the size of a typical RIVD table, the inputs to this group are not listed in this report. Instead, typical inputs to Program AR9102, used to generate the RIVD tables for the simulations, are listed in Figure 16. Utilization instructions for AR9102 are given in Section 7.2 of Volume II of Reference 3.

All wake tables were generated with a constant chord (BATA(3) = 28.625) at normal operating RPM (BATA(5) = 324.1) and with the appropriate density ratio (BATA(6)) for the flight condition being analyzed.

<sup>24</sup>Abbott, I. H., and Von Doenhoff, A. D., THEORY OF WING SECTIONS, Dover Publications, New York, 1959, pages 454 and 462.

PAGE 1

BHT PROGRAM AR9102 - COMPILED 10/11/77

04/24/79

DL5 ROTUR, FLIGHT 35A. COUNTERS 611, 612, 614, 615, 610  
 SIGMA-PRIME = 0.8636  
 QLS35A.610-615.324.1.0.8636

INPUT DATA

2.0000	22.0000	28.0000	0.0	324.1001	0.8636	0.0
20.0000	10.0000	0.0	0.0	0.0	0.0	0.0
3.0000	3.0000	3.0000	20.0000	0.0	0.0	0.0
3.0000	10.0000	6.0000	0.0	0.0	0.0	0.0
7525.0000	7525.0000	66.0000	-4.5000	142.0000	0.0	0.0
0.0	0.0	0.0	0.0	0.0	0.0	0.0

RADIUS DISTRIBUTION INPUT FOR INTERPOLATION

0.000	20.575	37.500	52.000	66.000	81.500	92.400
103.000	118.800	132.000	145.200	155.000	171.000	184.800
198.000	212.300	224.400	236.100	250.000	264.000	0.0

Figure 16. Inputs to the Rotor Wake Program AR9101 for Flight 35A, Counters 610 through 615.

Twenty radial segments were used (BATA(8)) with an azimuth increment (BATA(9)) of 10.0 degrees. Default values were used for the vortex core radius and vortex bursting factor (BATA(10) = BATA(11) = 0.0). No asymmetric blade loading was used (BATA(12) = 0.0) and the AR9102-computed average induced velocity was used to nondimensionalize the induced-velocity coefficients punched out by the program (BATA(14) = 0.0).

The number of advance ratios and wake-plane angles of attack (BATA(15) and BATA(16)) were chosen to cover the range of values experienced in each particular C81 simulation. BATA(17) was set to 3.0 to give the proper logic flow through AR9102. BATA(18) was set to 20.0 so that an input radius distribution would be used for interpolating the induced-velocity coefficients punched by AR9102.

BATA(23) was set to 10.0 so that one set of induced-velocity distribution tables would be punched out, and BATA(24) was set to 6.0, as induced-velocity harmonics were only needed through six-per-rev.

The inputs on AR9102 CARD 9 were chosen to given wake tables for values bracketing those experienced in C81 simulations.

The radius distribution input on OPTIONAL CARDS A was identical to that used in the C81 Main Rotor Group.

No wake tables were used for the tail rotor.

### 3.9 ROTOR WAKE AT AERODYNAMIC SURFACES TABLES GROUP

No Rotor Wake at Aerodynamic Surfaces Tables were used.

### 3.10 FUSELAGE GROUP

The input format for the Fuselage Group is given in Section 2.12 and 3.12 of Volume II of Reference 3. The Fuselage Group for the Flight 35-A aircraft configuration is given in Figure 17.

The fuselage group contains both mass and aerodynamic properties for the airframe. For mass inputs, the airframe is defined to have the mass properties of the entire aircraft without external stores. The mass properties of the stores are input in a separate group, and the mass properties of the airframe are adjusted appropriately in the analysis to yield total-aircraft mass characteristics. The aerodynamic inputs pertain only to the fuselage-portion of the aircraft, i.e., the aerodynamic properties of the aircraft minus the rotors, wings, stores and stabilizing surfaces.



The bailed AH-1G aircraft was weighed and its longitudinal and lateral center-of-gravity locations determined after the weapons and armor were removed and the instrumentation and instrumented rotor installed. The measured weight was 6289 pounds, with the center of gravity located at station 203.3 and buttline 0.455. These were the base quantities to which the weight of the crew, fuel and any stores were added. In addition to these three measured quantities, the computer analysis requires the vertical center-of-gravity location, the aircraft mass moments of inertia about the three body axes, and the pitch-yaw product of inertia. These latter quantities are normally computed using a detailed weights analysis for the configuration, as they are quite difficult to measure. For this study, the weights analysis for the last AH-1G constructed was available, but in the basic configuration (bailed ship minus weapons and armor, plus instrumentation and instrumented rotor), the analysis gave a weight of 6030 pounds and a center-of-gravity station of 204.9 and buttline of 0.059. The cause of these discrepancies is assumed to be due to differences between the original production configuration of the bailed ship (Ship Number 20391) and the production configuration described in the weights data (applicable to Ship Number 21134), and due to modifications made to the ship in the field. A lumped point-mass of 258.6 pounds would have to be added at station 165.2 and buttline 12.7 to make the computations agree with the measurements. Due to the known lateral symmetry of the AH-1G and the very small lateral center-of-gravity offset computed from known mass data, the measured lateral cg offset was presumed to be in error. The weights data were modified to include 258.6 pounds at station 165.2 and buttline zero. The weight of the crew, fuel and any stores were then added to this basic configuration to calculate the gross weight, center of gravity and inertias for the configurations tested. These quantities are summarized in Table 6.

The fuselage reference center location (defined by XFS(2) through XFS(4)) is identical to the reference center location of the wind tunnel model.<sup>25</sup> The force and moment equation use indicator, XFS(12), was set to indicate that forward flight was being simulated, while the phasing angles, XFS(13) and XFS(14), were set to reflect the range of data input to the Nominal Angle and High Angle equations.

<sup>25</sup>Oldenbottle, R. H., White, R. M., and Cooksey, J. M., A LOW SPEED WIND TUNNEL TEST OF THE BELL HELICOPTER COMPANY 0.200 SCALE AH-1G/AH-1S MODEL INVESTIGATING AERODYNAMIC CHARACTERISTICS, Vought Systems Division Report LSWT 490, Vought Corporation, Dallas, Texas, 1975.

TABLE 6. AIRCRAFT MASS PROPERTIES FOR FUSELAGE GROUP.

Flight	Counter	Gross Weight, lb	Center-of-Gravity			Inertias, * slug-Ft <sup>2</sup>			
			Station	Butt- line	Water- line	Roll	Pitch	Yaw	Cross-Product
32A	558-561	8289.0	196.7	0.0	74.88	2650.8	12977.4	10613.8	-464.2
35A	610-615	8319.0	200.6	0.0	68.0	2904.0	11883.4	10233.5	-585.0
36A**	635	8461.0	195.787	0.0	74.425	2904.0	11883.4	10233.5	-585.0
37A**	675	8460.0	199.125	0.0	74.425	2904.0	11883.4	10233.5	-585.0
45B	1078	8289.0	196.7	0.0	74.88	2904.0	11883.4	10233.5	-585.0
45C	1093	8300.0	191.6	0.0	75.00	2904.0	11883.4	10233.5	-585.0

\*Inertias need only be a consistent set for trim cases, as they are not used in the trim analysis. Therefore, the inertias given here for Flights 35A, 36A, 37A, 45B and 45C are only representative.

\*\*Fuselage-only values - mass properties of stores added by C81 after all input data have been read.

The six fuselage aerodynamic forces and moments are computed in Program C81 using six independent sets of wind-axis equations that are third order in complex angle of attack and sideslip. For this study, the 84 inputs to these equations were found by processing 1/5-scale model wind tunnel test data (Reference 25) with program AN9101 (Section 7.7, Volume II, Reference 3). This program was written specifically to perform a least-squares curve-fit on test data to compute the inputs required by C81. Due to some inconsistencies in the wind tunnel test data, the resulting curve fit was not very good; several fuselage-only C81 runs were made to improve the correlation between C81 and the faired wind-tunnel data.

Additionally, very little data were available for the fuselage with the landing gear installed, so the AN9101 runs had been made using test data for the bare fuselage. The additional lift (nondimensionalized by dynamic pressure) due to the gear was estimated to be 1.0 square foot; the additional equivalent flat plate drag area to be 1.75 square feet; and the additional nose-down pitching moment to be 7.05 cubic feet. The increments to aerodynamic side force, rolling moment, and yawing moment due to the skid gear were assumed to be very small in comparison to the fuselage-only values, and were ignored.

The fuselage equivalent flat plate drag area, XFS(29), that was determined by Program AN9101 also had to be increased to account for Reynolds number effects. The number used was 5.5 square feet for the aft- and mid-cg flight conditions.

XFS(29) was set to 8.5 square feet for the simulation of the forward-cg test cases, based on test data given in Reference 26. This increase in flat plate drag area is well documented, and is not a  $C_{D_\alpha}$  effect.

### 3.11 LANDING GEAR GROUPS

The landing gear model has not been implemented in AGAJ77, so no inputs are required for this group.

<sup>26</sup>Finnestead, R. L., Laing, E., Connor, W. J., and Buss, M. W., ENGINEERING FLIGHT TEST AH-1G HELICOPTER (HUEY COBRA), PHASE D, PART 2, PERFORMANCE, FINAL REPORT, U. S. Army Aviation Systems Test Activity, Edwards Air Force Base, California, 1970, page 21.

### 3.12 WING GROUP

The input format for the Wing Group is described in Sections 2.14 and 3.14 of Volume II of Reference 3. The inputs to this group are listed in Figure 18.

The wing area, including carry-through (XWG(1)), was scaled directly from the AH-1G Basic Lines Data, Figure 8.

The spanwise location of the center of pressure of the right wing panel, XWG(3), was calculated using the method for determining the mean geometric chord, as described in Reference 23. The chordwise and vertical locations of the center of pressure (XWG(2) and XWG(4)) were interpolated between those of the root section (a NACA 0030) and the tip section (a NACA 0025) as given in Reference 27.

The incidence angle, dihedral angle, quarter-chord sweep angle, geometric aspect ratio (including the carry-through) and taper ratio (XWG(5) through XWG(8) and XWG(10)) were determined from the Basic Lines Drawing. The spanwise efficiency factor, XWG(9), was determined from data presented in Reference 23.

XWG(11) through XWG(13), the coefficients in the equation for the dynamic pressure reduction at the stabilizers due to the wing, the dynamic pressure reduction at the wing due to the fuselage, and the coefficient in the equation for the wing-wake-centerline deflection were all estimated to be 0.0 based on experience.

There is no moveable control surface on the AH-1G wing, so XWG(14) through XWG(23) were input as 0.0.

The coefficients for the downwash and sidewash at the wing due to the fuselage, XWG(24) through XWG(28), were also estimated to be 0.0.

<sup>27</sup>Jacobs, E. A., and Abbott, I. H., AIRFOIL SECTION DATA OBTAINED IN THE N.A.C.A. VARIABLE DENSITY TUNNEL AS AFFECTED BY SUPPORT INTERFERENCE AND OTHER CORRECTIONS, NASA TR 669, National Advisory Committee for Aeronautics, Washington, D. C., 1939.





Determination of the main and tail rotor downwash at the right and left wing center-of-pressure positions is difficult in the absence of a reliable rotor wake program. A simple method was used to determine the rotor far-field downwash characteristics in this study, as described in Section 3.12.1.

The aerodynamic coefficients in the moment equations, XWG(33) through XWG(42), were all set to zero based on previous experience.

Equations were used to represent the wing aerodynamics instead of a table. The inputs to the equations, YWG(1) through YWG(28), were developed over the course of several years by using standard procedures for finite aspect ratio airfoils and using wind tunnel data for isolated airfoils and scale models of this aircraft with and without the wings.

There are no moveable control surfaces on the wing, and the wing incidence is fixed, so the wing control linkages group, XCWG(1) through XCWG(14), was not included in the deck.

### 3.12.1 Iterative Method for Determining Main Rotor Downwash on Wings, Horizontal Stabilizers, and Fuselage

A simple graphical method for determining the downwash at a point away from the rotor was utilized, assuming an uncontracted, momentum theory wake, and no rotor coning. Initially, a C81 case was run for the flight condition of interest, preferably with zero downwash at the elevator, wing, and fuselage centers of pressure. The resulting computed pitch attitude, flapping, and induced velocity were used to graphically determine the position of the wake in body axes. The rotor was drawn in its flapped, unconed position on a Basic Lines Drawing, and the wake was assumed to be convected away from the rotor at an angle equal to

$$x_{\text{wake}} = -\theta + \beta_m \frac{V \sin \alpha + v_i}{V \cos \alpha} \quad (3)$$

where

- $\theta$  is the fuselage pitch attitude, positive nose up
- $\beta_m$  is the longitudinal mast tilt, positive forward
- $V \sin \alpha$  is the body-axis vertical component of the free stream flow, positive down
- $V \cos \alpha$  is the body-axis longitudinal component of the free stream flow, positive aft
- $v_i$  is the main rotor average induced velocity, positive down

A line was drawn from the tip of the blade, at an angle  $\chi_{wake}$  downward from the flapped position, at both the 0 and 180 degree azimuth positions. The uncontracted wake was assumed to be between these two lines.

If the horizontal stabilizer, wing, or fuselage center of pressure was entirely outside these boundaries, then no downwash factor was applied. If the center of pressure was inside the boundaries, a downwash factor greater than 0 but less than 2 was used.

If non-zero downwash factors were computed, they were included in the input deck, the case rerun, and the wake position plotted again. Convergence was achieved after one or two iterations.

Using this method, non-zero downwash factors were computed only for the 10-knot case, Counter 1078. These factors were

Main rotor downwash factor for fuselage center of pressure, XMR(33)	2.0
Main rotor downwash factors for right and left wing panels, XWG(29) and XWG(30)	2.0
Main rotor downwash factor for right and left horizontal stabilizers, XSTB2(29) and XSTB3(29)	1.75

The rotor-two wake was assumed to have no effect on the fuselage, wing, or stabilizer aerodynamics, so XTR(33), XWG(31), XWG(32), XSTB1(32), XSTB2(32) and XSTB3(32) were all set to zero.

### 3.13 STABILIZING SURFACE NUMBER 1 GROUP

The input format for the Stabilizing Surface Groups is described in Sections 2.15 and 3.15 of Volume II of Reference 3. The Stabilizing Surface Number 1 Group contains the inputs for the AH-1G vertical stabilizer, and is listed in Figure 19.

The geometric inputs were obtained in a manner similar to that described for the wing. In the absence of detailed aerodynamic data for the airfoils used in the fin, the aerodynamic center was assumed to be at buttline zero, and at a stationline and buttline computed by the method described for the wing.

The tailboom was assumed to be effectively rigid for the fin model, so XSTB1(11) was set to zero.

The fin has no moveable control surfaces, so XSTB1(15) through XSTB1(28) were set to zero.

The vertical stabilizer was assumed to be unaffected by the main rotor wake, so XSTB1(29) through XSTB1(31) were set to zero. The effect of the tail rotor wake on the fin was unknown, so XSTB1(32) through XSTB1(34) were also set to zero.

The aerodynamic inputs for the fin, YSTB1(1) through YSTB1(28), were derived over several years and had been found to give reasonable correlation with AH-1G test data.

XCS1(1) through XCS1(14) were not input because the fin incidence is fixed and the fin has no moveable control surfaces.

### 3.14 STABILIZING SURFACE NUMBER 2 GROUP

The input format for the Stabilizing Surface Groups is described in Sections 2.15 and 3.15 of Volume II of Reference 3. The Stabilizing Surface Number 2 Group contains the inputs for the AH-1G right horizontal stabilizer, and is listed in Figure 20.

The geometric inputs were obtained in a manner similar to that described for the wing. The elevator is an inverted Clark-Y airfoil, so the chordwise and vertical center of pressure locations were determined from data in Reference 28.

<sup>28</sup>Pinkerton, R. M., and Greenberg, H., AERODYNAMIC CHARACTERISTICS OF A LARGE NUMBER OF AIRFOILS TESTED IN THE VARIABLE-DENSITY WIND TUNNEL, NACA TR 628, National Advisory Committee for Aeronautics, Washington, D.C., 1938.

95

Figure 19. OLS Stabilizing Surface Number 1 Group.

AD-A089 008

BELL HELICOPTER TEXTRON FORT WORTH TX

F/6 1 3

VALIDATION OF THE ROTORCRAFT FLIGHT SIMULATION PROGRAM (C81) US--ETC(U)

JUL 80 J R VAN SAASBEEK

DAAJ02-77-C-0003

UNCLASSIFIED

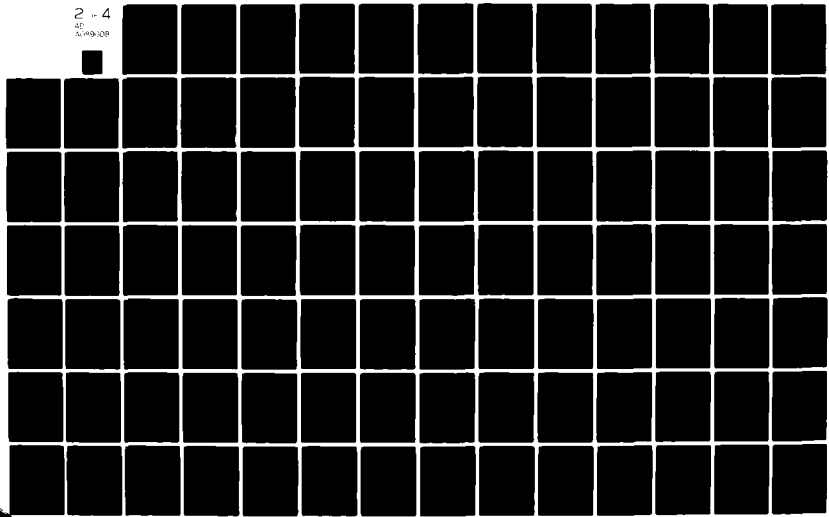
BHT-699-099-006

USAAVRADCOM-TR-80-D-4

NL

2 - 4

AD  
15-09-000





The tailboom was also assumed to be effectively rigid for the elevator calculations, so XSTB2(11) was set to zero.

The downwash at the elevator due to the wing, XSTB2(13), was estimated to be 1.0 since the wing wake was assumed to be only partially developed at the elevator location.

The main rotor downwash factor for the elevator was determined by the method described in Section 3.12.1.

Equations were used to represent the elevator aerodynamics. Two-dimensional Clark-Y airfoil data were taken from Reference 28 and three-dimensional data created using techniques such as those given in Reference 23. Inputs were then generated for YSTB2(1) through YSTB2(28) to give a good representation of the low-aspect ratio, inverted Clark-Y elevator.

The elevator incidence angle is controlled by the longitudinal cyclic stick. The values of the Stabilizing Surface Number 2 Control Linkage Inputs, plus the incidence angle, XSTB2(5), were determined so that the computed incidence angle agreed with the schedule given on page 5 of Layout Drawing 209-008-037, page A-30 of Reference 29. The chart gives the angle of the flat upper surface of the inverted Clark-Y, relative to a waterline, as a function of the stick position. This angle was also measured on the OLS aircraft, but the measured schedule did not agree with the published data, which are based on the kinematics of the control system geometry, so the data of Reference 29 were used.

The elevator incidence angle computed by XSTB2(5), XCS2(4) and XCS2(5), is that of the zero lift line, not the flat upper surface. The angle between the flat surface and the zero lift line was found in Reference 28 and the schedule of the zero-lift-line incidence with longitudinal cyclic was calculated. A parabolic least-squares curve fit of this schedule yielded the inputs for the incidence angle (XSTB2(5)), linear term (XCS2(4)) and second-order term (XCS2(5)) in the elevator control linkage.

### 3.15 STABILIZING SURFACE NUMBER 3 GROUP

The Stabilizing Surface Number 3 Group contains the inputs for the left horizontal stabilizer, which is antisymmetric

<sup>29</sup>Davis, J. M., STABILITY AND CONTROL DATA SUMMARIES FOR THE AH-1G AND UH-1H HELICOPTERS, Technical Report 699-099-012, Bell Helicopter Textron, Fort Worth, Texas, 1976.



to the right elevator. Therefore, the inputs to this group are identical to those of the Stabilizing Surface Number 2 Group, except for a sign change on the center-of-pressure buttline, XSTB3(3).

### 3.16 JET GROUP

Auxiliary propulsion was not installed on the OLS aircraft, so the Jet Group was not input.

### 3.17 EXTERNAL STORE/AERODYNAMIC BRAKE GROUP

Four simulated XM-159 rocket pods were carried on the aircraft during some of the flights selected to be analyzed in this study. The input format for the External Store/Aerodynamic Brake Group is given in Sections 2.17 and 3.17 of Volume II of Reference 3. The inputs used for the stores-on simulations are listed in Figure 21.

The mass properties of the stores were determined from the flight test engineer's weight-and-balance estimation sheets and from unpublished data covering the XM-159 pods. The center-of-gravity locations were transformed to the body axis coordinate system using these data plus the AH-1G Basic Lines Drawing and detailed design drawings of the pylons.

The aerodynamic inputs were estimated by assuming the pods to be bodies of revolution. These quantities were modified to include all the estimated wing-store interference effects. Finally, the flat-plate drag area was adjusted to give the observed total difference in drag between a stores-off and stores-on Cobra.

### 3.18 ROTOR CONTROLS GROUP

The input format for the Rotor Controls Group is described in Sections 2.18 and 3.18 of Volume II of Reference 3. The inputs to this group are listed in Figure 22. Only the Basic Controls Subgroup is required, as the AH-1G rotor controls do not have nonlinear rigging or coupling. The first three inputs on each of the four cards completely define the rotor control rigging.

The range of the collective and cyclic sticks and pedals (XCON(1), XCON(8), XCON(15) and XCON(22)) were reported in Reference 29.

The limits of the swashplate angles for both the main and tail rotor were measured on the OLS test vehicle. These unpublished data were initially used to compute the limits and ranges that



10-000000	12-000000	12-000000	0-500000	AH-16 CONTROLS GROUP	S/N 20391	(OLS CORRELATION)	CONTROLS GROUP	00	00	00
7-800000	19-50000	00	00	00	00	00	00	00	00	00
-15-50000	30-50001	00	00	00	00	00	00	00	00	00
-11-00000	16-87000	00	00	00	00	00	00	00	00	00
10-00000	-28-17000	00	00	00	00	00	00	00	00	00

Figure 22. OLS Controls Group.

are the second and third inputs on CARDS 191 through 194. Initial simulation runs showed a significant discrepancy between measured and computed stick and pedal positions, while the computed feathering angles were in good agreement with the test data. The flight-test measured feathering angles were plotted versus the flight-test measured stick positions and a new set of control limits and ranges determined from the plots. The flight-test measured control riggings were used for the collective, longitudinal cyclic and pedal. The plot of the flight-test measured lateral cyclic angle versus the flight-test measured lateral cyclic stick position showed a great deal of scatter and, due to a very steep slope, a lateral swashplate range well in excess of that available on the AH-1G. Therefore, the lateral cyclic rigging used in the simulations was derived from the ground-measured data.

### 3.19 ENGINE-GOVERNOR GROUP

The input format for the Engine-Governor Group is described in Sections 2.19 and 3.19 of Volume II of Reference 3. The inputs are listed in Figure 23.

Engine power available curves were created by cross-plotting the sea level data in Figures 27 and 29 of Reference 30, with the Normal Rated Power data used for the maximum continuous horsepower available inputs (XNG(2) through XNG(7)) and the Military Rated Power used to derive the maximum take-off horsepower inputs (XNG(9) through XNG(14)). Both of the referenced figures give the transmission limit of 1134.0 horsepower, which is the value input for both XNG(1) and XNG(8).

The normal engine rpm, XNG(15), was given as 6600.0 in Reference 30. The governor power gain and time constants for power increase and decrease, XNG(16) through XNG(18), are values that had been used successfully in the hybrid computer version of C81. XNG(19) and XNG(20) were input as 0.0 so that the default inertias, based on the rotor flapping inertias, would be used. The drive system rotational inertia, XNG(21), was not known, and is small in comparison with the rotor rotational inertias, so it was set to zero.

<sup>30</sup>Smith, R. P., AH-1G AERODYNAMIC SUBSTANTIATING DATA REPORT FOR STANDARD AIRCRAFT CHARACTERISTICS CHARTS AND FLIGHT MANUAL BASED ON ARMY PHASE D FLIGHT TEST RESULTS, Technical Report 209-099-274, Bell Helicopter Textron, Fort Worth, Texas, 1971.



Individual main rotor and tail rotor gearbox efficiency factors were not known, so XNG(22) and XNG(23) were input as 1.0. The overall drive train efficiency, XNG(24), was set to 0.97 based on unpublished bench-test data showing losses between 0 and 6 percent from test to test. The accessory horsepower, XNG(25), was estimated to be 12 horsepower.

### 3.20 ITERATION LOGIC GROUP

The input format for the Iteration Logic group is described in Sections 2.20 and 3.20 of Volume II of Reference 3. The inputs are listed in Figure 24.

The iteration limit, XIT(1), was set to 41.0 so that a partial derivative matrix would be computed and output for the last iteration should the trim fail.

The azimuth increment for time-variant trim, XIT(2), was set to 10.0, but is internally reset, if necessary, to ensure that there are 10 time-points per cycle of the highest frequency mode input.

The limiter for the maximum change in the average induced velocity is twice the value input for XIT(3). The value of 0.5 was chosen based on experience.

The STAB analysis was not to be used, but a normal value for the partial derivative increment, XIT(4), was included in the inputs.

Data for the last two revolutions of the time-variant trim were to be plotted, so XIT(5) was set to 2.0.

Five revolutions in time-variant trim have been found to be sufficient to ensure convergence for teetering rotors, so XIT(6) was set to 5.0.

A value of 0.3 was input for XIT(7), the torsional bounce damper.

All the inputs on the second card, XIT(8) through XIT(14), are traditional values used successfully in the numerical procedures for several years.

The allowable errors on the third card in this group, XIT(15) through XIT(21), were chosen to yield convergence to a trim condition with small net accelerations in an acceptably small number of iterations.



### 3.21 FLIGHT CONSTANTS GROUP

The input format for the Flight Constants Group is described in Sections 2.21 and 3.21 of Volume II of Reference 3.

The inputs for this group vary from case to case, and are not listed here. The true airspeed, XFC(1), yaw or roll angle, XFC(4) or XFC(6), and atmospheric properties, XFC(26), XFC(27) and XFC(28), for each counter simulated, are given in Table 7.

The lateral and vertical velocities, XFC(2) and XFC(3), were input as zero for all cases. The geometric altitude, XFC(4), was always input as 1000.0, which ensures that the ground effect calculations were not invoked. The yaw angle and pitch angle, XFC(5) and XFC(6), were estimated and input as initial conditions for the trim procedure, except for the 10-knot case. In this latter simulation, the pitch and roll angles, XFC(6) and XFC(7), were estimated inputs. The inputs for the control positions, XFC(8) through XFC(11), were also estimates. XFC(12) was input as zero, as the trims were for unaccelerated flight. The initial flapping angles and thrust values for both rotors were estimated and input as XFC(15) through XFC(20).



TABLE 7. ESSENTIAL FLIGHT CONSTANTS GROUP INPUTS.

Flight	Counter	True Airspeed XFC(1)	Euler Yaw Angle XFC(5)*	Euler Pitch Angle XFC(6)	Euler Roll Angle XFC(7)*	Atmospheric Logic Switch XFC(26)	Altitude XFC(27)	Temperature XFC(28)
32A	561	133.5	0.56	-6.08	-2.5	0.0	5000.0	0.0
	562	133.5	-4.75	-6.07	2.0	0.0	5000.0	0.0
35A	611	66.7	-4.9	-1.23	0.090	-1.0	2900.0	27.0
	612	85.6	-4.6	-1.1	0.731	-1.0	2900.0	27.0
	614	116.2	-0.8	-3.8	-1.566	-1.0	2900.0	27.0
	615	129.3	-1.9	-4.9	-1.232	-1.0	2900.0	27.0
36A	610	142.0	-1.8	-4.3	-0.321	-1.0	2900.0	27.0
	635	135.9	-0.8	-7.7	-1.049	-1.0	2900.0	28.2
37A	675	138.0	-0.85	-6.65	-1.306	-1.0	2900.0	28.2
45B	1078	10.0	0.0	0.95	-1.5	-1.0	900.0	28.58
45C	1093	144.5	-0.8	-9.9	-0.993	-1.0	3300.0	24.0

\*Trim-to-constant yaw angle only for the low-speed flight condition.  
All other cases were trim-to-constant roll angle cases.

#### 4. C81 NUMERICAL SOLUTION METHODS

The rotor modeling techniques, trim options and maneuver solution methods used in the simulations affect the results computed by C81. Therefore, the options available are discussed in this section so that the data comparisons discussed in subsequent sections of the report can be evaluated in the context of the specific rotor models and numerical methods used.

Two separate rotor models, three different numerical trim procedures and two maneuver methods are available in C81. There are also two mechanisms for modeling the rotor induced velocity, yielding twelve ways to simulate a trimmed flight condition and eight ways to simulate a maneuver. The options available, and those chosen, are discussed in the remainder of this section.

##### 4.1 ROTOR MODELS

The rotors can be modeled as inelastic or elastic, with the choice for one rotor independent of that for the other. Only teetering or gimbaled rotors can be properly modeled using the inelastic model, since the rotor is assumed to have only rigid-body flapping freedom about a central hinge, with moment carryover between the blades. Articulated rotors with inelastic blades may be accurately represented using the elastic model with only the rigid blade mode. Any type of rotor can be modeled as elastic, with up to eleven normal modes being used to represent the rotor.

The tail rotor was always modeled as inelastic for these simulations, while both inelastic and elastic models were used for the main rotor.

##### 4.2 C81 TRIM METHODS

The three trim algorithms are the quasi-static, time-variant and fully time-variant trim procedures. Any of the three can be used to analyze either an inelastic or an elastic rotor. Generally, the quasi-static trim (QST) procedure is used to analyze inelastic rotors or to generate the initial conditions for a time-variant trim (TVT). The fully time-variant trim (FTVT) is used only on rare occasions in an attempt to create an exceptionally well-trimmed condition to initiate a maneuver run.

##### 4.2.1 Quasi-Static Trim Procedure

A problem of up to ten independent variables is solved in the quasi-static trim procedure, using a multi-dimensional Newton-Raphson technique. The ten independent variables used in the

quasi-static trim analysis of a complete rotorcraft are listed in Table 8, as are the ten constraint quantities. The method iterates to a solution from an initial estimate of the trim condition, provided by initial values for the ten independent variables input in the Flight Constants Group (see Section 3.21).

If the absolute value of one or more of the ten constraint quantities is greater than the appropriate allowable error at the end of an iteration (other than the last), the constraint quantities are used as an error vector. A matrix containing the partial derivatives of each constraint quantity with respect to each independent variable is periodically computed during the trim, and the error vector is premultiplied by the inverse of this partial derivative matrix to yield a correction vector. The correction vector is added to the state vector of independent variables, providing a revised estimate of the trim condition to begin the next iteration.

The iterations continue until the absolute values of all ten constraint quantities are less than the input allowable errors (XIT(15) through XIT(21)) or until a user-specified number of iterations (XIT(1)) have been completed.

Whether the rotor is modeled as inelastic or elastic, the rotor analysis in the quasi-static trim computes the forces and moments on a single rotor blade at each of twelve equally spaced azimuth locations. At each azimuth, the blade is flapped through the angle

$$\beta = -a_1 \sin \psi - b_1 \cos \psi \quad (4)$$

relative to the mast. Forces and moments of the single blade computed for each of the twelve azimuth locations are transformed into the nonrotating system, summed, divided by twelve and multiplied by the number of blades. The results are the hub shears and moments imparted to the ship at the top of the rotor mast.

The salient features of the quasi-static rotor analysis are that the flapping angles,  $a_1$  and  $b_1$ , are the independent variables, regardless of rotor model, that the coning angle is zero, and that the rotor responds at one-per-rev. If the rotor is modeled as elastic, the modal participation factors are dependent variables throughout the quasi-static analysis, and a one-per-rev time history will be computed for each.

Because the one-per-rev response of the elastic modes is included in the QST, a trim with elastic modes will yield slightly different results from a QST in the same flight conditions with an inelastic rotor.

TABLE 8. TEN INDEPENDENT VARIABLES AND TEN CONSTRAINT  
QUANTITIES IN A NORMAL QUASI-STATIC TRIM.

---

Independent Variables:

Collective Stick Position  
Longitudinal Stick Position  
Lateral Stick Position  
Pedal Position  
Fuselage Euler Pitch Attitude  
Fuselage Euler Yaw or Euler Roll Attitude  
Rotor I Longitudinal Tip-Path-Plane Flapping Angle  
Rotor I Lateral Tip-Path-Plane Flapping Angle  
Rotor II Longitudinal Tip-Path-Plane Flapping Angle  
Rotor II Lateral Tip-Path-Plane Flapping Angle

Constraint Quantities:

Rotorcraft Longitudinal Force  
Rotorcraft Lateral Force  
Rotorcraft Vertical Force  
Rotorcraft Pitching Moment\*  
Rotorcraft Rolling Moment\*  
Rotorcraft Yawing Moment\*  
Rotor I Longitudinal Flapping Moment  
Rotor I Lateral Flapping Moment  
Rotor II Longitudinal Flapping Moment  
Rotor II Lateral Flapping Moment

---

\*These moments are resolved about the rotorcraft center of gravity.

#### 4.2.2 Time-Variant Trim Procedure

The time-variant trim procedure analyzes only the response of a rotor. Consequently, during the TVT analysis of a rotor, the fuselage attitudes, control positions and the response of the other rotor are unmodified. The fuselage attitudes (which define the position of the rotor mast in space) and the control positions are essentially boundary conditions for the analysis. Since the TVT is entered only after the execution of at least one QST iteration, the values of these variables are assumed to correctly define the overall trim condition, within the allowable errors.

The TVT procedure uses a fourth-order Runge-Kutta algorithm to forward-integrate the modal participation factors (generalized coordinates) for XIT(6) rotor revolutions with an azimuth increment equal to, or less than, XIT(2).

The time-variant trim procedure is identical whether the rotor is modeled as inelastic or elastic, as a rigid-body flapping mode is assumed for an inelastic rotor. In either case, the initial conditions for the integration of the participation factors are derived from the one-per-rev time histories generated during QST.

Although the fuselage attitude and control positions are held constant during the procedure, the rotor response at the end of the TVT will generally differ from that at the end of the QST. There are no convergence criteria for the TVT: XIT(6) revolutions are analyzed. The quality of the trim is determined by examining time-history plots of the participation factors for evidence that a stabilized condition existed at the end of the TVT and by comparing the resulting rotor forces with those computed in the preceding QST. Since the main rotor response is slightly different at the end of TVT than it is at the end of QST, the net forces and moments at the aircraft center of gravity, and the main rotor flapping moments, are usually larger than the allowable errors. A typical set of these net forces and moments, as computed after the TVT with the internal induced velocity distribution, are given for Counter 610 in Table 9. The corresponding accelerations are also given in the table. Smaller net unbalanced forces and moments were computed at lower speeds, and slightly larger values were computed for the other  $V_H$  cases.

The net center-of-gravity translational accelerations are very small, while the net yaw and roll accelerations are larger, because the fuselage, fin, and tail rotor are not retrimmed during the main rotor TVT. The main rotor torque and lateral

TABLE 9. ABSOLUTE VALUE OF NET UNBALANCED FORCES AND MOMENTS, AND CORRESPONDING ACCELERATIONS, AFTER TIME-VARIANT TRIM FOR COUNTER 610 (8319 POUNDS, AFT CG, CLEAN WING, 142 KTAS) USING THE INTERNAL INDUCED VELOCITY DISTRIBUTION

Absolute Value of Net Unbalanced Forces at Center of Gravity, Pounds			Absolute Value of Net Unbalanced Moments at Center of Gravity, Foot-Pounds*			Absolute Value of Net Unbalanced Main Rotor Flapping Moments, Foot-Pounds	
Longitudinal	Lateral	Vertical	Yaw	Pitch	Roll	Longitudinal	Lateral
10	35	112	293	64	245	19	195
$g's$			Accelerations rad/sec			rad/sec	
0.001	0.004	0.013	0.029	0.005	0.084	0.006	0.065

\*Body axis

flapping moment changed significantly between the QST and the TVT, changing the contribution of the main rotor to the yawing and rolling moment at the aircraft center of gravity. Considering all the cases, the net unbalanced center-of-gravity translational accelerations were less than 0.02g, and the net unbalanced angular accelerations, both at the center of gravity and at the teetering pin, were generally less than 5.0 degrees per second per second. These small deviations from a "perfect" trim are normally considered to be acceptable.

#### 4.2.3 Fully-Time-Variant Trim Procedure

The fully-time-variant trim, which is not normally used, is a combination of the quasi-static and time-variant trim methods. The QS Newton-Raphson technique is used to trim the airframe, controls and the non-time-variant rotor. Instead of using the QS rotor analysis for the rotor of interest, the time-variant analysis is used, with XIT(6) rotor revolutions with an angular increment equal to, or less than, XIT(2). This is a very time-consuming process, but can yield a very accurate trim. This procedure was used to perform the trims leading into the maneuver simulations.

#### 4.3 MANEUVER METHODS

The fourth-order Runge-Kutta forward integration procedure is used to solve the airframe equations of motion in a maneuver simulation in C81. Regardless of the rotor model chosen, the quasi-static or time-variant rotor analysis can be used to compute the response of each rotor. If the quasi-static rotor analysis is selected, the rotor flapping angles are the independent variables, even for an elastic rotor, and the rotor loading is computed for twelve blade azimuths at each time cut. If the time-variant rotor analysis is chosen, the modal participation factors are the independent variables, and a rigid body flapping mode is assumed for the rotor if it is modeled as inelastic. In the time-variant rotor analysis, rotor loading is computed only for the actual number of blades comprising the rotor, at their actual azimuth locations for that time cut.

Each rotor can use either of the rotor analyses independently. Generally, a maneuver simulation will run faster if a two-bladed rotor is analyzed using the time-variant procedure instead of the quasi-static procedure. When the time-variant trim procedure is used, the time increment will generally correspond to between 6.0 and 7.5 degrees of azimuth, while the quasi-static procedure will be convergent with a time increment corresponding to as much as thirty degrees of azimuth. Analyzing two blades every six degrees is faster than analyzing twelve every thirty degrees.

#### 4.4 ROTOR-INDUCED VELOCITY MODELS

Two different rotor-induced velocity representations are available in C81. By default, the program will use a reasonably simple, empirical triangular distribution or the user can input a bivariate table of normalized induced velocity harmonics and average induced velocities. The induced velocity computed by either analysis is assumed to be parallel to the rotor resultant force vector, and is of the form

$$v_i(r, \psi) = \bar{v}_i F(r, \mu, \psi) \quad (5)$$

where

$\bar{v}_i$  is a nominal induced velocity that is constant across the disc

$F(r, \mu, \psi)$  is the distribution function

The "average induced velocity" printed on the trim or maneuver page is  $\bar{v}_i$ .

Both models used during the simulations are reviewed in this section. (The models are described in detail in Section 3.4.2 of Volume I of Reference 3.)

##### 4.4.1 Built-in Induced Velocity Model

The built-in induced velocity distribution is the option normally used, and is selected by default. Both  $\bar{v}_i$  and  $F(r, \mu, \psi)$  are computed empirically. The distribution function is

$$F(r, \mu, \psi) = \frac{4}{3} \frac{r}{R} (1 + f_1(\mu) \cos \psi) + \\ (f_2(\frac{r}{R}, \psi) f_1(\mu) K_{27})^* \\ \sqrt{-0.5V_N^2 + \sqrt{0.25V_N^4 + (\bar{v}_i)_N^2}} \quad (6.a)$$

where  $f_1(\mu)$  is a distribution function

$f_2(\frac{r}{R}, \psi)$  is a distribution function



$K_{27}$  is the tip-vortex effect input,  
XMR(27) or XTR(27)

$V_N$  is the flight path airspeed in ft/sec  
divided by 1.0 ft/sec

$\bar{v}_{iN}$  is  $\bar{v}_i$  in ft/sec divided by 1.0 ft/sec

The variable  $K_{27}$  is XMR(27) or XTR(27), which were input as zero, yielding

$$F(r, \mu, \psi) = \frac{4}{3} \frac{r}{R} (1 + f_1(\mu) \cos \psi) \quad (6.b)$$

For rotor rotational speeds larger than one radian per second,

$$f_1(\mu) = \begin{cases} 11.25 \mu & \text{for } \mu < 0.1067 \\ 1.36 - 1.5 \mu & \text{for } 0.1067 < \mu < 0.5733 \\ 0.5 & \text{for } \mu \geq 0.5733 \end{cases} \quad (6.c)$$

Equation (6.b) yields a triangular distribution that has a cosine one-per-rev variation.

The nominal value of induced velocity,  $\bar{v}_i$ , for the built-in model is computed from

$$\bar{v}_i = \frac{C_B(\Omega R)}{\sqrt{0.866 \bar{\lambda}^2 + \bar{\mu}^2} + \frac{0.6 |C_B|^{1.5} (|C_B| + 8 |\bar{\lambda}| \bar{\lambda}/3)}{(C_B + 8 \bar{\lambda}^2)(C_B + 8 \bar{\mu}^2)}} \quad (7)$$

where  $C_B$  is the thrust coefficient corrected for tip loss and hub extent

$\bar{\lambda}^2$  is  $(V \sin \alpha_m - \bar{v}_i)/\Omega R$

$\bar{\mu}^2$  is  $V \cos \alpha_m/\Omega R$

Equation (7) must be solved iteratively since  $\bar{\lambda}$  is a function of  $\bar{v}_i$ . The solution proceeds until 100 iterations have been performed or until  $\bar{v}_{i_{NEW}}$  is within 0.0001 foot per second of  $\bar{v}_{i_{OLD}}$ .

In this model,  $\bar{v}_i$  is 8/9 the average value computed by integrating Equation (6.b) over the disc and dividing by the disc area.

An empirical correction is applied to  $\bar{v}_i$  to account for ground effect whenever the airspeed is less than 30 feet per second and the aircraft altitude is between one-quarter and one rotor diameter above the ground.

#### 4.4.2 Input Rotor-Induced Velocity Model

The user can choose to use a different rotor-induced velocity model by inputting a Rotor-Induced Velocity Distribution Table. The table contains the reference rotor resultant force for which the table was generated, a bivariate table of rotor induced velocity harmonics, and a bivariate table of rotor average induced velocities. Program C81 computes a wake-plane angle of attack,  $\alpha_{wp}$  (where the wake plane is the plane perpendicular to the resultant force), and a wake-plane phase angle,  $\phi_{wp}$ . The instantaneous values of  $\alpha_{wp}$  and  $\mu$  are used to extract the harmonics from the table, yielding

$\eta_s(r, n, \alpha_{wp}, \mu)$  = the n-per-rev sine component of the distribution function at the radius r

$\eta_c(r, n, \alpha_{wp}, \mu)$  = the n-per-rev cosine component of the distribution function at the radius r

The distribution function at a given radius and azimuth is then computed as

$$F(r, \mu, \psi) = \sum_{n=0}^{n=N} \left\{ \eta_s(r, n, \alpha_{wp}, \mu) \sin(n\psi - \phi_{wp}) + \eta_c(r, n, \alpha_{wp}, \mu) \cos(n\psi - \phi_{wp}) \right\} \quad (8)$$

where N is the maximum number of harmonics.

In like manner, a bivariate interpolation of the average induced-velocity table is used to extract a value of  $\bar{v}_i$  for the instantaneous values of  $\alpha_{wp}$  and  $\mu$ . This value,  $\bar{v}_i(\alpha_{wp}, \mu)$ , is modified to yield  $\bar{v}_i$ , according to Equation 9:

$$\bar{v}_i = \left\{ \frac{\bar{v}_{iC81} (F_{C81})}{\bar{v}_{iC81} (F_R)} + 0.0763 \left( 1 - \frac{F_{C81}}{F_R} \right) \right\} \bar{v}_i(\alpha_{wp}, \mu) \quad (9)$$

where  $\bar{v}_{iC81} (F_{C81})$  is the value of  $\bar{v}_i$  computed iteratively by Equation (7) using a thrust coefficient based on the total average or filtered instantaneous rotor resultant force computed by C81.

$\bar{v}_{iC81} (F_R)$  is the value of  $\bar{v}_i$  computed iteratively by Equation (7) using a thrust coefficient based on the resultant force input with the RIVD table

$F_{C81}$  is the total instantaneous average or filtered value of the resultant force computed by C81

$F_R$  is the total resultant force input with the RIVD table

The values of  $F(r, \mu, \psi)$  and  $\bar{v}_i$  computed in Equations (8) and (9) are then substituted into Equation (5) to give the instantaneous induced velocity.

## 5. PERFORMANCE COMPARISONS

One of the primary requirements of a rotorcraft flight simulation program is that it accurately compute the performance characteristics of the aircraft. Preliminary design studies require an accurate calculation of power required and a reasonable estimate of aircraft attitudes. Handling qualities and flightpath stability analyses depend on computed stick positions and aircraft attitudes that are in close agreement with those actually obtained on the aircraft. Helicopter dynamics analyses, such as blade loads, vibrations and aeroelastic stability, must start with the rotor positioned correctly with respect to the flight path and the rotor mast to ensure correct calculation of the aerodynamic and dynamic loading on the rotor.

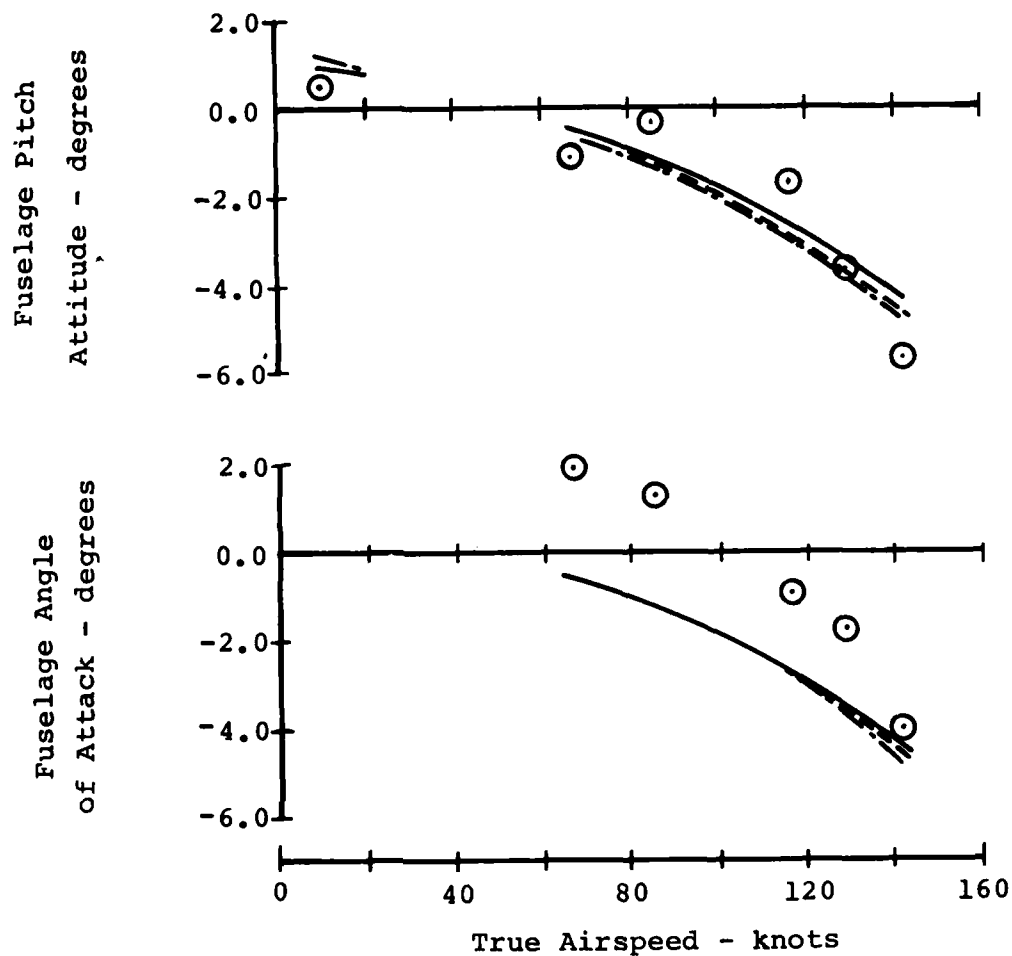
The ability of the AGAJ77 version of C81 to accurately compute the performance characteristics of the OLS-rotor-equipped AH-1G test aircraft is assessed in this section of the report. Computed aircraft attitudes, control positions, main rotor feathering and flapping angles, and required horsepower are compared with data measured in level flight. Comparisons of results are made for the following trim and induced velocity combinations; inelastic quasi-static, time variant with internal induced-velocity representation, and time-variant with an RIVD table.

Additionally, the aerodynamic environment of the main rotor is described for four of the level flight test conditions in Appendix A by examining contour plots of blade element normal force coefficient, pitching moment coefficient and angle of attack derived from measured pressure distributions and hot-wire anemometer data. Contour plots generated by C81 are compared with the measured data for two other level flight conditions in this section of the report.

### 5.1 AIRCRAFT ATTITUDES

The computed aircraft orientations with respect to the earth and the flight path are compared with measured data for several level flight test conditions in Figures 25 and 26 and Table 10.

The computed Euler pitch attitude is in reasonable agreement with the measured data for all three trim types. It is suspected that the pitch-up experienced by the test vehicle between 66 and 85 knots was due to increased main rotor wake impingement on the elevator. The pitch-up is not reflected in the computed pitch data because the simple downwash model,



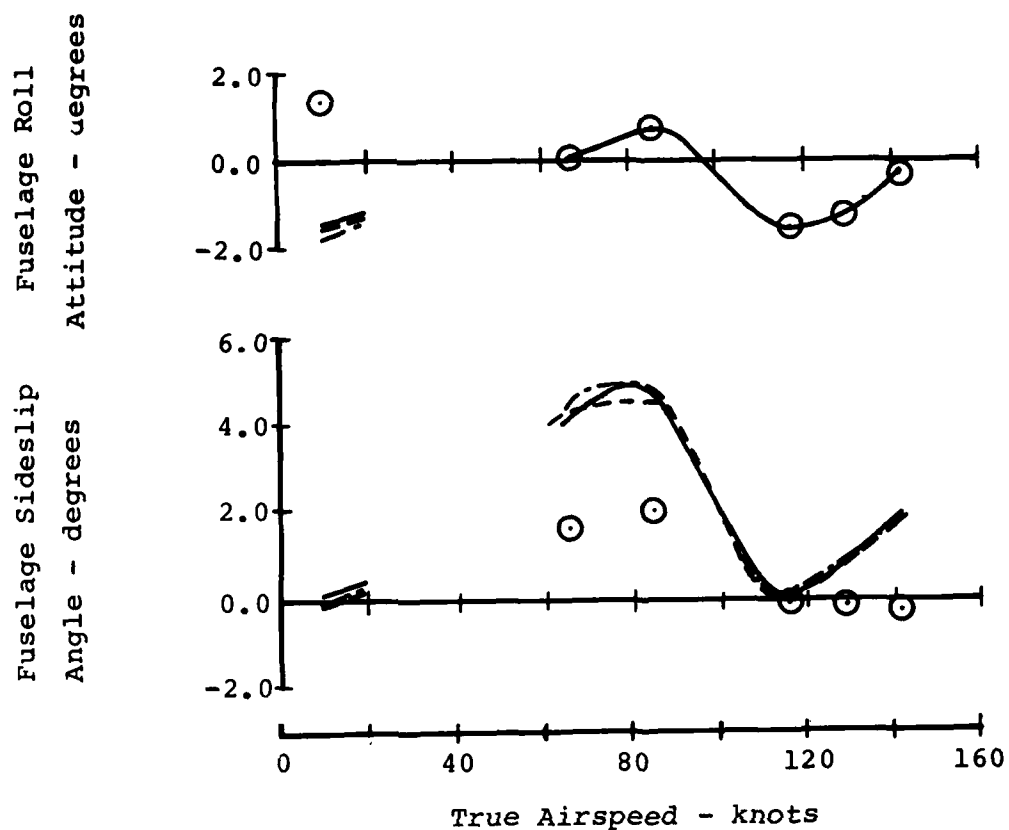
⊙ Test Data

C81 Data:

- Inelastic Quasi-Static Trim
- Time-Variant Trim, No RIVD
- .- Time-Variant Trim, with RIVD

10 KTAS case is Flight 45B, Counter 1078; 8289 pounds, mid center-of-gravity, clean wing.  
 66 through 142 KTAS cases are Flight 35A, Counters 611, 612, 614, 615 and 610: 8319 pounds, aft center-of-gravity, clean wing.

Figure 25. Comparison of Measured and Computed Aircraft Pitch Attitude and Angle of Attack in Level Flight.



⊙ Test Data

C81 Data:

— Inelastic Quasi-Static Trim  
 ---- Time-Variant Trim, No RIVD  
 --- Time-Variant Trim, with RIVD

10 KTAS case is Flight 45B, Counter 1078; 8289 pounds, mid center-of-gravity, clean wing.  
 66 through 142 KTAS cases are Flight 35A, Counters 611, 612, 614, 615 and 610: 8319 pounds, aft center-of-gravity, clean wing.

Figure 26. Comparison of Measured and Computed Aircraft Roll Attitude and Sideslip Angle in Level Flight.

TABLE 10. COMPARISON OF MEASURED AND COMPUTED  
AIRCRAFT ATTITUDES FOR COUNTERS  
635, 675 AND 1093

		<u>Trim Type</u>		
	Test	QST	TVT	TVT+RIVD
<u>Counter 635:</u>				
9069 lb, mid cg, 4 XM-159 rocket pods, 136 KTAS				
Euler Pitch Attitude, degrees	-6.843	-7.752	-7.959	-8.153
Angle of Attack, degrees	-	7.740	-7.940	-8.140
Euler Roll Attitude, degrees	-1.049	-1.049	-1.049	-1.049
Sideslip Angle, degrees	-	0.960	0.950	1.020
<u>Counter 675:</u>				
9068 lb, aft cg, 4 XM-159 rocket pods, 138 KTAS				
Euler Pitch Attitude, degrees	-6.654	-6.431	-6.694	-6.920
Angle of Attack, degrees	-5.270	-6.410	-6.680	-6.900
Euler Roll Attitude, degrees	-1.306	-1.306	-1.306	-1.306
Sideslip Angle, degrees	0.270	0.840	0.830	0.890
<u>Counter 1093:</u>				
8300 lb, fwd cg, clean wing, 145 KTAS				
Euler Pitch Attitude, degrees	-9.414	-9.990	-10.201	-10.394
Angle of Attack, degrees	-	-9.970	-10.190	-10.380
Euler Roll Attitude, degrees	-0.993	-0.993	-0.993	-0.993
Sideslip Angle, degrees	-	1.040	1.040	1.110

discussed in Section 3.12.1, does not account for this type of change in rotor wake velocity at the elevator. Aircraft attitude data were also compared for three other test conditions, all at maximum level flight airspeed. These data are compared with computed data in Table 10, with the computed pitch attitude being about equal to, or more nose down than, the measured fuselage pitch angle. These data add to the high-speed pitch attitude data of Figure 25. They also lend support, in a negative manner, to the supposition that the pitch-up is due to an unmodeled change in wake impingement on the elevator, as main rotor downwash on the stabilizer has a smaller effect at 129 to 142 knots than at 66 to 85 knots.

It should be noted that the inelastic quasi-static trim generally yields the least nose-down pitch attitude while the time-variant trim with a RIVD table yields the most nose-down pitch angle.

Airspeed-boom-measured angle of attack is compared with C81-computed fuselage angle of attack in Figure 25. The boom instrumentation is in a region of strong rotor-induced upwash at lower airspeeds. C81 computes the angle of attack at the fuselage center of pressure, which is exposed to the rotor downwash given in Section 3.12.1, and the free-stream velocity. Since the upwash at the boom location is not modeled at the center of pressure in C81, there is no reason to expect the computed angles of attack to agree with those measured in flight. In fact, the computed fuselage center-of-pressure angle of attack is very close to the computed pitch attitude, due to the rotor-induced velocity at this location being computed as zero (except for the 10-knot case). Test data for this low-speed test point are unavailable; C81 computed angles of attack of about -75 degrees.

Angle-of-attack information was also unavailable for counters 635 and 1093. C81 computed a center-of-pressure angle of attack about one degree more negative than that measured for counter 675, as shown in Table 10.

The boom-measured angle of attack is not a very meaningful quantity, for in level flight the airframe angle of attack, with respect to the free-stream, is essentially the aircraft pitch attitude. The actual local angle of attack of the airframe varies over the length of the aircraft, and is influenced by the local rotor downwash, not the rotor-induced upwash several feet in front of the fuselage.



The comparison of measured and computed Euler roll angle given in Figure 26 and Table 10 merely emphasizes the fact that all the level-flight simulations, except that at 10 knots, were trimmed at a constant roll angle set equal to that measured in flight. C81 cannot trim to a constant roll angle at low forward speed because the yaw angle is not well defined, so the level flight case at 10 knots was trimmed to a constant yaw angle of zero degrees. The discrepancy between measured and computed roll angle at 10 knots (Figure 26) may be due to an injudicious choice of yaw angle for the trim. Rotor aerodynamic contour plots (Appendix A) indicate that this counter may actually have been flown at a sideslip angle in excess of 40 degrees. Had sideslip data been available and the C81 simulations performed at an appropriate yaw angle, a positive roll angle would probably have been computed since the fuselage center of pressure is below the fuselage center of gravity.

Computed yaw angles are not compared with measured yaw data, as the recorded yaw angle is merely a measure of yaw deviation from the time that the prime data button was activated at the beginning of the record.

Airspeed-boom-measured and C81-computed sideslip angles are compared in Figure 26 and Table 10. Measured sideslip angle data are not available for the 10-knot case (counter 1078), counter 635 and counter 675. The comparison for the remainder of the test points is considered inadequate.

The test program reports do not document the uncertainty of the angular measuring devices. It was assumed that this uncertainty was of the order of 0.1 degree. If the uncertainty was 1.0 degree, then all the comparisons shown in this subsection demonstrate reasonable agreement between the test and the calculated data.

## 5.2 CONTROL ANGLES AND POSITIONS

### 5.2.1 General Considerations

Measured and computed main rotor feathering angles and control positions are compared in this section. Although the stick positions are reported in percentage of full throw, these data are angular measurements, as are the feathering angles. Also, the sensitivity of this instrumentation is not documented in the flight test reports, and is an unknown. The possibility of a trace-zero shift is also unknown. The quality of the feathering data can be investigated by examination of the measured feathering time histories for several counters.

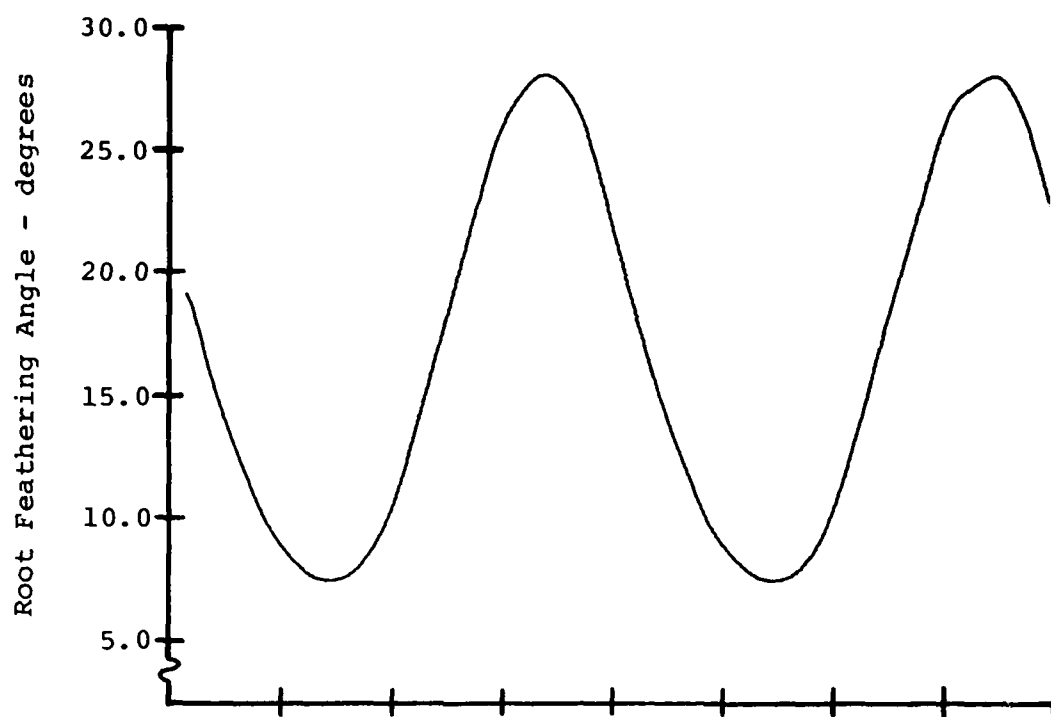
A constant feathering angle was measured for both counters 561 and 562, as demonstrated in time-history plots of item code D111, M/R Hub Pitch. As these two counters were the most severe maneuvers flown in the test program, and the stick position traces show a good deal of control motion, the feathering traces must be in error. Short segments of the feathering time-histories measured for counters 610, 615, 635, 675 and 1078 are plotted in Figure 27. The feathering time-histories for counters 610 and 615 are perfect one-per-rev waves, indicating that the problem with the feathering instrumentation experienced during counters 561 and 562 has been eliminated by counter 610. The quality of the time histories degrades slightly over the course of the flight tests investigated, with some deviations from a pure one-per-rev occurring at higher counters. These deviations can be seen in the time histories for counters 675 and 1078. The deviations are most likely due to higher harmonic response in the control system.

Although the quality of the feathering test data is high over the range of test conditions, the absolute accuracy is not known, as discussed in the opening paragraph of this subsection. The difference between the ground-measured and flight-test-data-derived control riggings (Section 3.18) raises unanswered questions about the control measurements.

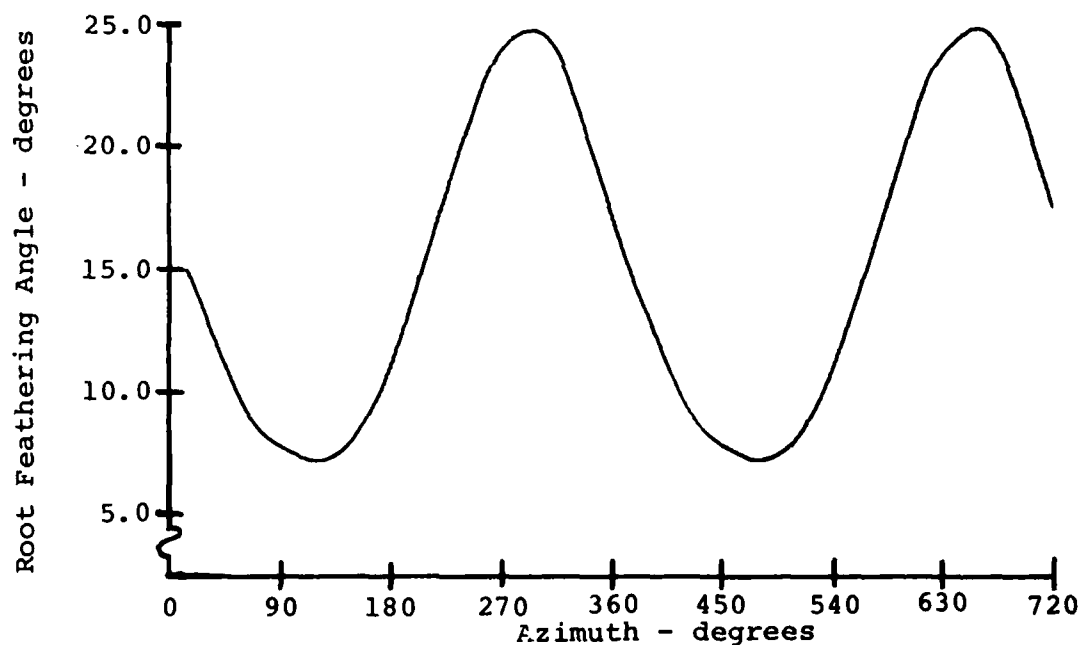
#### 5.2.2 Collective Pitch Angle and Stick Position

Measured and computed root collective pitch angles and stick positions are compared in Figure 28 and Table 11. In Figure 28, the root collective pitch angle for the TVT case with the internal induced-velocity distribution (dashed line) is the same as that for the QST case (solid line) at 10 KTAS. In like manner, the 10-knot TVT-with-RIVD case (chain-broken line) has the same computed collective stick position as the QST case (solid line).

The computed root collective pitch is lower than that measured in flight for the six highest speed cases. The root collective computed in the TVT with the internal induced velocity distribution is generally lower than that computed in the QST. This indicates that more nose-up pitch-cone coupling is computed in the TVT than in the QST. At 116 knots, for example, the coning mode (first collective mode) has a steady participation factor of -0.30841, which gives a steady nose up torsional deflection of 0.55 degree at the feathering bearing. During the comparable QST case, the pitch-cone coupling is computed as 0.03288 degree by evaluating Equation 303 of Volume I of Reference 3.

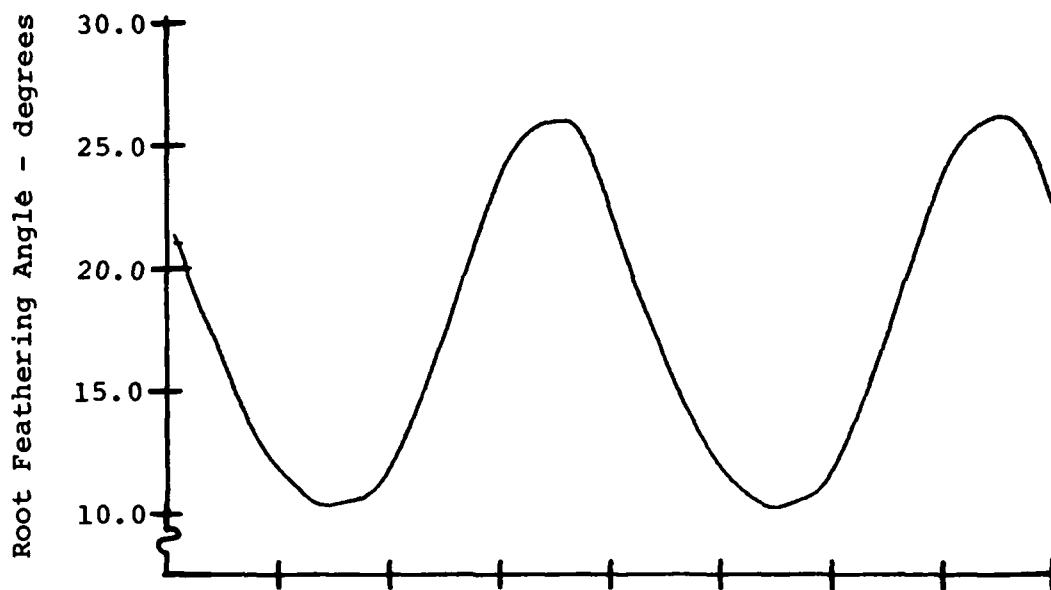


a) Counter 610, 8319 lb, 142 KTAS.

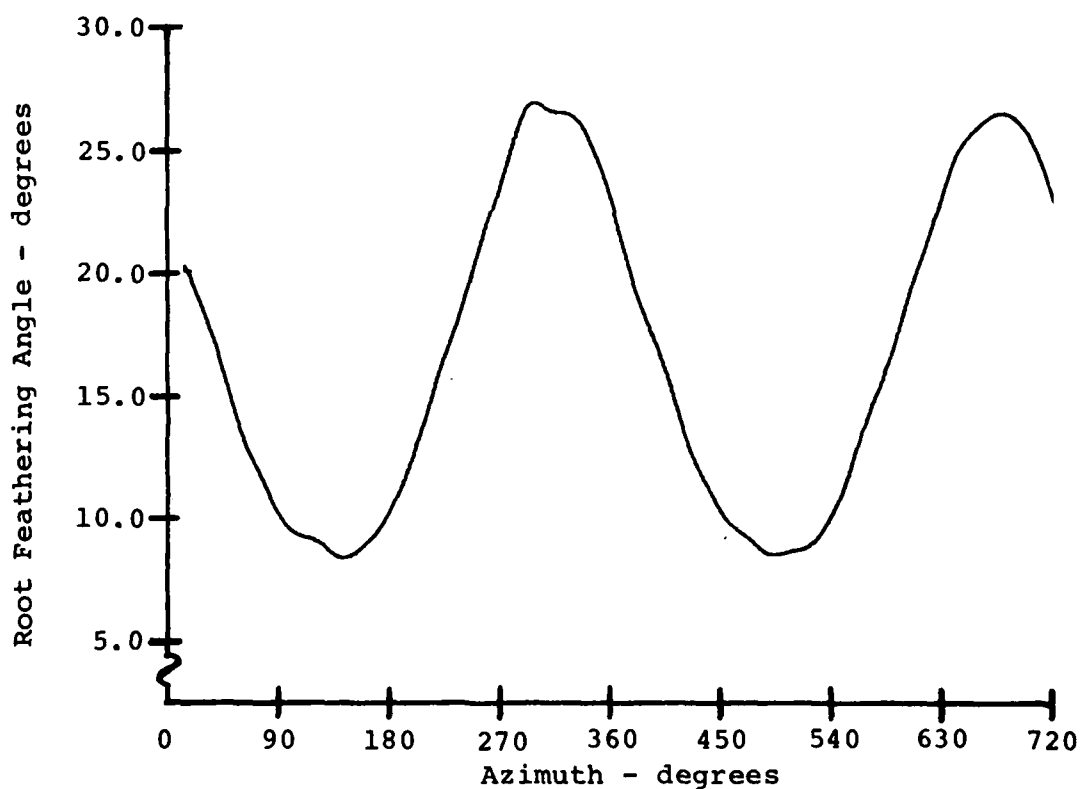


b) Counter 615, 8319 lb, 129 KTAS.

Figure 27. Measured Hub Feathering Time Histories for Counters 610, 615, 635, 675 and 1078.

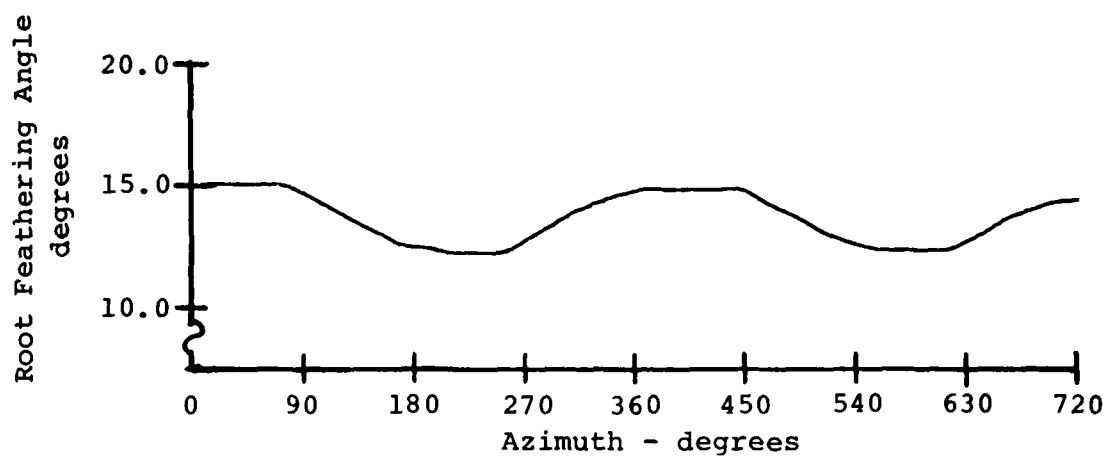


c) Counter 635, 9069 lb, 136 KTAS.



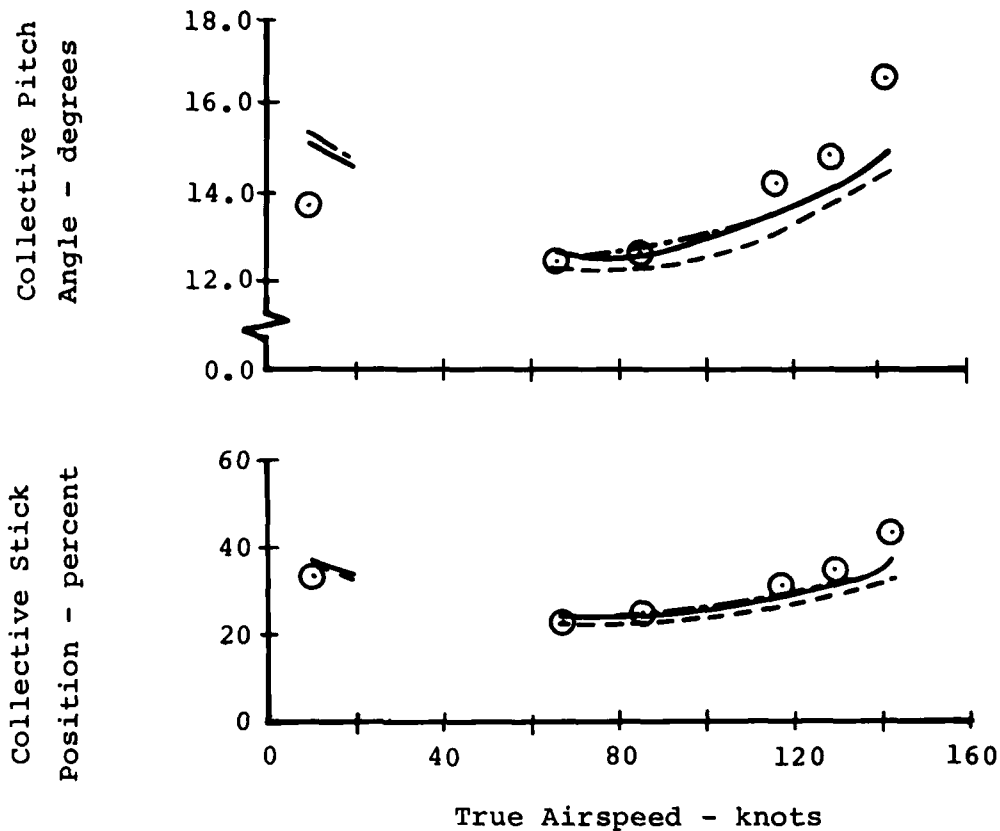
d) Counter 675, 9068 lb, 138 KTAS.

Figure 27. Continued.



e) Counter 1078, 8289 lb, 10 KTAS.

Figure 27. Concluded.



⊙ Test Data

C81 Data:

— Inelastic Quasi-Static Trim  
 ---- Time-Variant Trim, No RIVD  
 -.- Time-Variant Trim, with RIVD

10 KTAS case is Flight 45B, Counter 1078; 8289 pounds, mid center-of-gravity, clean wing.  
 66 through 142 KTAS cases are Flight 35A, Counters 611, 612, 614, 615 and 610: 8319 pounds, aft center-of-gravity, clean wing.

Figure 28. Comparison of Measured and Computed Collective Pitch Angle and Stick Position.

TABLE 11. COMPARISON OF MEASURED AND COMPUTED  
CONTROL POSITIONS AND ANGLES FOR  
COUNTERS 635, 675, AND 1093

		<u>Trim Type</u>		
	Test	QST	TVT	TVT+RIVD
<u>Counter 635</u>				
9069 lb, mid cg, 4 XM-159 rocket pods, 136 KTAS				
Root Coll Pitch Angle, deg	17.369	16.02	15.91	16.22
Collective Stick Position, %	43.610	41.50	40.94	42.51
Long. Cyclic Pitch Angle, deg	-6.137	-3.90	-5.06	-5.83
Long. Cyclic Stick Position, %	70.060	63.73	67.52	70.04
Lateral Cyclic Pitch Angle, deg	-5.303	-1.95	-2.11	-1.81
Lat Cyclic Stick Position, %	47.360	53.65	52.69	54.46
Pedal Position, %	43.195	47.46	47.26	45.76
<u>Counter 675</u>				
9068 lb, aft cg, 4 XM-159 rocket pods, 138 KTAS				
Root Coll Pitch Angle, deg	16.730	16.09	15.98	16.31
Collective Stick Position, %	41.690	41.88	41.33	43.00
Long. Cyclic Pitch Angle, deg	-6.675	-5.71	-6.85	-7.57
Long. Cyclic Stick Position, %	75.840	69.64	73.36	75.57
Lateral Cyclic Pitch Angle, deg	-6.493	-2.03	-2.71	-2.43
Lat Cyclic Stick Position, %	48.380	53.14	49.13	50.83
Pedal Position, %	39.850	47.14	47.06	45.57
<u>Counter 1093</u>				
8300 lb, fwd cg, clean wing, 145 KTAS				
Root Coll Pitch Angle, deg	16.760	16.24	16.03	16.31
Collective Stick Position, %	48.130	42.61	41.57	43.00
Long. Cyclic Pitch Angle, deg	-5.718	-2.62	-3.84	-4.63
Long. Cyclic Stick Position, %	69.020	59.53	63.52	66.12
Lateral Cyclic Pitch Angle, deg	-5.009	-1.98	-1.70	-1.33
Lat Cyclic Stick Position, %	49.540	53.49	55.15	57.31
Pedal Position, %	48.940	47.11	46.76	45.39

The TVT cases computed with an RIVD require a root collective pitch for trim that is very close to that required in the QST cases (except for Counters 635 and 675, as shown in Table 11). This is due to a higher average induced velocity being computed in the cases with RIVD than in the QST cases. For example, the 116 KTAS QST case has an average induced velocity of 6.96 feet/second, while the TVT-with-RIVD case has an average induced velocity of 9.22 feet/second. The increased collective pitch required due to the extra induced velocity compensates for the additional nose-down pitch-cone coupling.

Both the collective pitch angle and the collective stick position measured for the 142 KTAS case (Figure 28) appear to be higher than the trend established by the test data between 66 and 129 KTAS. This could indicate the onset of severe retreating blade stall. The discrepancy between the measured and computed collective angle does not indicate a trim imbalance, as the overall rotorcraft Z-force is in balance to within 25 pounds at the end of quasi-static trim. If the C81-computed QST collective angle agreed with the measured collective angle at 129 KTAS, for example, the vertical force imbalance would be 1300 pounds, based on the Z-force-with-collective partial derivative for this case. The fact that C81 does trim at a lower collective indicates that the airfoil table used in the simulation has a slightly larger lift-curve slope than the actual airfoil.

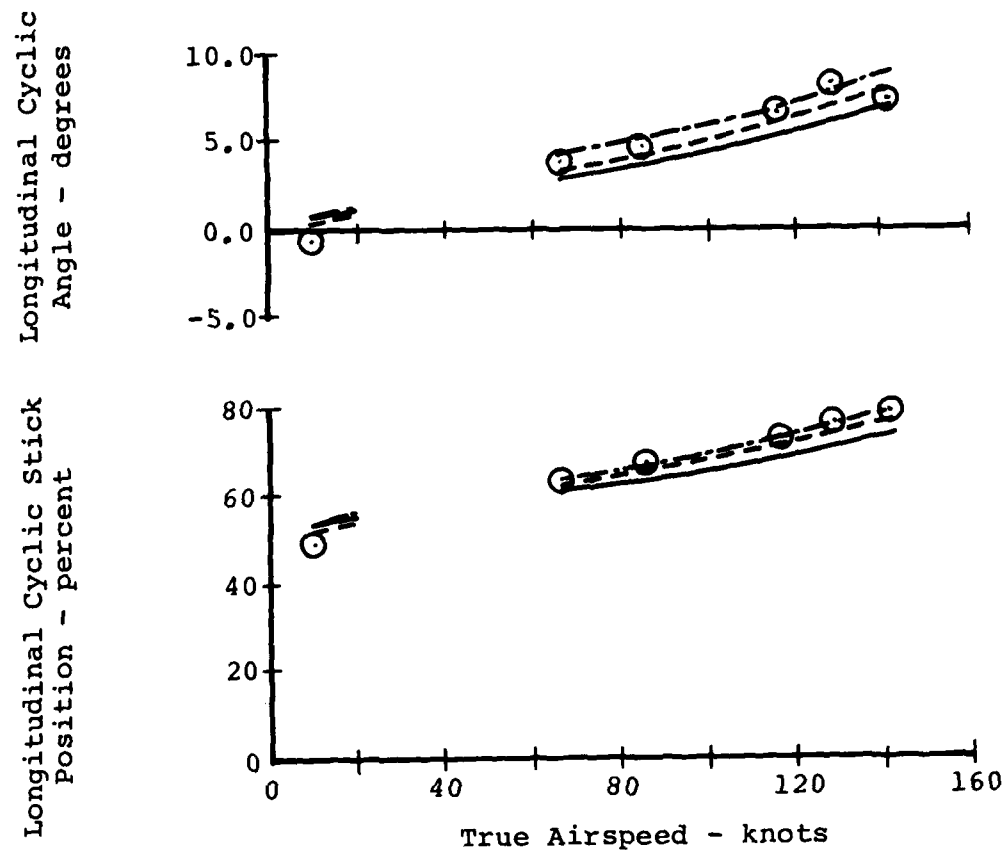
### 5.2.3 Longitudinal Cyclic Pitch Angle and Stick Position

Measured and computed values of main rotor longitudinal cyclic pitch angle and longitudinal cyclic stick position are compared in Figure 29 and Table 11. In general, the agreement is quite good for the test points compared in Figure 29, with the best agreement given by the TVT simulations using the internal induced velocity distribution.

The longitudinal cyclic pitch angles computed for the three  $V_H$  cases of Table 11 are less than those measured for counters 635 and 1093 (mid and forward cg) and bracket the measured value for counter 675. The computed longitudinal cyclic stick positions are in closer agreement with those measured, except for counter 1093.

The discrepancy between the QST-computed longitudinal cyclic pitch angle and that measured at 116 KTAS would imply a longitudinal force imbalance of about 26 pounds, based on the X-force-with-longitudinal-cyclic partial derivative, even though the actual computed force imbalance is zero. Again, this indicates a small difference between the rotor aerodynamics in the simulation and on the actual aircraft.





⊙ Test Data

C81 Data:

— Inelastic Quasi-Static Trim

--- Time-Variant Trim, No RIVD

--- Time-Variant Trim, with RIVD

10 KTAS case is Flight 45B, Counter 1078; 8289 pounds, mid center-of-gravity, clean wing.  
66 through 142 KTAS cases are Flight 35A, Counters 611, 612, 614, 615 and 610: 8319 pounds, aft center-of-gravity, clean wing.

Figure 29. Comparison of Measured and Computed Longitudinal Cyclic Pitch Angle and Stick Position.

#### 5.2.4 Lateral Cyclic Pitch Angle and Stick Position

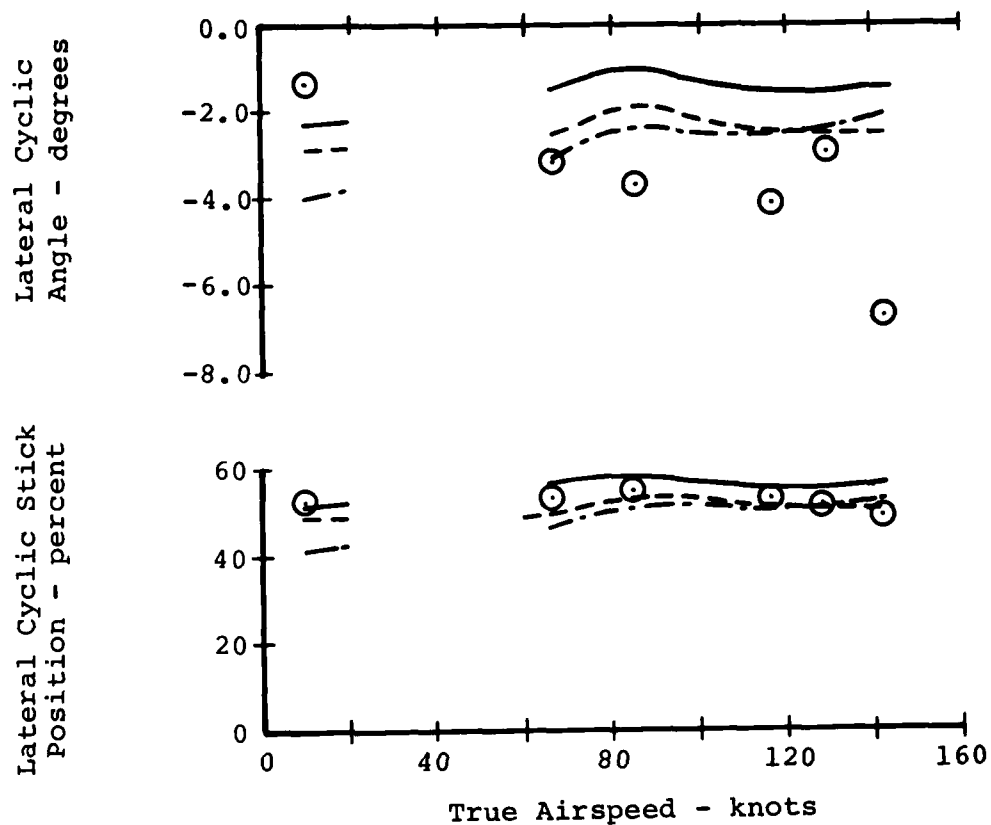
Computed and measured main rotor lateral cyclic pitch angles and lateral cyclic stick position are compared in Figure 30 and Table 11. The measured lateral cyclic pitch angle data are highly suspect, for, as discussed in Section 3.18, the data have a high degree of scatter and indicate an almost infinite slope with respect to the measured lateral cyclic stick position. There is negligible agreement between the computed lateral cyclic pitch angle and the measured data for any of the trim conditions for any of the trim types. Computed stick position, conversely, agrees quite well with the measured stick position for all the cases shown in Figure 30. The agreement is not as good for the three  $V_H$  cases of Table 11, but it is still reasonable in view of the questionable quality of the measured data.

#### 5.2.5 Pedal Position

Computed and measured pedal positions are compared in Figure 31 and Table 11. The agreement is good for most cases, but the pedal positions computed by the QST and the TVT with internal induced velocity distribution have an unusual trend between 116 and 142 KTAS. These three cases show the largest discrepancy from the measured data, while the values computed in the TVT-with-RIVD cases show almost perfect agreement with the test data. If the pedal position computed by the QST at 116 KTAS had been in agreement with the measured pedal position, C81 would have computed a yaw imbalance of 6300 foot-pounds, based on the partial derivative of yawing moment with respect to pedal. The actual yawing moment imbalance displayed in the force and moment summary was 9 foot-pounds for this case. This indicates that the tail rotor and fin generate a different yawing moment in the simulation than on the test vehicle.

#### 5.2.6 Summary of Control Comparisons

The comparisons of measured and computed control positions given in this subsection of the report indicate that C81 generally computes stick positions in good agreement with those measured in flight, but the computed control angles do not agree as well. This latter discrepancy must be considered, though, in conjunction with the questionable swashplate angle data.



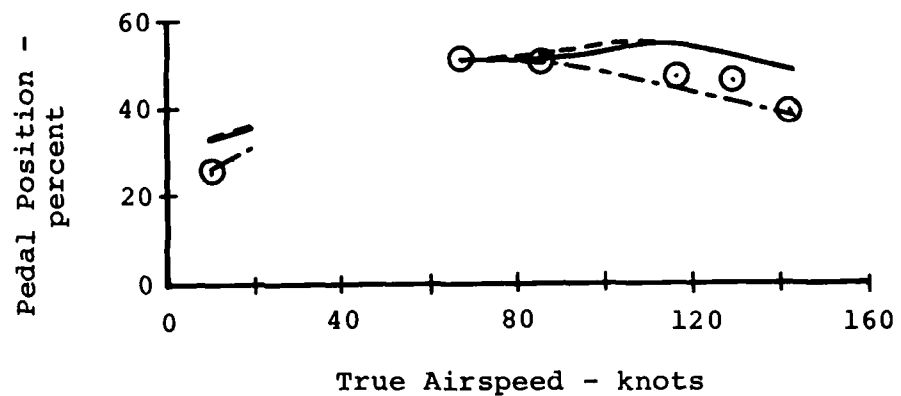
⊙ Test Data

C81 Data:

— Inelastic Quasi-Static Trim  
 --- Time-Variant Trim, No RIVD  
 -.- Time-Variant Trim, with RIVD

10 KTAS case is Flight 45B, Counter 1078; 8289 pounds, mid center-of-gravity, clean wing.  
 66 through 142 KTAS cases are Flight 35A, Counters 611, 612, 614, 615 and 610: 8319 pounds, aft center-of-gravity, clean wing.

Figure 30. Comparison of Measured and Computed Lateral Cyclic Pitch Angle and Stick Position.



⊙ Test Data

C81 Data:

— Inelastic Quasi-Static Trim  
 --- Time-Variant Trim, No RIVD  
 -.- Time-Variant Trim, with RIVD

10 KTAS case is Flight 45B, Counter 1078; 8289 pounds, mid center-of-gravity, clean wing.  
 66 through 142 KTAS cases are Flight 35A, Counters 611, 612, 614, 615 and 610: 8319 pounds, aft center-of-gravity, clean wing.

Figure 31. Comparison of Measured and Computed Pedal Position.

### 5.3 MAIN ROTOR HUB FLAPPING ANGLES

#### 5.3.1 General Considerations

The hub flapping angle recorded during the flight test program, item code D110, is the angle between a plane perpendicular to the mast and the hub in the trunnion area. This is not a tip-path-plane flapping angle. C81 computes this angle by the following formulas

$$Z_{\text{NBSG-1}} = \sum_{n=1}^{n=N_{\text{cyc}}} \delta_{n_{\text{cyc}}} Z_{\text{NBSG-1}}_{n_{\text{cyc}}} \quad (10.a)$$

$$\beta_H = (Z_{\text{NBSG-1}})/(r_{\text{NBSG-1}}) \quad (10.b)$$

in which  $Z_{\text{NBSG-1}}$  is the instantaneous out-of-plane displacement at the first station outboard of the center-of-rotation, due to the cyclic modes only

$\delta_{n_{\text{cyc}}}$  the instantaneous participation factor (generalized coordinate) for the  $n^{\text{th}}$  cyclic mode

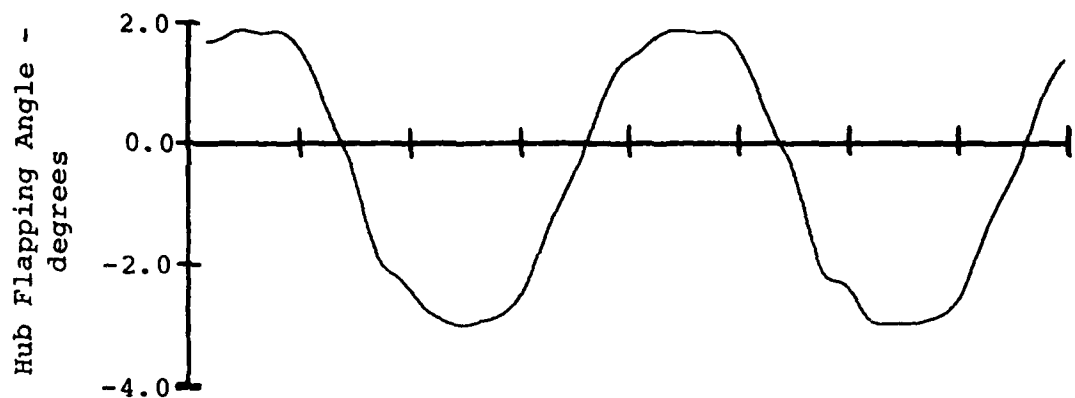
$Z_{\text{NBSG-1}}_{n_{\text{cyc}}}$  the out-of-plane component of the  $n^{\text{th}}$  cyclic mode at the first station outboard of the center of rotation

$\beta_H$  is the instantaneous hub flapping angle

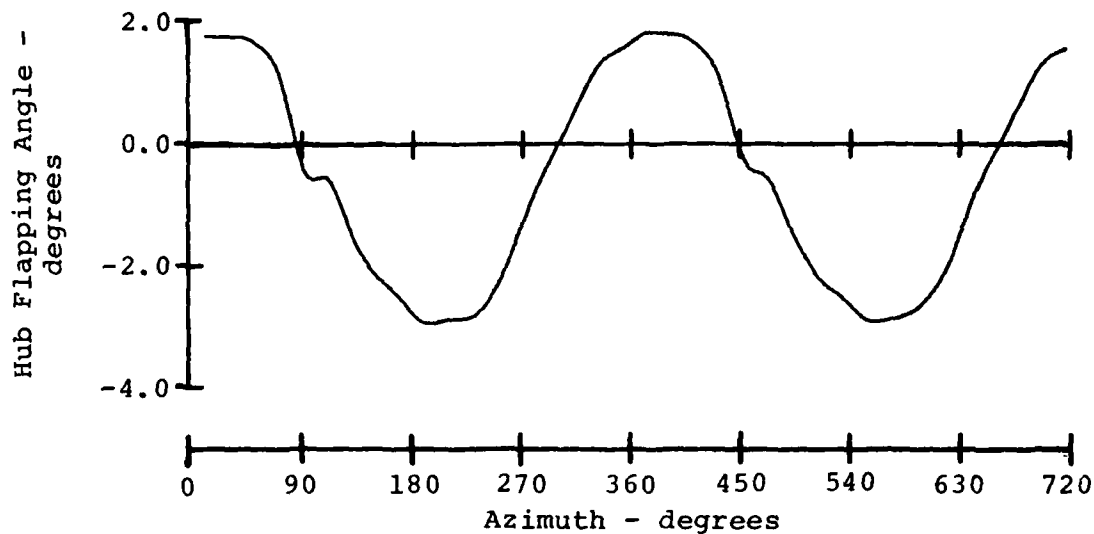
$r_{\text{NBSG-1}}$  is the radius to the first station outboard of the center of rotation

The values of  $\beta_H$  at zero and ninety-degree rotor azimuth are printed out near the bottom of the C81 trim page.

The quality of the hub flapping measurement can be determined by examination of the five time histories presented in Figure 32. As can be seen, there is a zero offset for all traces. By definition, the steady, or mean, hub flapping, must be zero, which is not what is shown in Figure 32. The time histories should also have a predominantly one-per-rev characteristic, which is shown for counters 610 and 615. Some higher harmonic response is visible in the flapping traces for counters 610 and 615. Larger higher harmonic response is visible in the traces for counters 635 and 675. This higher harmonic content is large enough by counter 675 to suggest a possible instrumentation problem. By counter 1078, the quality of the



a) Counter 610, 8319 lb, 142 KTAS.



b) Counter 615, 8319 lb, 129 KTAS.

Figure 32. Measured Hub Flapping Angle Time Histories for Counters 610, 615, 635, 675 and 1078.

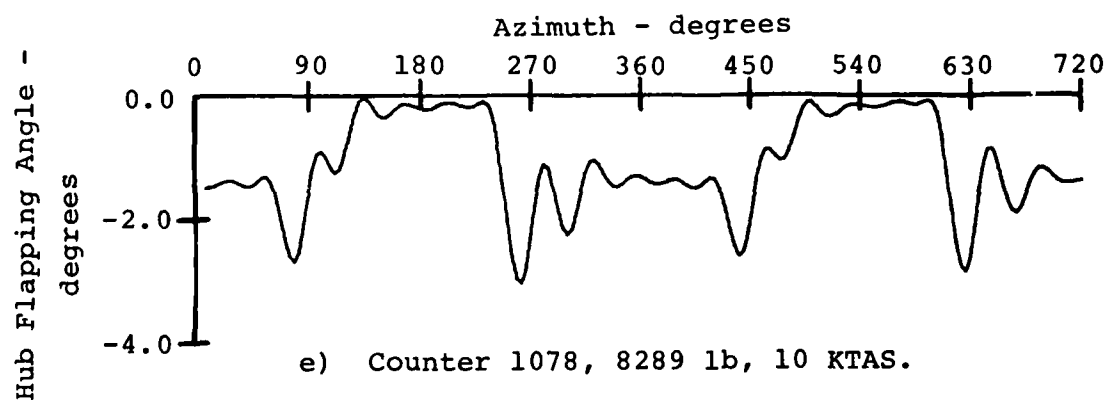
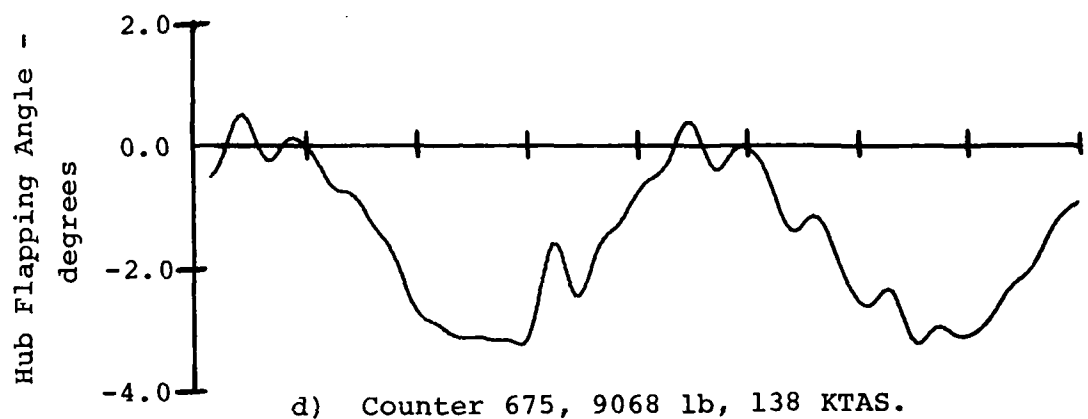
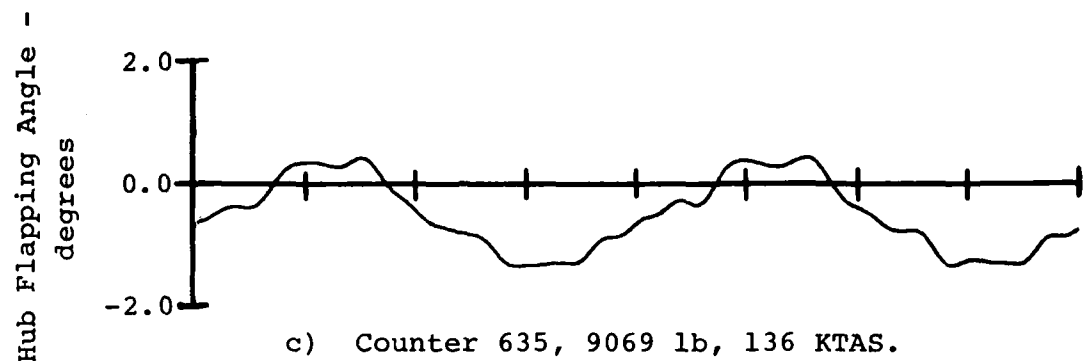


Figure 32. Concluded.

trace has deteriorated completely - it is periodic, but the one-per-rev trigonometric curve expected is not evident. The measured hub flapping for counter 1078 and, by extension, 1093, is obviously inadequate. The hub flapping for the other cases is somewhat suspect, due to the zero shift and the ultimate breakdown in the instrumentation for this data item.

#### 5.3.2 Comparison of Measured and Computed Hub Flapping

Figure 33 and Table 12 contain the comparison of measured and computed main rotor hub flapping angles. The results show that the rotor trims at different flapping angles in the analysis than those measured in flight.

The discrepancy between the measured and computed longitudinal flapping angles is significant for all cases, with larger discrepancies demonstrated after TVT than after QST. The reasons for these large differences in longitudinal flapping are not known but should be determined, as flapping is an important measure of rotor response.

Better agreement was achieved between measured and computed lateral flapping, especially for the time-variant trims computed with the internal induced velocity distribution.

The computed hub flapping data presented in Figure 33 and Table 12 show that the rotor model chosen and the induced velocity model used both have a significant effect upon the rotor response. These modeling effects should be investigated further.

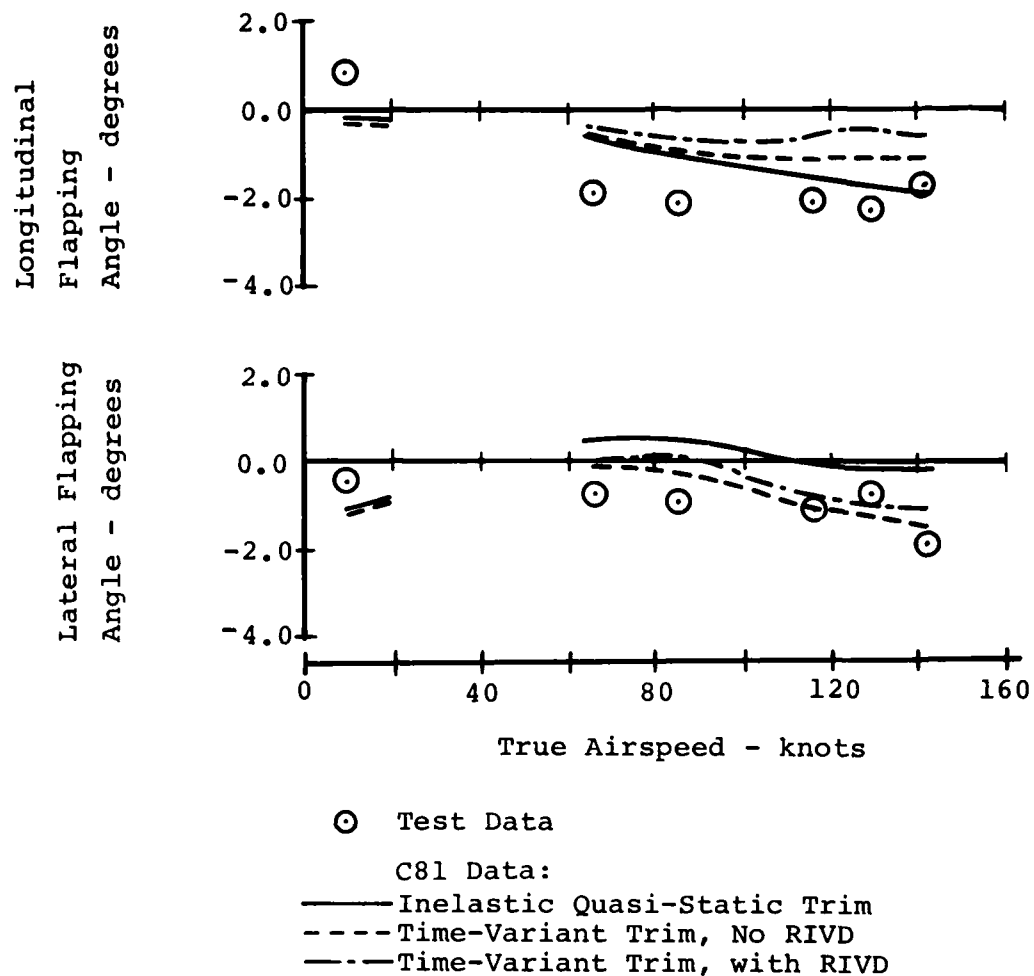
#### 5.4 HORSEPOWER COMPARISONS

Computed and measured main-rotor, tail-rotor and engine horsepower data are compared in Figure 34 and Table 13.

##### 5.4.1 Main Rotor Horsepower

Computed main-rotor horsepower required is in good agreement with that measured in flight for the 66, 85 and 129 KTAS cases (Figure 34a) and for counters 635 and 675 (Table 13). Measured data are derived from steady mast torque, which was not available for counters 1078 and 1093. The measured main-rotor horsepower required is probably in error for the 116 KTAS case shown in Figure 34a, as it is above the trend-line established by the measured data for the 66, 85 and 129 KTAS cases. The 142 KTAS measured main-rotor horsepower required is also above this trend line, indicating either that the aircraft was climbing or that more stall was experienced on the actual rotor than in the simulation. It is also possible that the



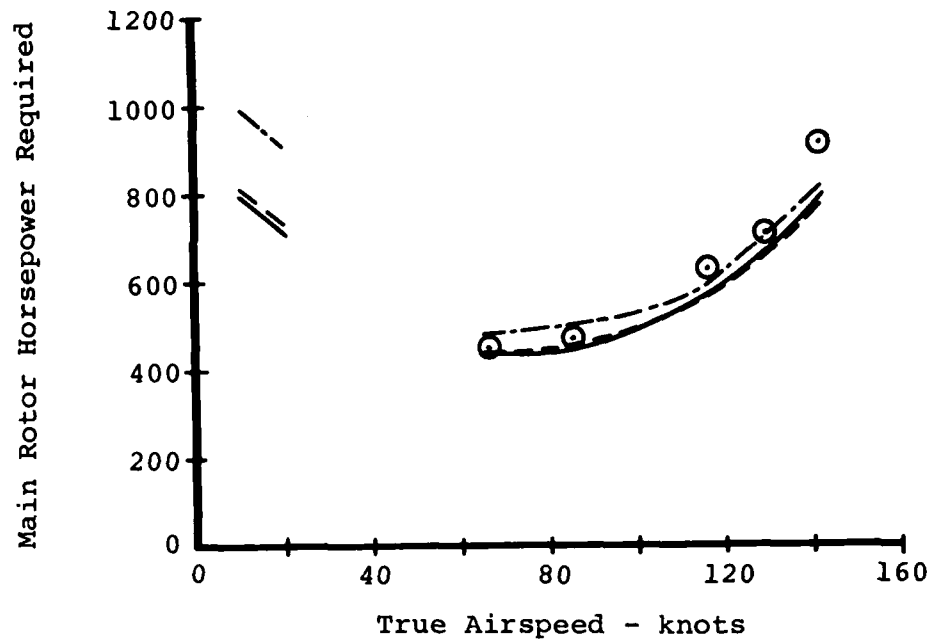


10 KTAS case is Flight 45B, Counter 1078; 8289 pounds, mid center-of-gravity, clean wing.  
 66 through 142 KTAS cases are Flight 35A, Counters 611, 612, 614, 615 and 610: 8319 pounds, aft center-of-gravity, clean wing.

Figure 33. Comparison of Measured and Computed Hub Flapping Angles.

TABLE 12. COMPARISON OF MEASURED AND COMPUTED  
HUB FLAPPING ANGLES FOR COUNTERS 635,  
675 AND 1093

	<u>Trim Type</u>			
	Test	QST	TVT	TVT+RIVD
<u>Counter 635</u>				
9069 lb, mid cg, 4 XM-159 rocket pods, 136 KTAS				
Long. Hub Flapping Angle, deg	0.213	1.422	2.13	2.895
Lat Hub Flapping Angle, deg	-0.830	-0.397	-1.63	-1.384
<u>Counter 675</u>				
9068 lb, aft cg, 4 XM-159 rocket pods, 138 KTAS				
Long. Hub Flapping Angle, deg	-0.758	-0.305	0.492	1.283
Lat Hub Flapping Angle, deg	-1.365	-0.500	-1.802	-1.564
<u>Counter 1093</u>				
8300 lb, fwd cg, clean wing, 145 KTAS				
Long. Hub Flapping Angle, deg	0.776	2.973	3.663	4.475
Lat Hub Flapping Angle, deg	-0.376	-0.468	-1.753	-1.517



○ Test Data

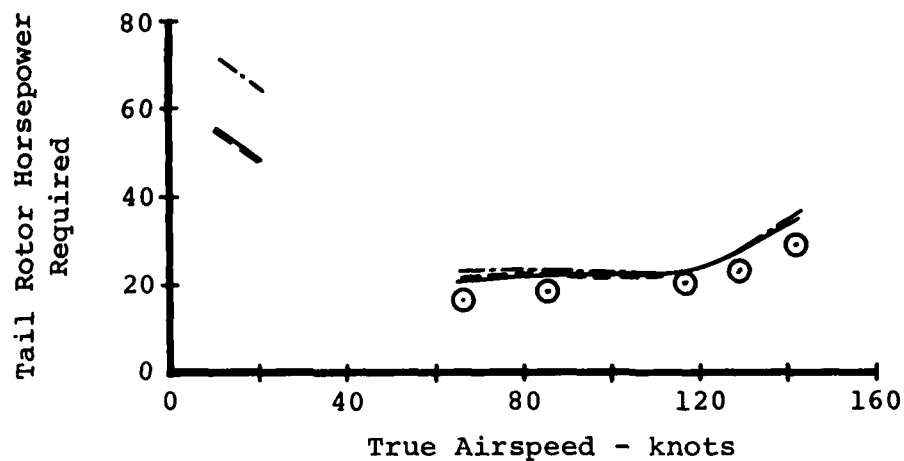
C81 Data:

— Inelastic Quasi-Static Trim  
 --- Time-Variant Trim, No RIVD  
 -.- Time-Variant Trim, with RIVD

10 KTAS case is Flight 45B, Counter 1078; 8289 pounds, mid center-of-gravity, clean wing.  
 66 through 142 KTAS cases are Flight 35A, Counters 611, 612, 614, 615 and 610: 8319 pounds, aft center-of-gravity, clean wing.

a) Main Rotor Horsepower Required.

Figure 34. Comparison of Measured and Computed Horsepower.



⊙ Test Data

C81 Data:

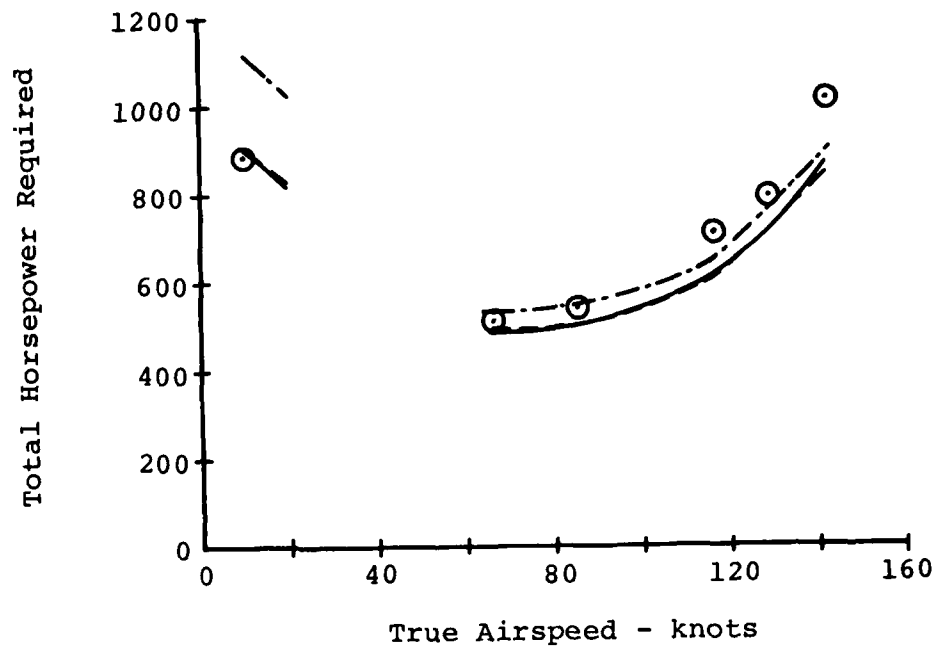
—— Inelastic Main Rotor Quasi-Static Trim  
 ---- Main Rotor Time-Variant Trim, No RIVD  
 ---- Main Rotor Time-Variant Trim, with RIVD

The quasi-static analysis was used for the inelastic tail rotor in all cases.

10 KTAS case is Flight 45B, Counter 1078; 8289 pounds, mid center-of-gravity, clean wing.  
 66 through 142 KTAS cases are Flight 35A, Counters 611, 612, 614, 615 and 610: 8319 pounds, aft center-of-gravity, clean wing.

b) Tail Rotor Horsepower Required.

Figure 34. Continued.



○ Test Data

C81 Data:

— Inelastic Quasi-Static Trim  
 --- Time-Variant Trim, No RIVD  
 -.- Time-Variant Trim, with RIVD

10 KTAS case is Flight 45B, Counter 1078; 8289 pounds, mid center-of-gravity, clean wing.  
 66 through 142 KTAS cases are Flight 35A, Counters 611, 612, 614, 615 and 610: 8319 pounds, aft center-of-gravity, clean wing.

c) Total Horsepower Required.

Figure 34. Concluded.

TABLE 13. COMPARISON OF MEASURED AND COMPUTED  
HORSEPOWER REQUIRED FOR COUNTERS  
635, 675 AND 1093

	<u>Test Type</u>			
	Test	QST	TVT	TVT+RIVD
<u>Counter 635</u>				
9069 lb, mid cg, 4 XM-159 rocket pods, 136 KTAS				
Main Rotor Horsepower Req'd.	938.77	910.93	918.05	977.3
Tail Rotor Horsepower Req'd.	21.47	33.81	33.99	35.5
Total Horsepower Required	1020.50	986.33	993.85	1056.6
<u>Counter 675</u>				
9068 lb, aft cg, 4 XM-159 rocket pods, 138 KTAS				
Main Rotor Horsepower Req'd.	968.00	923.02	923.41	973.2
Tail Rotor Horsepower Req'd.	26.93	34.79	34.82	36.5
Total Horsepower Required	1048.80	999.80	1000.24	1053.3
<u>Counter 1093</u>				
8300 lb, fwd cg, clean wing, 145 KTAS				
Main Rotor Horsepower Req'd.	-	992.08	993.93	1059.1
Tail Rotor Horsepower Req'd.	-	38.11	38.43	39.9
Total Horsepower Required	1062.90	1074.42	1076.66	1145.4

flat plate drag area of the aircraft was underestimated. The excellent agreement between the measured and computed main-rotor horsepower in the vicinity of the minimum-power point, at 66 and 85 KTAS (Figure 34a), indicates that the  $\Delta C_D$  of 0.003 chosen for this rotor was a good estimate.

The main-rotor horsepower required computed in the QST and the TVT with the internal induced velocity distribution model are almost identical for all cases, while that computed in the TVT-with-RIVD simulations is larger, particularly for the three  $V_H$  cases of Table 13 and for the 10-KTAS case of Figure 34a. The Crimi wake analysis is known to be inaccurate at low speeds, and the difference computed in main-rotor horsepower required between cases with and without the RIVD table supports this contention. The  $V_H$  cases with the RIVD are most likely experiencing more retreating-blade stall than those without the input table.

#### 5.4.2 Tail Rotor Horsepower Required

The tail rotor horsepower required computed by C81 is larger than that measured in flight for all nine level flight cases (Figure 34b and Table 13). There are two possible reasons for this difference, but it is not known how much either of them is contributing to the discrepancy. One possible source of the error is that more tail rotor thrust is required to balance the main rotor torque in C81 than in flight, with higher power being required. This suspicion cannot be checked, as tail rotor thrust was not measured. It is also possible that the tail rotor, as modeled in C81, is less efficient than the actual rotor.

The tail-rotor horsepower required computed for the 10 KTAS simulation with main rotor RIVD is very much larger than that computed for the low-speed simulations without RIVD. This increase is required because the tail rotor thrust had to increase a great deal to balance the significantly increased main rotor torque.

The tail-rotor horsepower required did not increase very much for the RIVD-included simulations of counters 635, 675 and 1093. In these three high forward speed flight conditions, the fin assists the tail rotor in counteracting the main rotor torque. The airframe trimmed to a larger sideslip angle when the RIVD table was included in the simulation of these three test conditions, increasing the yawing moment due to the fin. Therefore, the tail rotor thrust did not have to increase as much for these cases as it did for the 10-KTAS case. Since the tail rotor thrust did not increase a great deal for the high speed cases with RIVD, its horsepower required did not increase either.

### 5.4.3 Total Engine Horsepower

Measured and computed engine horsepower-supplied data are compared in Figure 34c and Table 13. The agreement is generally quite good, with the computed data bracketing the measured data for six of the nine test conditions. The computed horsepower is less than that measured for all trim types for the 116, 129 and 142 KTAS cases, shown in Figure 34c. The computed total horsepower is lower than that measured for these three cases because the computed main rotor horsepower is lower than the measured main rotor horsepower, as seen in Figure 34a. The total horsepower-required computed for counters 635, 675 and 1093 when the RIVD table was included is higher than that computed when the internal induced velocity model was used. This is due to a higher main rotor horsepower required being computed for these cases with the RIVD than without.

The equation used to compute the total horsepower required, which is the engine horsepower supplied in level flight, is

$$\frac{\frac{HP_{MR}}{XNG(22)} + \frac{HP_{TR}}{XNG(23)}}{XNG(24)} + XNG(25) = HP_{TOT} \quad (11.a)$$

where  $HP_{MR}$  is the computed main-rotor horsepower required  
 $HP_{TR}$  is the computed tail-rotor horsepower required  
 $XNG(22)$  is the input main-rotor transmission efficiency  
 $XNG(23)$  is the input tail-rotor transmission efficiency  
 $XNG(24)$  is the input overall drive-train efficiency  
 $XNG(25)$  is the input accessory horsepower required

Since  $XNG(22)$  and  $XNG(23)$  were input as 1.0, Equation (11.a) simplifies to

$$\frac{HP_{MR} + HP_{TR}}{XNG(24)} + XNG(25) = HP_{TOT} \quad (11.b)$$

Substituting horsepower data measured for the 129 and 142 KTAS cases into Equation (11.b) and solving yields values for  $XNG(24)$  and  $XNG(25)$  of 0.964 and 34.06, while performing the substitution for the 85 and 116 KTAS cases yielded values of



0.936 and 17.13, indicating either that the drive-train efficiency and accessory horsepower are functions of airspeed, or that Equation (11.a) does not completely represent the engine horsepower-supplied model. The values used in the simulations were 0.97 and 12.0, which were slightly optimistic on both the efficiency and the accessory horsepower in comparison with the values extracted from the curve-fit of Equation (11.b) to the test data.

## 5.5 MAIN ROTOR AERODYNAMIC ENVIRONMENT

The aerodynamic environment of the main rotor in trimmed level flight has been investigated by examination of contour plots of the blade-element normal force coefficient, pitching moment coefficient and angle of attack. Comparisons of contour plots derived from test data and those generated by C81 for two flight conditions are presented in this section, while contour plots derived from test data for four other conditions are given in the Appendix. The comparisons are preceded by a brief description of the data reduction methods and a guide to the interpretation of the C81-generated contour plots.

### 5.5.1 Creation of Rotor Contour Plots from OLS Test Data

The DATAMAP program<sup>11</sup> was used to create main rotor contour plots of normal force and pitching moment coefficients. A Master File partition was created containing data for 10 rotor revolutions for all the pressure taps at the 40, 75, 86, and 95 percent radius locations. (The pressure data for the 60 percent radius station were not included, since the data for the upper surface leading edge tap were invalid.) The pressure data at each radial station were cycle-averaged to yield a representative single-revolution time history for each tap. These were integrated over the chord at each time point to yield instantaneous values of the local blade-element normal force and pitching moment coefficients. The former quantity is the coefficient of the force perpendicular to the chord line, or

$$c_N = c_L \cos \alpha + c_D \sin \alpha \quad (12)$$

where  $\alpha$  is the local angle of attack. The normal force coefficient is not calculated from Equation 12, but rather by nondimensionalizing the integral of the pressure force perpendicular to the chord reference line.

Once  $c_N$  and  $c_M$  time histories had been calculated from the cycle-averaged pressure data for each radial station, they were interpolated radially and azimuthally to create the main

rotor contour plots. The resulting plots consist of a plane-polar plot of lines of constant value of the variable of interest.

Angle-of-attack contour plots were generated from the hot-wire anemometer data. At each radial station, the instantaneous position of the stagnation point was plotted versus azimuth. The data of Figure 3 were then used, in conjunction with the Mach number time history for that radial station, to create a plot of blade-element angle of attack versus azimuth. These latter plots were interpolated both in radius and azimuth to find the locus of points at which a particular angle of attack was observed. The locii were then plotted in a plane polar-plot to create the angle-of-attack contour plot.

#### 5.5.2 Interpretation of C81-Generated Contour Plots

Contours of constant values of the variable of interest are not plotted in the contour plots output by the C81 postprocessor, GDAJ77. Instead, an alphanumeric symbol or blank space is plotted in the region between two contours, with the limiting values associated with that symbol printed to the right of the contour plot. Therefore, the boundary between two regions constitutes the contour.

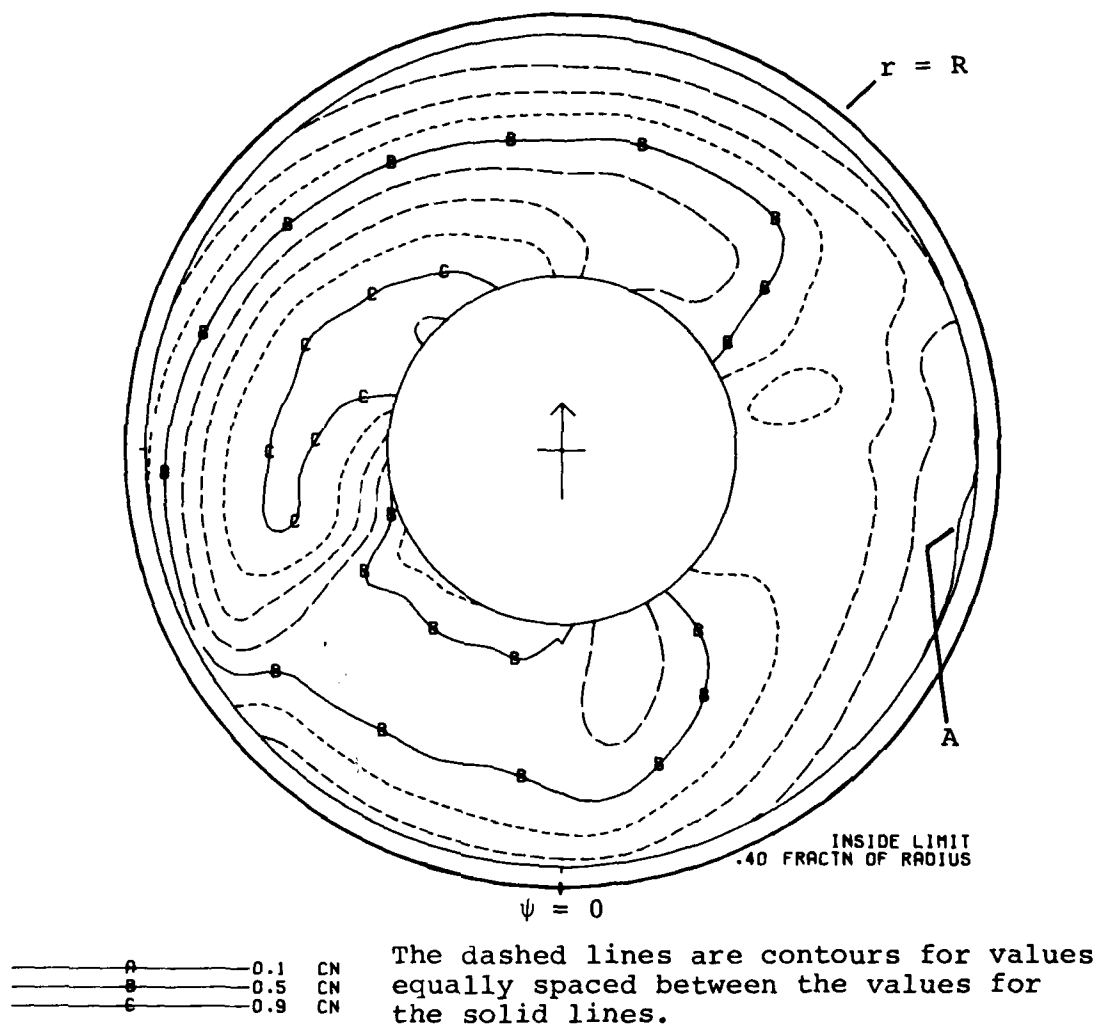
Comparison of contour plots generated by DATAMAP and GDAJ77 is hampered somewhat by the different methods of data representation. Comparison is also rendered difficult by the inability of the analyst to control the increments used in the plots generated by either program, which leads to different increments between the contours in two plots of the same variable for the same flight condition.

#### 5.5.3 Comparison of Rotor Variables for Counter 611

Counter 611, Flight 35A, was a 66 KTAS level flight condition at 8319 pounds gross weight, aft cg, with a clean wing.

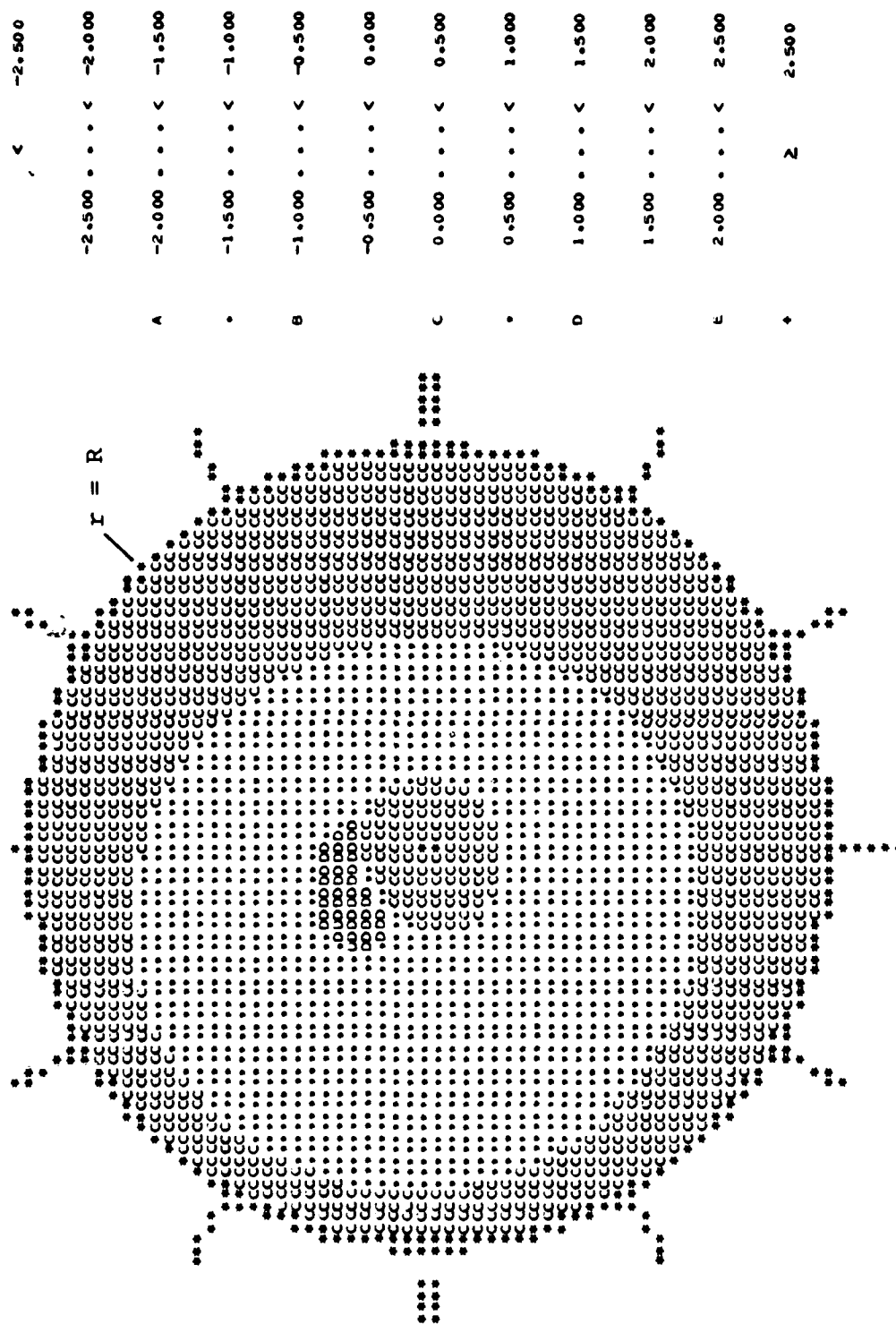
##### 5.5.3.1 Normal Force Coefficient Contour Plots

The contour plot of the normal force coefficient derived from test data is given in Figure 35a. A very short contour for  $0.1 c_N$  is observed between 70 and 90 degrees azimuth near 95 percent radius. The  $0.5 c_N$  contour (the "B" contour) is at 40 percent radius at about 140 degrees, slowly moves out to 95 percent radius at about 300 degrees azimuth, moves back in to about 75 percent radius until about 5 degrees azimuth, and then

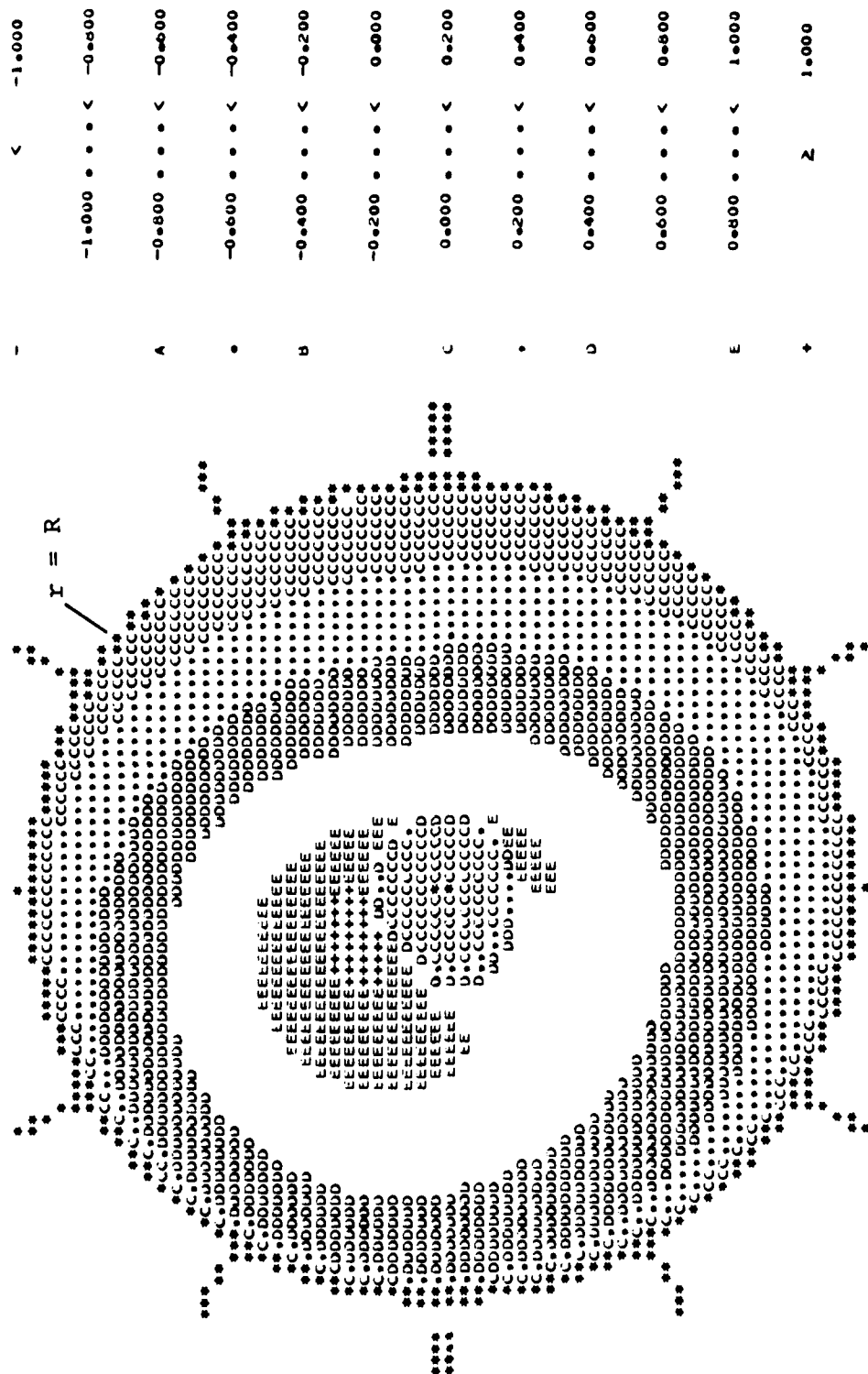


a) Contour Plot Derived from Test Data.

Figure 35. Comparison of Main Rotor Normal Force Coefficient Contour Plots Generated from Flight Test and C81 Data for Flight 35A, Counter 611 (8319 Pounds Gross Weight, Aft CG, Clean Wing, 66 KTAS).

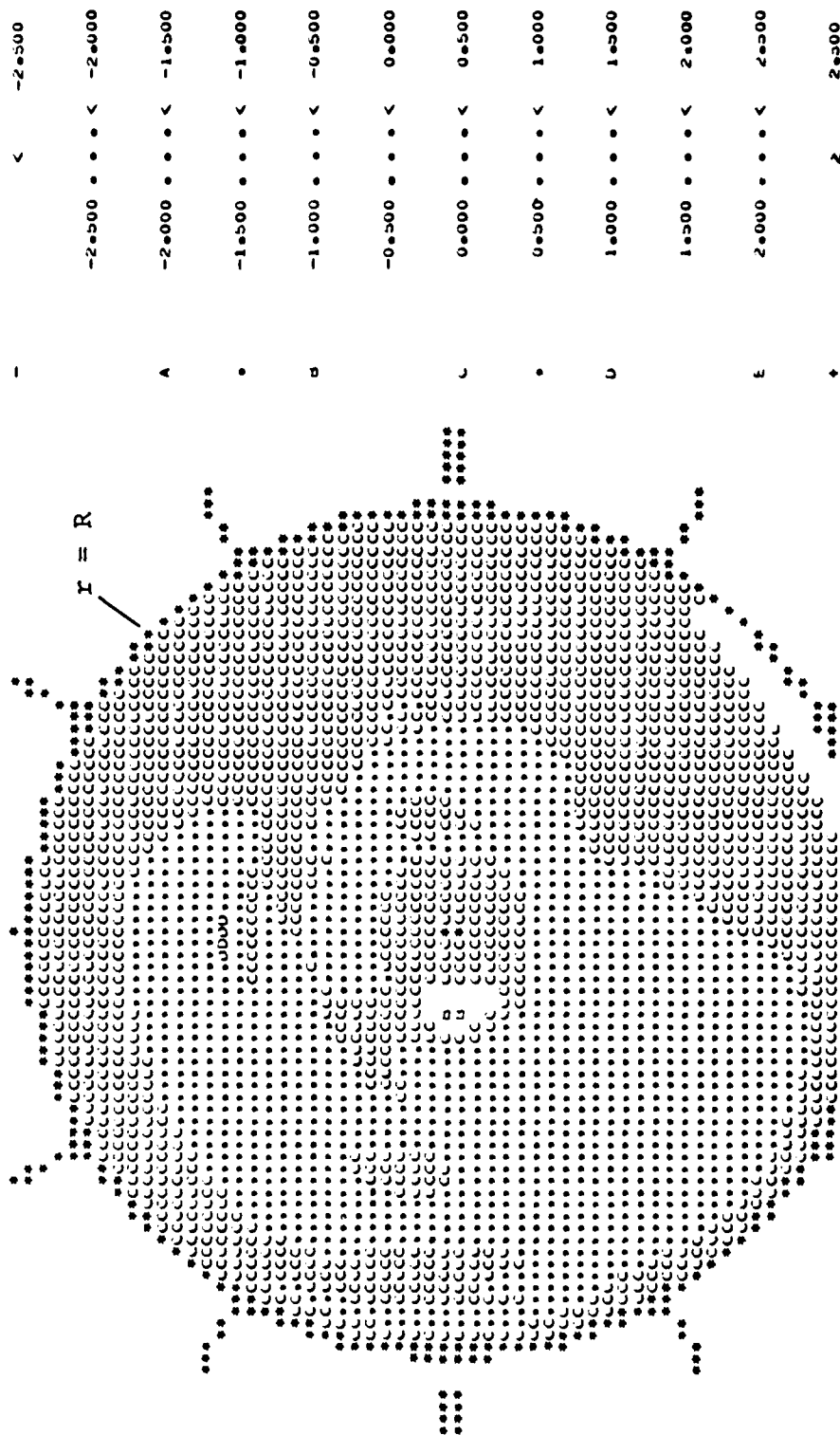


b) Contour Plot from C81 Quasi-Static Trim.  
Figure 35. Continued.



c) Contour Plot from C81 Time-Variant Trim Using the Internal Induced Velocity Distribution.

Figure 35. Continued.



PSI=0

d) Contour Plot from C81 Time-Variant Trim Using a Rotor Induced Velocity Distribution Table.  
Figure 35. Concluded.

spirals in to 40 percent radius at about 20 degrees azimuth. A short  $0.5 c_N$  contour is also observed between 40 and 50 percent radius between about 280 degrees and 5 degrees azimuth. The  $0.9 c_N$  contour ("C") is observed between 40 and 70 percent radius between 200 and 300 degrees azimuth. There is no evidence of strong retreating blade stall.

The C81-generated plot resulting from the QST, Figure 35b, is similar to that of Figure 35a. Due to the selection of the variable increment, the  $0.9 c_N$  contour is not specifically visible. A normal force coefficient of 0.1 is not experienced anywhere on the disc. The  $0.5 c_N$  contour is the line defined by the boundaries between the "C-region" and the "-region", and is reasonably similar to that seen in the test-data contour plot of Figure 35a. A  $0.9 c_N$  contour can be visualized by sketching a line one-quarter of the way between the "D-region" and the "C-region" in the midst of the decimal points. Such a contour would be similar to that seen in Figure 35a, but closer to the center of the rotor.

The normal force coefficient contour plot resulting from the TVT with the internal induced velocity model is given in Figure 35c. This plot is also quite similar to the plot derived from the test data, Figure 35a. (The increments have been changed again, though, requiring an adjustment in interpretation.) The  $0.1 c_N$  contour is in the middle of the "C-region," which shows that a  $c_N$  of 0.1 is obtained at a slightly more advanced azimuth in this C81 simulation than in flight. The  $0.5 c_N$  contour, in the middle of the "D-region", is similar to that observed in Figure 35a. The  $0.9 c_N$  contour is in the midst of the "E-region", which is reasonably similar to its position specified by the test data, as shown in Figure 35a.

Figure 35d contains the  $c_N$  contour plot resulting from the TVT with a RIVD table. It bears little relationship to either the test-data-derived plot (Figure 35a) or to the two other C81-generated plots (Figures 35b and 35c). No  $0.1 c_N$  contour is observed and the  $0.5 c_N$  contour (boundary of the "C-region" and "-region") differs from that of Figure 35a, particularly in the 160-degree to 180-degree, and 240-degree to 290-degree azimuth ranges. The  $0.5 c_N$  contour is much further outboard in the 300-degree to 0-degree azimuth range than was shown in Figure 35a, and higher  $c_N$ 's are observed inboard in this azimuth range.

#### 5.5.3.2 Pitching Moment Coefficient Contour Plots

The symmetric airfoil used on the OLS main rotor has a steady, unstalled pitching moment coefficient of zero. Assuming that the CLCD5474 table is representative of this airfoil, examination of the pitching moment table in Figure 5 shows that as static stall occurs at positive angles of attack, the pitching moment coefficient becomes negative, although  $C_M$  is first slightly positive between  $M = 0.4$  and  $M = 0.7$ . In like manner, the pitching moment becomes positive when the rotor stalls at negative angles of attack.

The plot of the test-data-derived  $c_M$  contour plot (Figure 36a) demonstrates a small region of negative pitching moment coefficients between 180 and 270-degree azimuth at radii in excess of 90 percent radius, indicating a region of positive angle-of-attack stall outboard of the reverse flow region. This contour plot indicates that the rotor is experiencing very little retreating blade stall, supporting the same conclusion drawn from the  $c_N$  contour plot (Figure 35a).

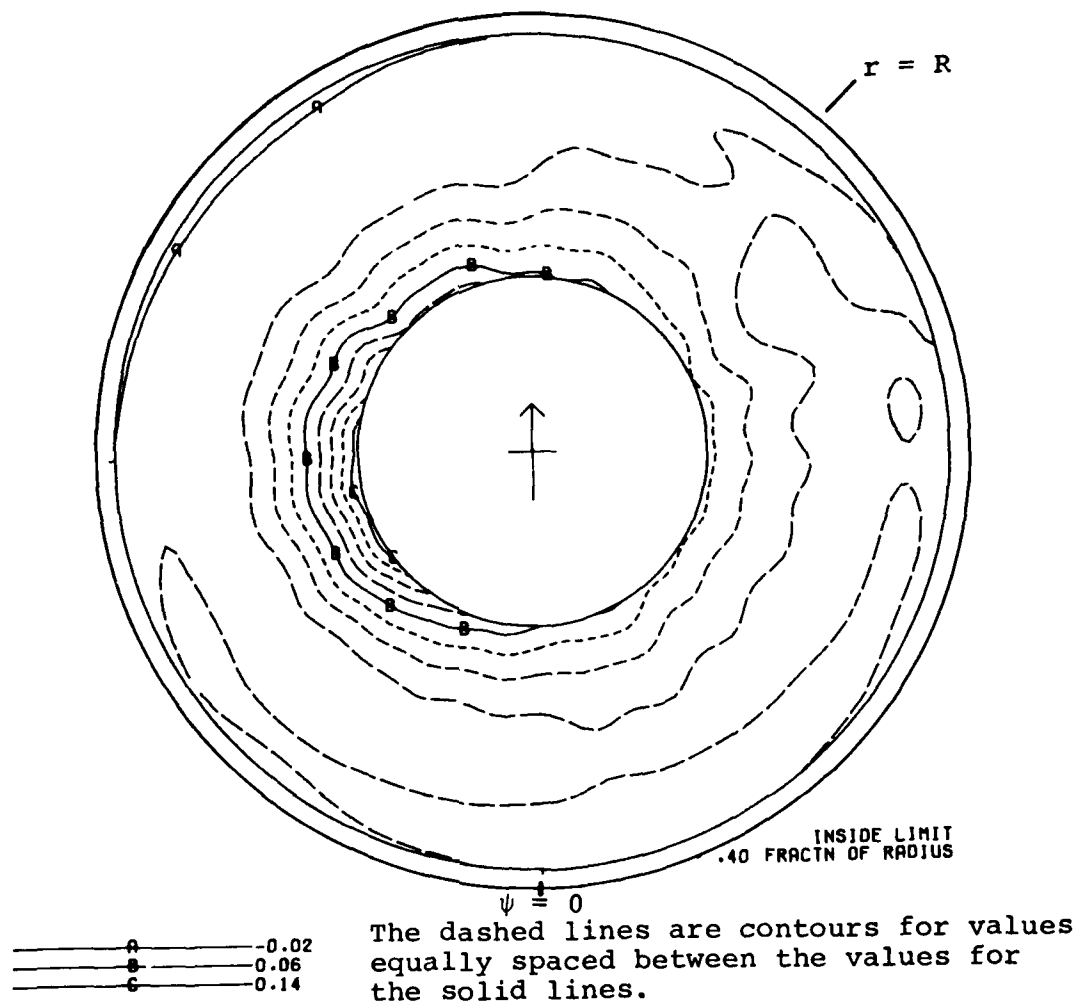
The pitching moment coefficient contour plot generated by the QST, Figure 36b, shows that the pitching moment is negative over a large portion of the disk. The only non-negative values are along the boundary between the "blank-region" and the "C-region", near the tip of the advancing blade. The most negative values shown are greater than, or equal to, -0.008, which would correspond to a local angle of attack no more than two degrees larger than the local static stall angle. This does not agree with the  $c_M$  contour plot based on the test data.

The  $c_M$  contour plot resulting from the TVT using the internal induced velocity distribution, Figure 36c, is almost identical to that output from the QST, as shown in Figure 36b.

The contour plot of the pitching moment coefficients computed during the TVT with the RIVD table is given in Figure 36d. A very small region of non-negative pitching moment coefficients can be observed near the rotor tip in the 15-degree to 55-degree azimuth region. The pitching moment coefficients experienced over the remainder of the disc are negative, indicating angles of attack that are as much as two degrees greater than the static stall angle. These results clearly disagree with the test data presented in Figure 36a.

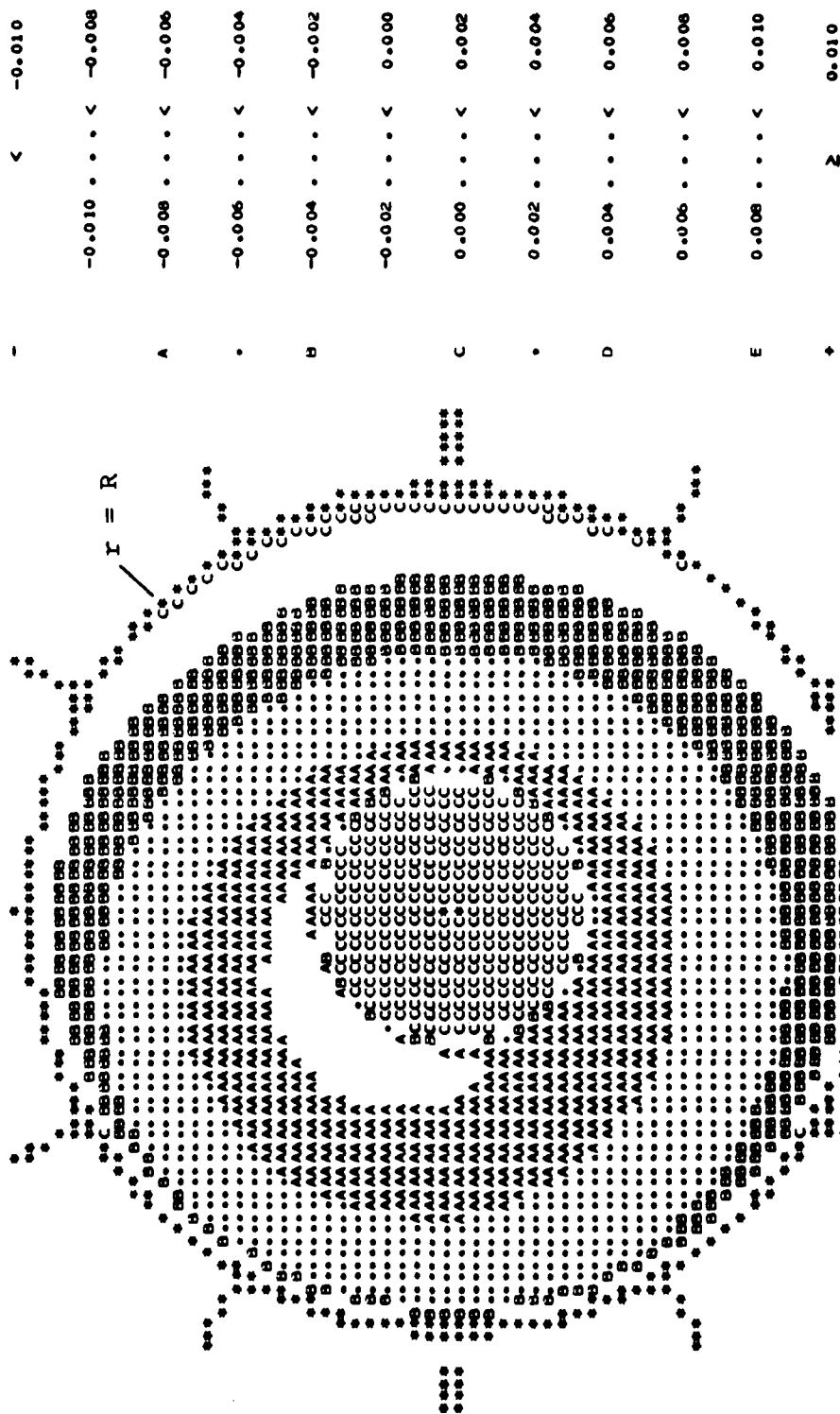
In defense of the C81 results, it should be noted that the integration of the pressure tap data to yield pitching moment coefficients may not be as accurate as desired due to the lack



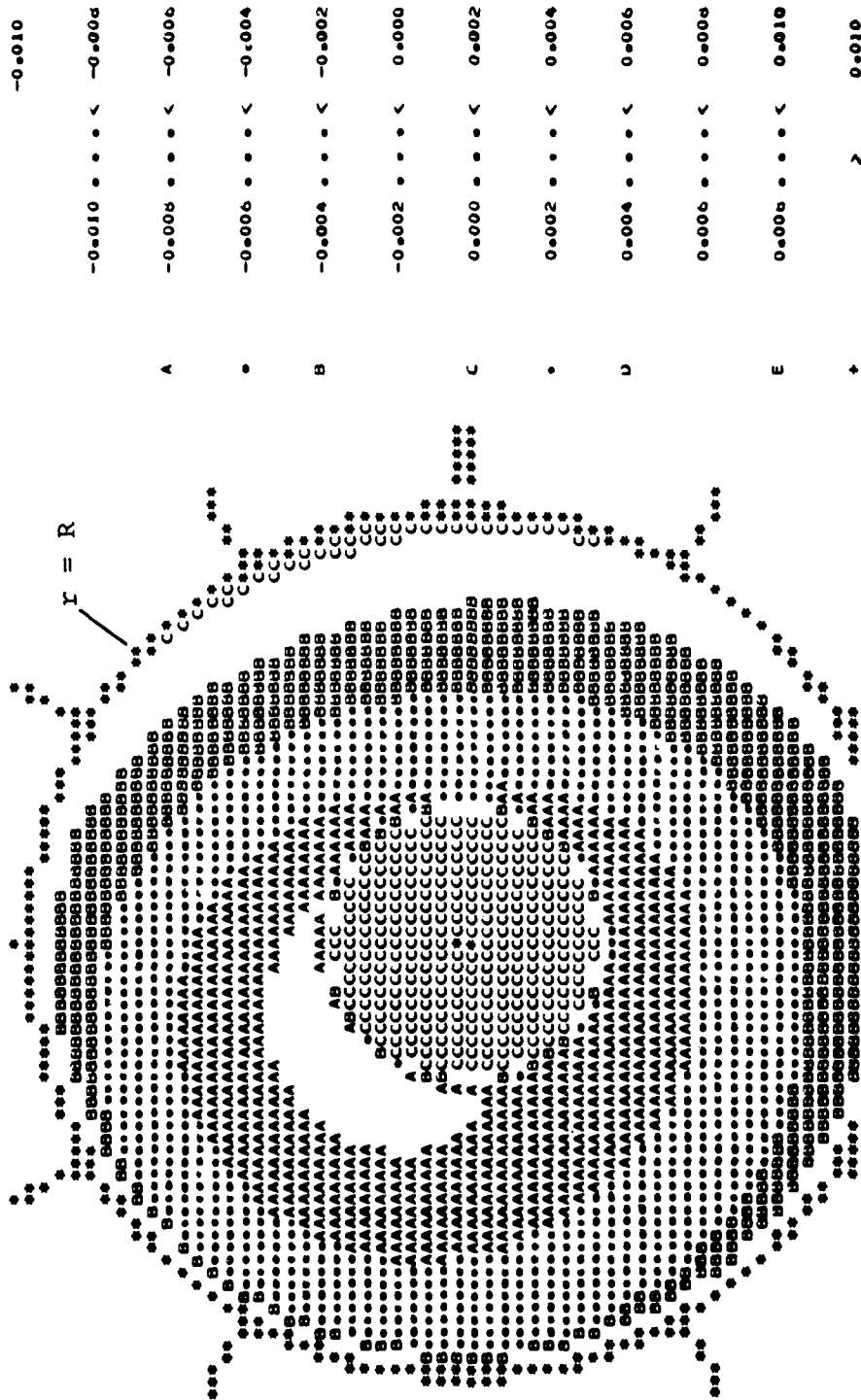


a) Contour Plot Derived from Test Data.

Figure 36. Comparison of Main Rotor Pitching Moment Coefficient Contour Plots Generated from Flight Test and C81 Data for Flight 35A, Counter 611 (8319 Pounds Gross Weight, Aft CG, Clean Wing, 66 KTAS).

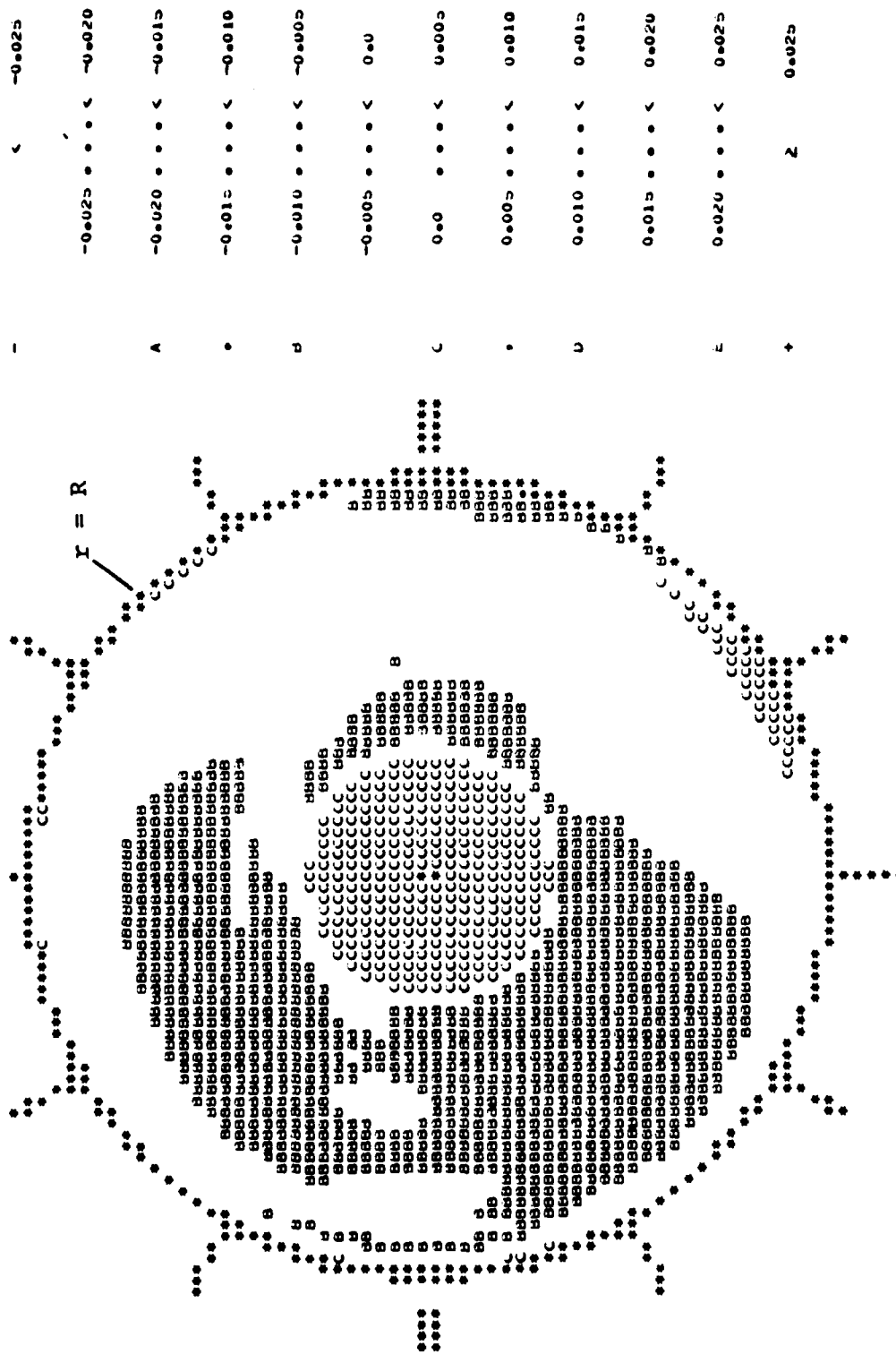


b) Contour Plot from C81 Quasi-Static Trim.  
Figure 36. Continued.



PSI=0

c) Contour Plot from C81 Time-Variant Trim Using the Internal Induced Velocity Distribution. Figure 36. Continued.



d) Contour Plot from C81 Time-Variant Trim Using a Rotor Induced Velocity Distribution Table.

Figure 36. Concluded.

of pressure taps near the airfoil trailing edge. The contribution of pressure differences near the trailing edge, which have the longest moment arm, are based on extrapolated data that assume that the Kutta condition has been satisfied. If the pressure difference has been incorrectly estimated, then the resulting pitching moment coefficient would be in error. Unfortunately, the magnitude of the error cannot be estimated.

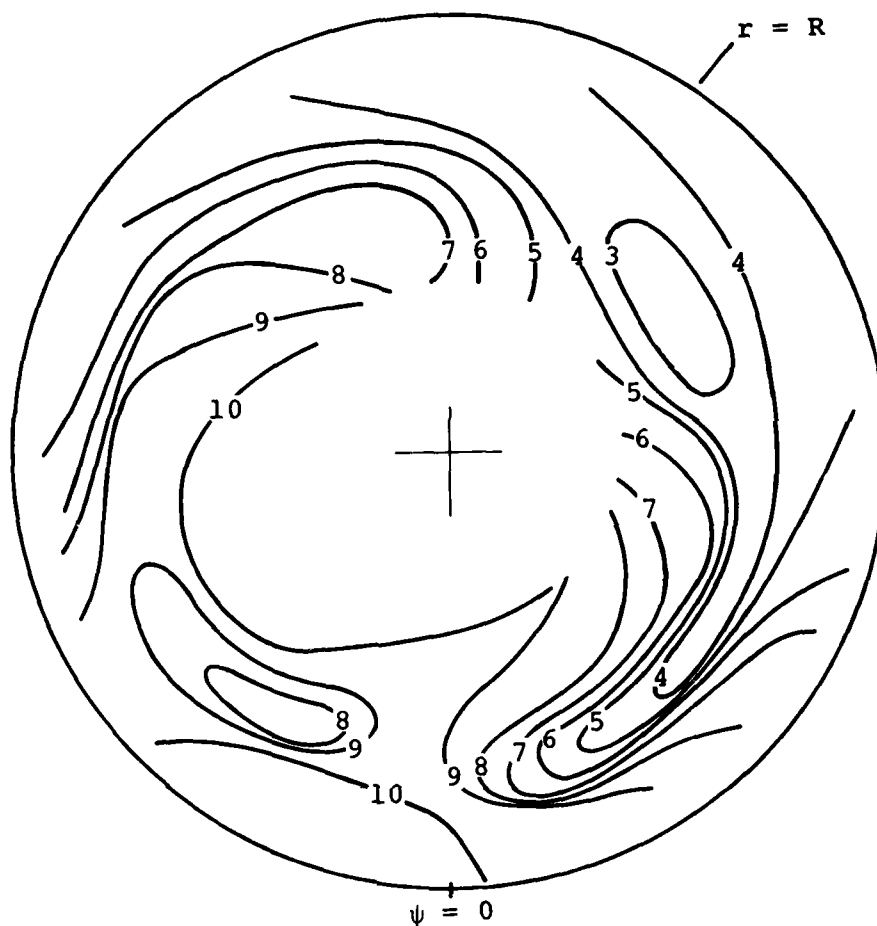
#### 5.5.3.3 Angle-of-Attack Contour Plots

The contour plot of the local blade element angle of attack for the 66 KTAS flight condition, as computed from hot-wire anemometer data and the calibration curves of Figure 3, is presented in Figure 37a. The test-derived data show an unusual ridge of high angles of attack between the dead aft and 180-degree azimuth positions at about 70 percent radius. This ridge does not agree with preconceived notions of a forward flight angle-of-attack distribution. A simple tip-vortex trajectory analysis was performed to see if the ridge was just inboard of the tip vortex, but the ridge does not parallel the simple trajectory. The angle-of-attack contours on the retreating blade side of the disc are much closer to the expected distribution, although the eight- and nine-degree angle-of-attack valley at about 60 percent radius between 300- and 350-degree azimuth was not anticipated. The highest retreating blade angle of attack computed from the test data, 10 degrees, is just below the static stall angle observed at these Mach numbers in the CLCD5474 table, Figure 5.

The unusual pattern of the angle of attack derived from the test data in the vicinity of 70 percent radius implies that there may be an undetected error in the test data itself, in the calibration curves, or the data reduction method. Further investigation of the angle-of-attack information contained in the OLS data base is definitely indicated, as is rapid investigation of the OLS rotor 40- x 80-foot wind tunnel test data (which will be acquired in the immediate future).

Comparison of the test-derived angle-of-attack contour plot of Figure 37a with the C81-generated plots is of some value, even though the quality of the test data is in question. The plots resulting from the QST and the TVT with the internal induced velocity distribution, Figures 37b and 37c, are almost identical, and have none of the unexpected attributes of the test data. The largest angle of attack observed, between 8 and 10 degrees, is near the hub in the 135- to 270-degree azimuth range.

The angle-of-attack contour plot generated from the TVT run with the RIVD table, Figure 37d, has a distribution that is

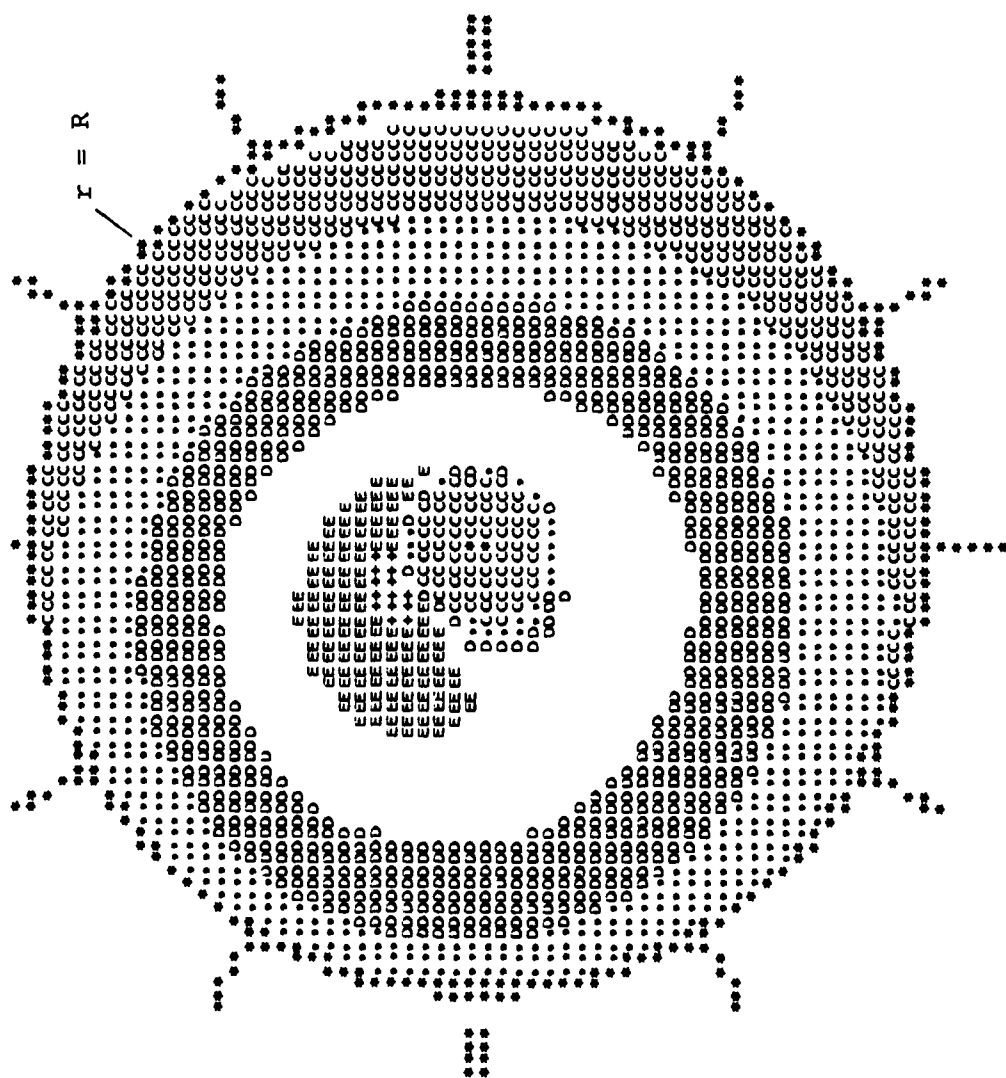


Angle of attack contours in degrees.

a) Contour Plot Derived from Test Data.

Figure 37. Comparison of Main Rotor Angle of Attack Contour Plots Generated from Flight Test and C81 Data for Flight 35A, Counter 611 (8319 Pounds Gross Weight, Aft CG, Clean Wing, 66 KTAS).

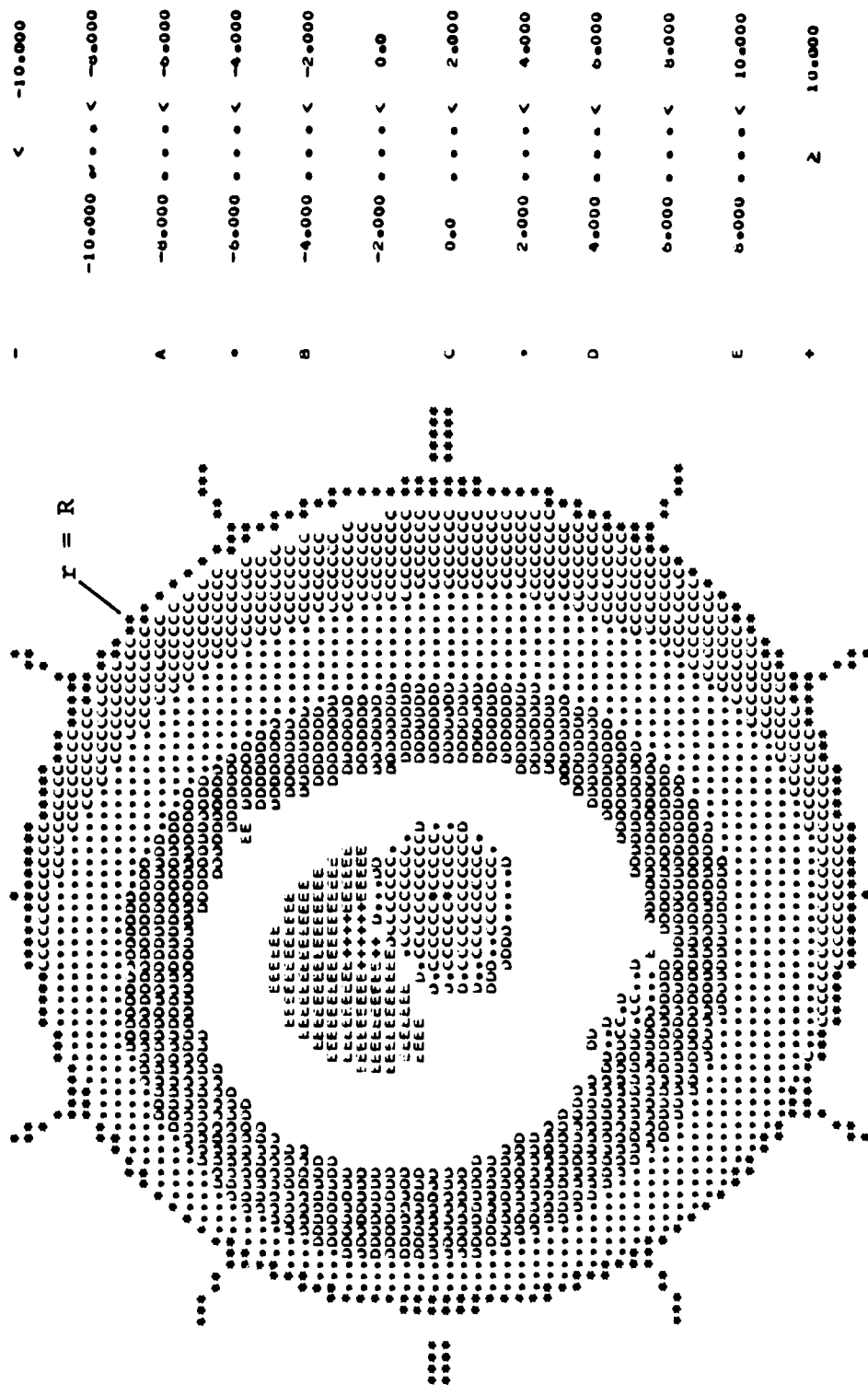
- < -10.000  
 -10.000 . . . < -8.000  
 -8.000 . . . < -6.000  
 -6.000 . . . < -4.000  
 -4.000 . . . < -2.000  
 -2.000 . . . < 0.0  
 0.0 . . . < 2.000  
 2.000 . . . < 4.000  
 4.000 . . . < 6.000  
 6.000 . . . < 8.000  
 8.000 . . . < 10.000  
 2 10.000



PSI=0

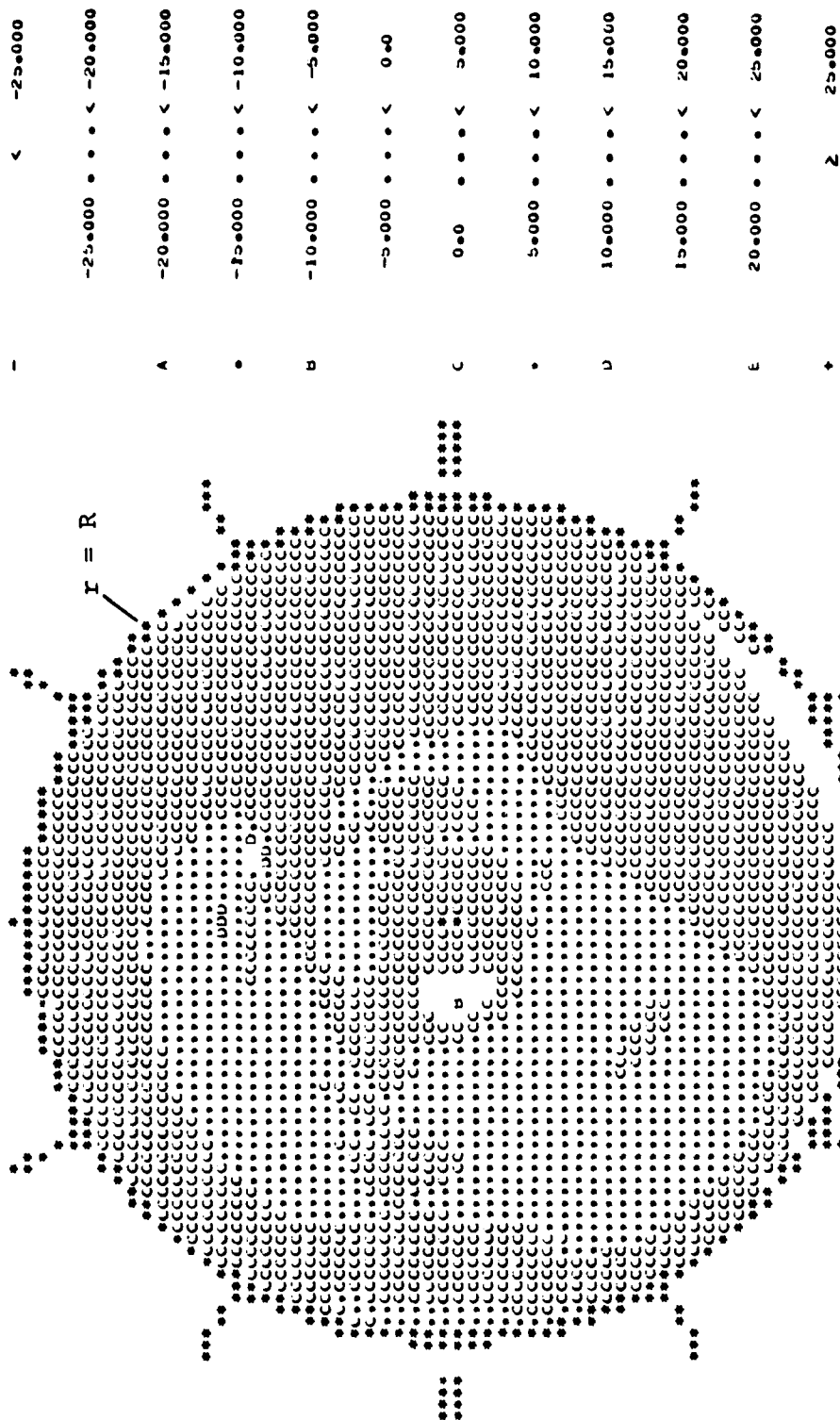
b) Contour Plot from C81 Quasi-Static Trim.

Figure 37. Continued.



c) Contour Plot from C81 Time-Variant Trim Using the Internal Induced Velocity Distribution. Figure 37. Continued.





d) Contour Plot from C81 Time-Variant Trim Using a Rotor Induced Velocity Distribution Table. Figure 37. Concluded.

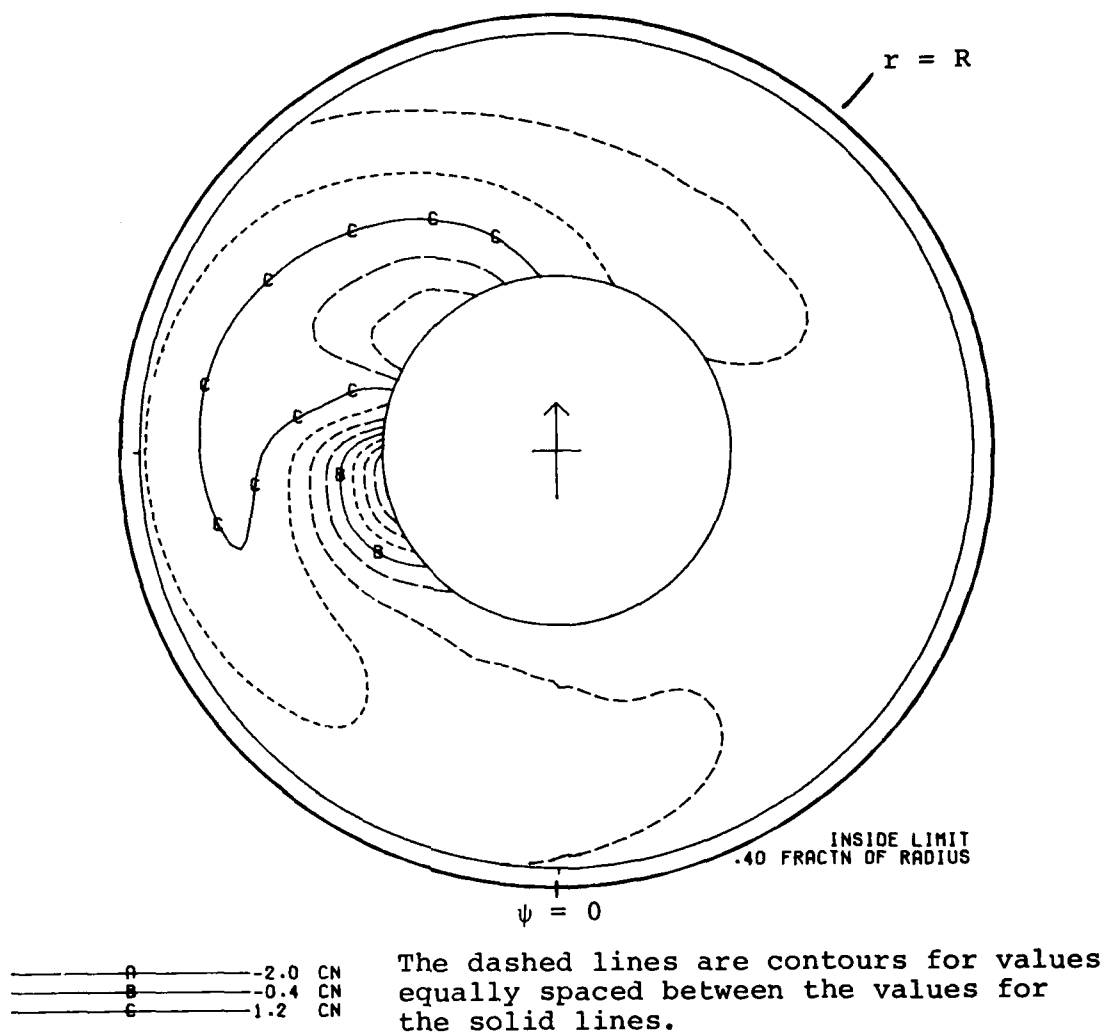
different from both the test data and the two other C81-generated plots. The 5-degree angle-of-attack contour (in the "D region" of Figures 37b and 37c, boundary of the "C-region" in Figure 37d) is approximately the same for cases with or without the RIVD table, although the plot generated with the RIVD table (Figure 37d) shows a radial region of rather low angles of attack in the "C-region" centered along the 270-degree azimuth position. The small "D-region" in Figure 37d, at about 50 percent radius and between 150- and 180-degree azimuth, signifies angles of attack in excess of 10 degrees, which are not experienced in either of the other C81 simulations nor observed in the test data.

#### 5.5.4 Comparison of Rotor Variables for Counter 610

The aerodynamic data presented in Section 5.5.3 was for a 66-KTAS flight condition in which the rotor wake is transported away from the disc slowly, and has a strong effect upon the rotor aerodynamics. The unusual nature of some of the test data indicated that a high-speed case, in which the wake is rapidly convected away from the rotor, should be examined. The rotor aerodynamic environment for such a case, counter 610, is discussed in this section. This was a 142-KTAS ( $V_H$ ) test condition at 8319 pounds gross weight, aft cg, with a clean wing.

##### 5.5.4.1 Normal Force Coefficient Contour Plots

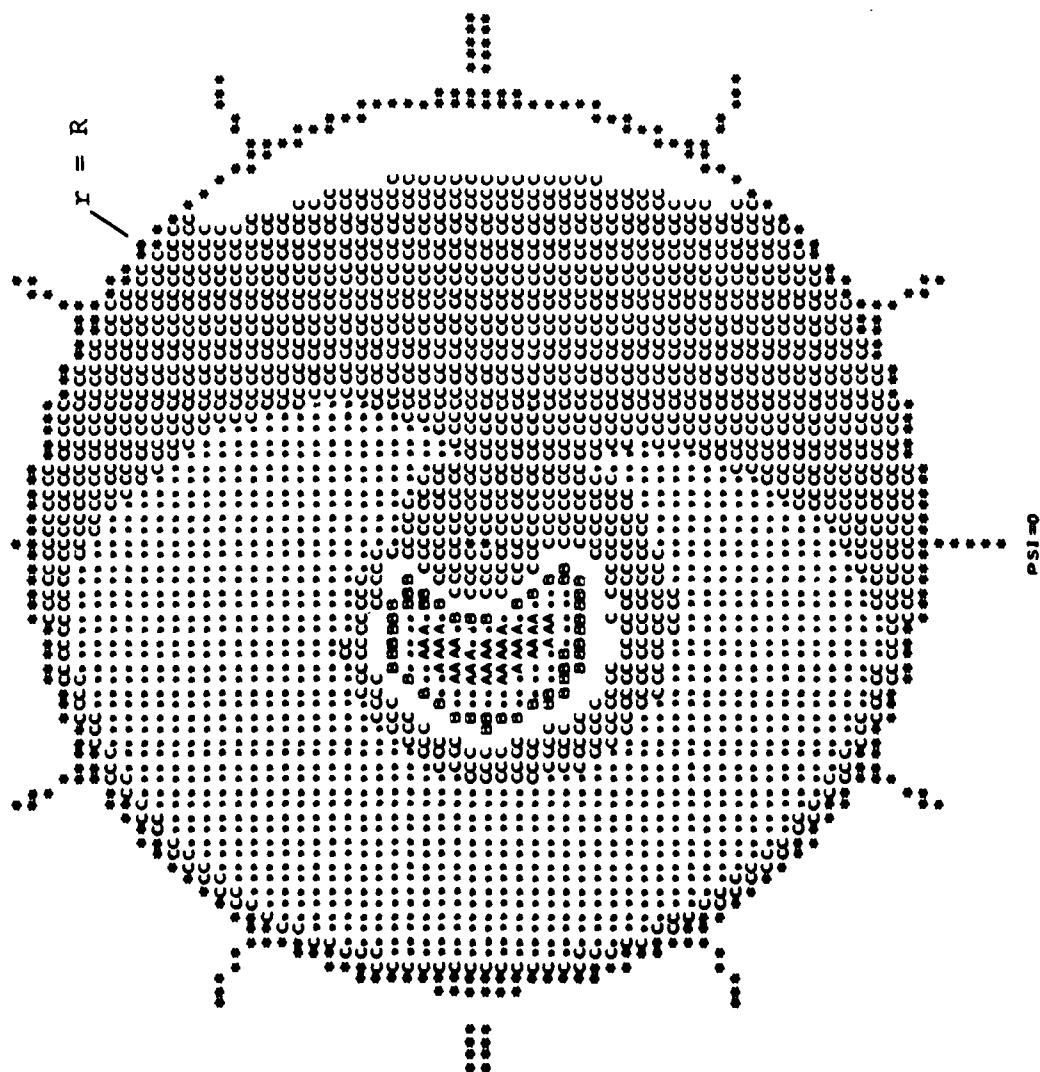
The  $c_N$  contour plot based on the measured pressure data is given in Figure 38a. It shows a region of very high normal force coefficients, with the  $c_N = 1.2$  contour (the "C" contour) being between 180- and 300-degree azimuth and 40- and 80-percent radius. The area inside this contour experiences higher values of  $c_N$ , with the small dashed-line contour between 40 and 50 percent at about 225 degrees azimuth corresponding to a  $c_N$  of 2.0. These large values of  $c_N$  could only arise from the simultaneous occurrence of large drag coefficients, due to retreating blade stall, and very large local angles of attack. Since the drag coefficient is multiplied by the sine of the angle of attack in Equation (12), and the largest  $c_D$  in CLCD5474 (Figure 5) is 2.0 at a 90-degree angle of attack, the large  $c_N$ 's shown in Figure 38a cannot be explained in terms of steady-state aerodynamics.



a) Contour Plot Derived from Test Data.

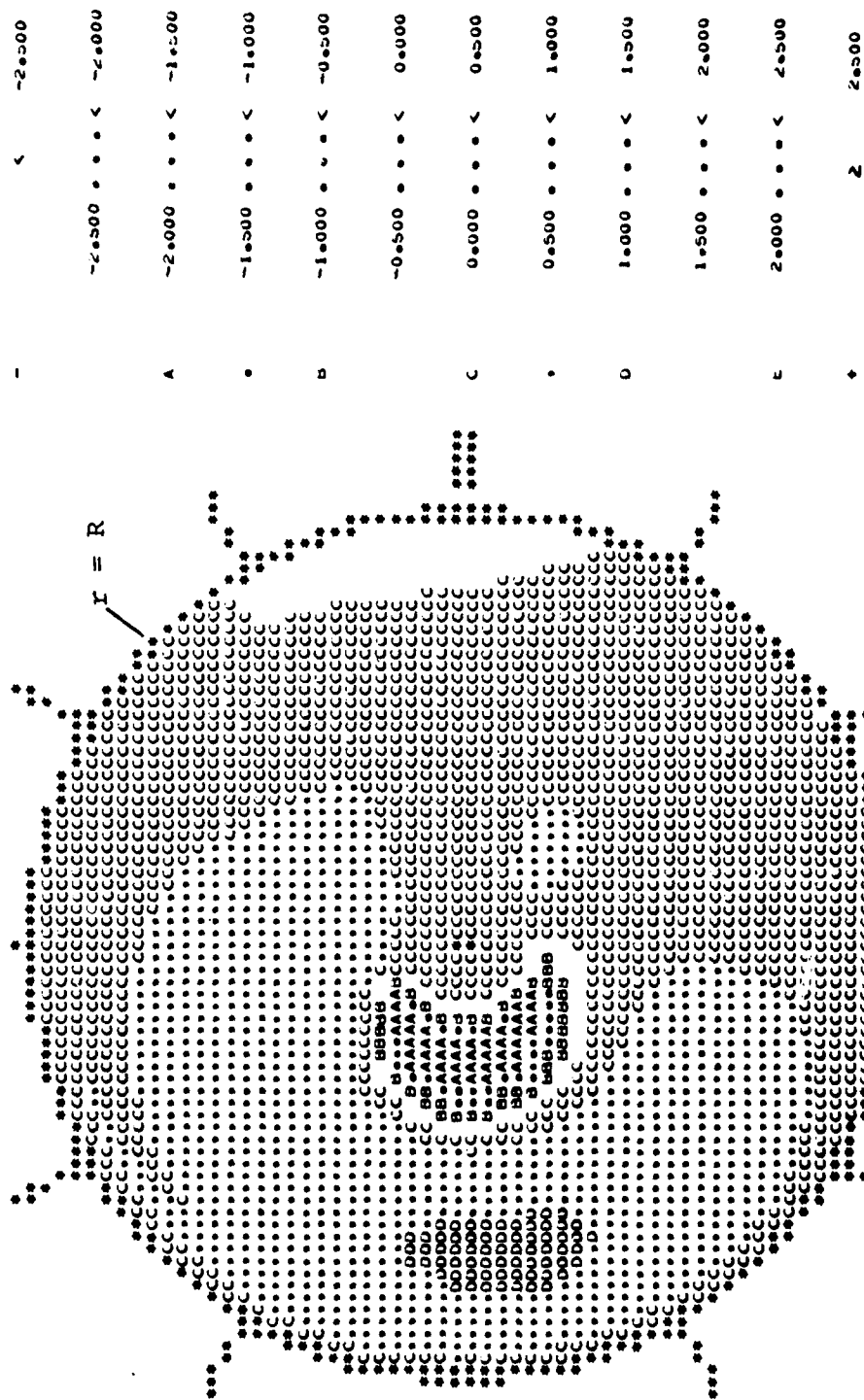
Figure 38. Comparison of Main Rotor Normal Force Coefficient Contour Plots Generated from Flight Test and C81 Data for Flight 35A, Counter 610 (8319 Pounds Gross Weight, Aft CG, Clean Wing, 142 KTAS).

-	<	-2.500
	-2.500 . . . <	-2.000
A	-2.000 . . . <	-1.500
.	-1.500 . . . <	-1.000
B	-1.000 . . . <	-0.500
	-0.500 . . . <	0.000
C	0.000 . . . <	0.500
.	0.500 . . . <	1.000
D	1.000 . . . <	1.500
	1.500 . . . <	2.000
E	2.000 . . . <	2.500
+	Z	2.500



b) Contour Plot from C81 Quasi-Static Trim.  
Figure 38. Continued.





PSI=0

d) Contour Plot from C81 Time-Variant Trim Using a Rotor Induced Velocity Distribution Table. Figure 38. Concluded.

The first dashed-line contour outboard of the "B" contour in Figure 38a designates the loci of points at which  $c_N$  is zero. Inboard of this contour, the normal force coefficient is negative, indicating a negative angle of attack.

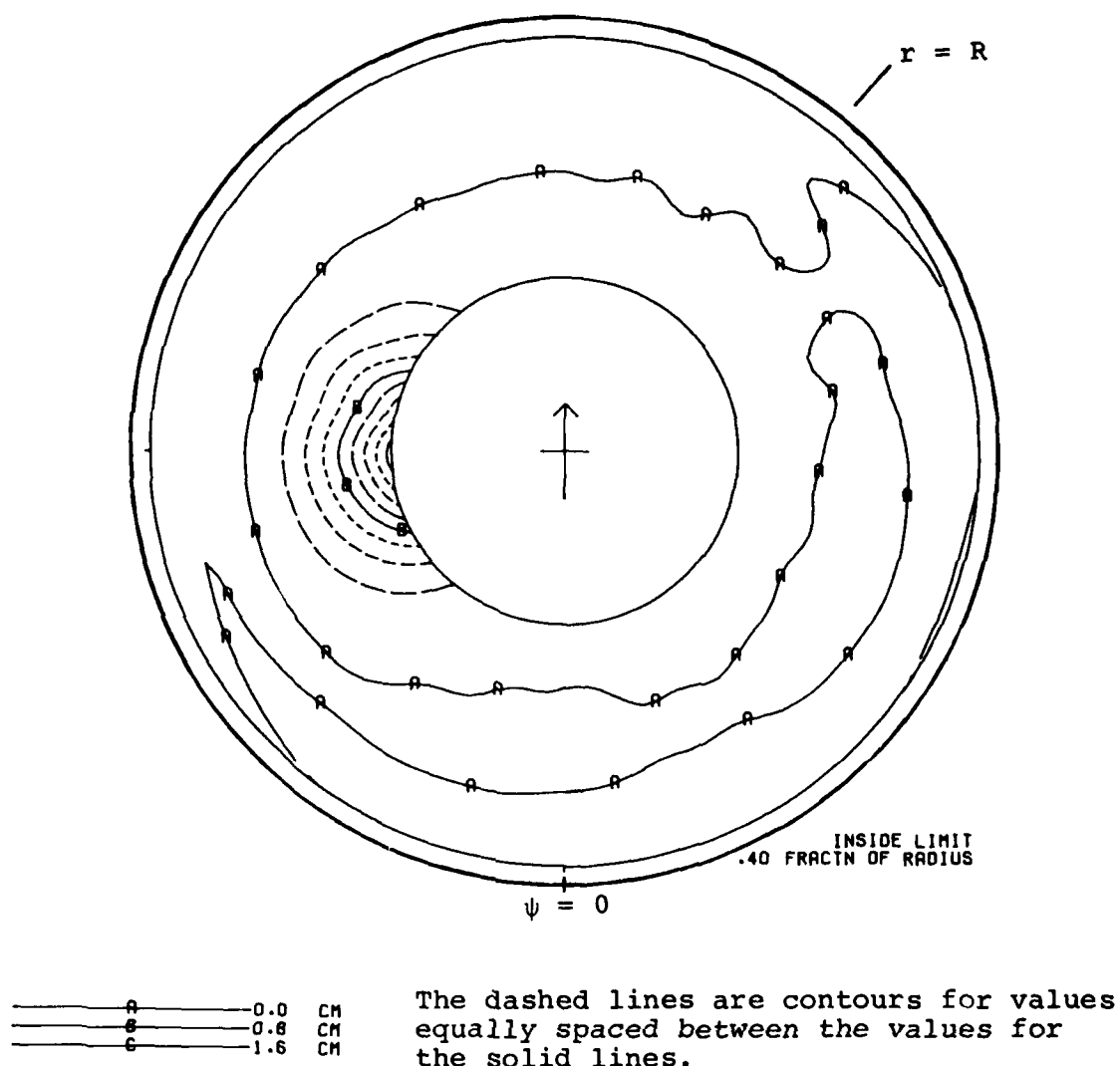
The  $c_N$  contour plots resulting from the C81 runs are given in Figures 38b, 38c, and 38d. All three are in reasonable correspondence, and do not agree with the test-data-derived contour plot of Figure 38a. All three analytical contour plots have a maximum  $c_N$  less than, or equal to, 1.5. The C81-computed  $c_N = 0$  contour on the retreating blade side of the disc is in about the same position as that shown in Figure 37a, but C81 also computes a  $c_N = 0$  contour near the tip on the advancing blade side of the disc, which is not reflected in the test data.

#### 5.5.4.2 Pitching Moment Coefficient Contour Plots

The pitching moment coefficient contour plot derived from the flight-test-measured pressure data, Figure 39a, also shows some unexpected large values of the variable.

The "A" contour in Figure 39a corresponds to  $c_M = 0$ , an unstalled condition. Outboard of this contour, and in the valley extending from about 300 degrees to about 120 degrees azimuth around the 70-percent radius,  $c_M$  is negative to some unknown extent. Over almost the whole disc, the pitching moment coefficient is positive at radii less than 60 percent. In the retreating blade stall area, the pitching moment coefficient is large and positive, reaching a value of 0.8 on the "B" contour and 1.6 on the "C" contour (which is the first contour line outboard of the 40-percent radius circle at  $\psi = 270$  degrees). According to the CLCD5474 table of Figure 5, the largest steady-state value of  $c_M$  obtainable is 0.4 (although this is merely an estimate). Pitching moment coefficients on the order of 0.8 to 1.2 are well beyond the steady-state capability of any airfoil. Ignoring the specific value of the pitching moment coefficient computed from the pressure data, the contour plot does indicate a region of large negative angle-of-attack stall in the 40- to 60-percent radius area on the retreating blade.

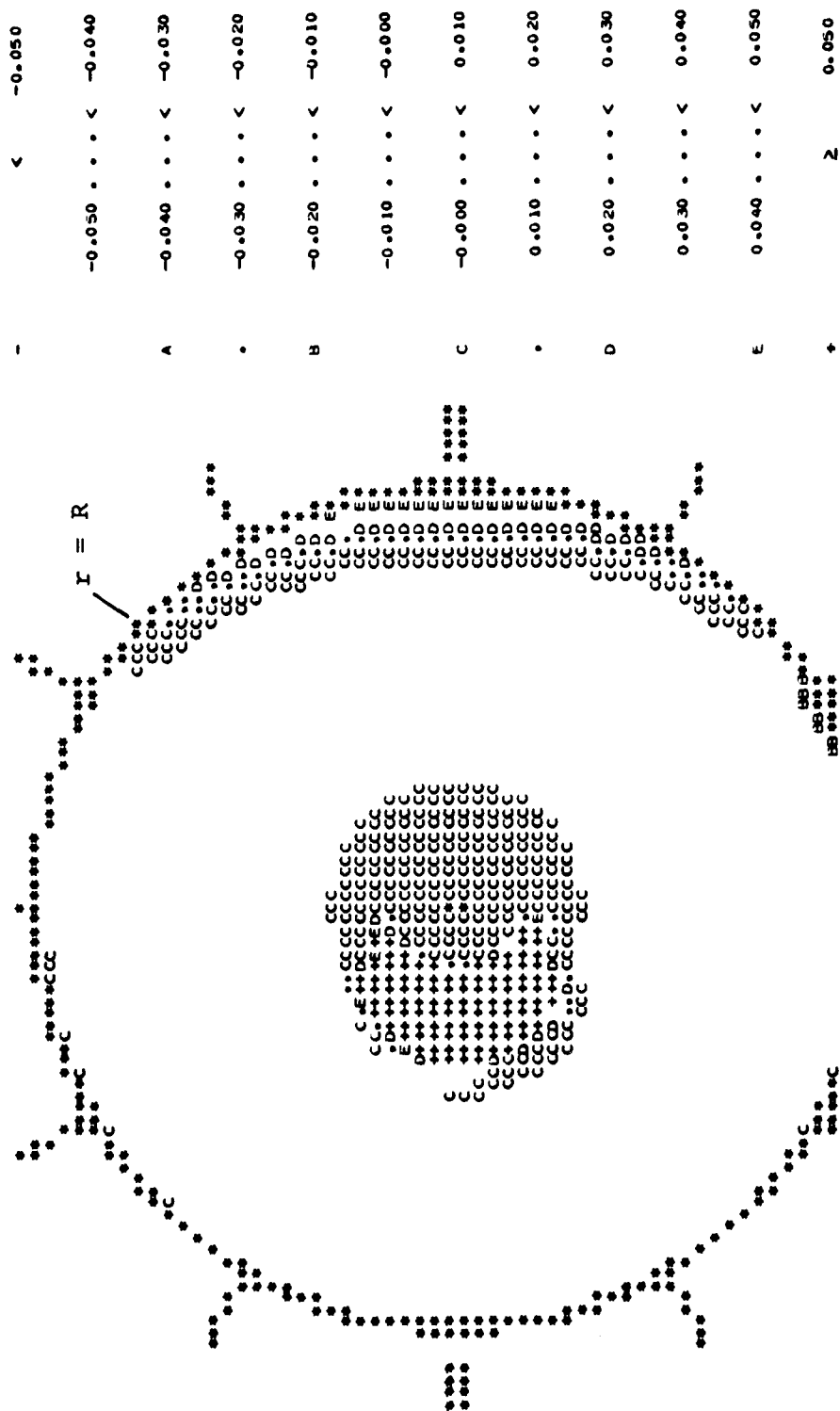
The  $c_M$  distributions as computed in the C81 simulations are contour-plotted in Figures 39b, 39c and 39d. The three computer-generated plots are similar to each other, and do not agree with the plot derived from the test data given in Figure 39a. A small region of positive pitching moment coefficients



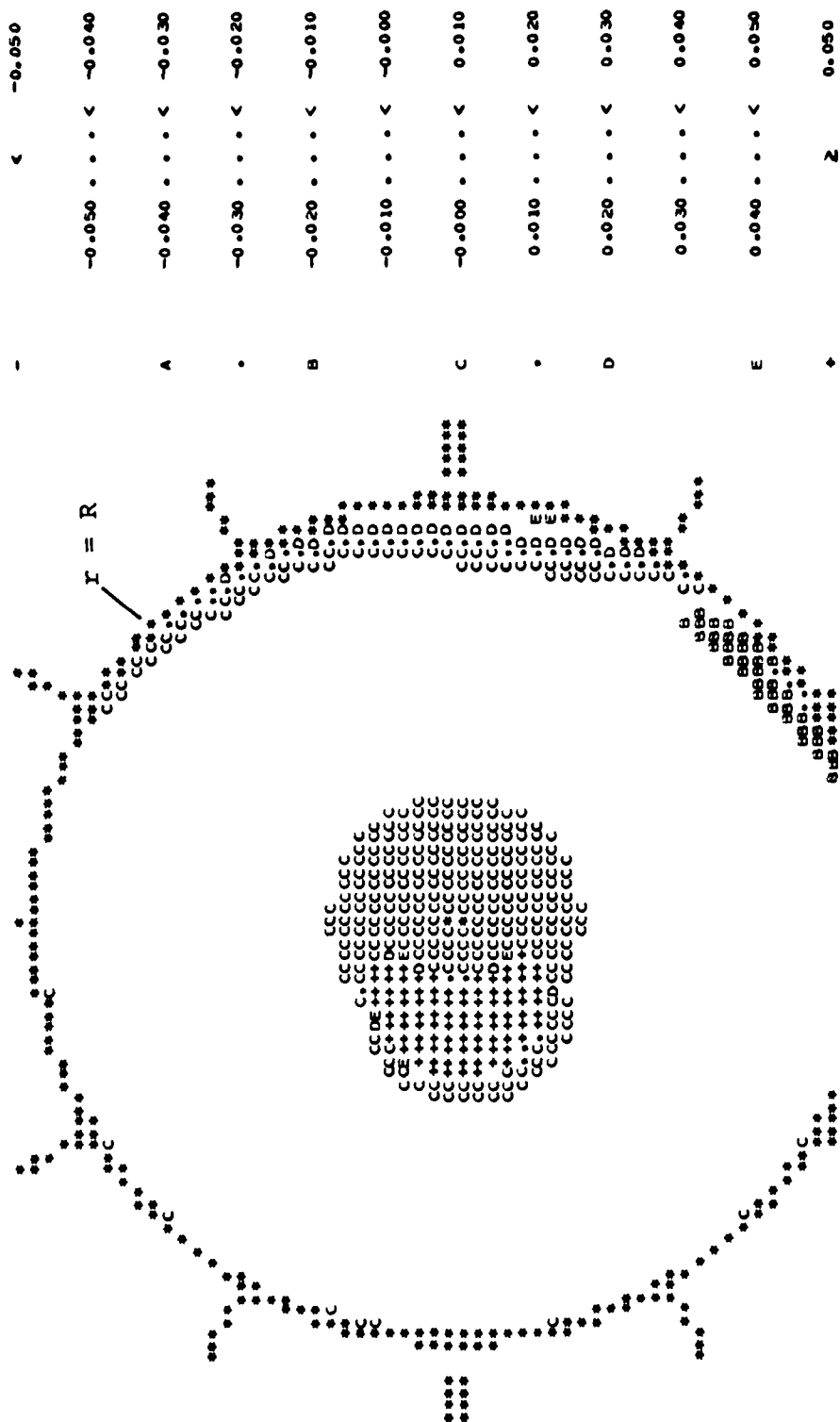
a) Contour Plot Derived from Test Data.

Figure 39. Comparison of Main Rotor Pitching Moment Coefficient Contour Plots Generated from Flight Test and C81 Data for Flight 35A, Counter 610 (8319 Pounds Gross Weight, Aft CG, Clean Wing, 142 KTAS).





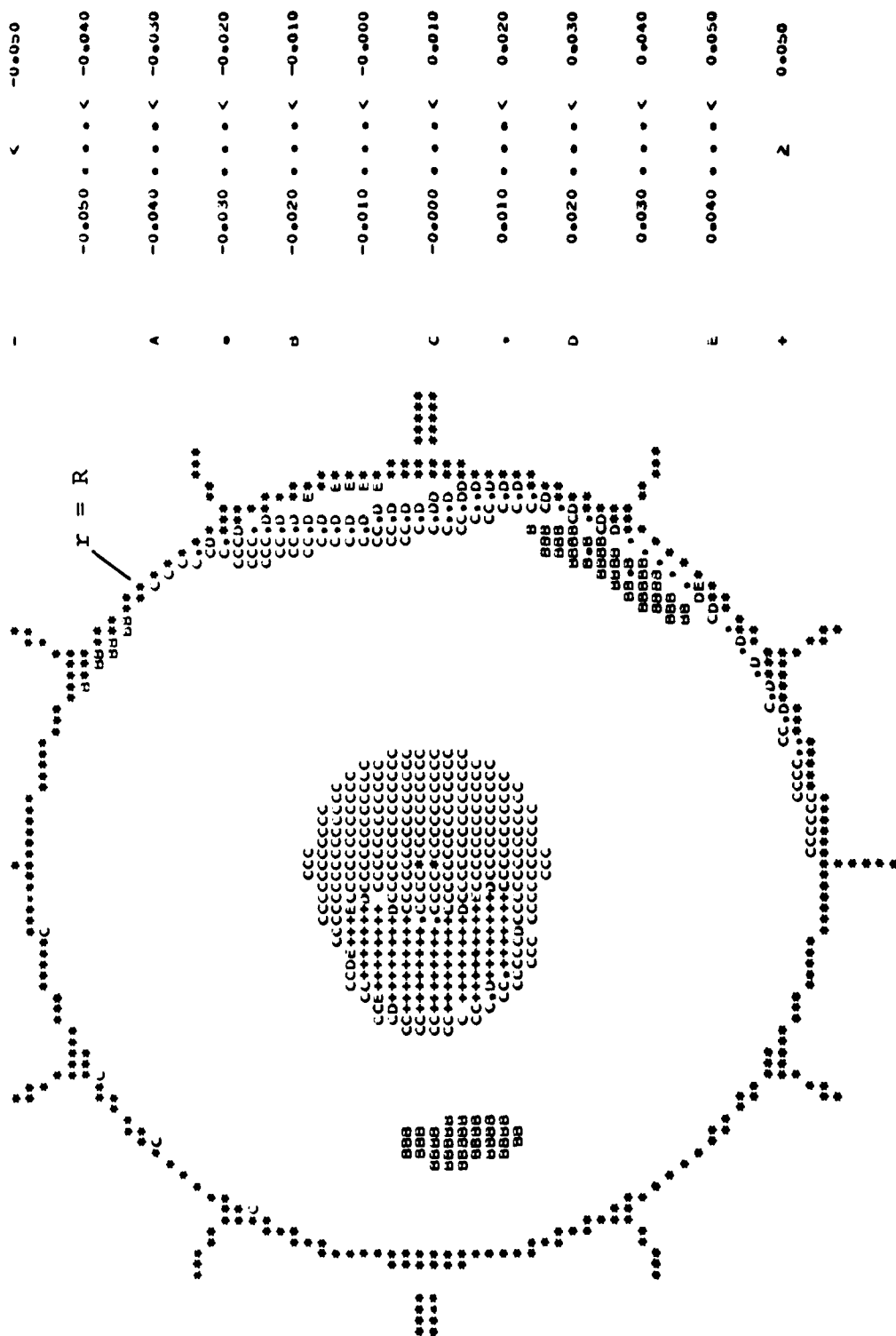
b) Contour Plot from C81 Quasi-Static Trim.  
Figure 39. Continued.



c) Contour Plot from C81 Time-Variant Trim Using the Internal Induced Velocity Distribution.

P 51=0

Figure 39. Continued.



d) Contour Plot from C81 Time-Variant Trim Using a Rotor Induced Velocity Distribution Table.  
Figure 39. Concluded.

is computed near the tip on the advancing blade, indicating negative angle-of-attack stall. (At the Mach numbers experienced in this area, the static stall angle is close to zero.) The value of  $c_M$  is slightly negative over the remainder of the disc, except in the vicinity of the hub. Large positive pitching moment coefficients exist in the hub region, indicating an area of strong positive angle-of-attack stall.

#### 5.5.4.3 Angle-of-Attack Contour Plots

The contour plot of main rotor angle of attack computed from measured hot-wire anemometer data is given in Figure 40a. This plot also demonstrates unusual values for the angle of attack in the vicinity of 70 percent radius, with a ridge being experienced between zero and 75 degrees azimuth and a valley from about 85- to about 225-degrees azimuth. This phenomenon cannot be explained at this time. The simple tip-vortex trajectory analysis did not show the vortex to be in proximity with either the ridge or the valley.

Angles of attack in excess of the static stall angle are experienced between 270 degrees and 30 degrees azimuth, delineating the region of retreating blade stall. The large positive angles of attack between 40 and 50 percent radius and between 260- and 315-degrees azimuth are in disagreement with the negative values of  $c_N$  calculated from the test data for this area of the disc (Figure 38a and Section 5.5.4.1) and in disagreement with the large positive values of  $C_M$  derived from the measured pressure data (Figure 39a and Section 5.5.4.2). Since large positive angles of attack are expected in this region, the hot-wire data tend to further discredit the pressure data in this region of the disc.

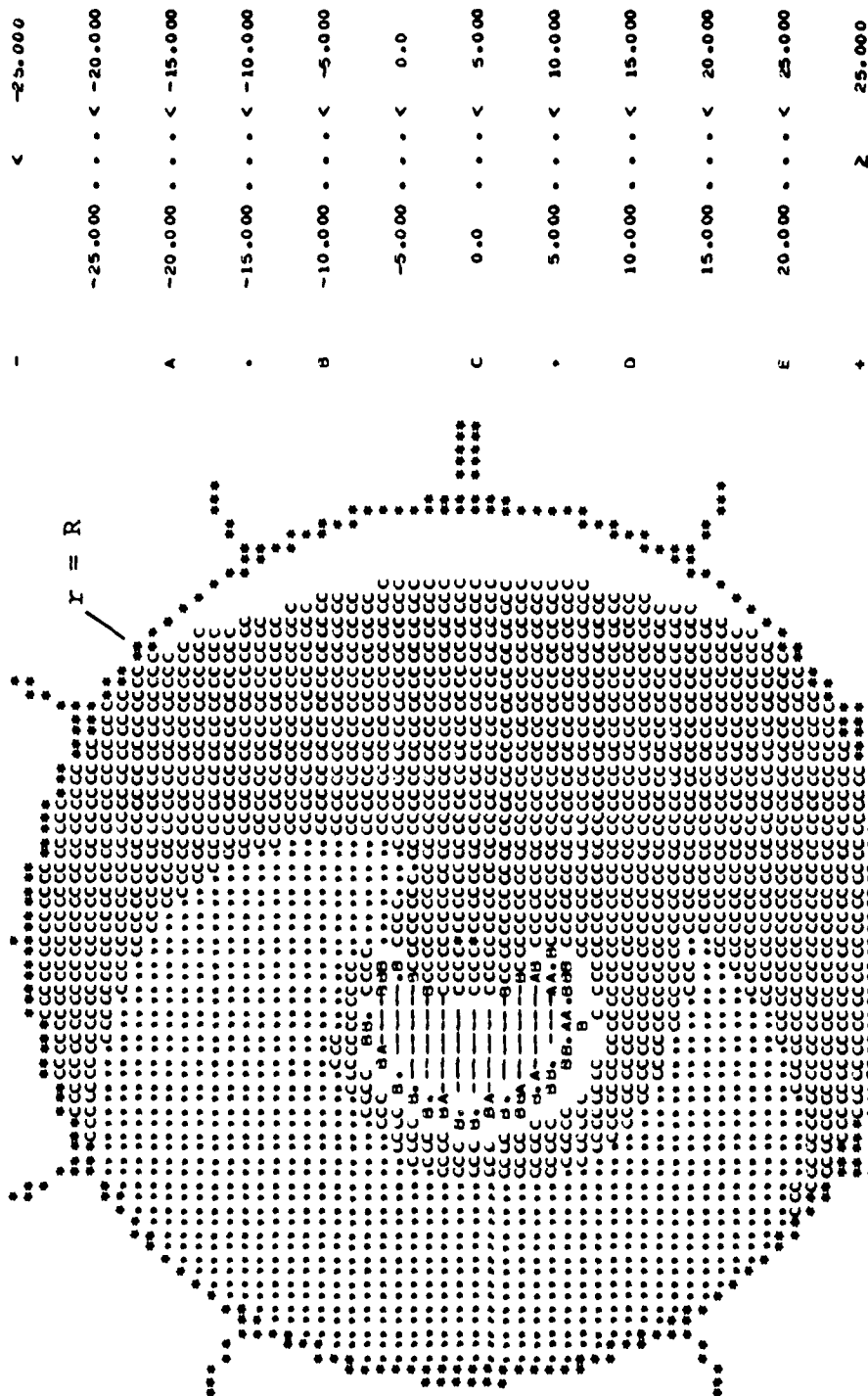
Figures 40b, 40c and 40d contain the C81-generated angle-of-attack contour plots for the 142 KTAS case. Qualitatively, they are very similar, with a small region of negative angle of attack on the advancing blade tip and no angles of attack greater than 10 degrees at any point on the disc. Additionally, the 5-degree contour is reasonably similar in all three plots. Comparison of the test data (Figure 40a) and the three C81 plots shows that significantly higher angles of attack were experienced in flight over the whole disc than in the simulation. This supports the suspicion voiced in the main rotor horsepower comparison discussion (Section 5.4.1) "that more stall was experienced on the actual rotor than in the simulation."



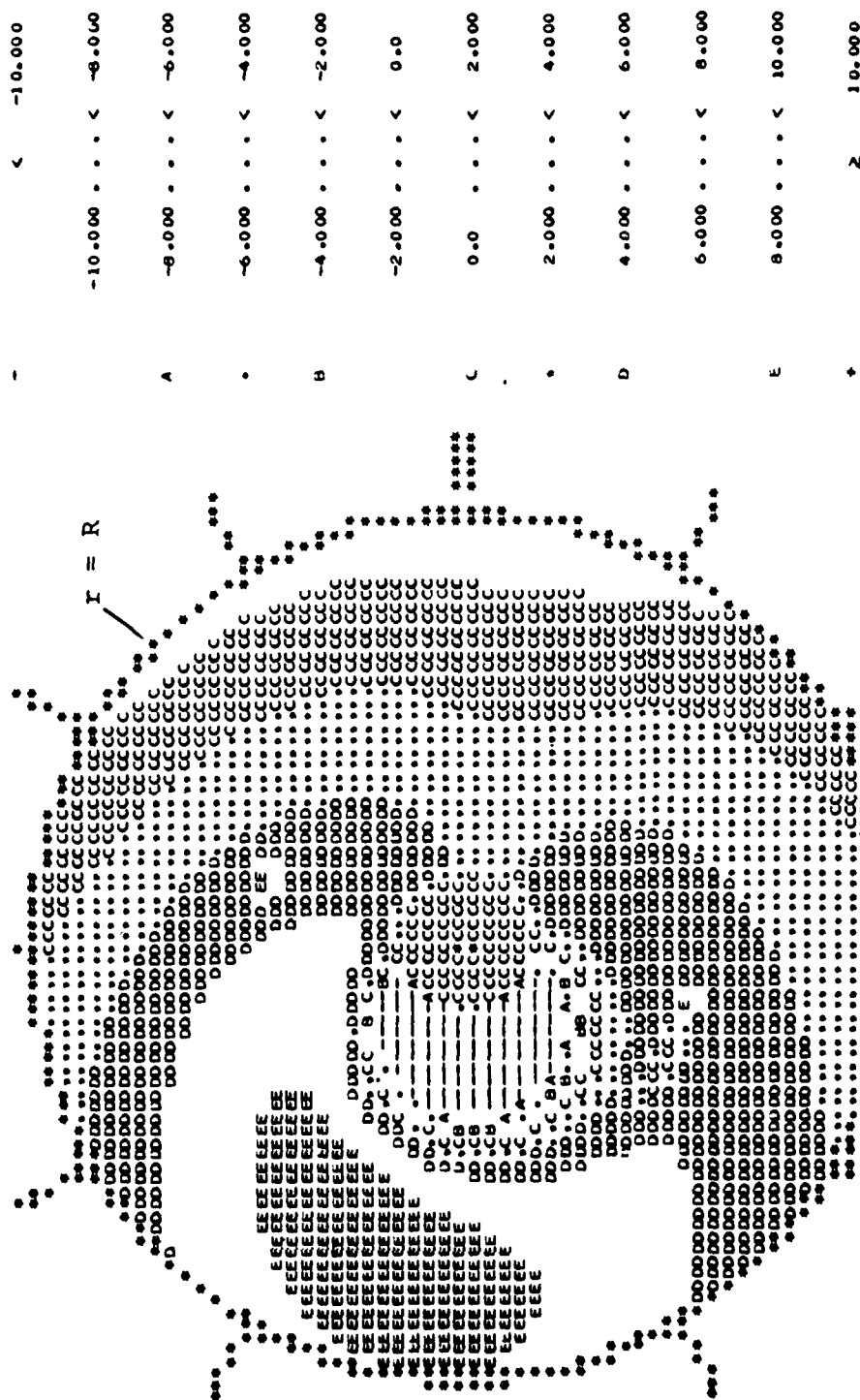
Angle of attack contours in degrees.

a) Contour Plot Derived from Test Data.

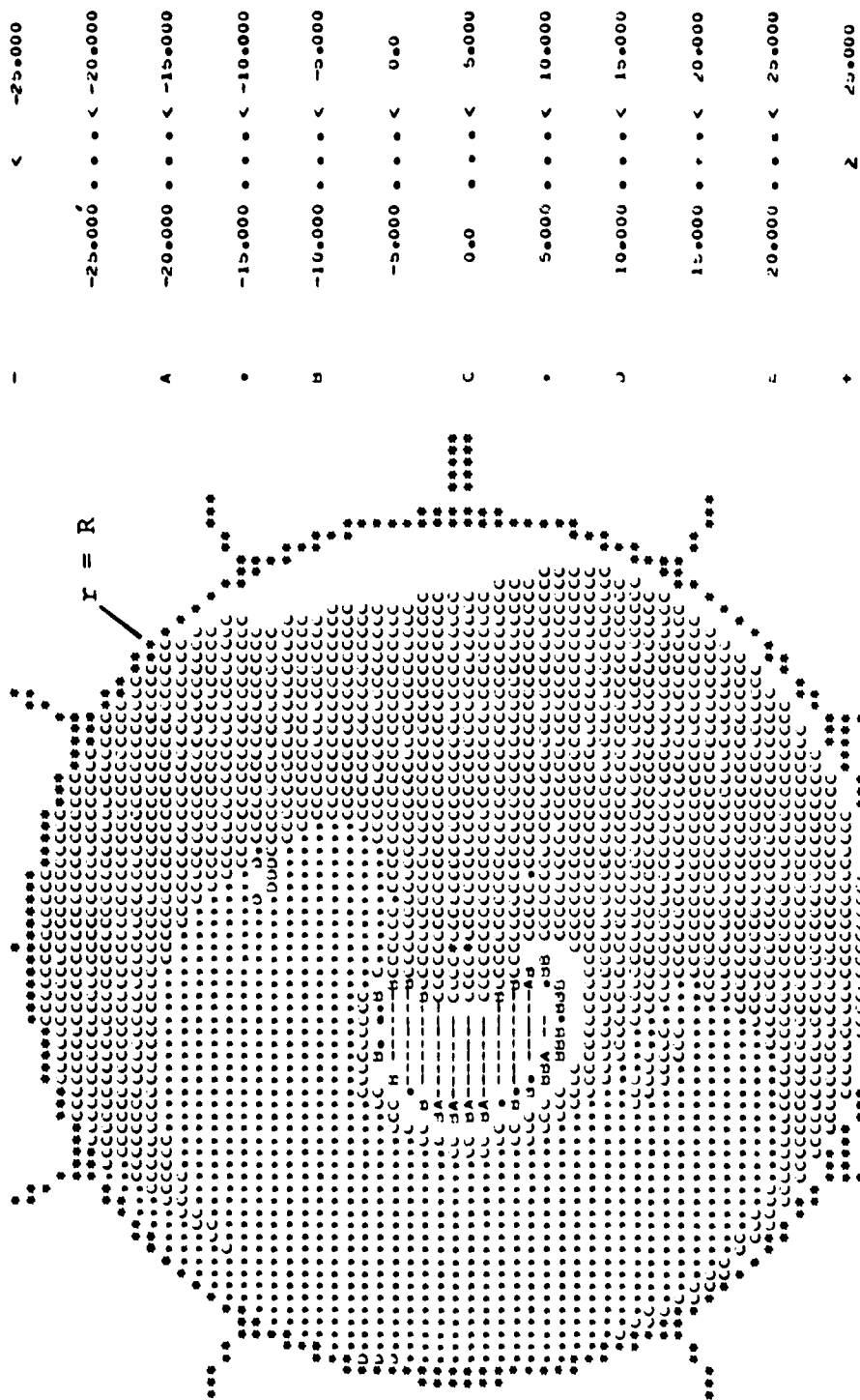
Figure 40. Comparison of Main Rotor Angle-of-Attack Contour Plots Generated from Flight Test and C81 Data for Flight 35A, Counter 610 (8319 Pounds Gross Weight, Aft CG, Clean Wing, 142 KTAS).



b) Contour Plot from C81 Quasi-Static Trim.  
Figure 40. Continued.



c) Contour Plot from C81 Time-Variant Trim Using the Internal Induced Velocity Distribution.  
Figure 40. Continued.



d) Contour Plot from C81 Time-Variant Trim Using a Rotor Induced Velocity Distribution Table.

Figure 40. Concluded.



## 6. MAIN ROTOR LOADS AND ACCELERATIONS

Main rotor hub vibrations and pitch link loads, hub and blade bending moments and accelerations were measured during the OLS test program. Hub vibrations can only be computed in C81 when the elastic pylon is used. Since no simulations were performed with the elastic pylon, the measured hub vibrations could not be compared with computed data. The remainder of the elastic rotor response parameters have been compared with measured data and typical results of those comparisons are reported in this section. Due to the large volume of main rotor loads data available, only typical results have been included. The discussion of those results is preceded by a description of the methods by which the rotor loads and accelerations are calculated in C81.

### 6.1 CALCULATION OF ROTOR RESPONSE OUTPUTS IN C81

Rotor pitch link loads, bending moments, and accelerations are computed using the participation factors that define the rotor response and using data input with the mode shapes.

#### 6.1.1 Calculation of Pitch Link Loads

The pitch link load coefficient, input with each mode shape as XGMS(7,i), is the pitch link tension, in pounds, for a unit deflection of that mode. The total pitch link load at a given instant of time is

$$PLL = \sum_{i=1}^{i=NMODE} \delta_i XGMS(7,i) \quad (13)$$

where PLL is the pitch link load, positive for tension

$\delta_i$  is the instantaneous participation factor for the  $i$ th mode.

NMODE is the number of mode shapes being used to model the rotor.

### 6.1.2 Calculation of Rotor Bending Moments

The method of computation of rotor bending moments is similar to that used to calculate the pitch link loads. Coefficients for the out-of-plane, inplane and torsional moment are input for each radial station for each mode shape. Denoting these coefficients, respectively as OPBMC(r,i), IPBMC(r,i) and TBMC(r,i), the bending moments at a given station are

$$\text{OPBM}(r) = \sum_{i=1}^{i=\text{NMODE}} \delta_i \text{OPBMC}(r,i) \quad (14.a)$$

$$\text{IPBM}(r) = \sum_{i=1}^{i=\text{NMODE}} \delta_i \text{IPBMC}(r,i) \quad (14.b)$$

$$\text{TBM}(r) = \sum_{i=1}^{i=\text{NMODE}} \delta_i \text{TBMC}(r,i) \quad (14.c)$$

where OPBM(r) is the instantaneous out-of-plane bending moment at radius r

IPBM(r) is the instantaneous inplane bending moment at radius r

TBM(r) is the instantaneous torsional moment at radius r

$\delta_i$  is the instantaneous participation factor for the ith mode

NMODE is the number of mode shapes being used to model the rotor

Outboard of the radius at which the pitch horn attaches (XMR (32) or XTR(32)), the out-of-plane and inplane moments are transformed into the beam-chord reference system, as

$$\text{BBM}(r) = \text{OPBM}(r) \cos\theta_k + \text{IPBM}(r) \sin\theta_k \quad (15.a)$$

$$\text{CBM}(r) = -\text{OPBM}(r) \sin\theta_k + \text{IPBM}(r) \cos\theta_k \quad (15.b)$$

Where BBM(r) is the instantaneous beam bending moment at radius r

CBM(r) is the instantaneous chord bending moment at radius r

$\theta_k$  is the sum of the elastic and built-in twist at the station, plus the collective pitch angle at which the mode shapes were generated

Inboard of the radius at which the pitch horn attaches,

$$\text{BBM}(r) = \text{OPBM}(r) \quad (16.a)$$

$$\text{CBM}(r) = \text{IPBM}(r) \quad (16.b)$$

The beam, chord and torsional bending moments are harmonically analyzed and a summary of the harmonics is automatically printed out. The pitch link load is also harmonically analyzed, and its harmonics are printed with the torsional bending moments.

### 6.1.3 Calculation of Rotor Accelerations

The rotor response is calculated based on the aerodynamic and dynamic loads imposed upon it. The dynamic loads result from the accelerations experienced by the rotor, including the elastic accelerations of its components. The elastic accelerations are not explicitly stated in the equations of motion because they are the variables being solved for. Since these accelerations are implicit to the solution, and hence not readily available, a separate routine was written to compute the rotor blade element accelerations from the results of the response analysis.

The accelerations at a given radial station on the rotor consist of the accelerations at the hub, the centripetal acceleration, and the elastic accelerations of the rotor. The accelerations at the hub are computed by a straightforward calculation of all rigid body accelerations in the fixed system, plus any accelerations of the rotor support system, with the results transformed into a nonrotating coordinate system aligned with the rotor mast. These accelerations are then transformed into a coordinate system rotating with the rotor that is also flapped through the instantaneous flapping angle  $\beta_H$ , Equation (10.b).

A plane is defined that is oriented, relative to the mast, by the instantaneous longitudinal and lateral hub flapping angles. The rotor analysis in the AGAJ77 version of C81 assumes that the rotor rotates about an axis perpendicular to this plane, and the centripetal acceleration is perpendicular to this axis. The angle defined by the out-of-plane slope of the blade, relative to the hub plane, is computed at each radial station, and the centripetal acceleration is transformed into local blade coordinates through the resulting angle.

The mode shape displacement components are input in a coordinate system aligned with the rotor mast. They are transformed into the local beam-chord coordinate system through the local geometric pitch angle,  $\theta_k$ , as used in Equation (15.b). The resulting modal displacement coordinates are multiplied by the second derivative of the participation factor for each mode and summed over all modes to yield the elastic accelerations.

## 6.2 MAIN ROTOR PITCH LINK LOADS

Measured and computed pitch link axial force harmonic amplitudes are compared in Figure 41 for several forward flight conditions. Measured data are provided for both the white and red blade for all but the 10 KTAS case. The data for both blades are reasonably similar. Most of the difference in measured loads between the two blades is probably a result of the aerodynamic and structural dissimilarities between the blades due to the different instrumentation installations. The sign convention for the pitch link axial force is not reported in any of the OLS test documentation; the normal convention at BHT is tensile loads positive.

C81 computes a negative steady pitch link load for all but one of the cases shown in Figure 41, while the measured data indicate a positive axial force for all cases. The positive pitch link load is typical for two-bladed teetering rotors with trailing-edge pitch horns, and is attributed to the nose-down tennis-racket moment. The negative values computed by C81 are further evidence of a problem with beam-torsion coupling. Table 14 contains a derivation of the steady pitch link load as computed for the 116 KTAS case, counter 614. As can be seen, the cyclic modes do not contribute to the steady pitch link load. The contribution from the second out-of-plane collective mode (mode 7) is positive, and about one-third of the measured value, while the contribution due to the third out-of-plane collective mode is strongly negative with an amplitude of about two-thirds of the measured value. This third mode has significantly less beam-torsion coupling than the second, but almost six times the steady response. Its pitch link load coefficient also has the opposite sign to that of the second mode. Had the sign been negative, the computed steady pitch link load would have been quite close to that measured for 116 KTAS.

The steady pitch link load computed by the TVT with the internal induced velocity model is very close to the measured value at 10 KTAS.

Pitch Link Loads - pounds

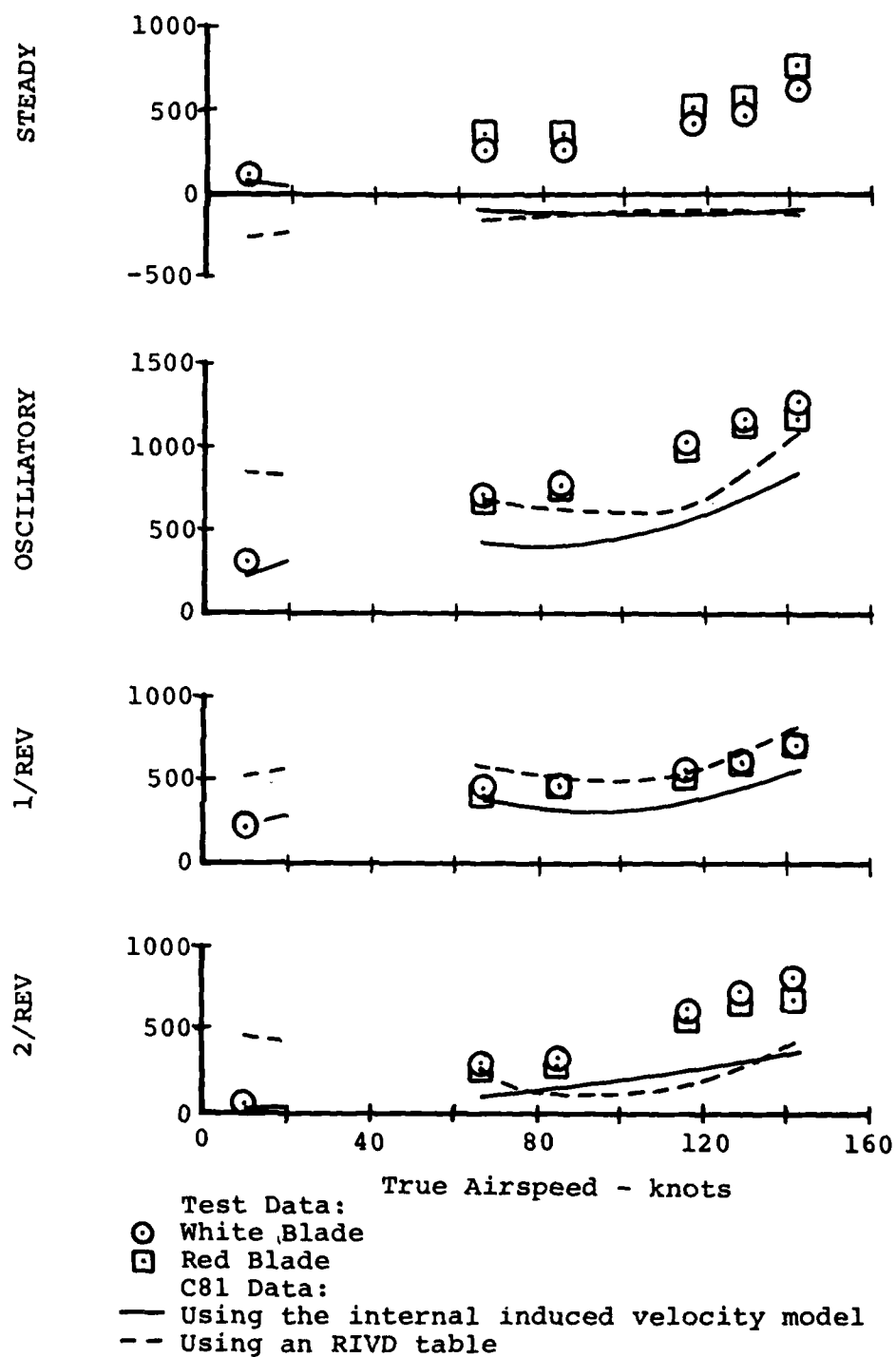
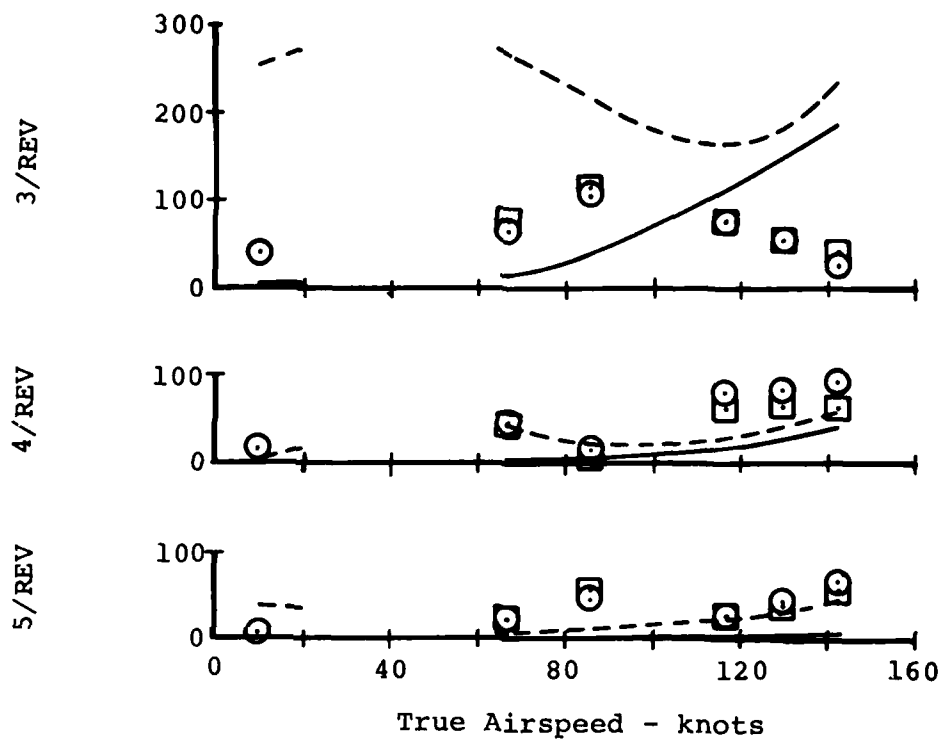


Figure 41. Comparison of Measured and Computed Main Rotor Pitch Link Loads in Forward Flight.

Pitch Link Loads - pounds



Test Data:  
 ○ White Blade  
 □ Red Blade  
 C81 Data:  
 — Using the internal induced velocity model  
 -- Using an RIVD table

Figure 41. Concluded.

TABLE 14. EXAMPLE OF CALCULATION OF STEADY PITCH LINK LOAD FOR C81  
SIMULATION OF COUNTER 614 (8319 POUND GROSS WEIGHT, AFT  
CG, CLEAN WING, 116 KTAS)

Simulation run with internal induced velocity distribution

Mode Number	Mode Type	Mode Name	Steady Component of Participation Factor	Pitch Link Load Coefficient	Contribution to Pitch Link Load, Lb
1	Cyclic	Rigid Body	$-5.55160 \times 10^{-4}$	$2.2340 \times 10$	0.0077856
2	Cyclic	Inplane	$1.90349 \times 10^{-4}$	$-1.3421 \times 10^3$	-0.2554674
3	Cyclic	Torsion	$1.97431 \times 10^{-5}$	$-4.4840 \times 10^4$	-0.8852806
4	Cyclic	"S-ing"	$-1.72067 \times 10^{-5}$	$7.6262 \times 10^3$	-0.1312217
5	Cyclic	Out-of-Plane	$2.53637 \times 10^{-6}$	$5.6574 \times 10^3$	<u>0.0143493</u>
Total for Cyclic Modes					1.2498
6	Coll	Coning	$-3.07409 \times 10^{-1}$	$1.2100 \times 10$	-3.71965
7	Coll	Out-of-Plane +	$-3.92412 \times 10^{-3}$	$-3.7321 \times 10^4$	146.45208
8	Coll	Out-of-Plane +	$-2.29648 \times 10^{-2}$	$1.1888 \times 10^4$	-273.00554
9	Coll	Out-of-Plane	$-7.35530 \times 10^{-3}$	$-7.1120 \times 10$	<u>0.52311</u>
Total for Collective Modes					-129.75001

Total Steady Pitch Link Load = -128.50

The oscillatory pitch link loads computed for these level flight conditions are in reasonable agreement with those measured in flight. The agreement for the low-speed flight condition is quite good for the TVT with the internal induced velocity distribution. At higher speeds, the pitch link loads computed with either induced velocity model demonstrate a different trend with airspeed from that shown by the test data. The data computed by the TVT with the internal induced velocity distribution are between 200 and 300 pounds lower than the measured values. Data computed by the TVT with the RIVD table are closer to the measured data, but the decrease in value in the mid-speed range is more pronounced than that of the basic TVT data, and reaches its lowest at 116 KTAS instead of 85 KTAS.

The measured and computed one-per-rev pitch link loads agree quite well. The one-per-rev value computed by the basic TVT simulation of the 10-KTAS case is in almost perfect agreement with the test data. The large discrepancy between the measured value at 10 KTAS and that computed by the TVT with the RIVD table is further evidence that the Crimi wake program is inadequate at low speeds. Over the remainder of the speed range, the measured and computed values are in close agreement, with the data computed by the TVT with the RIVD table being very close to the measured data. The cause of the initial decrease in computed values, between 66 and about 85 knots, is not known.

The two-per-rev loads computed by the TVT with the internal induced velocity distribution are about one-half of the measured values over the whole speed regime. The results of the simulation run with the TVT with the RIVD table do not agree with the test data, with a very large two-per-rev value being computed at 10 KTAS, and a negative slope with airspeed between 66 and about 90 KTAS.

The vertical plot scale has been changed for the plots of the three-, four- and five-per-rev components due to the small values measured in flight. The measured and computed three-per-rev components do not agree at all, with the measured data decreasing at higher speeds. This decrease in the measured data is totally unexpected and cannot be explained. The three-per-rev pitch link loads computed by the TVT using the internal induced velocity distribution have the expected trend with airspeed, with the values increasing with speed. The trend exhibited by the data generated by the TVT with the RIVD table does not agree with the trends established by either of the other sets of data, and the values are unacceptably large.



Much of the discrepancy between the measured and computed three-per-rev pitch link load data is most likely due to the incorrect calculation of the "S-ing" and cyclic torsion mode frequencies, as discussed in Section 3.4. Additionally, part of the discrepancy between the measured three-per-rev data and that generated by the TVT with the RIVD table must be attributed to the much larger computed three-per-rev airloads in the 66 to 120 KTAS speed range.

The agreement between the measured and computed four-per-rev pitch link loads is fair. The simulation with the RIVD table calculates higher loads than the simulation with the internal induced velocity distribution because the latter model has almost no four-per-rev aerodynamics. The agreement is also fair between the measured five-per-rev pitch link loads and those computed by the simulation with the RIVD table. Almost no five-per-rev pitch link loads are computed in the basic TVT, due to the lack of any five-per-rev aerodynamics.

Computed and measured harmonic amplitudes are compared for counters 635, 675 and 1093 in Table 15. The results are reasonably similar to those already discussed, with the simulation with the RIVD computing larger values for every harmonic than the simulation with the internal induced velocity distribution. The simulations compute a negative steady component, while a positive steady load was measured. The oscillatory and one-per-rev loads computed by the simulation with the RIVD are in reasonable agreement with the measured data, while those computed in the basic TVT are lower than the test data. Both simulations compute a two-per-rev pitch link load lower than that measured, and a three-per-rev load well in excess of the test value. The computed four-per-rev values are of the same order of magnitude as the test data. The five-per-rev pitch link load computed with the RIVD table is close to that measured, while the value computed by the basic TVT is smaller than the test data.

The comparison of harmonic amplitude does not provide any phase information. The rotor red blade pitch-link-load waveform and the waveforms plotted by C81 are compared in Figure 42 for the 66 KTAS flight condition of counter 611. The maximum positive value of the measured pitch link tension occurs at an azimuth of approximately 200 degrees, and the waveform is predominantly one- and two-per-rev. The pitch-link-load waveform computed by C81 using the internal induced velocity model has its maximum value at about 320 degrees, lagging the measured peak by 120 degrees. (The asterisks on the C81 waveforms are automatically generated as a key to the plot legend.) The pitch-link-load time history computed by the TVT with the RIVD table is primarily one- and three-per-rev. Based on the computed sine and cosine components of the

TABLE 15. COMPARISON OF MEASURED AND COMPUTED PITCH LINK  
AXIAL FORCE AMPLITUDES FOR COUNTERS 635, 675,  
AND 1093

Counter 635	Red Blade	White Blade	Basic TVT	TVT + RIVD
9069 lb, mid cg, 4 XM-159 rocket pods, 136 KTAS				
Steady	905.95	894.35	-31.00	-51.23
Oscillatory	1158.58	1243.29	863.71	1195.34
1/Rev	713.92	700.35	556.35	806.85
2/Rev	627.66	770.96	456.28	548.21
3/Rev	56.23	60.68	233.47	342.32
4/Rev	39.88	77.20	52.22	35.80
5/Rev	52.97	56.71	19.79	50.09
<u>Counter 675</u>				
9068 lb, aft cg, 4 XM-159 rockets pods, 135 KTAS				
Steady	706.43	597.68	-16.75	-31.59
Oscillatory	1133.03	1252.47	876.45	1160.67
1/Rev	726.37	712.66	563.01	807.01
2/Rev	652.20	786.70	444.85	493.83
3/Rev	27.39	32.88	236.63	284.15
4/Rev	44.29	80.59	54.69	41.35
5/Rev	35.45	51.39	18.08	41.28
<u>Counter 1093</u>				
8300 lb, fwd cg, clean wing, 145 KTAS				
Steady	-	363.91	-49.73	-80.37
Oscillatory	-	1247.17	878.66	1313.18
1/Rev	-	740.71	597.21	866.17
2/Rev	-	767.30	517.46	667.63
3/Rev	-	38.35	249.54	379.12
4/Rev	-	87.99	60.39	49.15
5/Rev	-	60.77	22.50	55.63

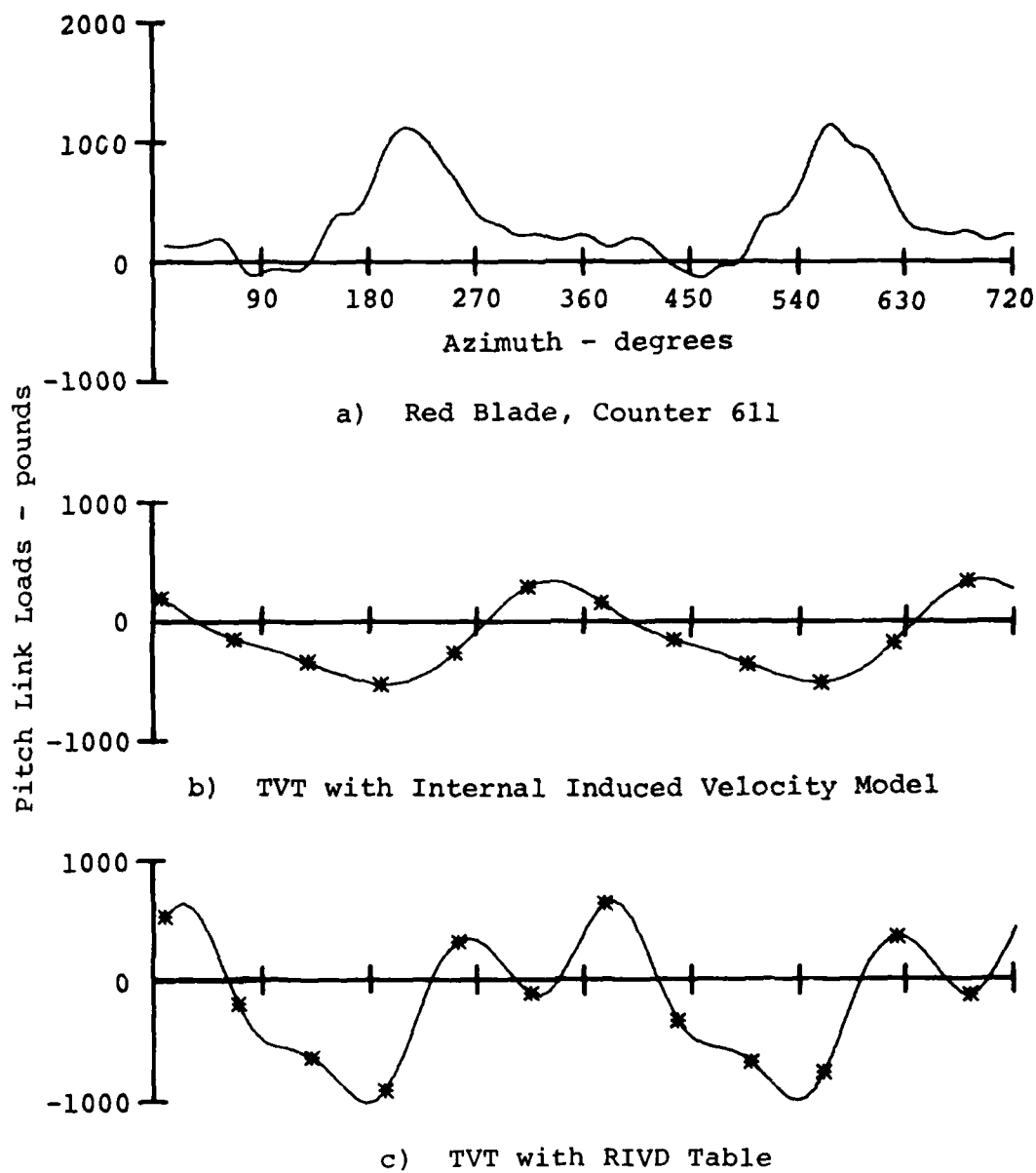


Figure 42. Comparison of Measured and Computed Main Rotor Pitch Link Load Waveforms for Counter 611 (8319 Pounds Gross Weight, Aft CG, Clean Wing, 66 KTAS).

pitch link tension, the one-per-rev constituent reaches its maximum value at an azimuth of -21.33 degrees, and the three-per-rev term peaks at 51.45 degrees.

### 6.3 MAIN ROTOR BEAM BENDING MOMENTS

Main rotor beam bending moments for the 129 KTAS (counter 615) and the 142 KTAS (counter 610) level flight cases are compared in this section of the report. It is assumed that positive beam bending moment corresponds to tension in the lower surface (which is the normal BHT convention), as the beam bending moment sign convention is not documented in any of the OLS test reports. The steady beam bending moment measured at 14.2 percent radius was in excess of 45,000 inch-pounds for all test conditions, and was assumed to be in error, as the value was well above any of the other measured data.

#### 6.3.1 Comparison of Measured and Computed Beam Bending Moments for Counter 615

Figure 43 contains plots of harmonic amplitudes of measured and calculated data for the 129 KTAS level flight test condition of counter 615. The aircraft had a gross weight of 8319 pounds for this counter, with an aft center of gravity, and was in the clean wing configuration.

Small positive values of the steady beam bending moment were measured near the hub and the tip. The values computed by both simulations are very similar to each other, and do not show these positive values. Several more higher-frequency out-of-plane collective modes would have to be included in the analysis to include the type of curvature implied by these positive measured values. The computed and measured steady beam bending moment radial distributions are in reasonably good agreement, with the large negative value in the vicinity of the flexure (2.2 percent radius) being closely matched. Both the test and computed data indicate that the rotor cones down from its preconed position.

The radial distribution of oscillatory beam bending moments computed by both simulations are reasonably close to each other in the inboard 10 percent and outboard 40 percent of the rotor and in reasonable agreement with the measured data. The data computed by the basic TVT have about the same radial distribution as the test data, with higher values being computed in the midspan region. The data resulting from the simulation with the RIVD table miss the peak value at 14.2 percent radius, show good agreement to midspan, and then have increased values not reflected in the test data.

Main Rotor Beam Bending Moments -  $10^3$  in.-lb

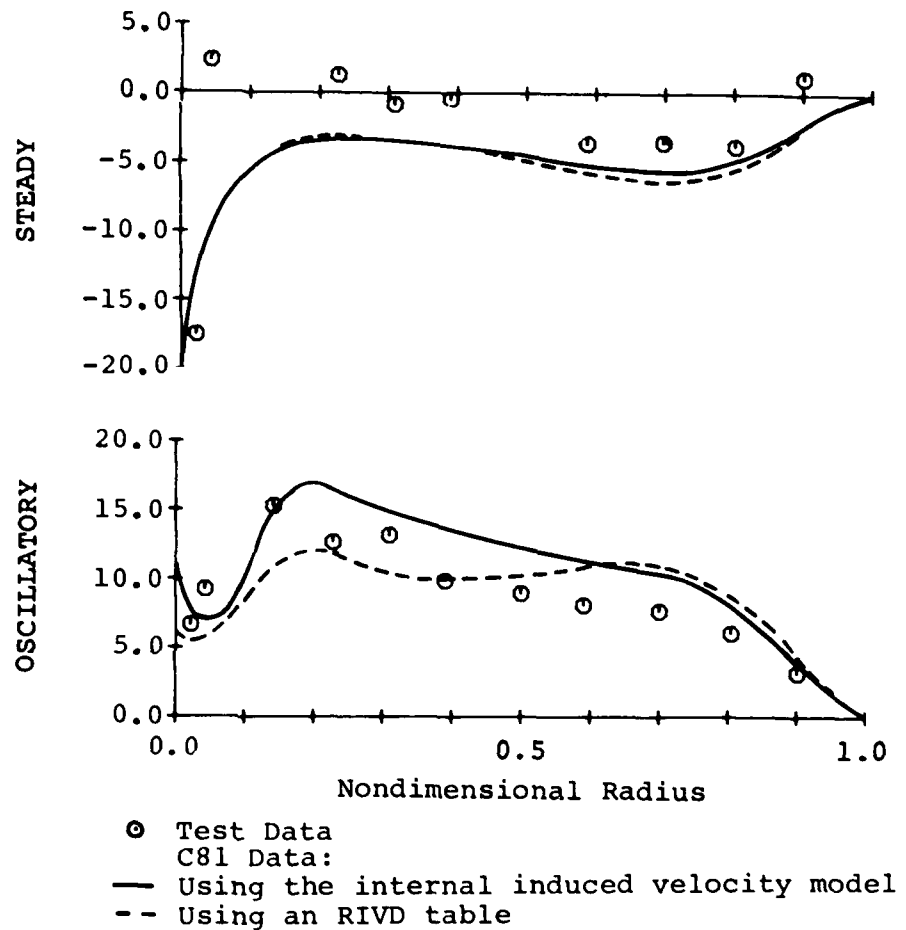


Figure 43. Comparison of Measured and Computed Main Rotor Beam Bending Moments for Counter 615 (8319 Pounds Gross Weight, Aft CG, Clean Wing, 129 KTAS).

Main Rotor Beam Bending Moments -  $10^3$  in.-lb

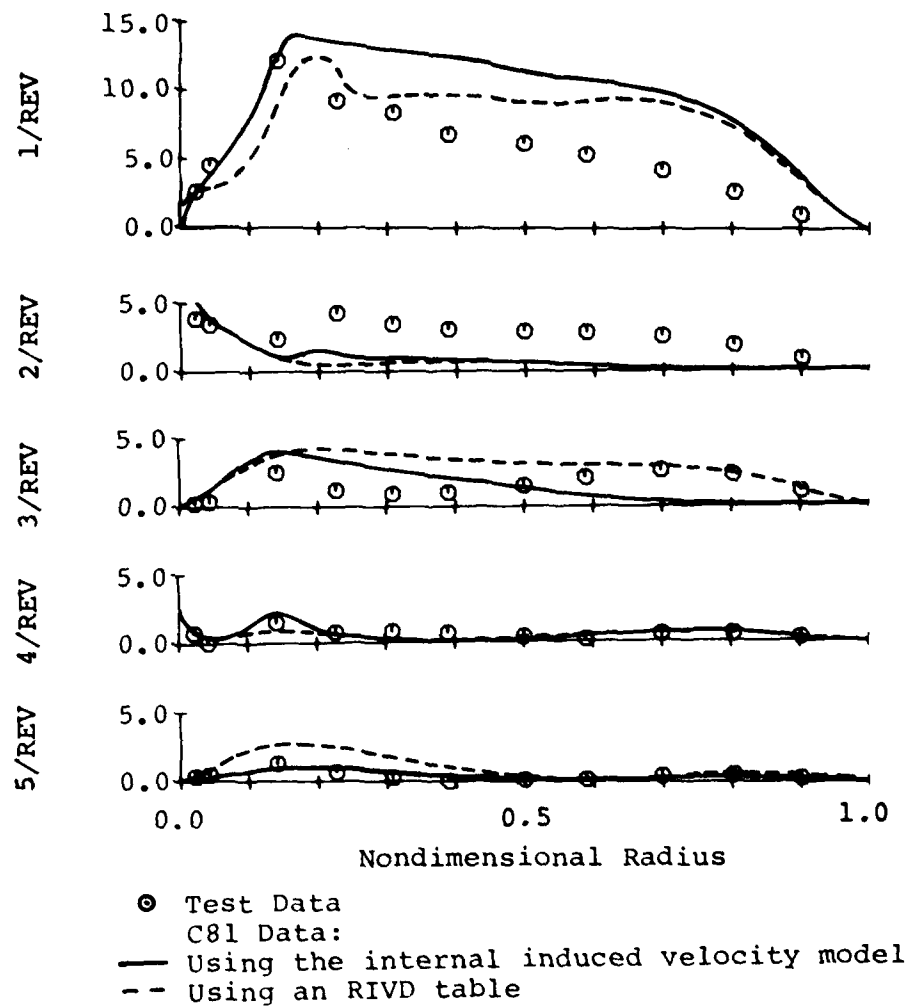


Figure 43. Concluded.

AD-A089 008

BELL HELICOPTER TEXTRON FORT WORTH TX

F/6 1 3

VALIDATION OF THE ROTORCRAFT FLIGHT SIMULATION PROGRAM (C81) US--ETC(U)

JUL 80 J R VAN GAASBEEK

DAAJ02-77-C-0003

BHT-699-099-006

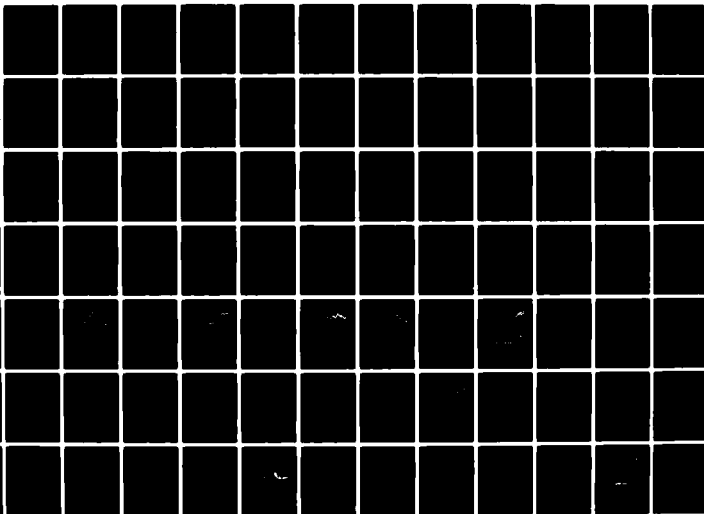
USAAVRADCOM-TR-80-D-4

NL

UNCLASSIFIED

3 of 4

AD  
A189-08



Both the measured and computed oscillatory beam bending moment is predominantly one-per-rev in frequency content, as seen by investigation of the radial distribution of one-per-rev loads. The beam bending moments computed by both simulations are reasonably close together, and generally greater than the measured data. A small "hump" is observed outboard in the one-per-rev beam moment distribution resulting from the simulation with the RIVD table. The hump is not as large as that seen in the oscillatory beam bending moments, but there is obviously a one-per-rev contribution.

The computed two-per-rev moments agree with the measured data only in the first 15 percent of the rotor, which is the yoke and grip assembly region. The use of the RIVD table has a negligible effect upon the computed two-per-rev beam bending moments in comparison with those computed by the basic TVT.

The radial distribution of the computed three-per-rev beam bending moment does not agree with the test data, and the large values computed outboard of 70 percent when the RIVD table is included contributes to the "hump" observed in the oscillatory bending moment in this region of the blade. The discrepancy between the computed and measured three-per-rev bending moment is most likely due to the incorrect computation of the cyclic torsion and "S-ing" mode frequencies (see Section 3.4).

Agreement between the measured and computed four- and five-per-rev beam bending moment is excellent over almost the whole rotor.

Phase information can be deduced from the comparison of beam bending moments in Figure 44. Station 41.0 is one of the points at which loads are monitored for fatigue life evaluation on the production 540 rotor. Station 37.5 is the nearest station that was instrumented on the OLS rotor, which is the reason that it was chosen for this comparison. The beam bending moment measured at station 37.5, Figure 44.a, is primarily one-per-rev in nature, reaching its maximum value at about 300 degrees azimuth. There is also a good deal of six- and seven-per-rev in the waveform, due to the near-resonance of an out-of-plane-torsion cyclic mode in the vicinity of the operating RPM (Figure 13.a). The steady beam bending moment measured at station 37.5 was 51,000 inch-pounds, and is assumed to be in error, as discussed at the beginning of Section 6.3.

The Station 37.5 beam bending moment waveform resulting from the simulation with the internal induced velocity model (Figure 44.b) achieves its maximum value at about 280 degrees, which is in almost perfect agreement with the measured waveform.



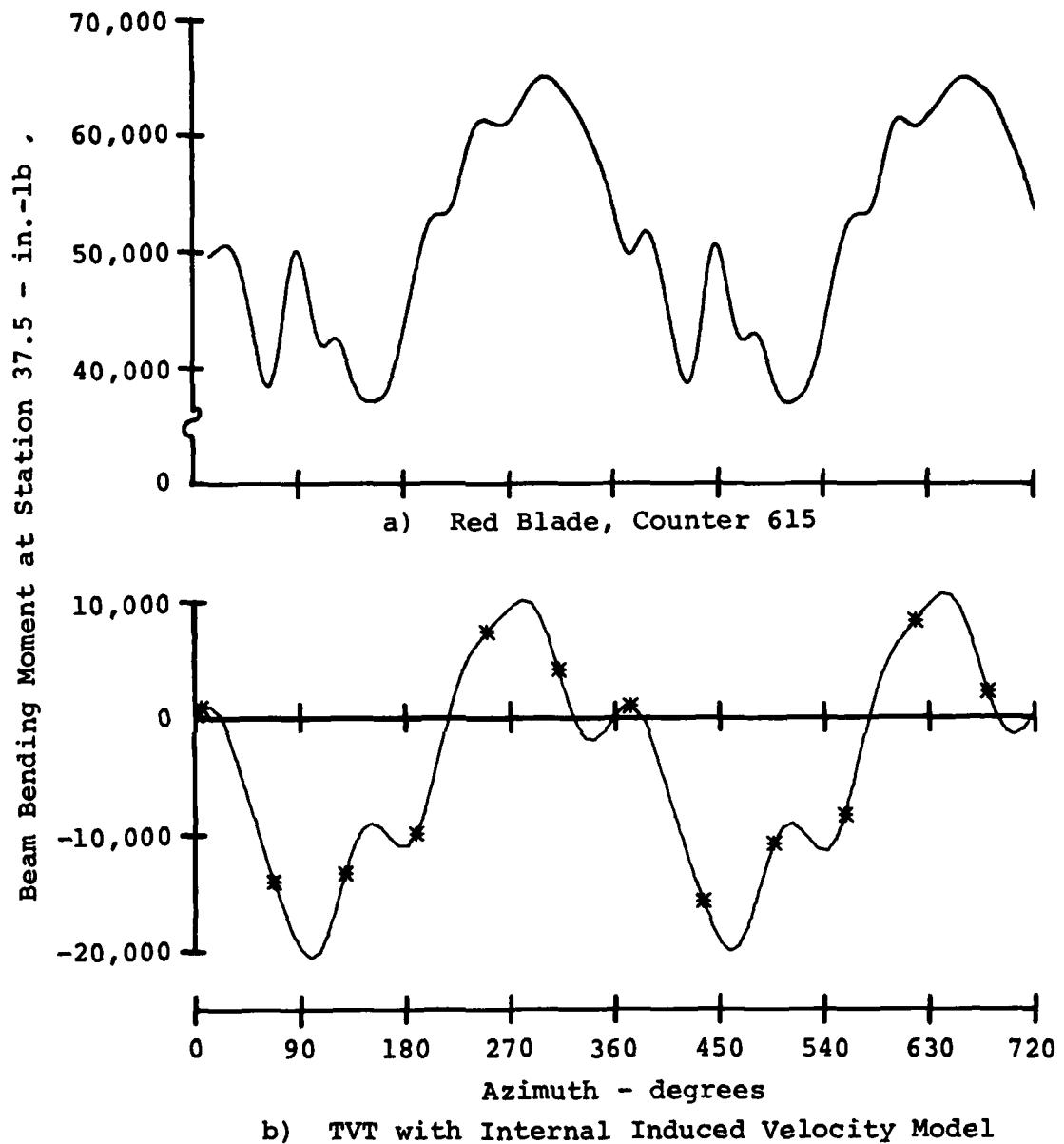
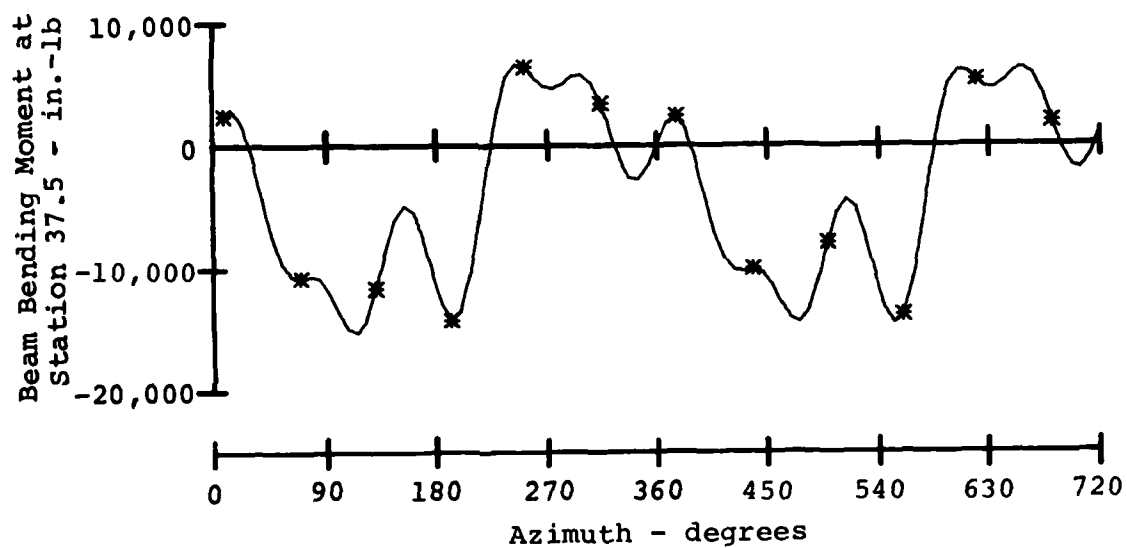


Figure 44. Comparison of Measured and Computed Main Rotor Beam Bending Moment Waveforms at Station 37.5 for Counter 615 (8319 Pounds Gross Weight, Aft CG, Clean Wing, 129 KTAS).



c) TVT with RIVD Table

Figure 44. Concluded.

This computed waveform is essentially one- and three-per-rev in nature.

When the RIVD table is included in the simulation, the maximum positive value of the bending moment in the waveform occurs at an azimuth of 240 degrees, with a secondary peak at about 300 degrees.

Again, the phase characteristics of the computed waveform are in good agreement with the measured data. The waveform computed with the RIVD table also shows some of the higher harmonic content of the measured time history, although the phase relationship of the computed higher harmonic components is different from that of the measured higher harmonic peaks.

#### 6.3.2 Comparison of Measured and Computed Beam Bending Moments for Counter 610

Harmonic amplitudes of measured and computed beam bending moments are presented in Figure 45 for the 142 KTAS level flight test condition of counter 610. The aircraft was in the same configuration as that of counter 615, as discussed in Section 6.3.1.

The data show about the same favorable comparisons. C81 computes a negative steady beam bending moment over the whole rotor, while the test data show positive values further out on the blade than at 129 KTAS.

The oscillatory beam bending moments computed by both simulations are in closer agreement with each other and with the test data than for the 129 KTAS case, although the moment peak at 14.2 percent radius is missed by both simulations. The outboard "hump" is still in evidence in the results from the simulation with the RIVD table.

Again, the largest constituent of the oscillatory bending moment is the one-per-rev component, which is overpredicted by both simulations outboard of 50 percent radius. The measured peak oscillatory load at 14.2 percent radius is primarily one-per-rev in nature, and it is this one-per-rev component that the simulation misses.

The simulations predict the two-per-rev bending moment reasonably accurately in the hub region, and underpredict this component in the blade, as in the 129 KTAS case.

The three-per-rev beam bending moments computed by the simulations do not agree with those measured. The TVT with the RIVD table included computed the three-per-rev component correctly

Main Rotor Beam Bending Moments -  $10^3$  in.-lb

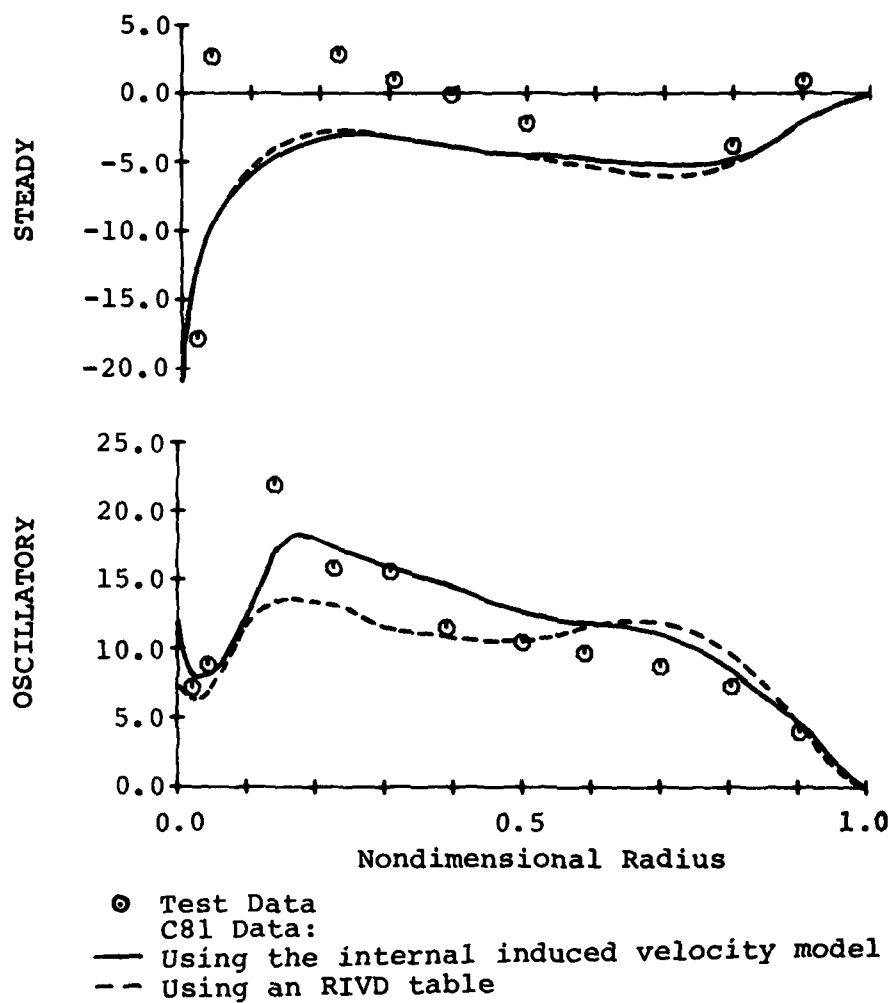


Figure 45. Comparison of Measured and Computed Main Rotor Beam Bending Moments for Counter 610 (8319 Pounds Gross Weight, Aft CG, Clean Wing, 142 KTAS).

Main Rotor Beam Bending Moments -  $10^3$  in.-lb

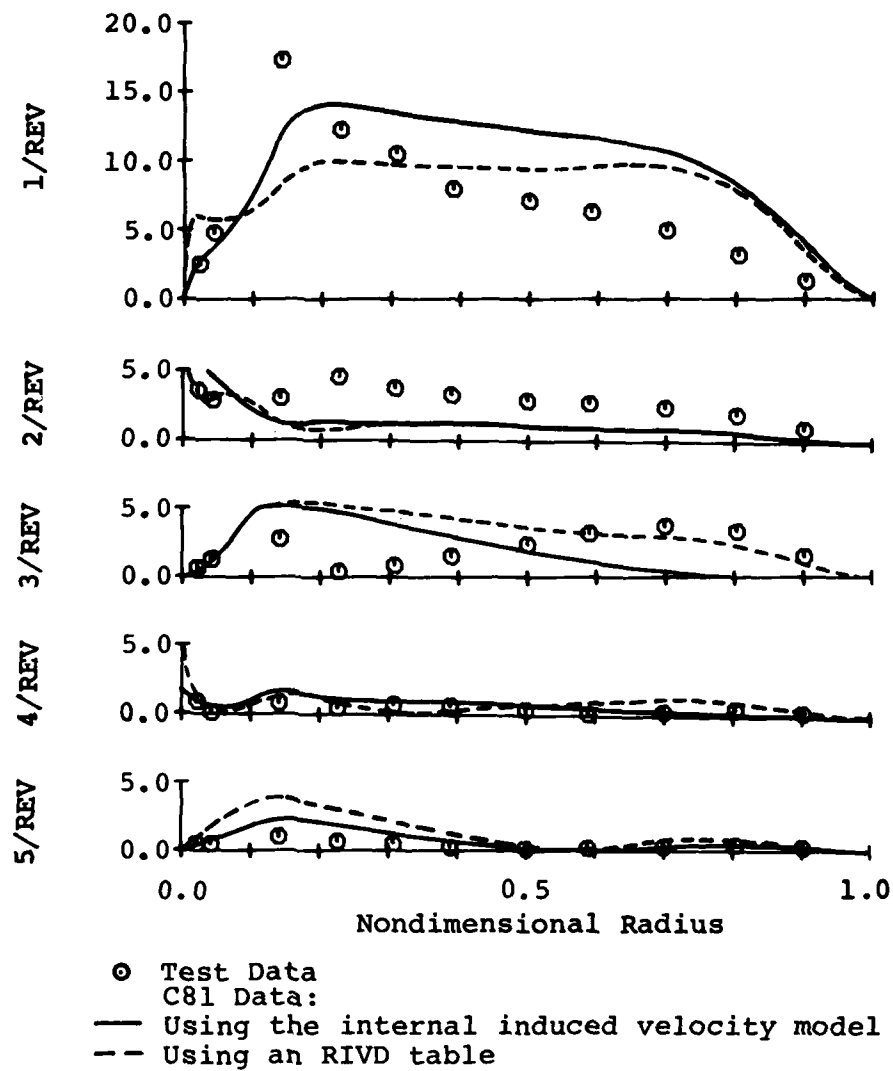


Figure 45. Concluded.

on the outboard section of the blade. These correctly computed three-per-rev data add to the computed one-per-rev bending moments to create the "hump" in the oscillatory distribution.

The four-per-rev beam moments computed at 142 KTAS are in very good agreement with the test data, as are the calculated five-per-rev data outboard of about 40 percent radius. The five-per-rev data computed in the hub region are about double the measured values.

#### 6.3.3 Summary of Beam Bending Moment Comparisons

The computed steady beam bending moments are in fair agreement with those measured in flight. The computed radial distribution does not show the positive values measured in the inboard region of the blade, but the strongly negative value measured in the flexure region, and the negative values measured outboard of midspan, are well represented.

The computed oscillatory beam bending moments are in reasonable agreement with the test data, although the computed oscillatory beam bending moment is larger than that measured on the outer sections of the blade for some cases. This discrepancy is conservative, in that it overstates the stresses in the blade and would lead to an underestimate of the fatigue life. The computed and measured waveforms demonstrate excellent agreement in the phase angle of the one-per-rev component, with reasonable agreement for the higher harmonic components.

In general, the harmonic content of the rotor beam bending moment is not as well computed. The discrepancies between the measured and computed harmonics indicate possible shortcomings in the dynamic analysis, although the incorrect frequency placement for the computed cyclic torsion and "S-ing" modes for this rotor makes it difficult to draw any final conclusions.

#### 6.4 MAIN ROTOR CHORD BENDING MOMENTS

Measured and computed main rotor chordwise bending moments were compared for all nine level flight test conditions, and typical results are discussed in this section. Sign conventions were not reported for the main rotor chord bending moments: the normal BHT convention, tension in the leading edge for positive moments, was assumed.

##### 6.4.1 Comparison of Main Rotor Chord Bending Moments for Counter 615

The AH-1G test vehicle was in its mid gross weight, aft center of gravity, clean wing configuration for counter 615, which

Main Rotor Chord Bending Moments -  $10^3$  in.-lb

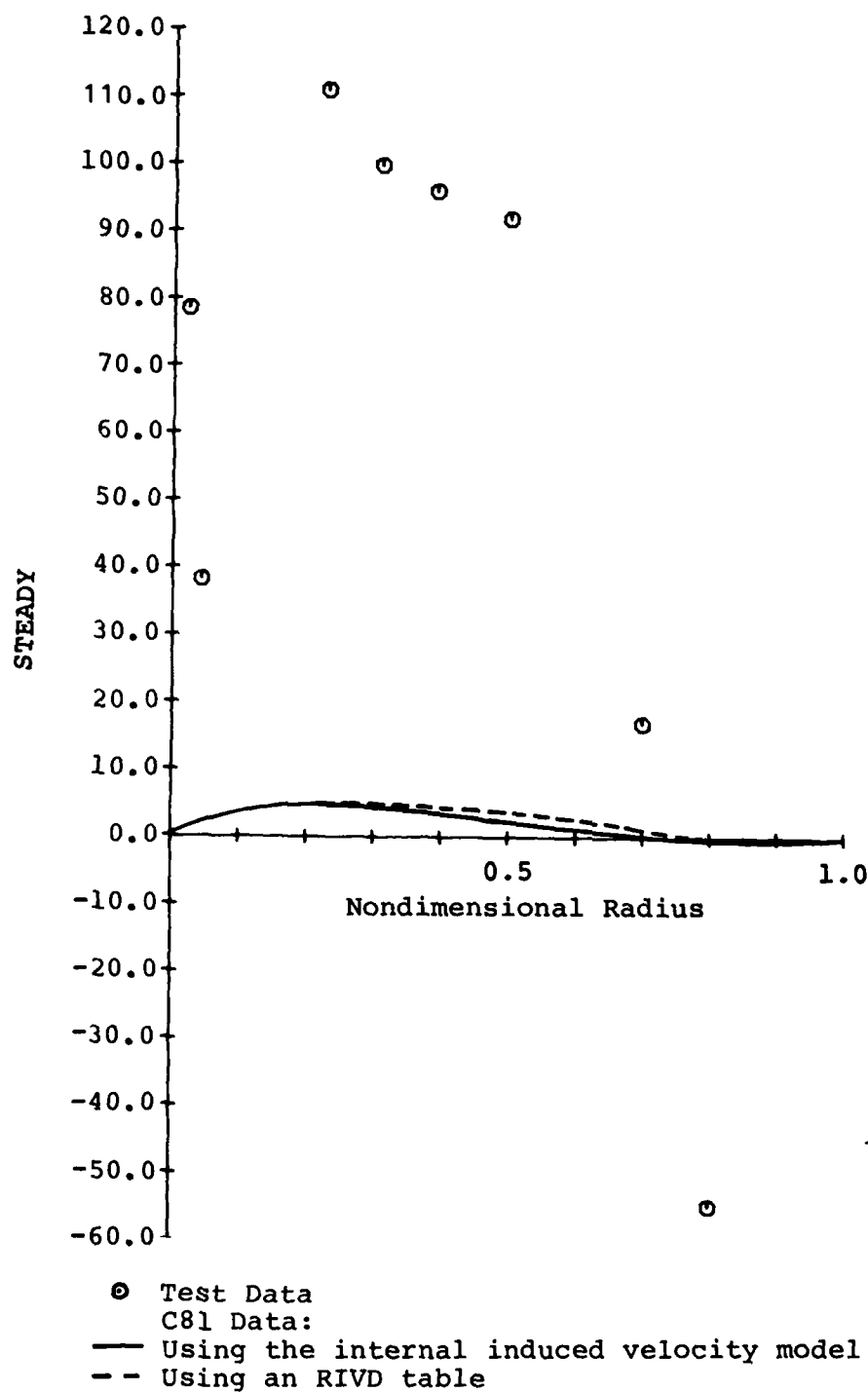


Figure 46. Comparison of Measured and Computed Main Rotor Chord Bending Moments for Counter 615 (8319 Pounds Gross Weight, Aft CG, Clean Wing, 129 KTAS).

Main Rotor Chord Bending Moments -  $10^3$  in.-lb

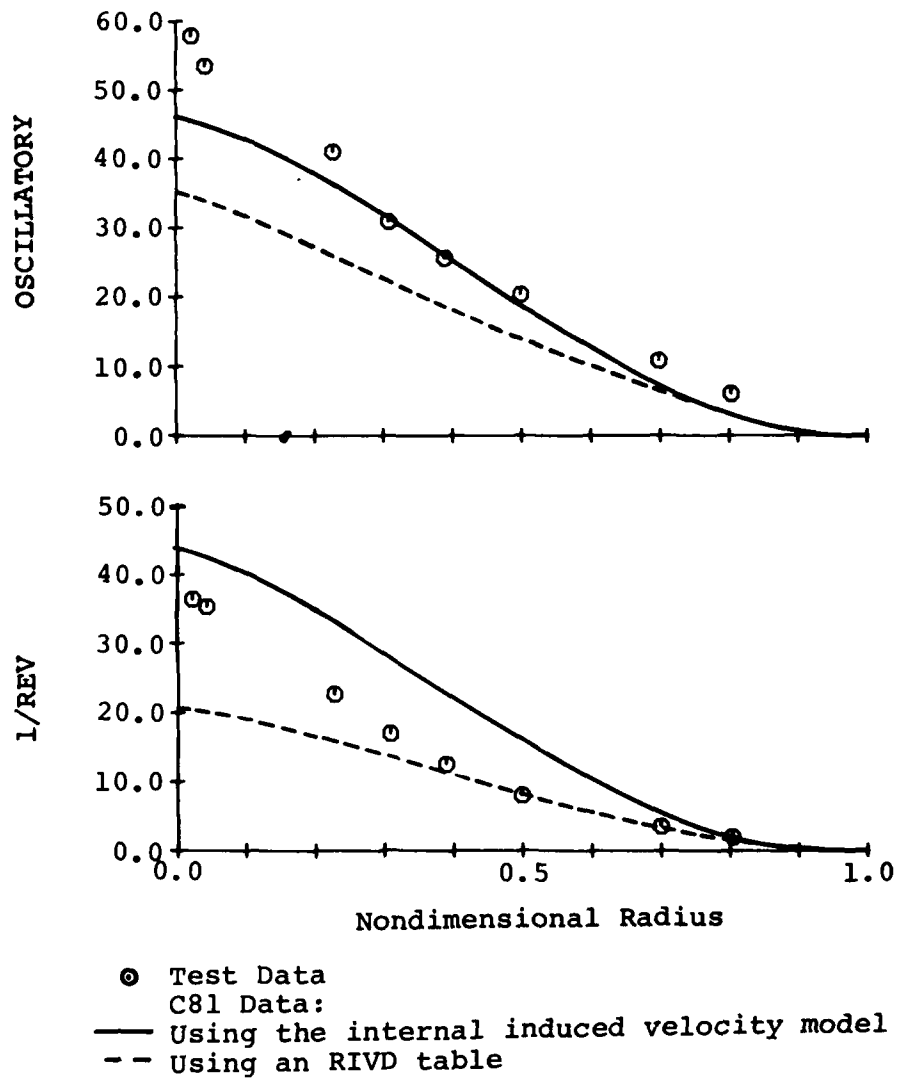


Figure 46. Continued.



Main Rotor Chord Bending Moments -  $10^3$  in.-lb

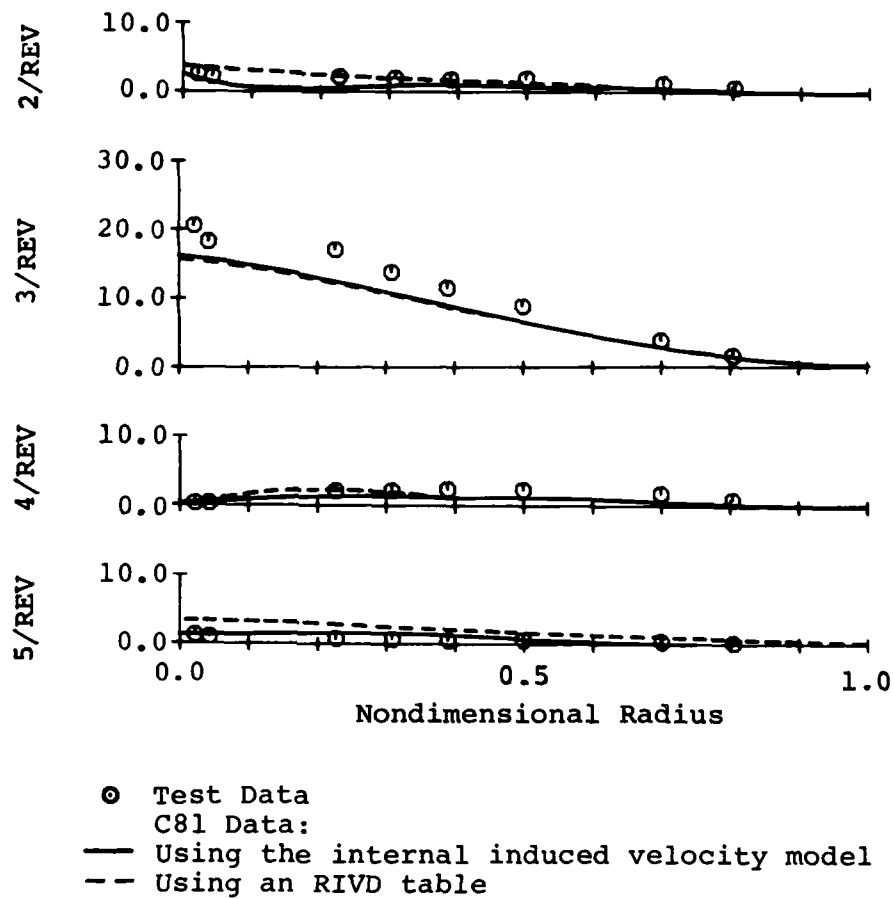


Figure 46. Concluded.

was a level flight condition at 129 KTAS. Measured and computed chord bending moments are compared on a harmonic amplitude basis in Figure 46.

The steady chordwise bending moment computed by both simulations are almost identical, and the calculated values are less than 10 percent of the measured value. The steady root chord bending moment, as computed from the mast torque, should be about 70,000 inch-pounds, but C81 computes a steady root chord bending moment of zero. This difference is due to the inability to model the mast wind-up degree of freedom in the absence of an elastic pylon. The only inplane mode in the rotor elastic representation is the first cyclic inplane mode, which can only respond at odd harmonics. The collective modes, which were generated with a pinned inplane boundary condition, are the source of the minimal steady chord loads computed by the program. The rotor could have been modeled by inputting an appropriate value for TORSO in DNAM05. This would have given an inplane boundary condition for the collective modes that could support a non-zero moment through a spring, resulting in a low-frequency inplane collective mode. Unfortunately, there are no data available to determine the correct value for TORSO.

The oscillatory chord bending moment computed by the TVT with the internal induced velocity distribution is in excellent agreement with the measured data over most of the blade, but is lower than the measured data in the hub region. The oscillatory chord bending moment computed by the TVT with the RIVD table is appreciably lower than the measured data over the whole rotor.

The one-per-rev chordwise bending moment computed by the basic TVT is approximately 10,000 inch-pounds greater than the measured data over the inboard 50 percent of the rotor, while that computed by the TVT with an RIVD table is lower than the measured data inboard and in excellent agreement over the outer 60 percent of the rotor.

The measured two-, four- and five-per-rev chord bending moments are small in comparison with the other components, and the computed data are in close agreement over the whole rotor. The computed two-per-rev chord bending moment should go to zero at the root, since only collective modes, with the pinned-inplane root boundary condition, can respond at this frequency. The source of the non-zero two-per-rev root chord bending moment is due to numerical noise in the participation factor for the inplane (second cyclic) mode which causes the two-per-rev component to be different from zero at the root.

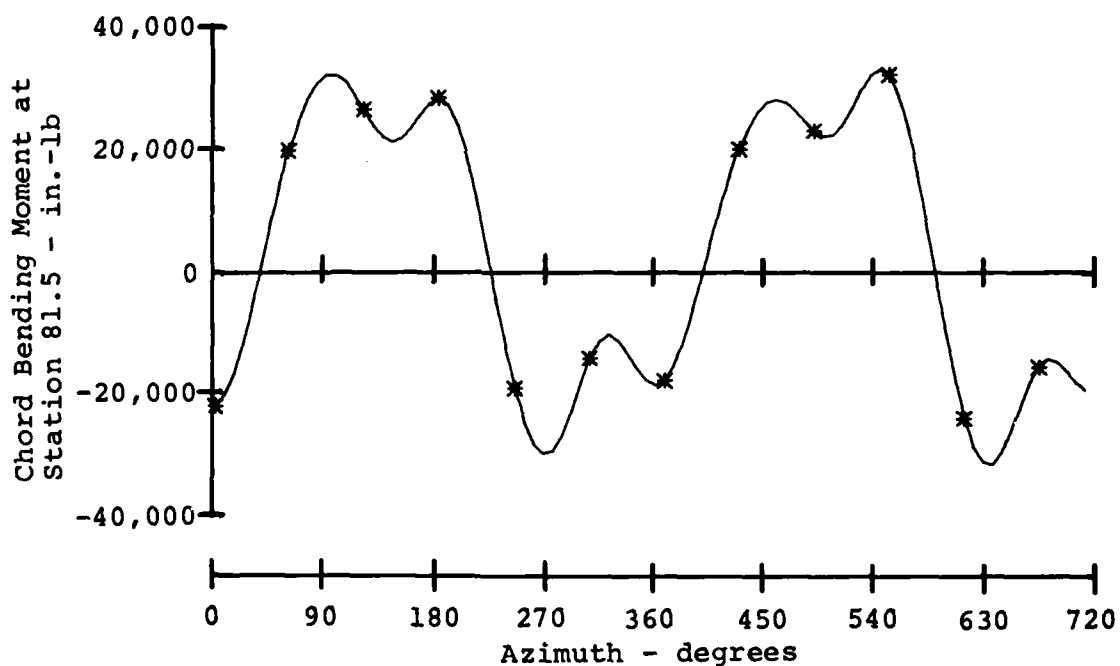
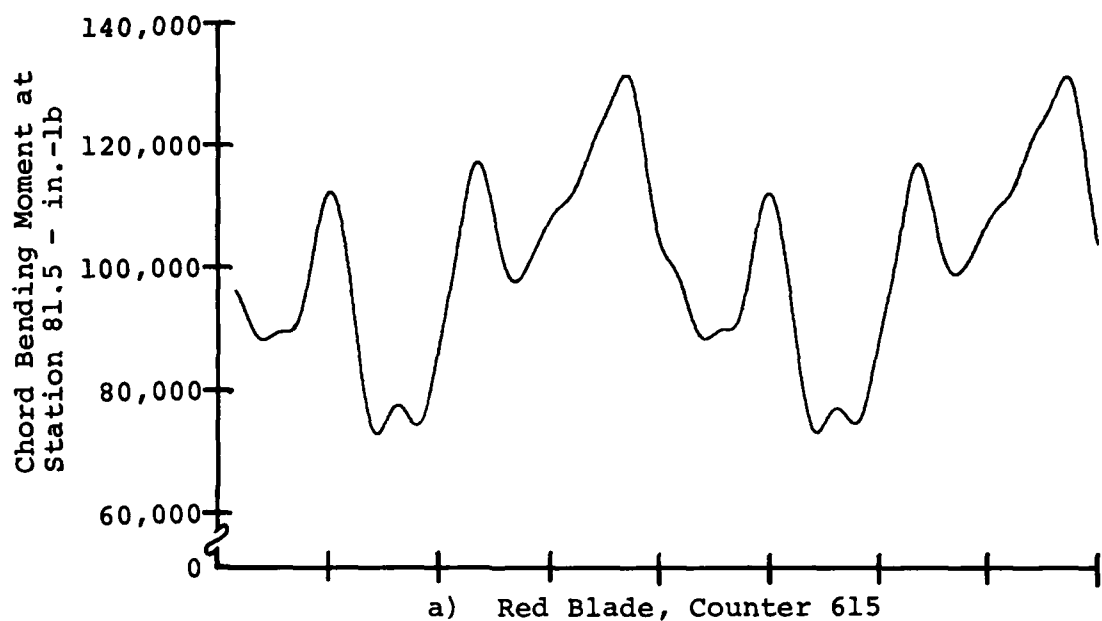
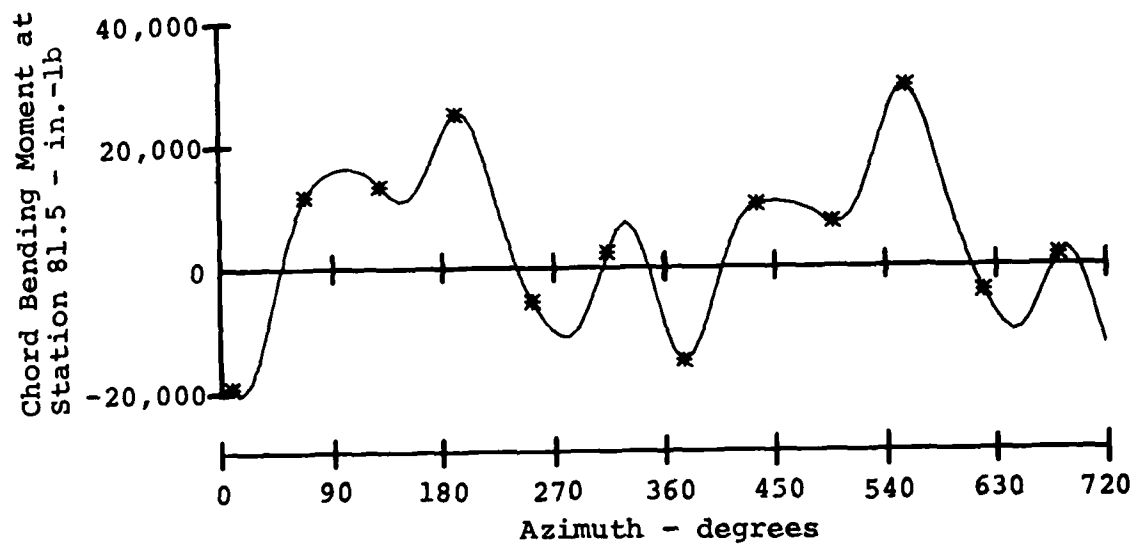


Figure 47. Comparison of Measured and Computed Main Rotor Chord Bending Moment Waveforms at Station 81.5 for Counter 615 (8319 Pounds Gross Weight, Aft CG, Clean Wing, 129 KTAS).



c) TVT with RIVD Table

Figure 47. Concluded.

The three-per-rev chord bending moment computed by the two simulations are almost identical, and in reasonable agreement with the measured data.

Time histories of the chord bending moment at blade radial station 81.5 are compared in Figure 47 for the 129 KTAS level flight condition of counter 615. The time history measured in flight (Figure 47a) reaches its minimum value at an azimuth of about 120 degrees and its maximum at about 330 degrees, with a good deal of higher harmonic content.

The waveform resulting from the simulation with the internal induced velocity distribution, Figure 47b, has maximum peaks at about 100 degrees and 190 degrees, with a minimum value at 270 degrees. This constitutes a phase lead (C81-computed relative to the measured data) of approximately 180 degrees. The waveform generated when the RIVD table is included has a maximum peak at about 210 degrees azimuth, demonstrating a phase lead (relative to the test data) of about 120 degrees.

#### 6.4.2 Comparison of Main Rotor Chord Bending Moments for Counter 610

Measured and computed chordwise bending moment harmonic amplitudes are compared for the 142-KTAS flight condition of counter 610 in Figure 48. The aircraft was in the clean wing configuration at a mid gross weight and aft center of gravity.

The steady chord bending moment data are not presented for this case, as the results are quite similar to those shown for the 129-KTAS case (Figure 46) due to the inability to properly model the inplane hub boundary condition.

The oscillatory chord bending moment computed using either induced velocity model is approximately 60 percent of the measured value over the majority of the rotor. Examination of the plot of the one-per-rev harmonic shows that the values computed with the internal induced velocity distribution are in excellent agreement with the measured data, while the values computed when the RIVD table was used are approximately one-half the measured values. The computed three-per-rev components are about two-thirds the measured values, while the two-, four-, and five-per-rev components computed by the program are in quite good agreement with the test data.

#### 6.4.3 Comparison of Main Rotor Chord Bending Moments for Counter 635

Oscillatory and one-per-rev chord bending moment amplitudes are plotted versus nondimensional radius in Figure 49 for Flight 36A, Counter 635. The aircraft was flying straight and level

Main Rotor Chord Bending Moments -  $10^3$  in.-lb

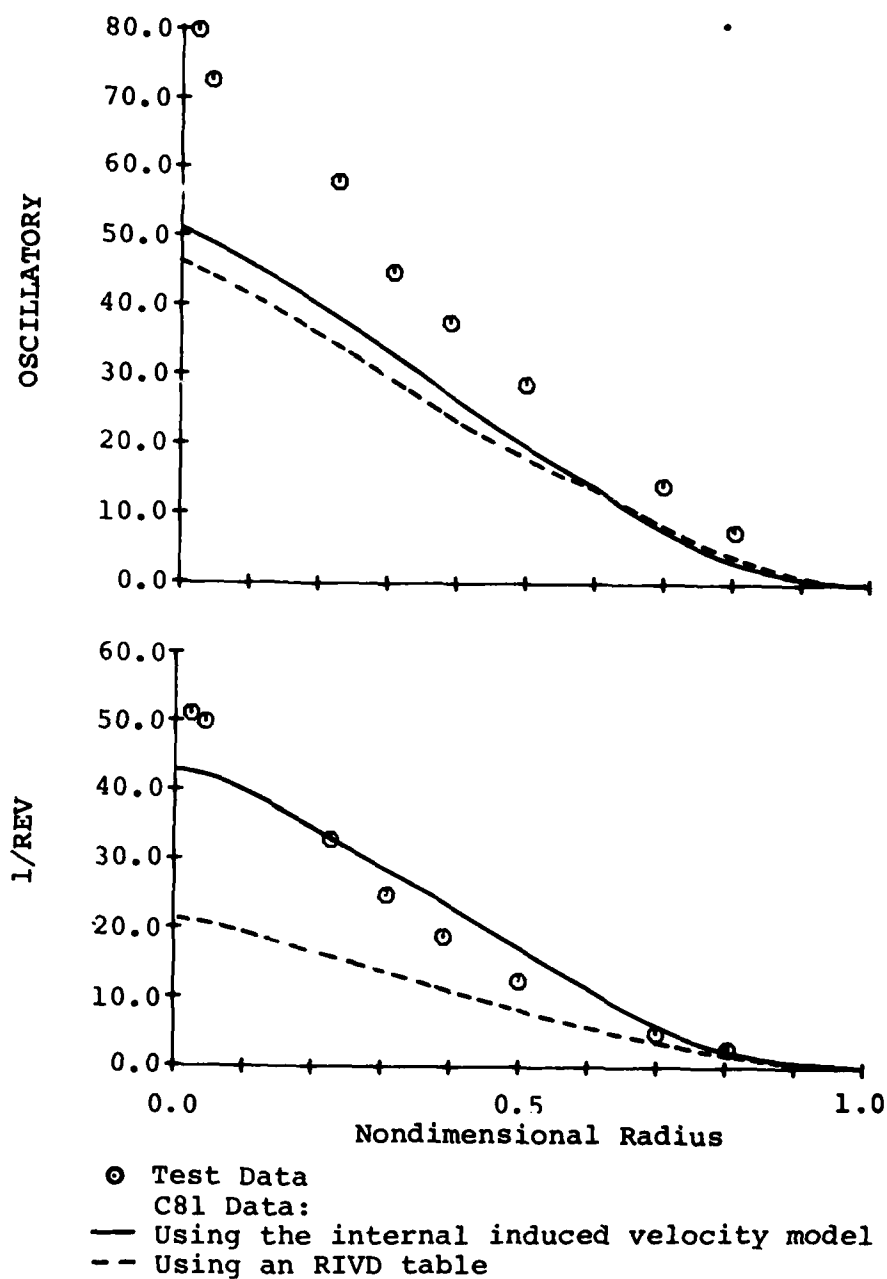


Figure 48. Comparison of Measured and Computed Main Rotor Chord Bending Moments for Counter 610 (8319 Pounds Gross Weight, Aft CG, Clean Wing, 142 KTAS).

Main Rotor Chord Bending Moments -  $10^3$  in.-lb

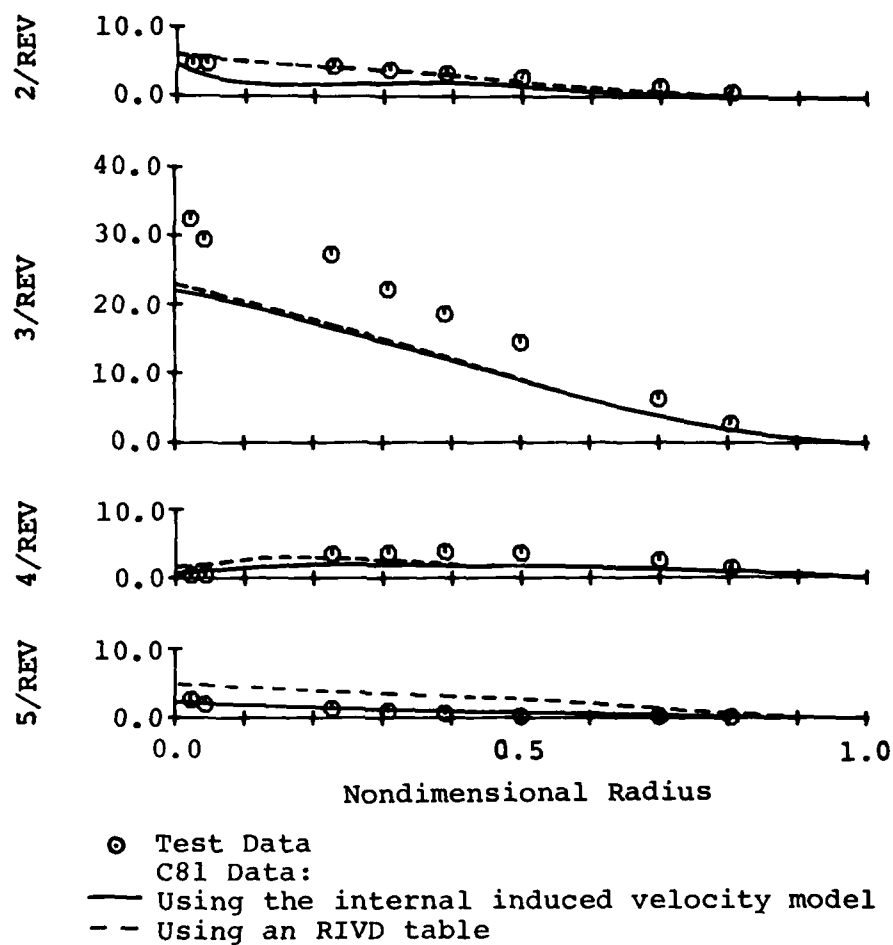


Figure 48. Concluded.

Main Rotor Chord Bending Moments -  $10^3$  in.-lb

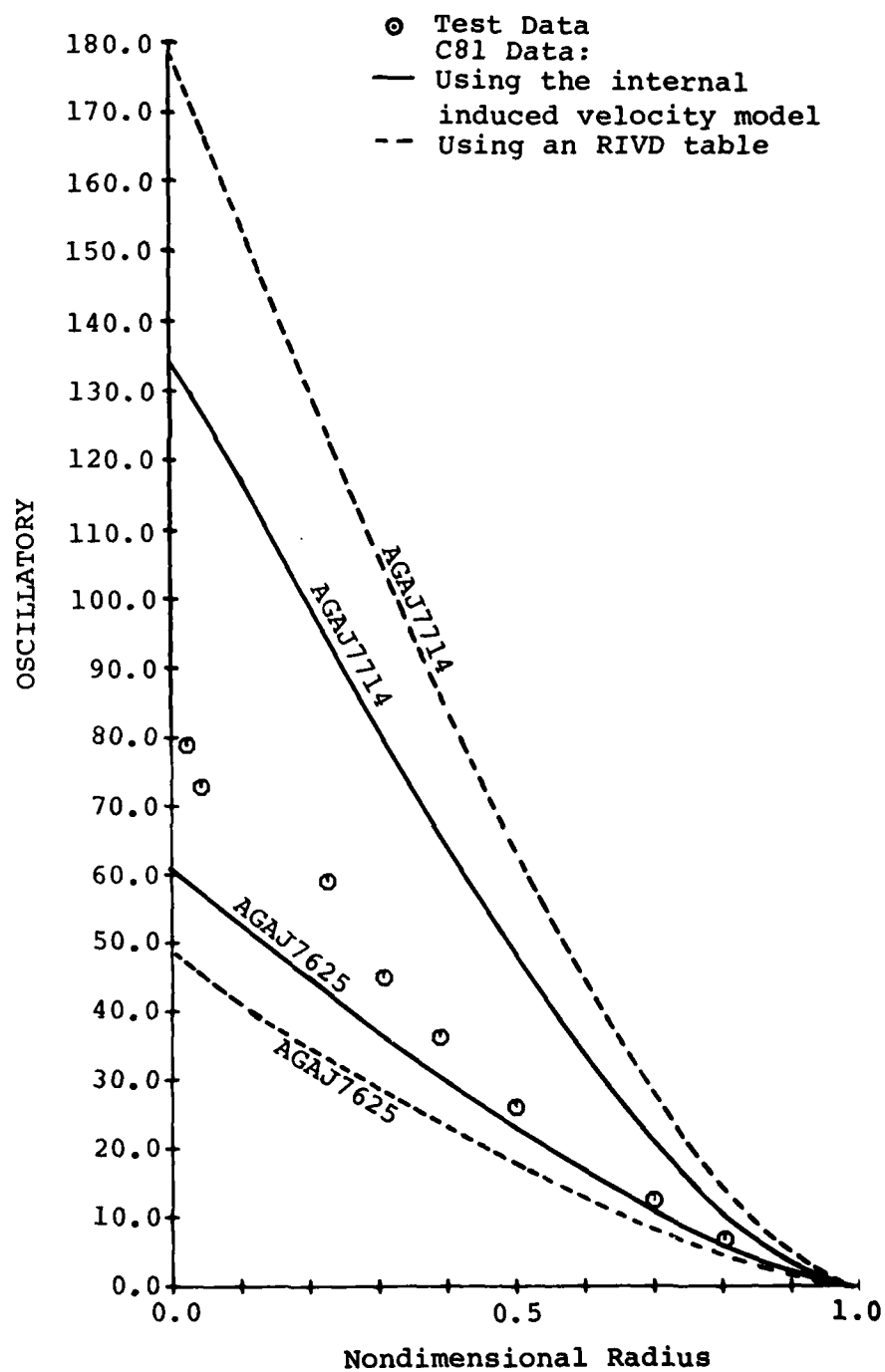


Figure 49. Comparison of Measured and Computed Main Rotor Chord Bending Moments for Counter 635 (9069 Pounds Gross Weight, Mid CG, Hog Configuration, 136 KTAS).



Main Rotor Chord Bending Moments -  $10^3$  in.-lb

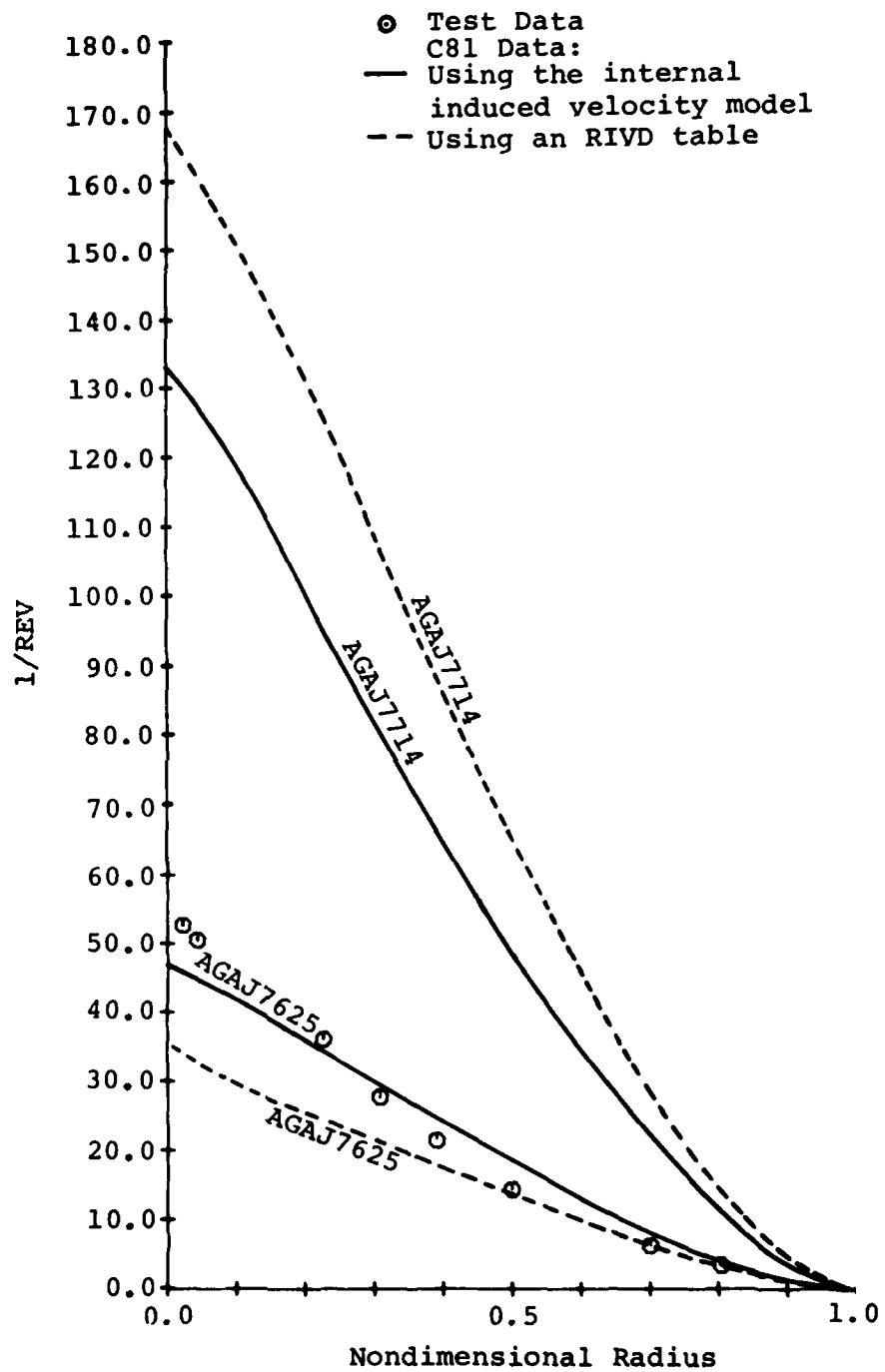


Figure 49. Concluded

at 136 KTAS, which is  $V_H$  for this 9069 pound, mid-center-of-gravity, heavy-hog configuration. The chordwise bending moments computed by AGAJ7714 are well in excess of the measured data. The chord moments computed by the previous edition of C81 (AGAJ7625) are included in the figure for comparison. The major difference between the two analyses is that the axis of constant rotor rotational speed is assumed to be collinear with the rotor shaft in AGAJ7625, while the analysis incorporated in AGAJ7714 assumes that the constant-speed axis is perpendicular to the plane defined by the hub flapping angles. The main rotor flapping angles computed for this flight condition are larger than those calculated for the simulation of the level flight cases of Flight 35A. The AGAJ7714 simulation of Flight 35A predicted chord bending moments in much better agreement with the test data (see Figures 46 and 48). It is suspected that the differences between the AGAJ7714-computed chord bending moments and those measured in flight are due to discrepancies in the inertia loads, but the precise source of the problem has not yet been identified.

#### 6.4.4 Summary of Chord Bending Moment Comparisons

Program C81 computes chordwise bending moments in fair agreement with the test data when the internal induced velocity distribution is used. The steady component is incorrectly predicted, but this can be directly traced to a lack of appropriate input data for DNAM05. The computed chord bending moment waveform is shifted in phase with respect to the test data.

#### 6.5 MAIN ROTOR TORSIONAL BENDING MOMENTS

Comparisons were made between the measured and computed main rotor torsional bending moments for the level flight conditions simulated, with typical results presented in this section. The sign convention for these data items was not documented; the normal sign convention at BHT is positive for a nose-up moment.

##### 6.5.1 Comparison of Main Rotor Torsional Bending Moments for Counter 615

The measured and computed torsional bending moment harmonic amplitudes are compared in Figure 50 for the medium gross weight, middle center-of-gravity, clean wing configuration of counter 615. This is a 129-KTAS level flight case.

The computed steady torsional bending moment distribution is almost identical for the simulations with either induced velocity model, and does not agree with the distribution measured in flight. Comparison cases were run in AGAJ7625

Main Rotor Torsional Bending Moments -  $10^3$  in.-lb

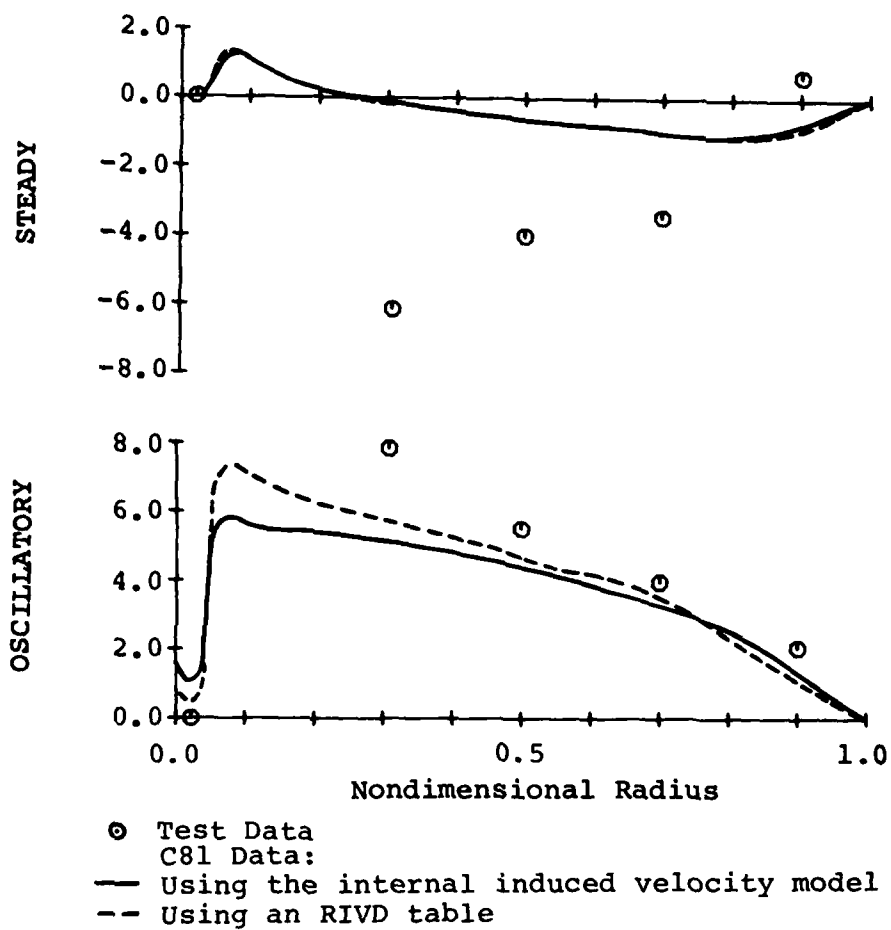


Figure 50. Comparison of Measured and Computed Main Rotor Torsional Bending Moments for Counter 615 (8319 Pounds Gross Weight, Aft CG, Clean Wing, 129 KTAS).

Main Rotor Torsional Bending Moments -  $10^3$  in.-lb

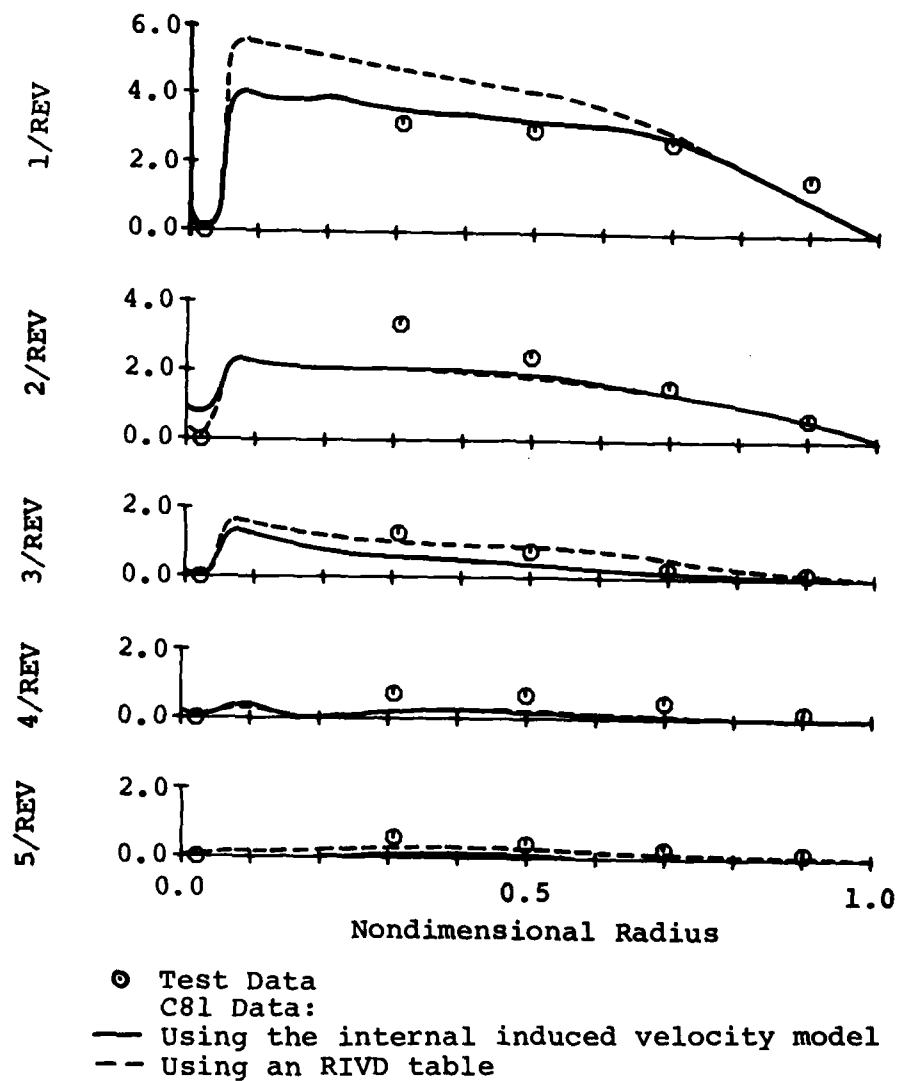


Figure 50. Concluded.

as part of the effort to locate the cause of the difference between the AGAJ7714-computed steady torsional moment and the test data. Typical results are presented in Figure 51, where it can be seen that the older version of the program computes a steady torsional moment distribution in good agreement with the experimental data. The salient difference between the -7625 and -7714 computed torsional loadings is in the inertia load calculations. AGAJ7625 accounts for the torsional acceleration ( $I_{\theta}\ddot{\theta}$ ) and tennis racquet terms explicitly in two lines of FORTRAN, while the appropriate terms of the  $Q_y$  equation (Equation A-65, pages 362 through 364 of Volume I of Reference 3) are coded in seven lines of FORTRAN in AGAJ7714. The source of the difference in solutions between the two programs has not been found.

The oscillatory torsional moment distributions computed with either induced velocity model are similar to those measured in flight, with good agreement over the outer portion of the rotor, and lower values calculated inboard. The data from the TVT with the RIVD table are in better agreement with the test data over the inboard portion of the rotor than the data calculated without the RIVD table.

The one-per-rev torsional moment distribution computed by the basic TVT is in almost perfect agreement with the test data. The distribution resulting from the TVT with the RIVD table predicts torsional moments greater than those recorded on the inboard section of the rotor.

The two-per-rev torsional moment distributions computed in both simulations are almost identical, and agreement with the test data is good over the outer sections of the blade. The predicted two-per-rev component is lower than that measured on the inboard portion of the rotor.

The three-per-rev torsional moment distribution computed by the TVT using the internal induced velocity model is similar to that measured, but is smaller in amplitude. The distribution computed by the TVT using the RIVD table is in excellent agreement with the test data.

The four- and five-per-rev distributions computed with either induced velocity model are similar to each other, and the values computed are smaller than those measured in flight.

Time histories of the measured and computed torsional bending moment at radial station 81.5 are compared in Figure 52 for the 129-KTAS level flight condition of counter 615. As can be seen, the overall phase of the calculated time-histories is shifted compared to that of the measured waveform, and the

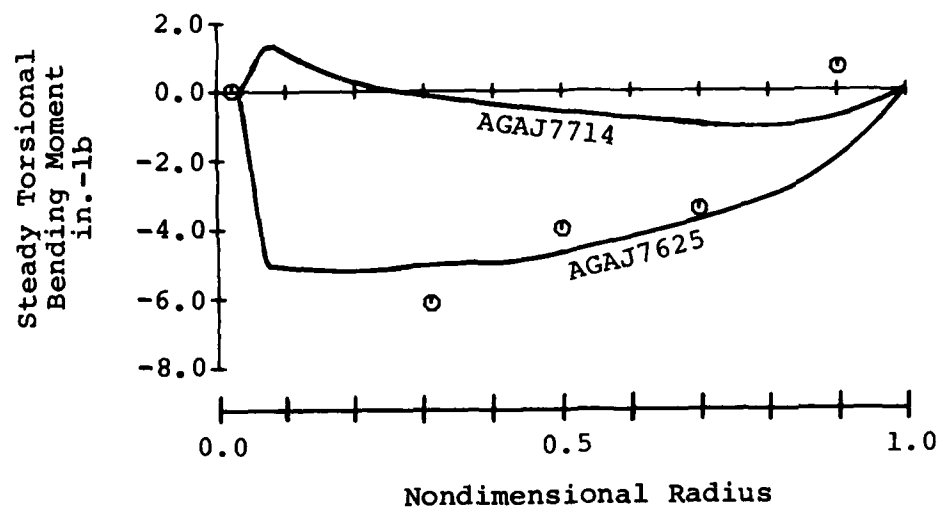


Figure 51. Comparison of Measured Steady Torsional Bending Moment Radial Distribution with Distributions Computed by the AGAJ7714 and AGAJ7625 Versions of C81 for Counter 615 (8319 Pounds Gross Weight, Aft CG, Clean Wing, 129 KTAS).

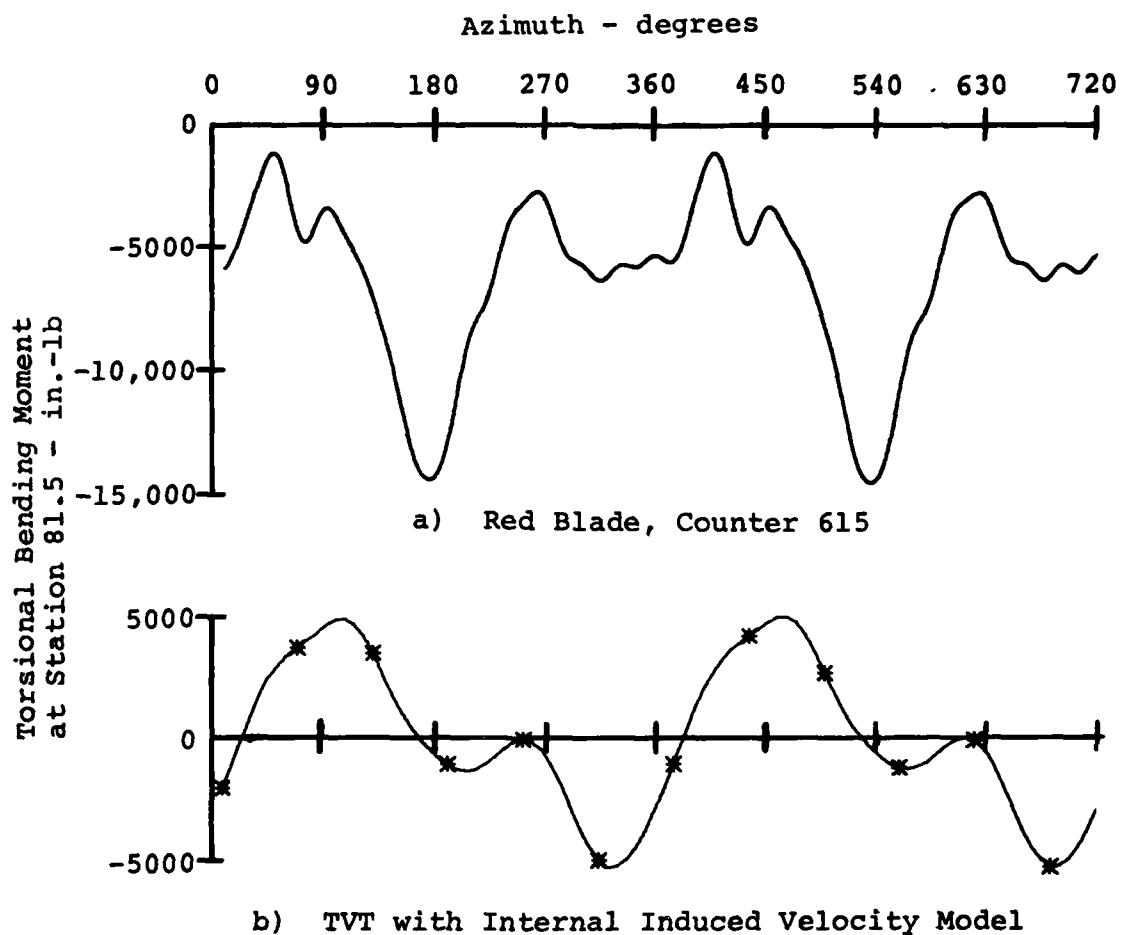
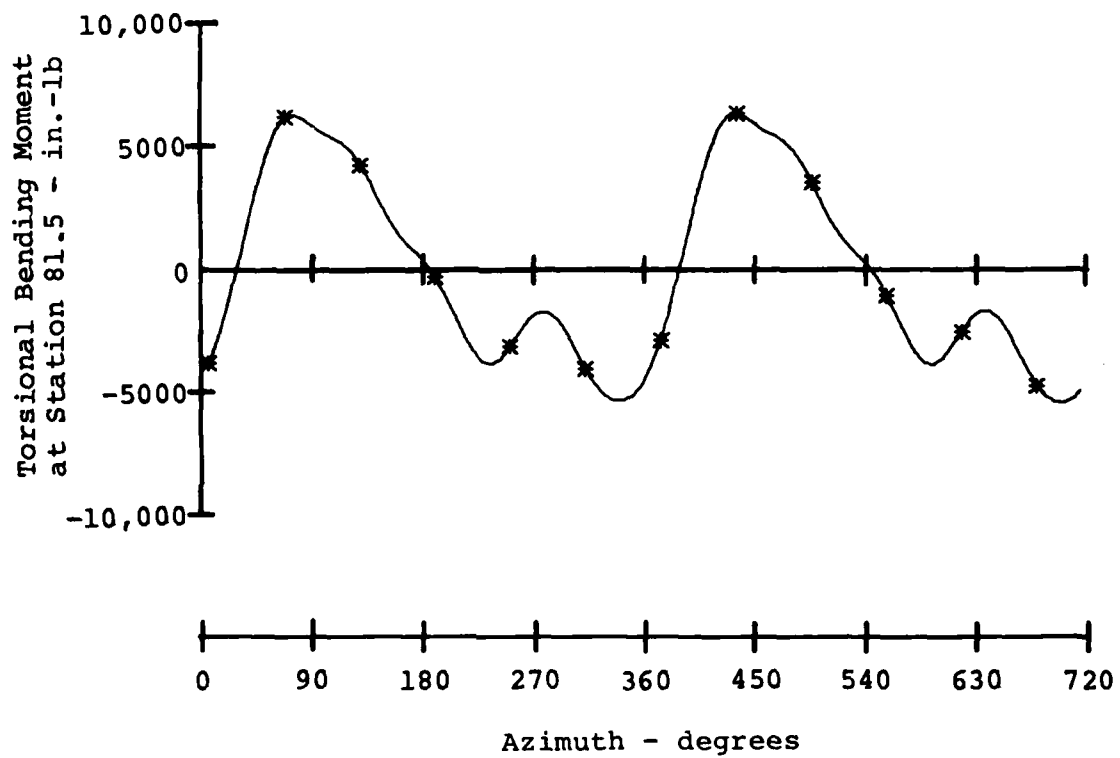


Figure 52. Comparison of Measured and Computed Main Rotor Torsional Bending Moment Waveforms at Station 81.5 for Counter 615 (8319 Pounds Gross Weight, Aft CG, Clean Wing, 129 KTAS).



c) TVT with RIVD Table

Figure 52. Concluded.



relative phase angles of the individual harmonics within the computed time-histories appear to be different from those of the measured data.

The waveform resulting from the TVT using the internal induced velocity model has a maximum peak at about 100 degrees azimuth and a minimum peak at about 315 degrees azimuth. When the RIVD table is used to model the induced velocity, the maximum value of the torsional moment occurs at about 75 degrees azimuth and the minimum value is observed at about 330 degrees azimuth. The waveform measured in flight has its maximum value at about 50 degrees azimuth and its minimum value occurs at about 170 degrees azimuth.

#### 6.5.2 Comparison of Main Rotor Torsional Bending Moments for Counter 610

Measured and computed torsional bending moment harmonic amplitudes are compared in Figure 53 for the 142 KTAS level flight test condition of counter 610 (medium gross weight, middle center-of-gravity, clean-wing configuration).

As for the 129-KTAS case (Figure 50), the simulation using either induced velocity model computes a steady torsional bending moment at variance with that measured in flight.

The oscillatory torsional bending moment distribution computed by the TVT using the internal induced velocity model shows lower values for all radial stations than those measured. The distribution computed when the RIVD table was utilized is in much better agreement with the test data.

The radial distribution of the one-per-rev torsional bending moment computed by the TVT without the RIVD table is in very good agreement with the measured data; that computed when the RIVD table is utilized over-predicts the values over most of the rotor.

The simulation with the internal induced velocity model also predicts lower two-per-rev torsional moments than those calculated with the RIVD, but the latter prediction is in much closer agreement with the measured data.

The three-per-rev moment distribution computed by the simulation using the RIVD table is in almost perfect agreement with the experimental distribution, while the values calculated using the internal induced velocity model are lower than those measured in flight.

The four- and five-per-rev torsional moment distributions computed by the program are in favorable agreement with the test data.

Main Rotor Torsional Bending Moments -  $10^3$  in.-lb

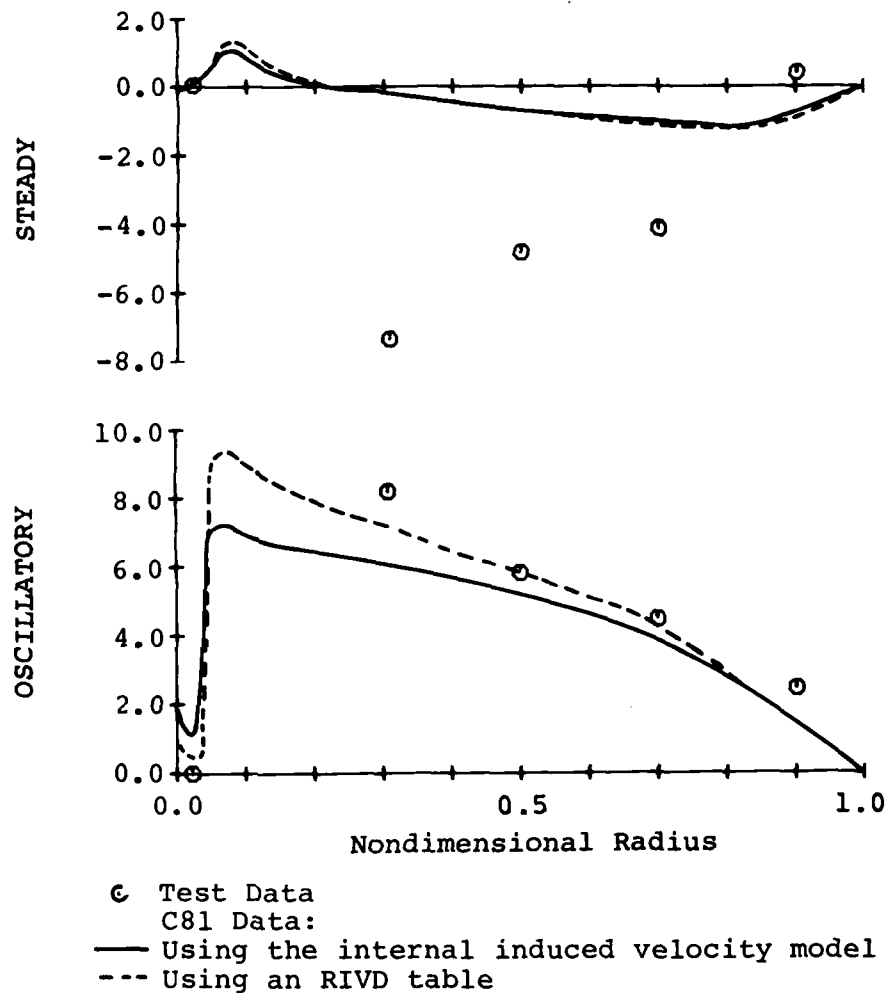


Figure 53. Comparison of Measured and Computed Main Rotor Torsional Bending Moments for Counter 610 (8319 Pounds Gross Weight, Aft CG, Clean Wing, 142 KTAS).

Main Rotor Torsional Bending Moments -  $10^3$  in.-lb

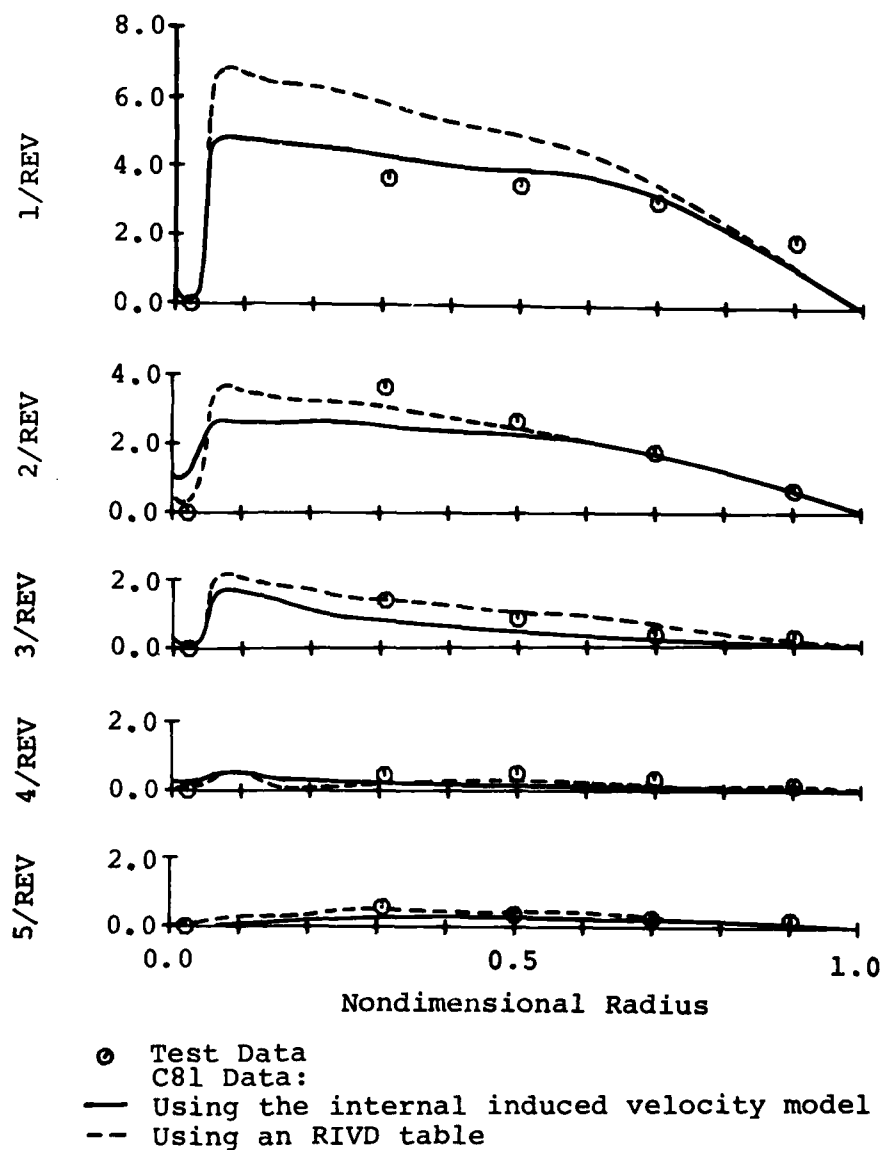


Figure 53. Concluded.

### 6.5.3 Summary of Torsional Bending Moment Comparisons

The AGAJ7714 version of C81 predicts torsional bending moments in good agreement with test data. The program is unable to compute the steady torsional moment for reasons that remain unknown and the waveforms computed by C81 have a phase shift with respect to the test data.

### 6.6 MAIN ROTOR BEAM ACCELERATIONS

Measured and computed beamwise accelerations were compared for all the level flight conditions simulated. Results of those comparisons for two of the test points are discussed in this section. The sign convention for the beamwise accelerometers was not documented in the project reports, but the instrumentation engineer's notes indicate that upward acceleration (in the beam-chord coordinate system) results in positive output from the accelerometer. The beamwise accelerometers were installed on the upper surface of the blade on the pitch-change axis to minimize the contribution of torsional accelerations.

#### 6.6.1 Comparison of Main Rotor Beamwise Accelerations for Counter 611

The radial distributions of the harmonic amplitudes of the main rotor beamwise acceleration, as measured in flight and computed by C81, are plotted in Figure 54 for counter 611. This is a straight and level flight condition at 66 KTAS, at medium gross weight, aft center of gravity in the clean wing configuration. The C81-computed accelerations are calculated by the program after the blade response has been determined, and are computed for output purposes only.

The steady accelerations computed by C81 do not agree with those measured in flight. The C81-generated distribution can be justified by a simple analysis of the source of the largest component of steady beamwise acceleration. Should the blade have an out-of-plane slope with respect to the hub plane (which is perpendicular to the axis of constant rotational speed), then a portion of the centripetal acceleration will be sensed in the local out-of-plane direction.

This acceleration is

$$a_{OP_c} = \Omega^2 r \sin\beta \quad (17)$$

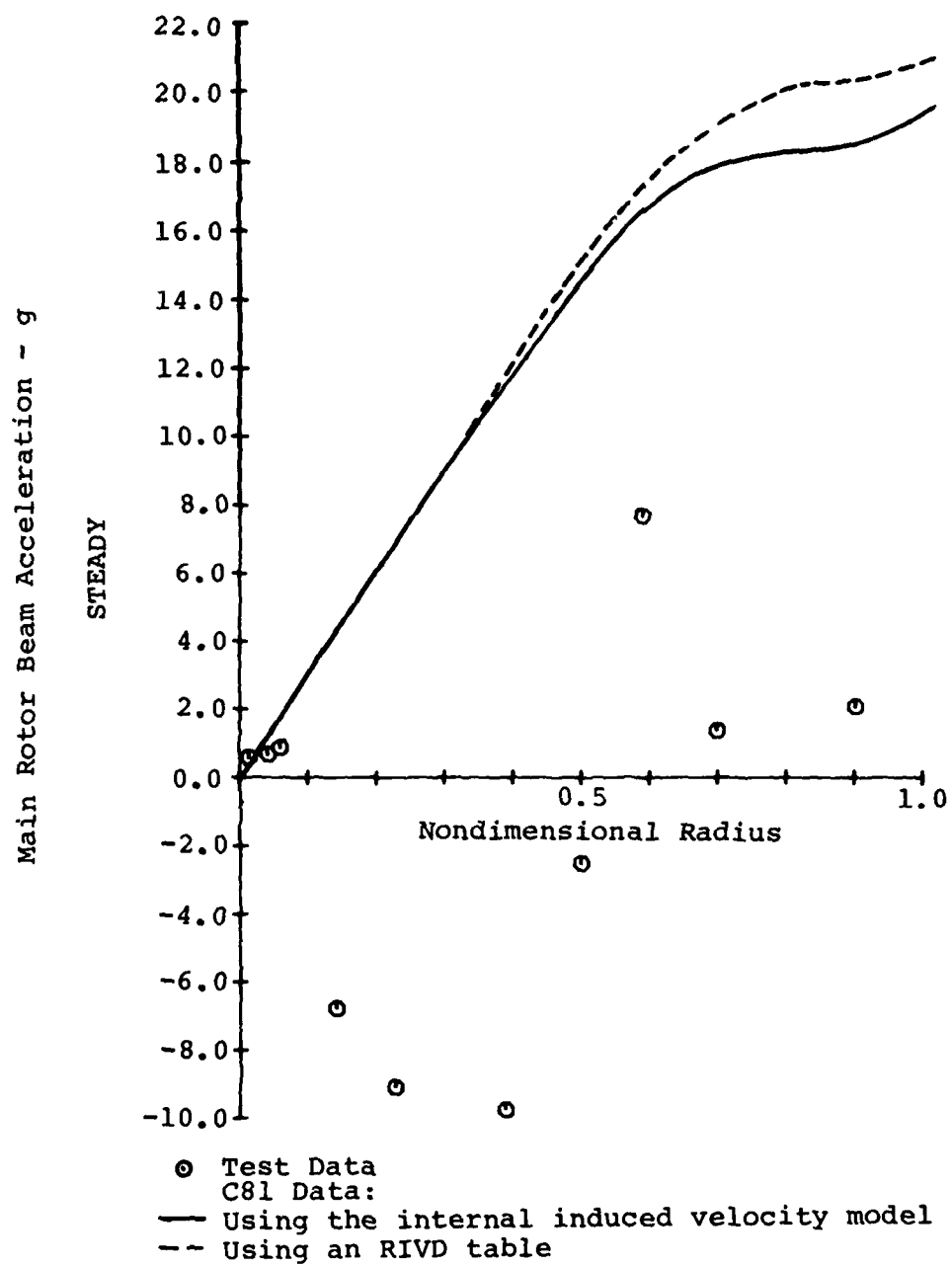


Figure 54. Comparison of Measured and Computed Main Rotor Beamwise Accelerations for Counter 611 (8319 Pounds Gross Weight, Aft CG, Clean Wing, 66 KTAS).

Main Rotor Beam Acceleration - g

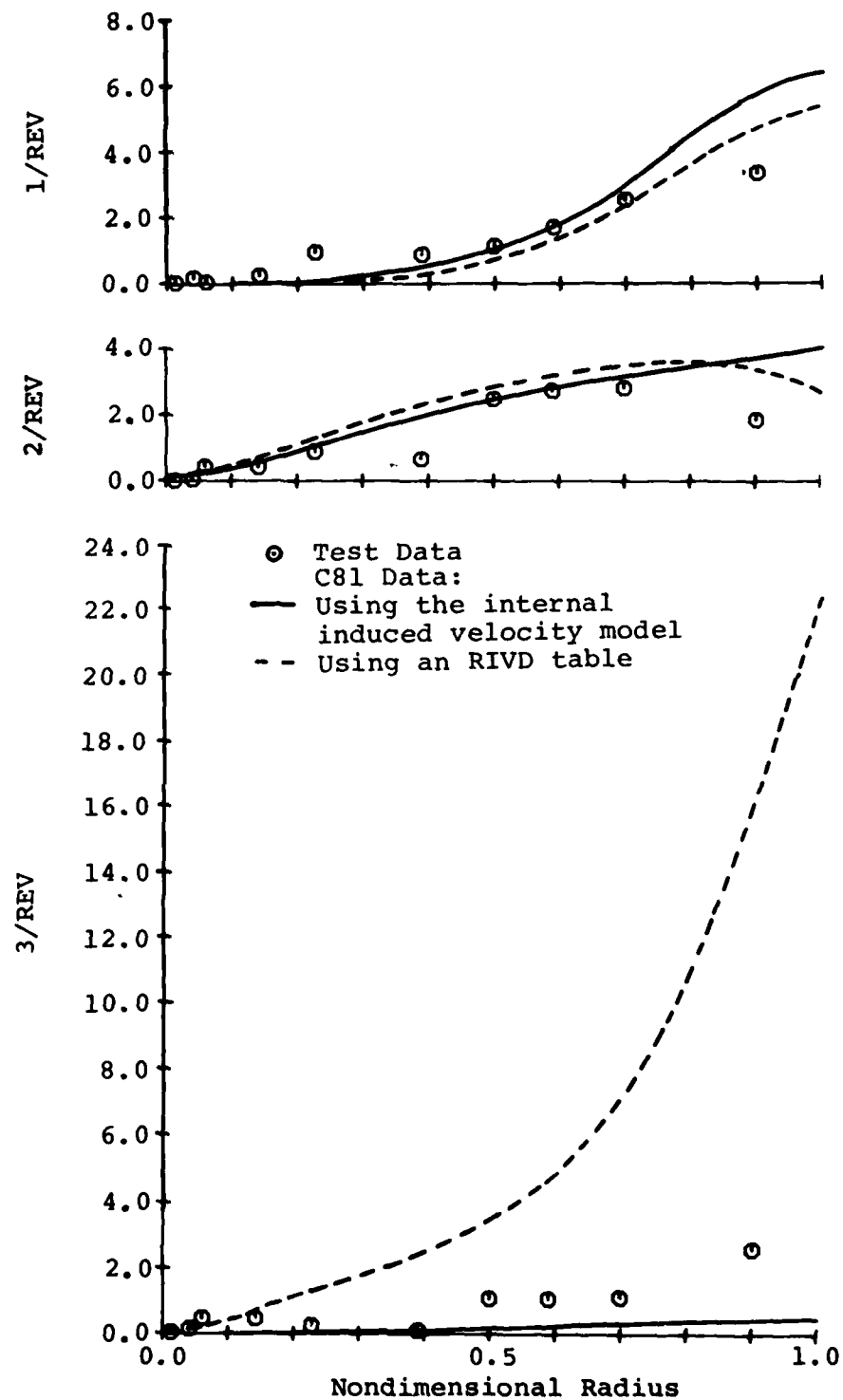
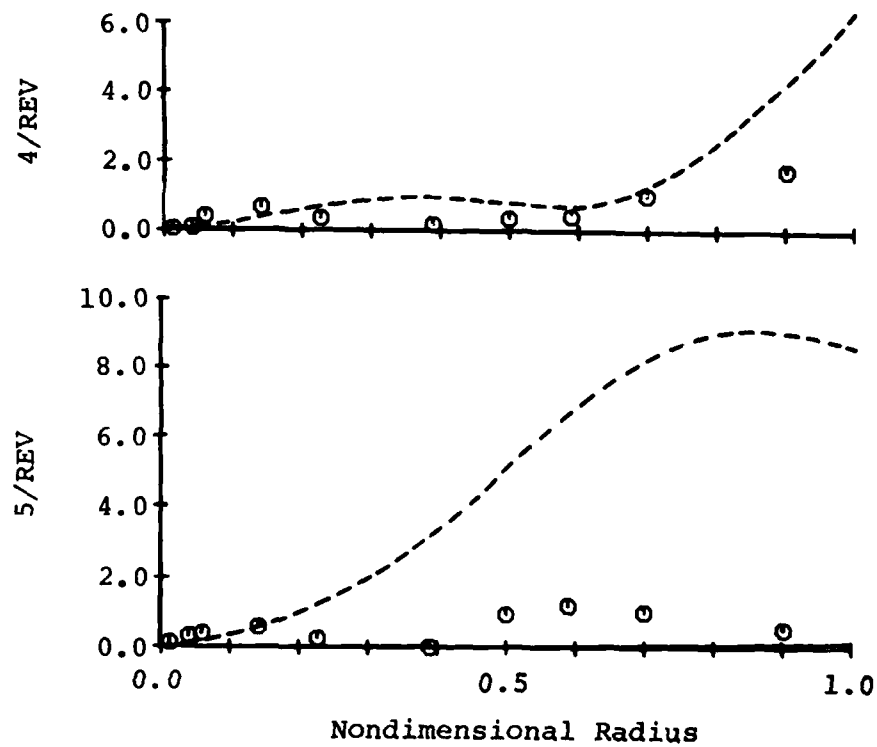


Figure 54. Continued.

Main Rotor Beam Acceleration - g



- Test Data
- C81 Data:
- Using the internal induced velocity model
- Using an RIVD table

Figure 54. Concluded.

in which

$a_{OP_C}$  is the out-of-plane acceleration due to centripetal acceleration, positive up

$\Omega$  is the rotational rate

$r$  is the radius to the sensor location

$\beta$  is the out-of-plane slope at the radius  $r$ , relative to the hub plane, positive up

When transformed into the beam-chord coordinate system, the contribution of this term to the beamwise acceleration is

$$a_{B_C} = a_{OP_C} \cos\theta = a_{OP_C} \sin\beta \cos\theta \quad (18)$$

where

$a_{B_C}$  is the local beamwise acceleration, due to centripetal acceleration, positive up

$\theta$  is the local geometric pitch angle, positive nose up

The local coning angle and geometric pitch angles can be expressed as the sum of a steady and unsteady part,

$$\beta = \beta_s + \beta_u \quad (19.a)$$

$$\theta = \theta_s + \theta_u \quad (19.b)$$

where

$\beta_s, \theta_s$  are the steady components

$\beta_u, \theta_u$  are the unsteady components

Substituting into Equation 18, expanding, and eliminating terms containing the sine of an unsteady term results in

$$a_{B_C} \cong \Omega^2 r \sin\beta_s \cos\beta_u \cos\theta_s \cos\theta_u \quad (20)$$

Assuming  $\beta_u$  and  $\theta_u$  to be small, the expression for the beamwise acceleration due to centripetal acceleration simplifies to

$$a_{B_C} \cong \Omega^2 r \sin\beta_s \cos\theta_s \quad (21)$$



Near the tip of the blade,  $\theta$  is a small angle, so

$$a_{B_c} \approx \Omega^2 r \sin\beta_s \quad (22)$$

Substituting in the appropriate values for the tip of the OLS rotor yields

$$a_{B_c} \approx 787.26 \sin\beta_s \quad (23)$$

The coefficient has been divided by 32.17 so that Equation (23) yields the acceleration in g's.

The 20 g's beamwise acceleration computed at the tip of the blade (Figure 54) corresponds to a steady out-of-plane slope of 1.46 degrees, which is quite plausible. The test data would indicate that the blade is almost parallel to the hub plane near the tip. Therefore, a discrepancy in the steady beamwise acceleration at the tip of 20 g's corresponds to a difference in steady out-of-plane slope of less than 1.5 degrees.

Note that this particular analysis is only valid near the tip of the rotor, where the centripetal acceleration is the major contributor to the steady beamwise acceleration. No conclusions can be drawn with regard to the discrepancies between the measured and computed data inboard on the rotor, except to suggest that the negative measured steady beamwise accelerations imply a downward motion of the blade that is totally unexpected.

The measured oscillatory accelerations are not compared with computed results because C81 does not calculate oscillatory accelerations.

The one- and two-per-rev beamwise accelerations computed for the 66-KTAS case are in very good agreement with the test data. The simulation using an RIVD table predicts the distributions of these two harmonics in better agreement with the test data than the simulation using the internal induced velocity model. The three-per-rev beamwise accelerations computed by C81 using the internal induced velocity model are smaller than those measured in flight, which is not unexpected due to the lack of higher harmonic loading when the simple induced velocity model is used. Inclusion of higher-harmonic airloading, by use of an RIVD table, causes the three-per-rev accelerations to be significantly overpredicted.

Negligible four- and five-per-rev beamwise accelerations are computed using the internal induced velocity model, due to the lack of excitation at these frequencies. The four-per-rev acceleration computed when the RIVD table is used shows good agreement with the test data to approximately 75 percent radius, while the five-per-rev component is significantly overpredicted. The cause of this overprediction (and the overprediction of the three-per-rev component) has not been identified.

#### 6.6.2 Comparison of Main Rotor Beamwise Acceleration Waveform at Station 132 for Counter 615

Measured and computed beamwise acceleration time histories were compared for the level flight cases. The time history at station 132 measured during the 129-KTAS flight condition (counter 615) is plotted in Figure 55, with the corresponding time histories computed by the two different simulations. The measured waveform has significant harmonic content at frequencies above five-per-rev, which is not reflected in either of the computed traces, as there is no excitation at these high frequencies. The waveform resulting from the simulation using the internal induced velocity is predominantly two-per-rev, with a smaller one-per-rev component. The waveform computed when the RIVD table is included is essentially three- and five-per-rev in content.

#### 6.6.3 Comparison of Main Rotor Beamwise Accelerations for Counter 610

The OLS test vehicle was in steady-state level flight at 142 KTAS for Counter 610. The aircraft was in the clean wing configuration at mid gross weight and aft center of gravity. The radial distribution of the beamwise acceleration harmonics measured during this flight are plotted in Figure 56.

A comparison shows that the steady, two-per-rev and four-per-rev components of the beamwise acceleration measured at 66 KTAS (Figure 54) and at 142 KTAS (Figure 56) are almost identical. These two sets of data are for test conditions flown at the same gross weight, and the similarity in the even-harmonic accelerations indicate that the symmetric beamwise response of the rotor is not particularly dependant upon air-speed.

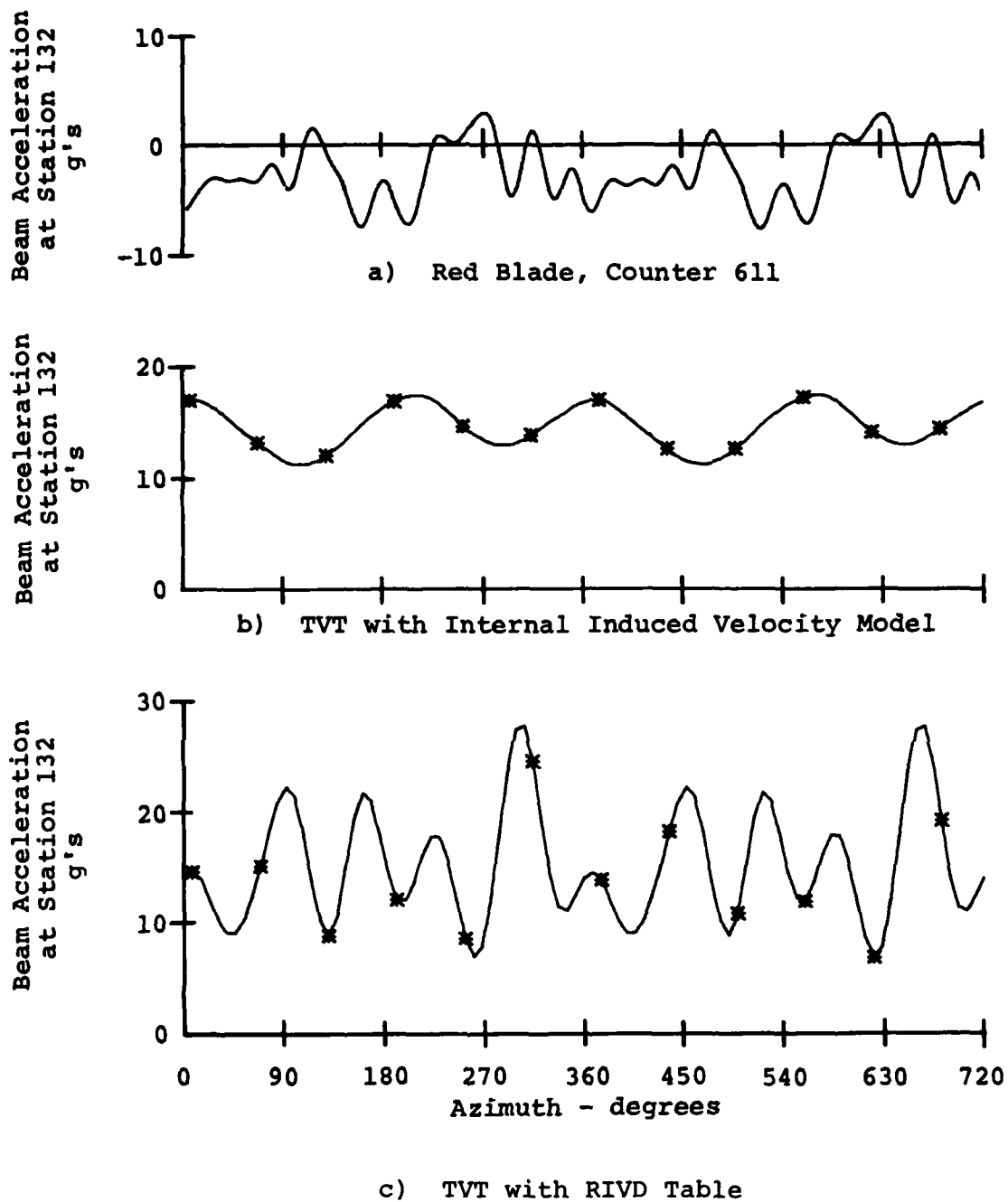


Figure 55. Comparison of Measured and Computed Main Rotor Beamwise Acceleration Waveforms at Station 132 for Counter 615 (8319 Pounds Gross Weight, Aft CG, Clean Wing, 129 KTAS).

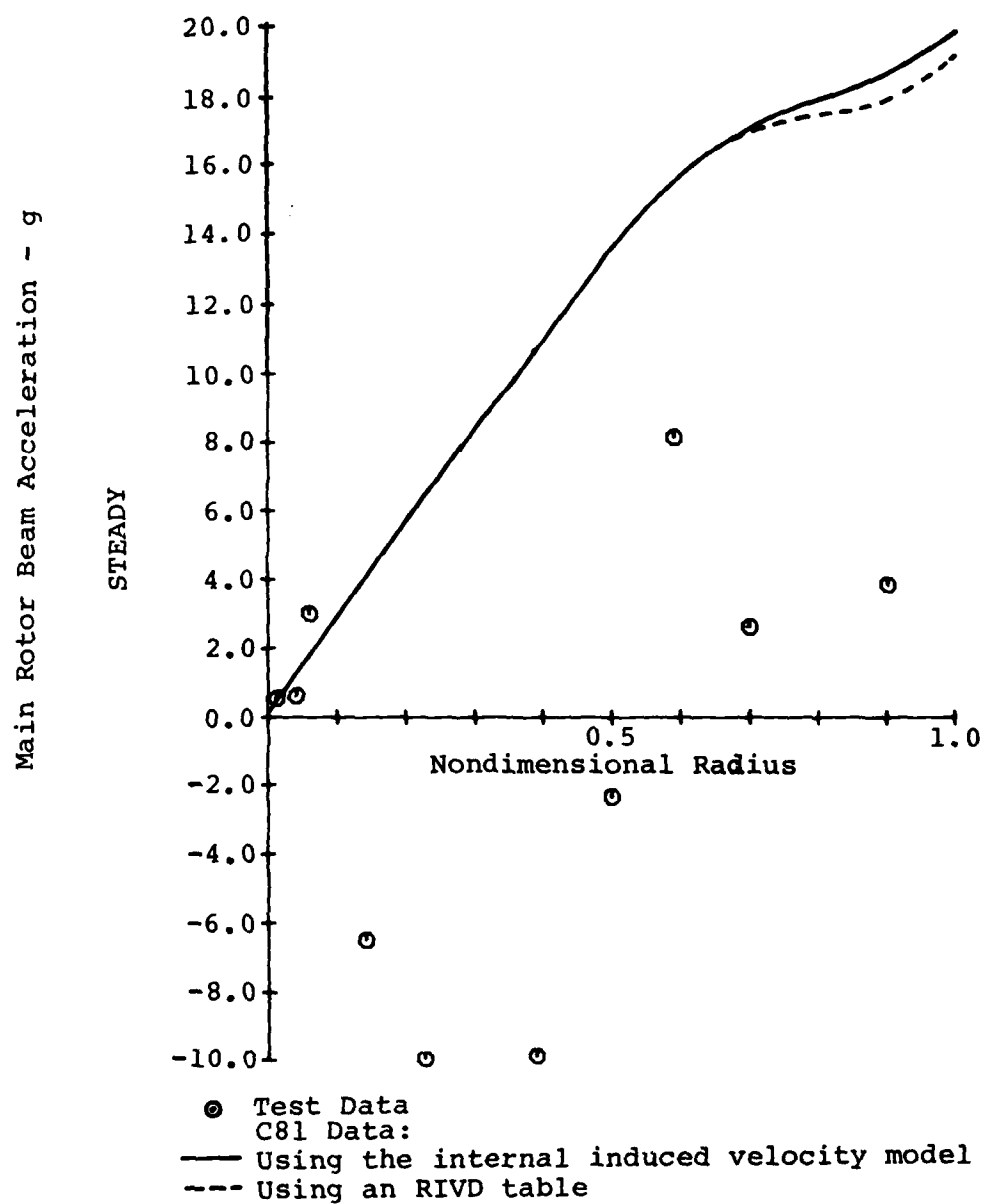
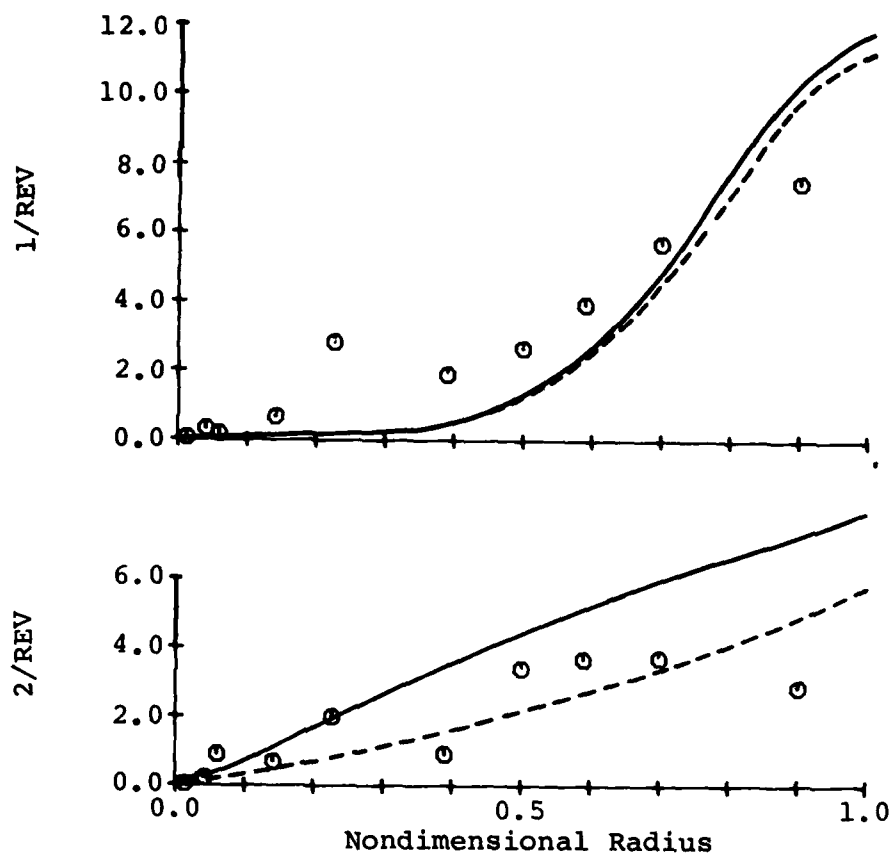


Figure 56. Comparison of Measured and Computed Main Rotor Beamwise Accelerations for Counter 610 (8319 Pounds Gross Weight, Aft CG, Clean Wing, 142 KTAS).

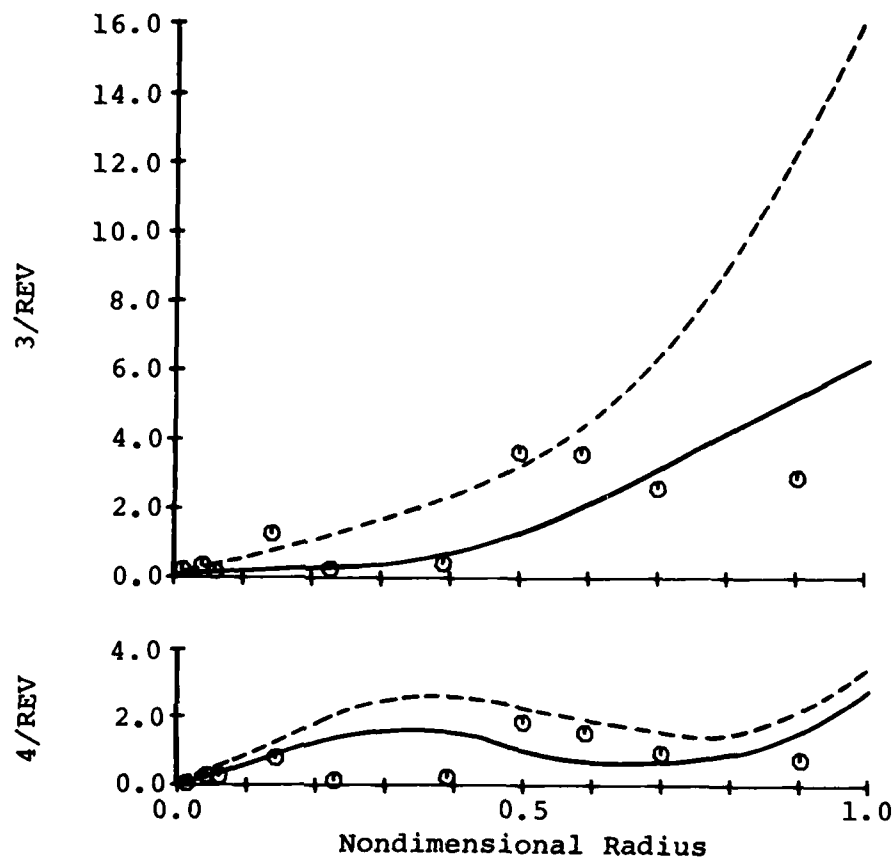
Main Rotor Beam Acceleration - g



- ⊙ Test Data
- C81 Data:
- Using the internal induced velocity model
- Using an RIVD table

Figure 56. Continued.

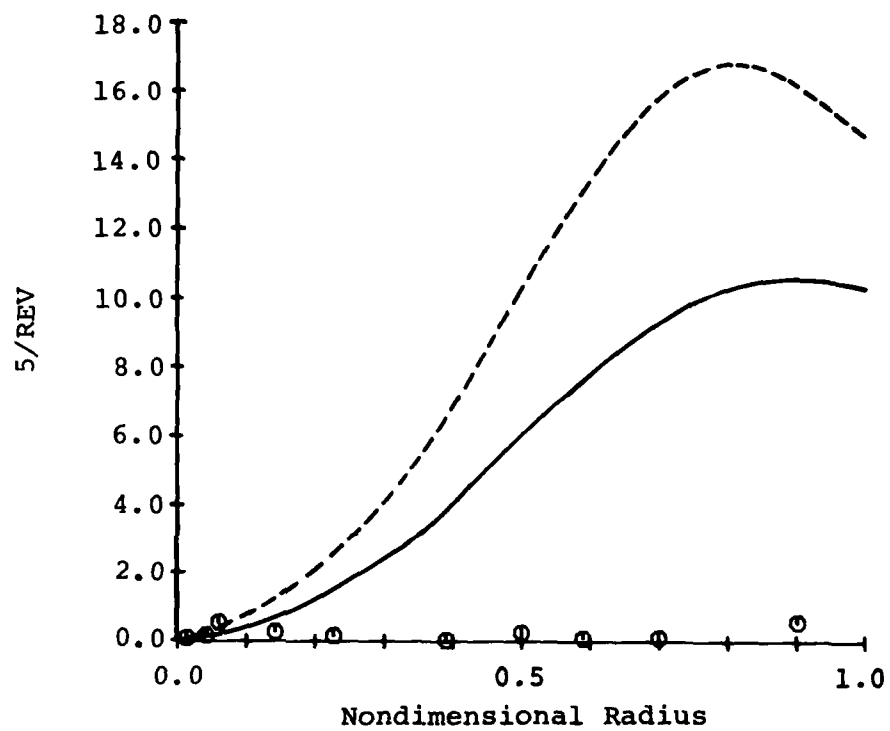
Main Rotor Beam Acceleration - g



⊙ Test Data  
 C81 Data:  
 — Using the internal induced velocity model  
 --- Using an RIVD table

Figure 56. Continued.

Main Rotor Beam Acceleration - g



- ⊙ Test Data
- C81 Data:
- Using the internal induced velocity model
- Using an RIVD table

Figure 56. Concluded.

The steady beamwise acceleration computed for the 142-KTAS test condition is very similar to that computed for the 66 KTAS counter, and is also at variance with the test data. The discussion of the steady beam acceleration given in Section 6.6.1 is applicable for this case also.

The one-, two-, and four-per-rev beam acceleration distributions computed by C81 are in good agreement with the measured data. The data generated by the simulation using the RIVD table are in closer agreement than those resulting from the simulation with the internal induced velocity distribution.

The three-per-rev beam accelerations computed by the analysis using the internal induced velocity model are of the same order of magnitude as those measured in flight. The three-per-rev beamwise accelerations computed using the RIVD table are similar to the test values on the inner half of the rotor and significantly larger than the experimental data near the tip. The program seriously overpredicts the five-per-rev beamwise accelerations with either rotor induced velocity representation.

#### 6.6.4 Summary of Main Rotor Beamwise Acceleration Comparisons

Program C81 computes one-, two-, and four-per-rev beamwise accelerations in reasonable agreement with measured data. The steady beam acceleration computed by the analysis does not agree with the test data, but the brief algebraic analysis given at the beginning of Section 6.6.1 outlines the source of the predominant terms in the computed results. The cause of the overprediction of the three- and five-per-rev components has not yet been determined.

#### 6.7 MAIN ROTOR CHORD ACCELERATIONS

Chordwise accelerations computed by C81 were compared with the experimental data for all the level flight conditions simulated. The results of those comparisons for two of the test points are presented in this section. By inspection of the instrumentation engineer's notes, the chordwise acceleration sign convention was determined to be positive aft. Two chordwise accelerometers were installed at each radial station of interest, with one placed on each surface of the airfoil at the local section quarter chord. The signals from the two sensors were averaged to eliminate the effects of pitch acceleration.



#### 6.7.1 Comparison of Main Rotor Chordwise Accelerations for Counter 611

Figure 57 contains the comparison of the computed and measured harmonic amplitudes of the main rotor chordwise accelerations for counter 611, which was a mid gross weight, aft center of gravity, clean wing, level flight test at 66 KTAS. The C81-computed accelerations are calculated by the program after the blade response has been determined, and are used for output purposes only.

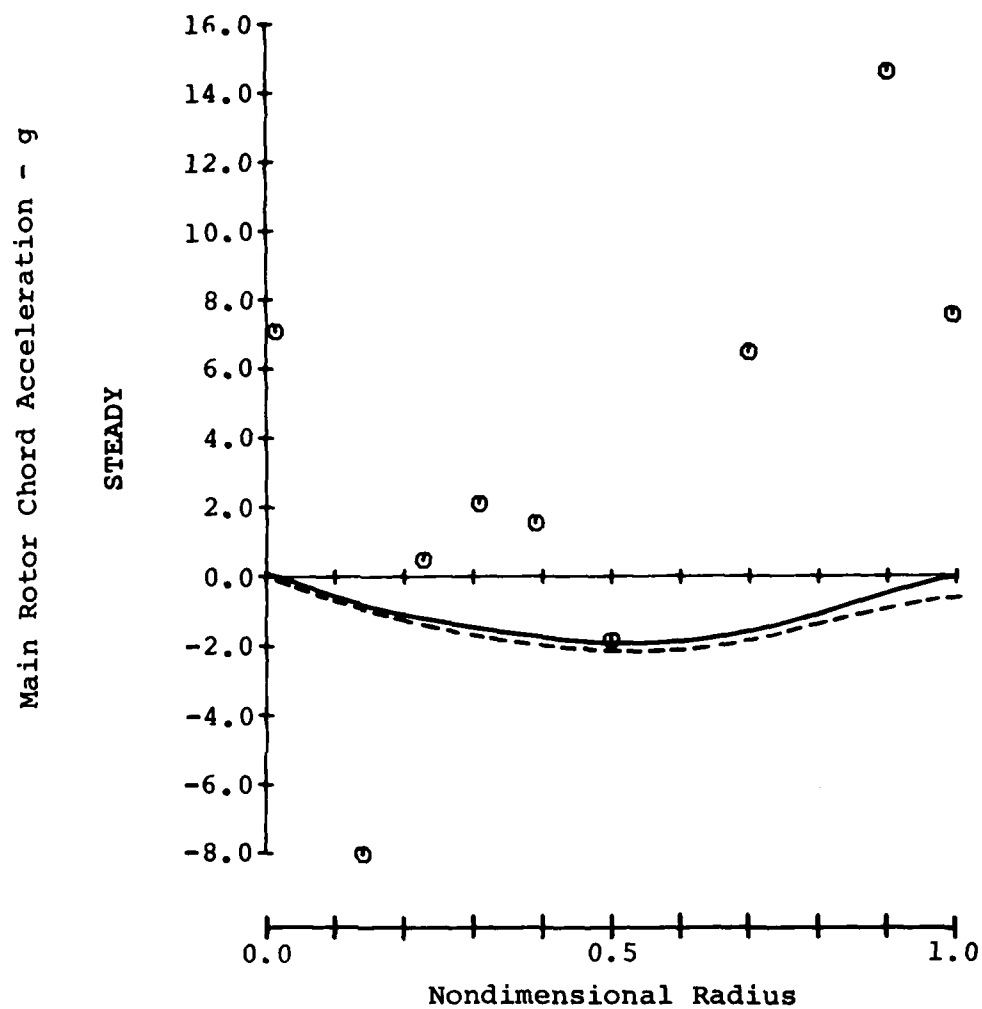
The test data indicate a steady forward acceleration over most of the rotor while C81 computes a steady lagging acceleration. It is suspected that the inability to properly model the inplane hub boundary condition, as discussed in the steady chord bending moment comparison (Section 6.4.1) is the primary cause of the discrepancy in the hub region. The source of the difference between the measured and computed data on the outboard portions of the rotor is not known.

The program computes the one-per-rev chordwise acceleration distribution in good agreement with the test data. The agreement is excellent when the RIVD table is used.

The two-per-rev component of the chordwise acceleration is overpredicted by the simulation using either induced velocity model, and the three-per-rev component of the chordwise acceleration is overpredicted by the simulation using either induced velocity model, and the three-per-rev harmonic amplitude is overpredicted when the RIVD table is used. The three-per-rev chordwise acceleration resulting from the simulation using the internal induced velocity model is in good agreement with the test data.

The measured four- and five-per-rev chordwise accelerations were quite small, as are the values calculated by C81 when the internal induced velocity model was used. The program overpredicts the value of the four-per-rev near the tip, and five-per-rev over most of the rotor, when the RIVD table was used. The overprediction of the five-per-rev chord acceleration probably results from the same source causing the overprediction of the five-per-rev beam acceleration.

The chordwise acceleration waveform measured at radial station 37.5 during counter 611 is compared with those computed by C81 in Figure 58. The computer-generated waveforms do not show the seven- and eight-per-rev content of the measured data. Additionally, the C81-computed chordwise acceleration has the same sign convention as the test data (positive aft),



- ⊙ Test Data
- C81 Data:
- Using the internal induced velocity model
- Using an RIVD table

Figure 57. Comparison of Measured and Computed Main Rotor Chordwise Accelerations for Counter 611 (8319 Pounds Gross Weight, Aft CG, Clean Wing, 66 KTAS).

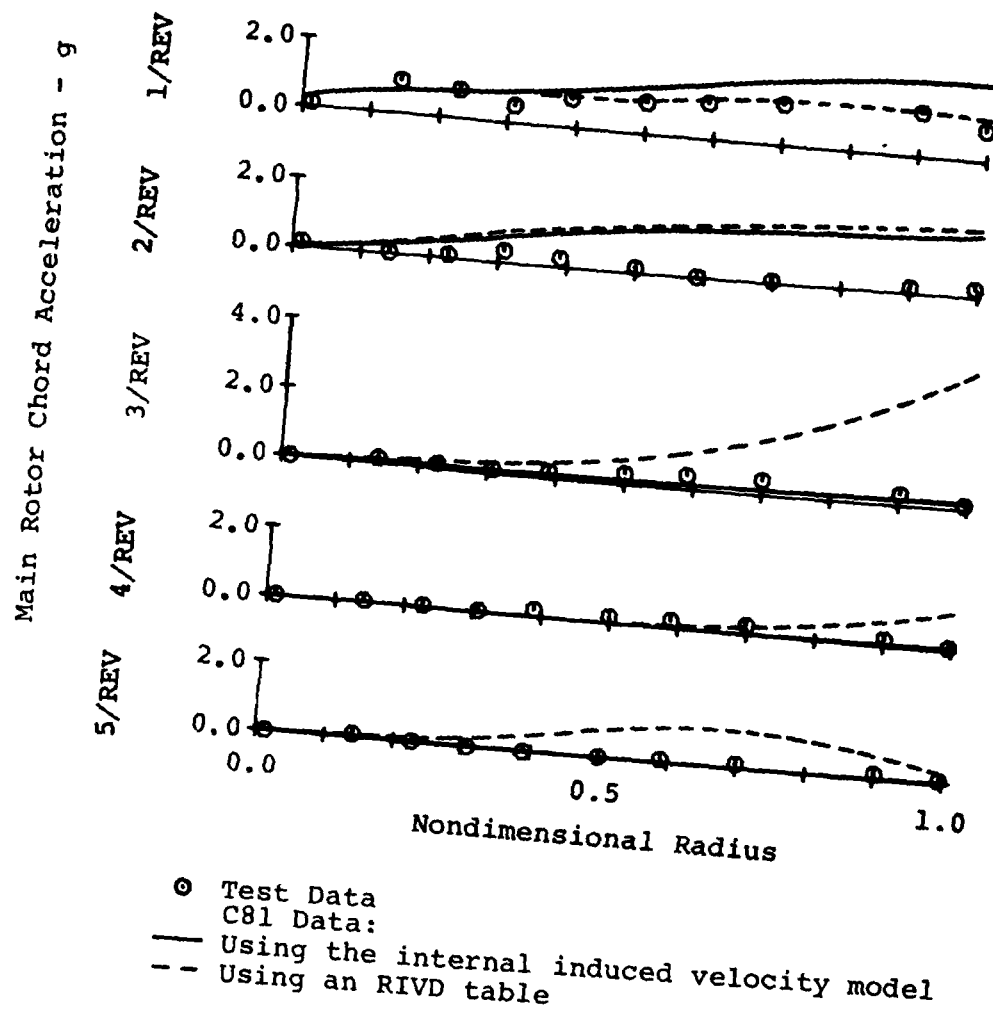


Figure 57. Concluded.

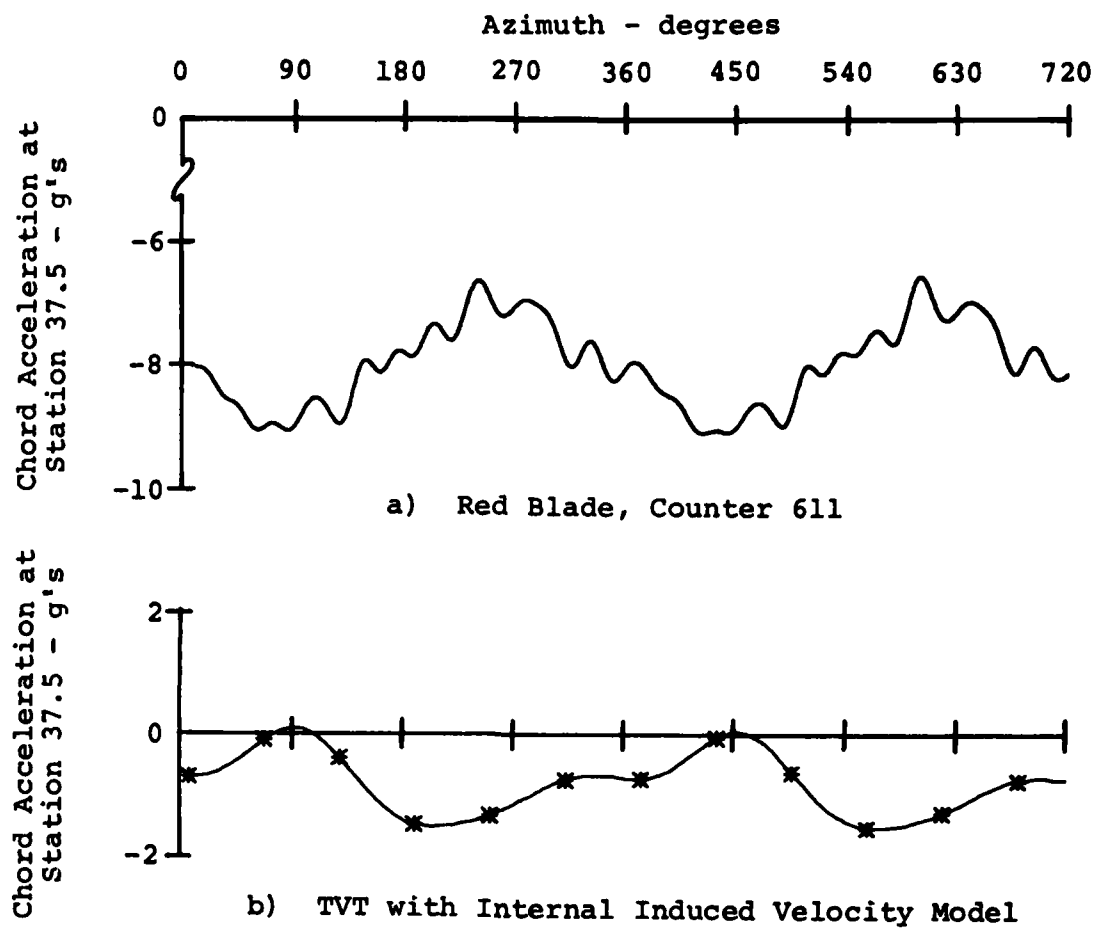
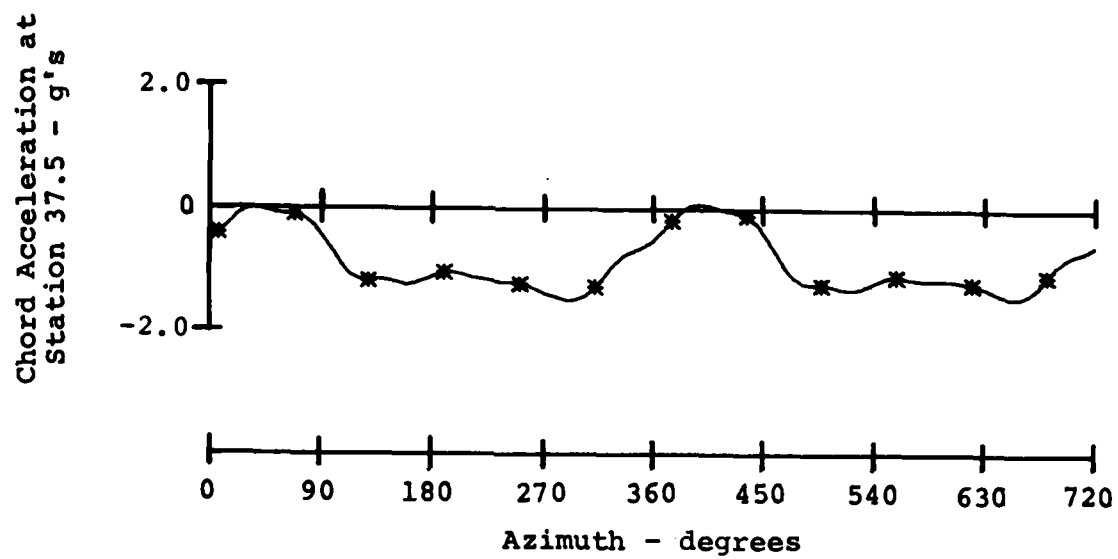


Figure 58. Comparison of Measured and Computed Main Rotor Chordwise Acceleration Waveforms at Station 37.5 for Counter 611 (8319 Pounds Gross Weight, Aft CG, Clean Wing, 66 KTAS).



c) TVT with RIVD Table

Figure 58. Concluded.

but the calculated waveforms appear to have a polarity opposite to that of the test data. This apparent sign reversal requires further study.

#### 6.7.2 Comparison of Main Rotor Chordwise Accelerations for Counter 610

The OLS test vehicle was flown at 142 KTAS in its mid gross weight, aft center of gravity, clean wing configuration for counter 610. The measured and computed chordwise accelerations for this flight condition are compared in Figure 59. The measured steady chord acceleration distribution for this case is almost identical to that measured for the 66-KTAS test point of counter 611 (Figure 57). The C81-computed steady accelerations do not agree with the measured data.

The predicted one- and two-per-rev chord accelerations are larger than the experimental data. The values computed using the RIVD table compare more favorably with the measured data than do the values calculated when the internal induced velocity model was used.

The computed three- and four-per-rev chord accelerations are in fair agreement with the data measured in flight, while the program seriously overpredicts the five-per-rev component.

#### 6.7.3 Summary of Main Rotor Chordwise Acceleration Comparisons

Program C81 does not correctly predict the steady chordwise acceleration. It does compute the one- through four-per-rev components of the chordwise acceleration with a reasonable amount of accuracy.

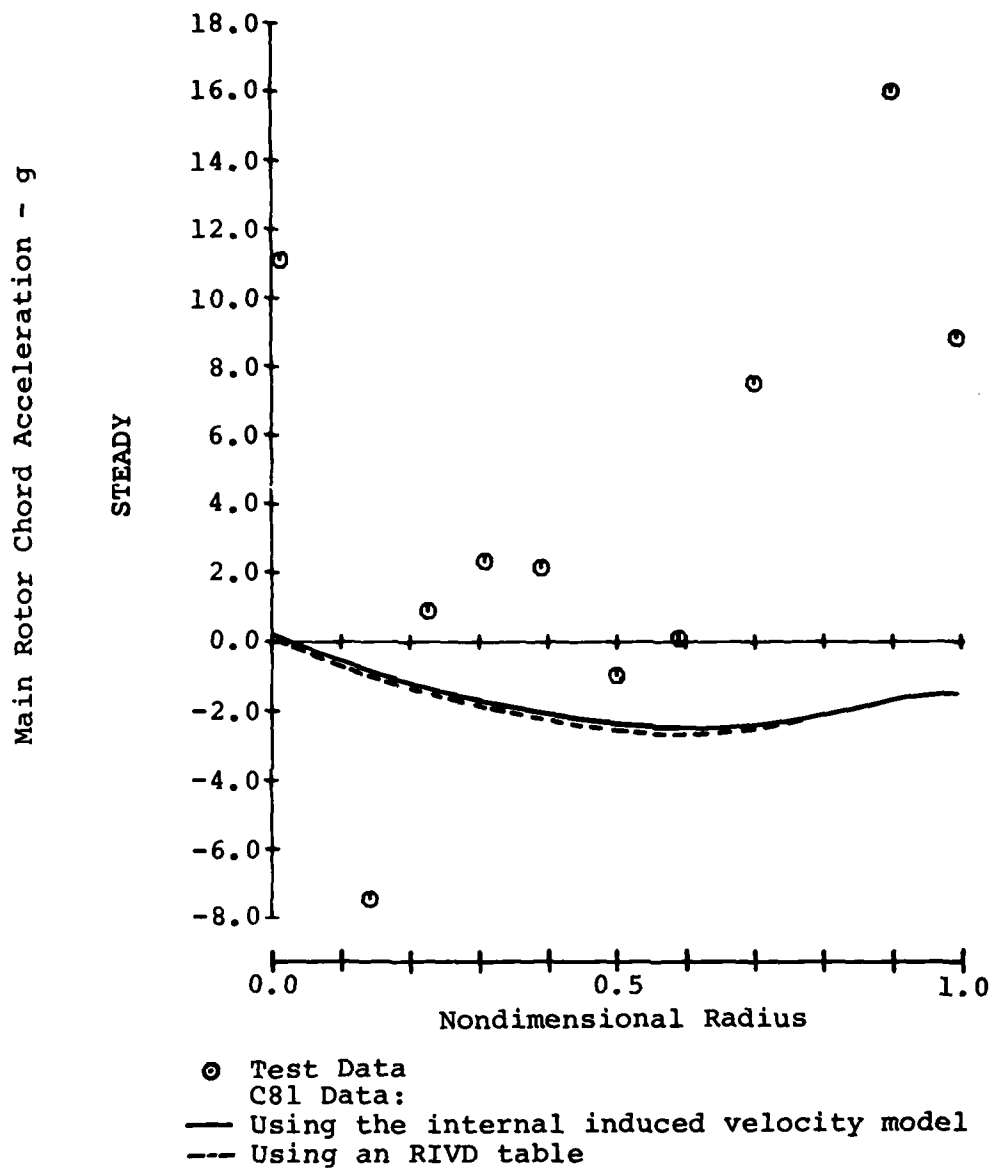
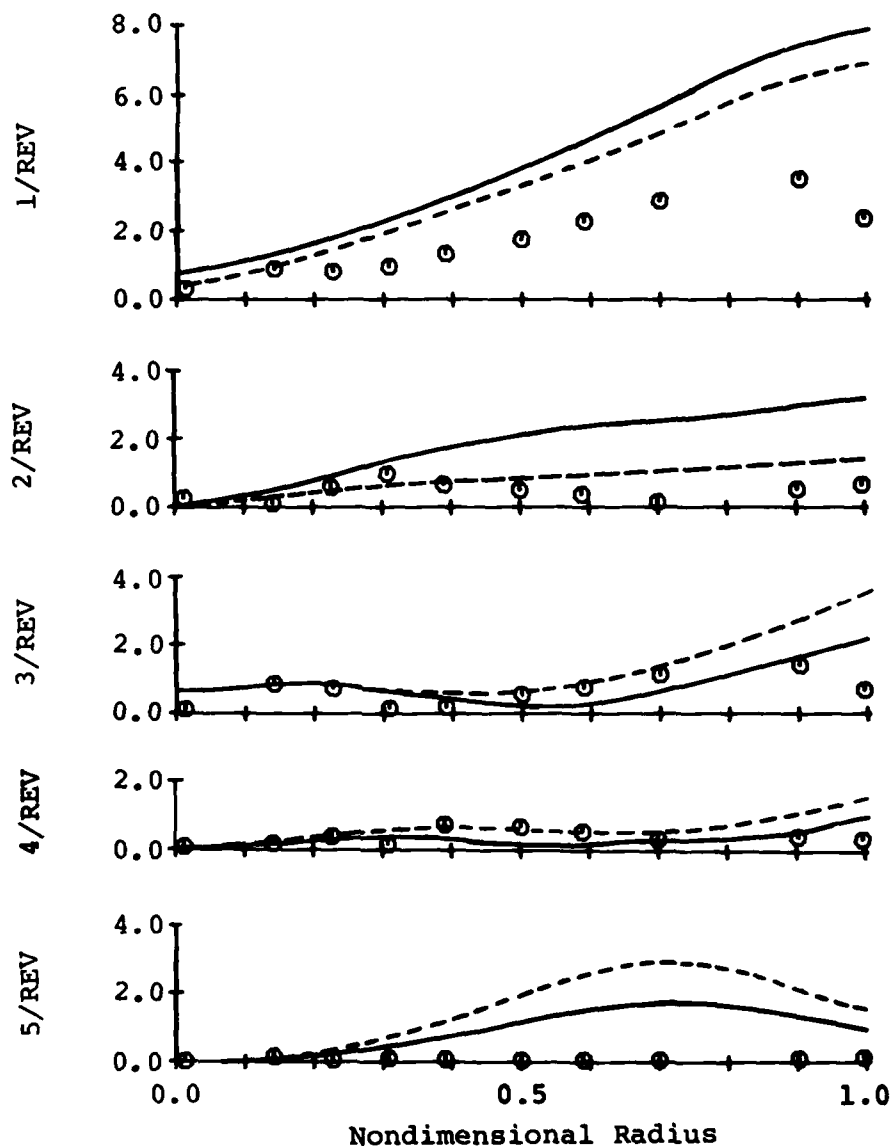


Figure 59. Comparison of Measured and Computed Main Rotor Chordwise Accelerations for Counter 610 (8319 Pounds Gross Weight, Aft CG, Clean Wing, 142 KTAS).

Main Rotor Chord Acceleration - g



● Test Data  
 C81 Data:  
 — Using the internal induced velocity model  
 --- Using an RIVD table

Figure 59. Concluded.



## 7. MANEUVER SIMULATION

Two OLS maneuvering flight records were simulated in addition to the nine level flight test conditions discussed in Sections 5 and 6. The banked turn and symmetric pullup experiencing the highest normal load factor were to be simulated in order to determine the program's ability to compute performance, loads and vibration data for high-g maneuvers. Investigation of the pilot cards and Table B.3 of Reference 10 indicated that the right rolling pullout of Flight 32A, counter 561, and the symmetric pullup of Flight 32A, counter 562, were the most severe maneuvers flown during the test program. The results of the simulations of these two maneuvers will be discussed after the method of simulation is outlined.

### 7.1 MANEUVER SIMULATION TECHNIQUE

The basic aircraft input deck, described in Section 3, was used for the maneuver simulations. The aircraft gross weight, center-of-gravity coordinates, and mass moments of inertia for the two maneuvers are listed in Table 6. The analysis for determining the rotor downwash at the fuselage, wing, and stabilizers (described in Section 3.12.1) was not performed for either maneuver. Since both maneuvers were flown at speeds approaching  $V_H$ , all the downwash factors (XMR(33), XTR(33), XWG(29) through XWG(32), XSTB2(29), XSTB2(32), XSTB3(29), and XSTB3(32)) were assumed to be zero.

Maneuvers are normally simulated by performing a quasi-static trim followed by a time-variant main rotor trim before entering the maneuver portion of the program. The partial derivative matrix is generated during the QST (assuming more than one iteration is required to trim), and the initial values of all the independent variables are set during the QST and TVT. This procedure was used initially for the simulation of the maneuvers of counters 561 and 562, with the aircraft being trimmed to a user-specified roll angle. (The value of roll angle input was the value measured at the beginning of the flight test record.) Unfortunately, the main rotor was not well trimmed at the end of the TVT, and a net roll moment was imposed on the aircraft, causing the ship to roll in the wrong direction at the beginning of the maneuver.

The fully-time-variant trim procedure (Section 4.2.3) was used to yield a better set of initial conditions for the maneuver. The values of the pitch and yaw attitude, control positions, and rotor flapping angles computed during the quasi-static trims already performed were used as the starting values in the Flight Constants Group, IPL(49) was set to 1, and IPL(50)

was set to 2. The resulting fully-time-variant trims required in excess of eight minutes to converge on an IBM 370/168. A slightly modified set of inputs to the Flight Constants Group, which provided more rapid convergence, was used to initiate the maneuver runs. The inputs to the Flight Constants Group used for the final maneuver runs are listed in Figure 60. Trim convergence was achieved in three iterations, requiring approximately 4.5 minutes of computing time (IBM 370/168).

The partial derivative matrix computed during the fully time-variant trim procedure is of higher quality than that calculated during the usual QST-TVT procedure. Since portions of the partial derivative matrix are used by the maneuver autopilot, this is an added benefit resulting from the use of the FTVT.

Quasi-static maneuvers were not run, as it was felt that the information to be gained did not justify the excessive computing time required for the simulations. The level-flight simulations indicated that the use of an RIVD table did not significantly improve the computed results, so the time-variant, elastic rotor maneuver simulations were performed using the internal induced velocity model.

The inputs for a maneuver simulation are those required for a trim, plus a series of cards which specifically control the maneuver. The maneuver time card (Sections 2.27 and 3.27 of Volume II, Reference 3) and the maneuver specification cards (Sections 2.28 and 3.28 of Volume II, Reference 3) used for both maneuver simulations are listed in Figure 61. Maneuver runs will always start at zero time unless the run is a maneuver restart (NPART = 5, Section 3.2, Volume II, Reference 3). The azimuth increment for the maneuver is chosen to satisfy the numerical stability criterion of the four-step Runge-Kutta algorithm used to forward integrate the equations of motion during the maneuver. The azimuth increment should be 7.6849 degrees to ensure that there are at least ten integration steps per cycle of the highest harmonic rotor elastic mode in the model (4.6845 per rev). The value of 7.5 degrees was chosen for convenience in evaluating the output (two time cuts represents 15 degrees, not 15.3698 degrees, etc.). The stop times (7.0 and 6.0 seconds for counters 561 and 562, respectively) were chosen to minimize the computer run time, while ensuring that the most significant portion of each maneuver was simulated.

133.5	ULS FLIGHT CONSTANTS GROUP		
32.81786	67.80389	50.14766	1000.0
0.024	-0.861	-1.40547	48.54878
			1.05593
		0.55556	
		7725.0	
		-6.08929	-2.5
		-325.0	
		5000.0	

a) Flight Constants Group Inputs for the Simulation of the Right Rolling Pullout Maneuver of Counter 561.

133.5	ULS FLIGHT CONSTANTS GROUP		
32.89127	68.47679	58.43159	1000.0
0.012	0.012	-1.90777	55.67685
		1.34750	
		-4.74554	
		7725.0	
		-0.07276	2.0
		-325.0	
		5000.0	

b) Flight Constants Group Inputs for the Simulation of the Symmetric Pullup Maneuver of Counter 562.

Figure 60. Flight Constants Group Inputs for Maneuver Simulations.

INPUT DATA FOR MANEUVER									
	START (SEC)	DELTA (SEC)	MAX1 (SEC)	DELTA (SEC)	MAX2 (SEC)	MAX3 (SEC)			
	0.0	7.500000	7.000000	7.500000	0.0	0.0			
	J	XCIT(J,1)	(J,2)	(J,3)	(J,4)	(J,5)			(J,6)
COLLECTIVE STICK	1	0.0	0.0	3.000	3.000	-0.140			7.500
COLLECTIVE PILOT	1	7.500	0.0	9.000	9.000	0.0			10.000
1-THACKER AUTO PILOT	41	0.0	0.0	0.550	0.550	6.903			2.100
2-THACKER AUTO PILOT	41	2.100	0.0	2.300	2.300	6.727			2.850
3-THACKER AUTO PILOT	41	2.850	-3.273	3.400	3.400	2.000			3.700
4-THACKER AUTO PILOT	41	3.700	-6.500	4.900	4.900	-7.500			5.900
5-THACKER AUTO PILOT	41	5.900	6.750	6.300	6.300	-5.714			6.900
6-THACKER AUTO PILOT	41	6.900	3.000	7.400	7.400	0.0			9.000
7-THACKER AUTO PILOT	42	0.0	0.0	1.100	1.100	2.222			1.550
8-THACKER AUTO PILOT	42	1.550	-0.909	2.650	2.650	3.135			4.000
9-THACKER AUTO PILOT	42	4.000	7.063	5.200	5.200	0.0			6.000
10-THACKER AUTO PILOT	42	8.000	-3.000	9.000	9.000	0.0			10.000
11-THACKER AUTO PILOT	43	0.0	5.400	0.500	0.500	-3.333			2.000
12-THACKER AUTO PILOT	43	6.000	2.520	4.500	4.500	8.125			5.300
13-THACKER AUTO PILOT	43	5.300	-3.692	6.600	6.600	6.333			7.000
14-THACKER AUTO PILOT	43	7.000	-1.176	9.000	9.000	0.0			10.000
SIMULATE	32	0.0	100.000	100.000	100.000	0.100			0.100

a) Maneuver Specification Inputs for the Simulation of the  
Right Rolling Pullout Maneuver of Counter 561.

Figure 61. Maneuver Specification Inputs for the Simulation  
of the Maneuvers of Flight 32A.

INPUT DATA FOR MANEUVER									
	START (SEC)	DELTA (SEC)	MAX1 (SEC)	DELTA (SEC)	MAX2 (SEC)	MAX3 (SEC)			
	0.0	7.500000	6.000000	7.500000	0.0	0.0			
	J	XCIT(J,1)	(J,2)	(J,3)	(J,4)	(J,5)			(J,6)
CULLECTIVE STICK	1	0.0	0.0	3.000	3.000	0.0			6.000
P-TRACKER AUTJ PILOT	41	0.0	0.0	1.000	1.000	-1.818			2.100
P-TRACKER AUTJ PILOT	41	5.100	5.833	2.700	2.700	-4.000			3.200
P-TRACKER AUTJ PILOT	41	3.200	5.692	3.850	3.850	-2.316			4.800
P-TRACKER AUTJ PILOT	41	4.800	4.167	5.400	5.400	-2.667			6.150
P-TRACKER AUTJ PILOT	42	0.0	2.600	1.000	1.000	-0.200			1.500
P-TRACKER AUTJ PILOT	42	1.500	5.417	2.700	2.700	-1.619			3.750
P-TRACKER AUTJ PILOT	42	3.750	-12.000	4.000	4.000	-2.025			6.000
P-TRACKER AUTJ PILOT	43	0.0	0.0	0.750	0.750	1.833			1.350
P-TRACKER AUTJ PILOT	43	1.350	-1.650	2.600	2.600	3.684			3.550
P-TRACKER AUTJ PILOT	43	3.550	-2.129	5.100	5.100	1.111			6.000
P-TRACKER AUTJ PILOT	32	0.0	100.000	100.000	100.000	0.100			0.100

b) Maneuver Specification Inputs for the Simulation of the Symmetric Pullup Maneuver of Counter 562.

Figure 61. Concluded.

The maneuver specification inputs available in C81 allow the analyst to stipulate control motions, desired airframe rates, weapons fire, store jettison, and several other events that can define a non-steady-state flight condition. Every maneuver simulated in C81 starts from the steady-state flight condition defined by the preceding trim, and the maneuver specification cards describe a series of variations of particular variables to be performed during the maneuver. The variations are generally described as a series of ramp changes in the value of the variable. A maximum of 20 maneuver specification cards ("J-cards") can be used, which was more than adequate for the two maneuvers simulated.

The observed variations in collective stick position are defined on the first maneuver specification cards for each of the simulations. The collective stick position was reduced from its trim position at a very slow rate between 3.0 and 7.5 seconds of counter 561 and was then held constant for the remainder of the maneuver. This variation was mimicked exactly during the simulation by the use of the two collective stick variation cards (Figure 61.a), even though the computed trimmed collective was lower than that measured in flight. No collective stick motion was measured during the symmetric pullup maneuver of counter 562, so only one collective stick variation card was input, stipulating constant stick position (Figure 61.b).

Whenever the maneuver autopilot is being used, the last maneuver specification card input must be the autopilot specification (J=32) card. This card gives the time to activate the autopilot logic (generally 0.0 seconds), the allowable maximum stick rates and two time constants. The AH-1G helicopter system allows maximum control rate inputs to the nonrotating swashplate of approximately 100 percent per second, which dictated the rate inputs on the J=32 card. It should be noted that a human pilot would be hard pressed to perform a maximum rate stick input, but these large allowable rates are instrumental in ensuring that the simulated aircraft angular rates are close to the desired rates.

The two time constants input on the maneuver autopilot card are used to compute moment imbalance signals for the autopilot logic. Assuming that a rate error exists on a channel, the moment imbalance is

$$M_i = M_{\text{actual}} - M_r \quad (25)$$

where  $M_i$  is the moment imbalance

$M_{\text{actual}}$  is the instantaneous value of the moment about the axis of interest

$M_r$  is the change in moment required to zero the rate error

The moment change is

$$M_r = \frac{I (\text{desired rate} - \text{actual rate})}{(\text{time to zero rates})} \quad (26)$$

in which  $I$  is the aircraft moment of inertia about the appropriate axis.

When a desired angular rate time history is not input for a channel, then the autopilot automatically tries to maintain the trimmed rate (usually zero) and angular displacement for that channel. In that case, an additional moment correction term,  $M_d$ , is subtracted from Equation (25):

$$M_d = \frac{I (\text{desired displacement} - \text{actual displacement})}{(\text{time to zero displacements})^2} \quad (27)$$

The input time constants, 0.1 second, are significantly smaller than any human pilot could generally realize but the small values help ensure that the autopilot can track the input desired rate time histories with minimal time lag.

The prime consideration in simulating the two maneuvers was to match the measured fuselage rates. No attempt was made to exactly reproduce the measured yaw, pitch, and roll rate time histories. Rather, the inputs to the roll rate autopilot channel ("p-tracker"), the pitch rate autopilot channel ("q-tracker"), and the yaw rate autopilot channel ("r-tracker") were chosen to yield aircraft response that captured the major features of the maneuver.

The measured rate time histories indicated that the aircraft was not in stabilized level flight at the beginning of either maneuver. The "J-card" inputs for a given channel were chosen to hold that fuselage rate constant (i.e., at zero) until the measured rate crossed zero. After that time, a series of ramps were input for that channel to correspond to the significant fuselage angular rate changes for the remainder of the maneuver.

When an acceptable simulation of the maneuver was achieved, the maneuver time histories of all variables were stored on tape (see Section 2.31 and 3.31, Volume II of Reference 3). The data could then be postprocessed, using an NPART of 8 (Sections 2.2 and 3.2, Volume II of Reference 3) without having to rerun the maneuver.

## 7.2 PERFORMANCE COMPARISONS

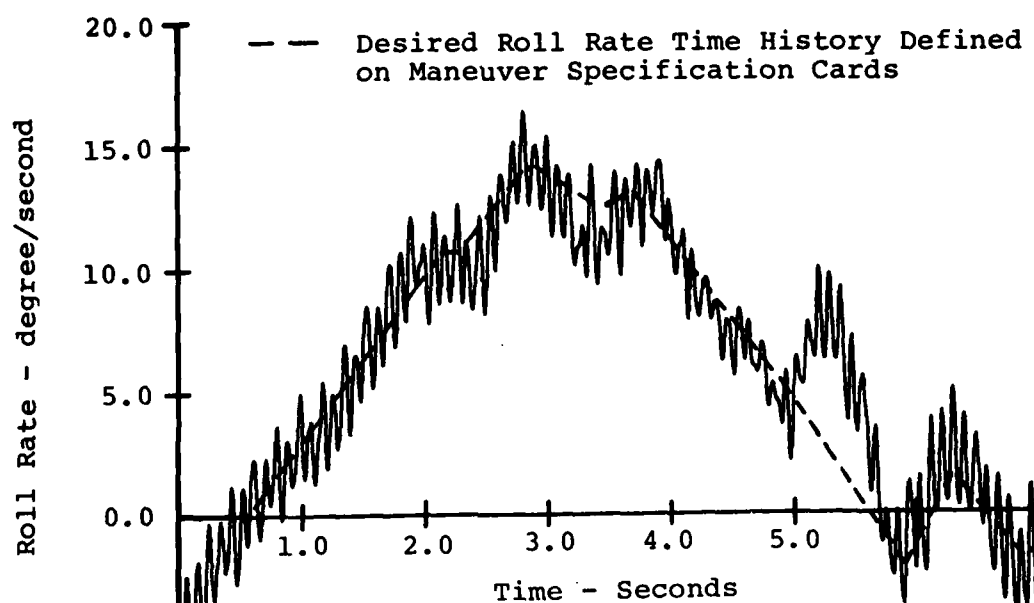
C81-computed performance data were compared with the measured data for both maneuvers in time-history form. The collective stick time histories measured in flight were input to the simulation, ensuring that the collective motion in the program matched that recorded in flight. The comparison of cyclic stick and pedal positions was inconclusive because the maneuvers were flown with the SCAS engaged, but they were simulated without a SCAS. The hub feathering angle was measured as constant throughout the maneuvers, which is obviously in error, so the computed hub feathering angle time histories were not compared with the test data. The measured performance data were filtered at 54 hertz before being plotted; almost all of the C81 results are unfiltered.

### 7.2.1 Comparison of Measured and Computed Fuselage Rates

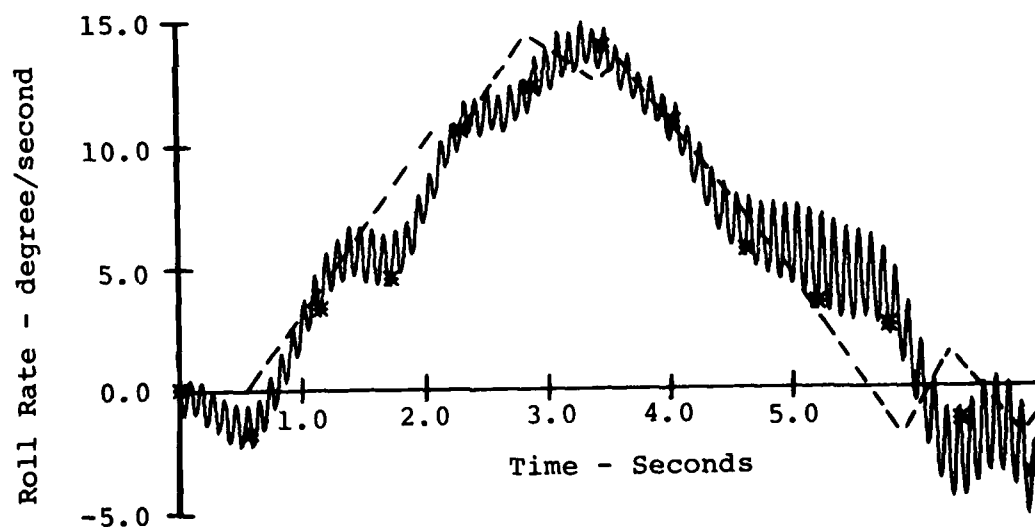
The roll rate time history measured during the right-rolling pullout maneuver of counter 561 is compared with that computed during the simulation in Figure 62. The dashed line superimposed on each plot is the desired roll rate time history input to the maneuver autopilot. It should be noted that both time histories are for the body roll rate ( $p$ ), not an Euler roll rate.

The test vehicle was rolling at approximately  $-4.0$  degrees per second at the beginning of the maneuver, and reached zero roll rate at approximately 0.6 second. The aircraft in the simulation starts the maneuver with zero roll rate, undergoes a small negative roll acceleration, and then accelerates rapidly in a right roll, tracking the input desired roll rate trace. The simulated aircraft then experiences a roll rate time history that is similar to that measured in flight. It is not known why the roll acceleration goes to zero between 1.4 and 1.8 seconds in the simulation, but the almost zero roll acceleration between 2.3 and 2.8 seconds in the simulation corresponds to the measured small roll acceleration between 2.1 and 2.3 seconds. The roll rate reaches its peak value at about 3.3 seconds, lagging the measured roll rate by about 0.4 second. It is suspected that the difference between the desired roll rate trace and that experienced in the simulation after about 4.5 seconds is due to the use of trimmed-flight partial derivatives in the maneuver autopilot calculations.





a) Measured Roll Rate Time History



b) Computed Roll Rate Time History

Figure 62. Comparison of Measured and Computed Airframe Roll Rate Time Histories for the Right Rolling Pullout Maneuver of Counter 561.

The measured and computed normal load factor time histories for the symmetric pullup maneuver of counter 562 are compared in Figure 69. The unfiltered time history produced by C81 is in reasonable agreement with the experimental data, although the simulation experiences a more oscillatory normal load factor early in the maneuver, while the test data show an increase in oscillatory load later in the maneuver. The filtered time history shows that the simulation achieves a peak normal load factor near 1.6g, while the peak mean value of the experimental data is about 1.7g.

The  $\dot{W}$  term must again be suspected as the cause for the difference between the maximum measured and computed normal load factors, as the measured and computed time histories for  $q$ ,  $\theta$  and  $\phi$  are quite similar. (The measured and computed roll rate time histories are not similar, but the lateral velocity is negligible, so the  $pV$  term is very small in comparison to the other terms in Equation 28.)

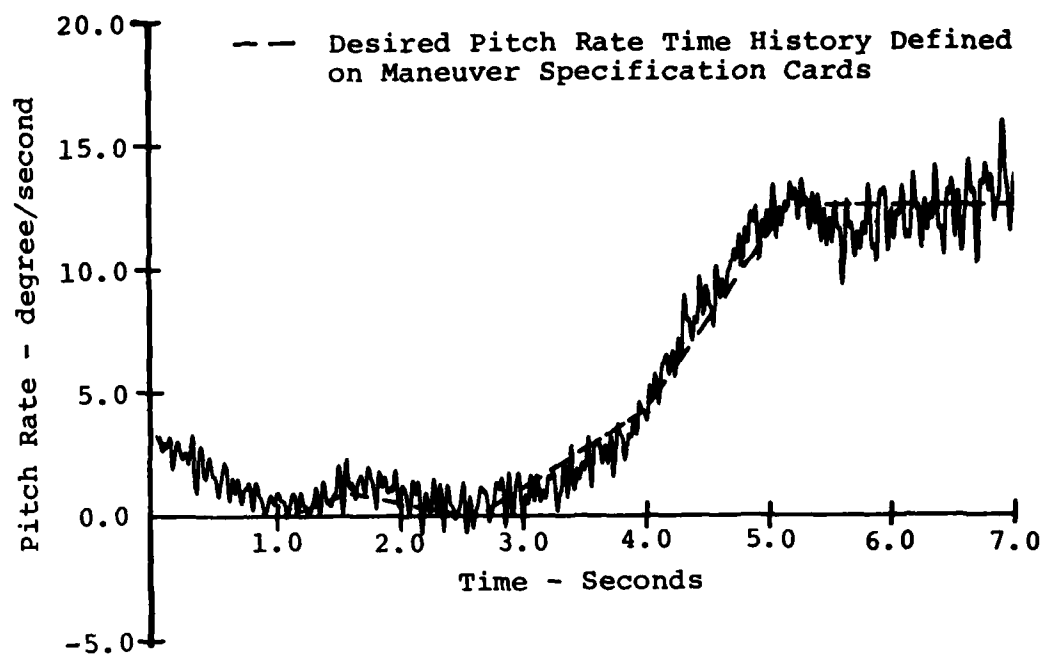
### 7.2.3 Comparison of Measured and Computed Fuselage Euler Attitudes

The attitude instrumentation installed in the OLS test vehicle measured the Euler angles of the aircraft with respect to the earth.

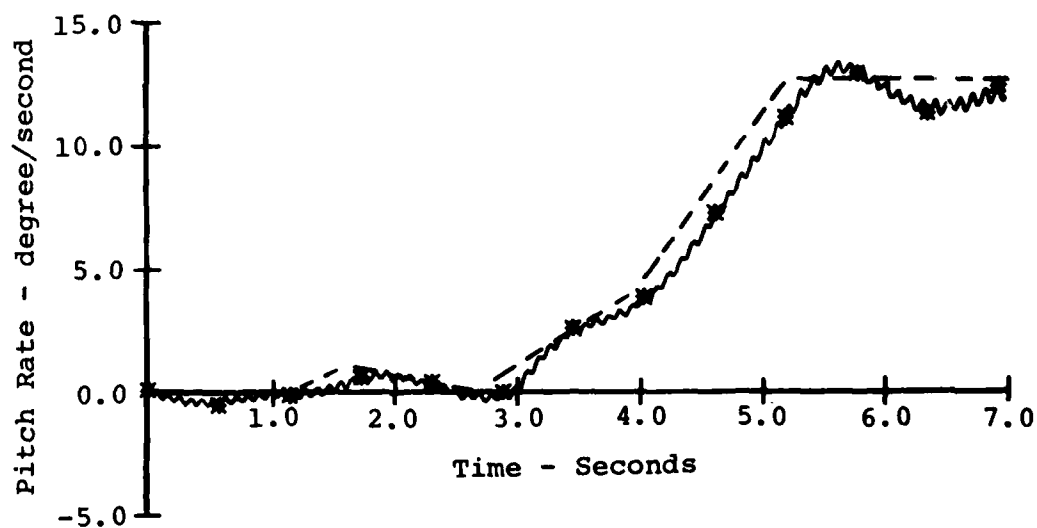
The roll attitude time histories measured in flight and computed in the simulation of the right-rolling pullout maneuver of counter 561 are compared in Figure 70. The two traces are almost identical, starting at -2.5 degrees at zero time. The roll attitude time history in the simulation passes through zero about 0.3 second later than the measured time history. The maximum roll angle achieved in the simulation is about 38 degrees, while the maximum measured roll angle was about 50 degrees.

The pitch attitude time histories for this maneuver are compared in Figure 71. The two time histories are remarkably similar. The simulated aircraft trims about one degree more nose down than the test aircraft, and the pitch attitude remained approximately constant for the first 3 seconds of the simulated maneuver and for the first 4 seconds during the actual maneuver. The pitch attitude time history goes through zero in the simulation about 0.2 second later than in the flight test and reaches a maximum value of about nine degrees, while the maximum experimental value was about five degrees.

The measured and computed yaw attitude time histories for the right-rolling pullout maneuver of counter 561 are plotted in Figure 72. The yaw gyro installed in the OLS aircraft did

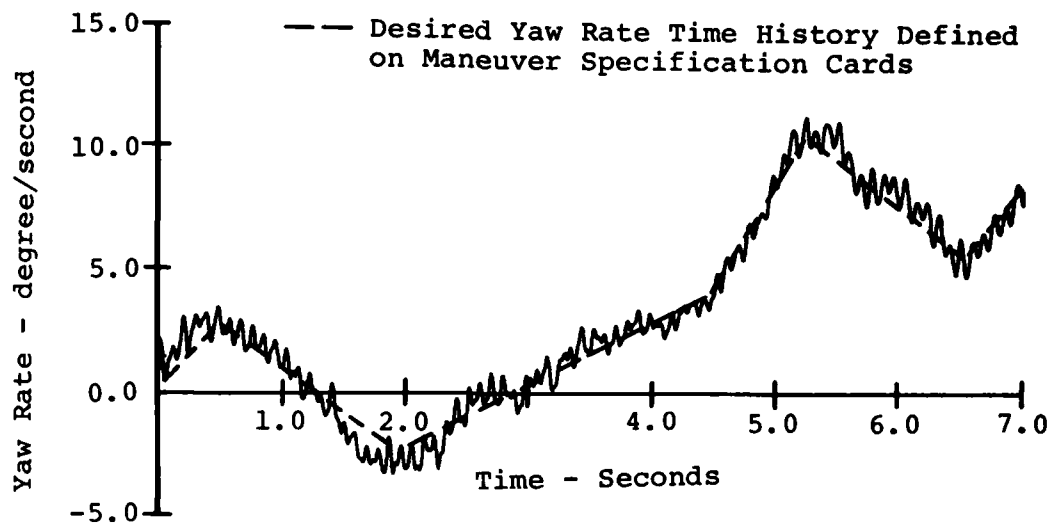


a) Measured Pitch Rate Time History.

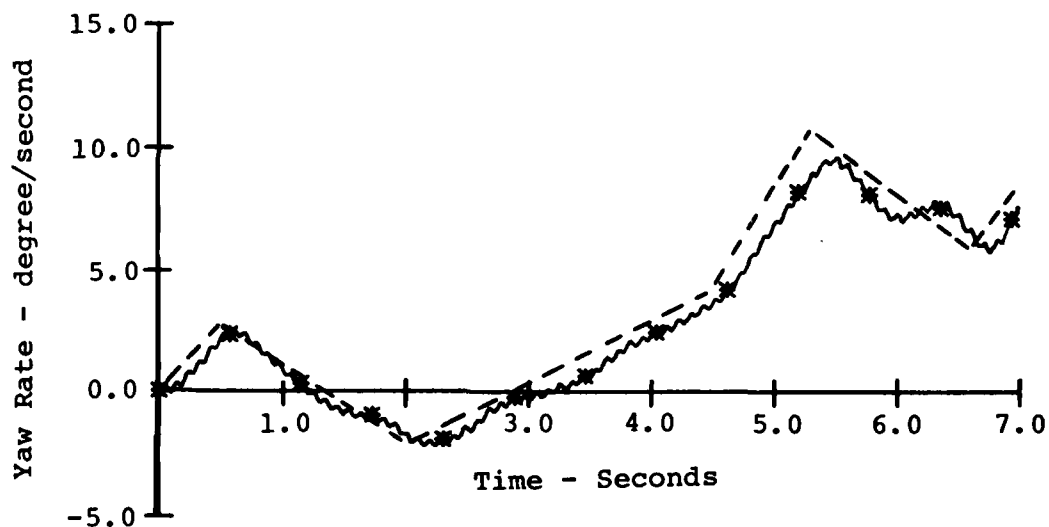


b) Computed Pitch Rate Time History.

Figure 63. Comparison of Measured and Computed Airframe Pitch Rate Time Histories for the Right Rolling Pullout Maneuver of Counter 561.



a) Measured Yaw Rate Time History.



b) Computed Yaw Rate Time History.

Figure 64. Comparison of Measured and Computed Airframe Yaw Rate Time Histories for the Right Rolling Pullout Maneuver of Counter 561.

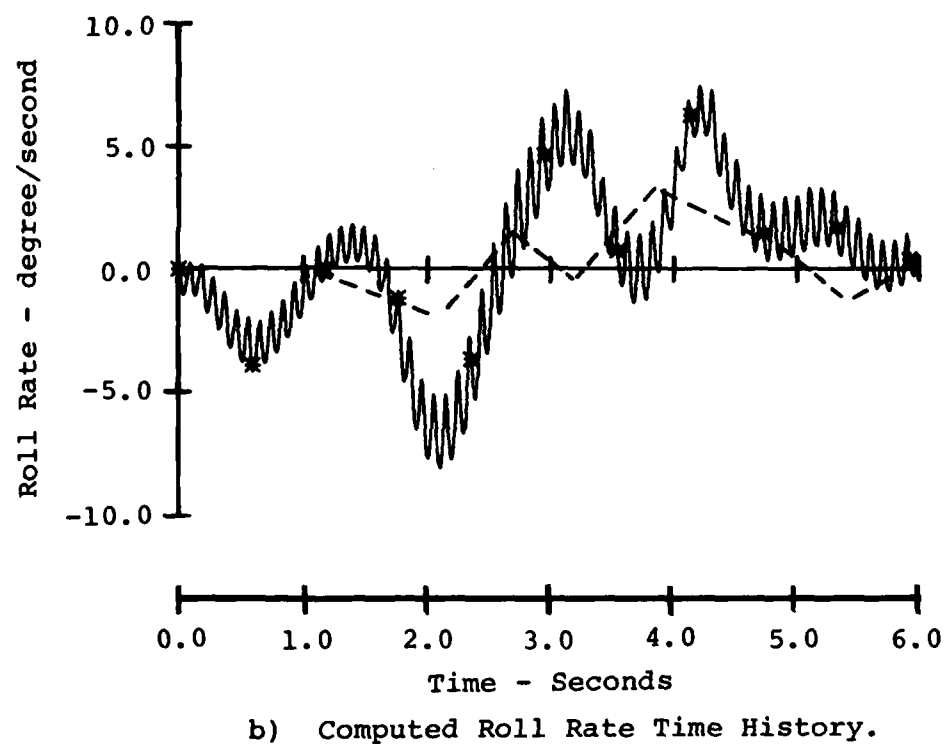
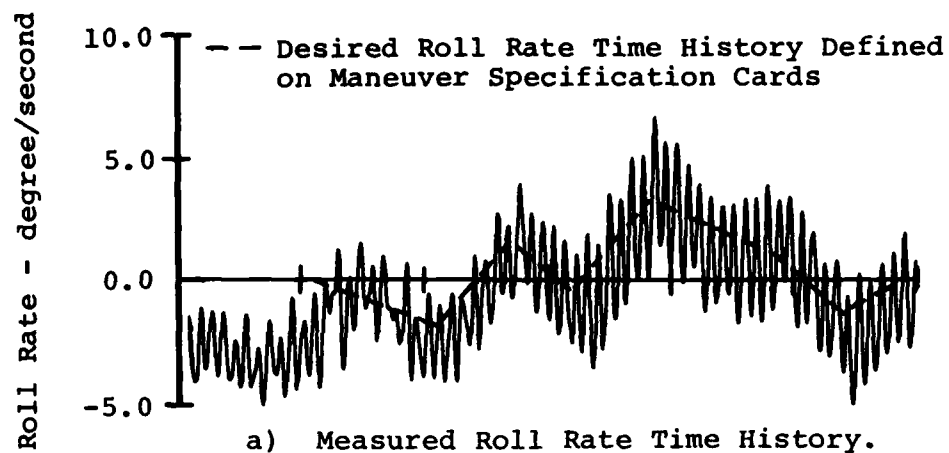
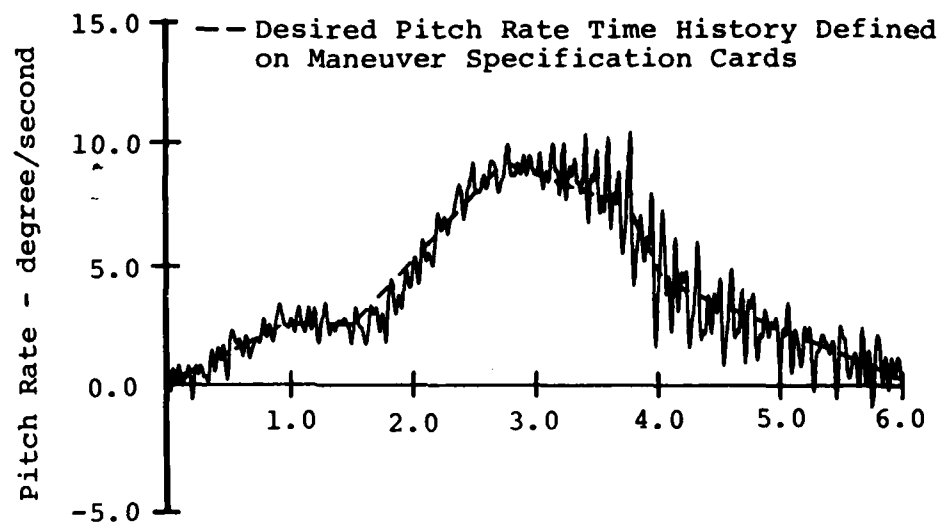
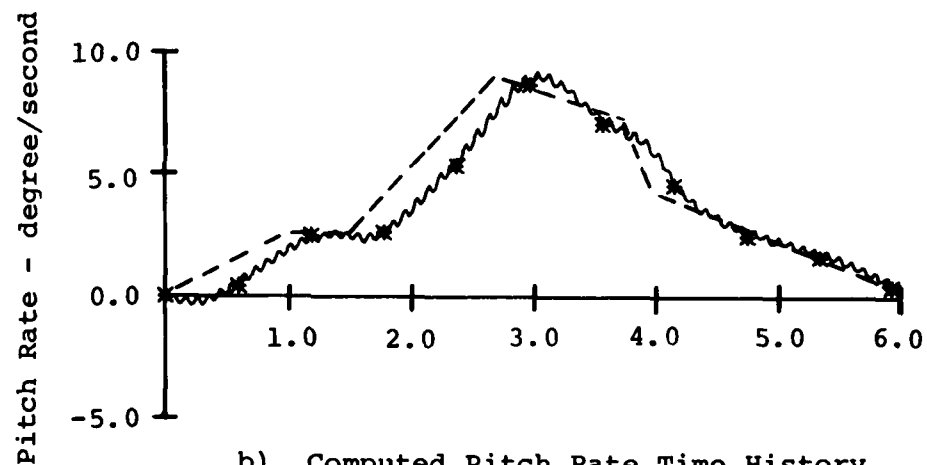


Figure 65. Comparison of Measured and Computed Airframe Roll Rate Time Histories for the Symmetric Pullup Maneuver of Counter 562.

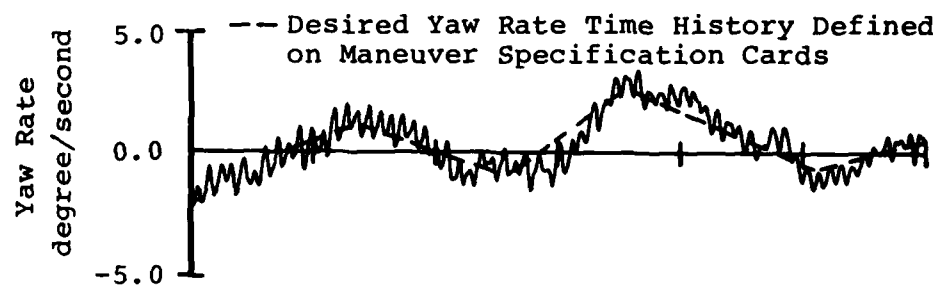


a) Measured Pitch Rate Time History.

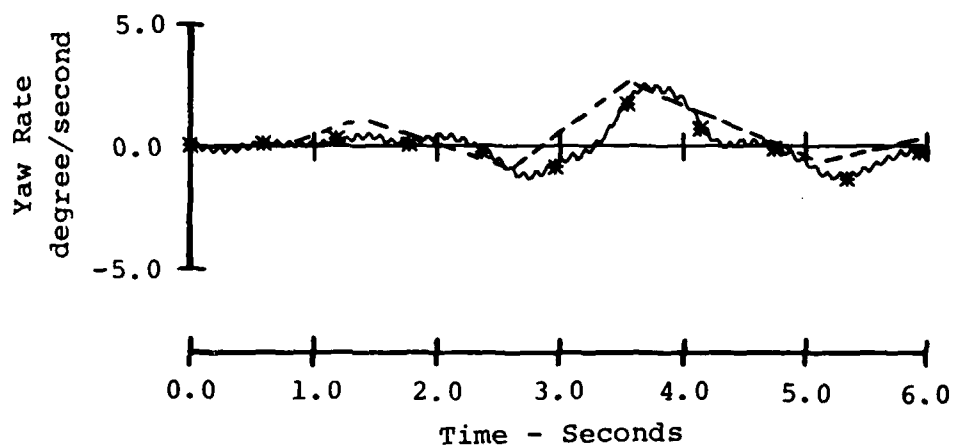


b) Computed Pitch Rate Time History.

Figure 66. Comparison of Measured and Computed Airframe Pitch Rate Time Histories for the Symmetric Pullup Maneuver of Counter 562.



a) Measured Yaw Rate Time History.



b) Computed Yaw Rate Time History.

Figure 67. Comparison of Measured and Computed Airframe Yaw Rate Time Histories for the Symmetric Pullup Maneuver of Counter 562.

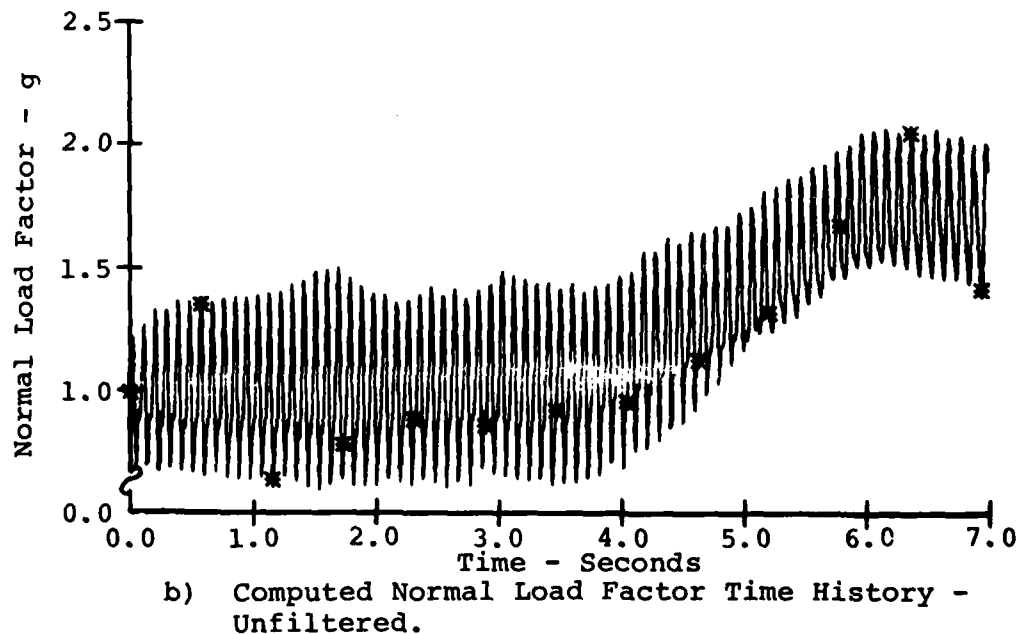
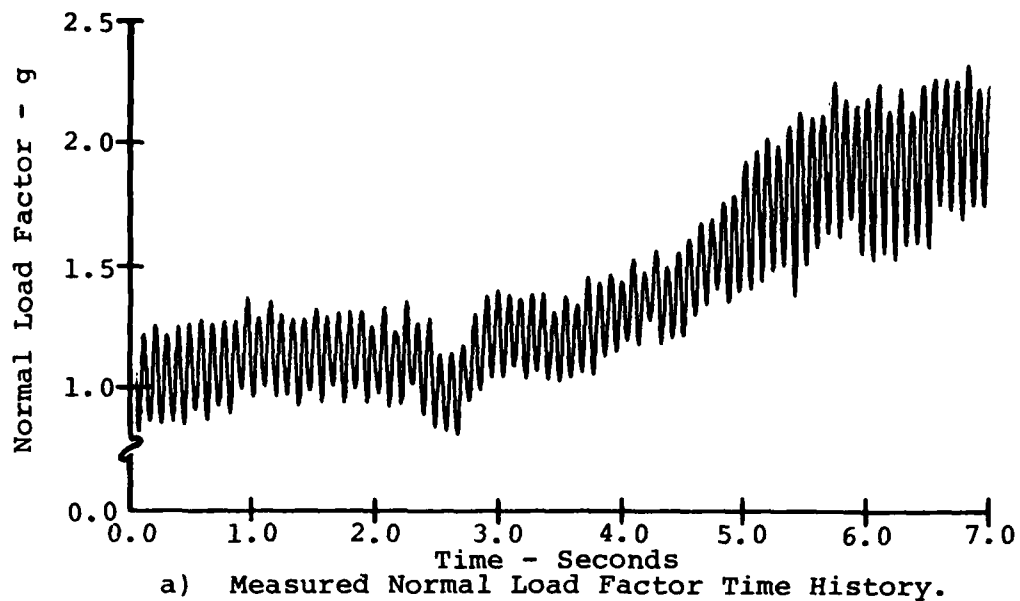
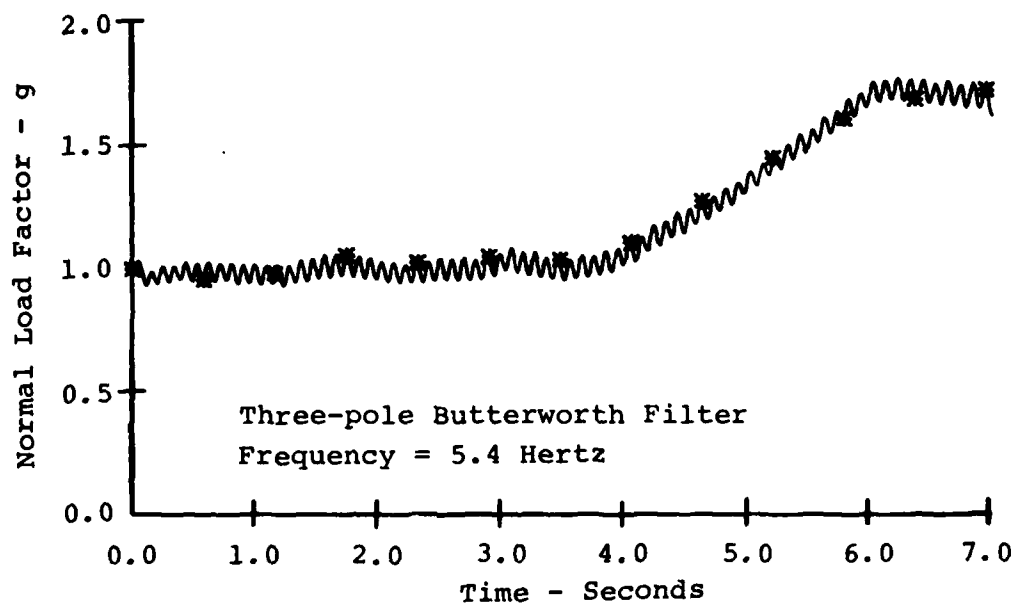


Figure 68. Comparison of Measured and Computed Normal Load Factor Time Histories for the Right Rolling Pullout Maneuver of Counter 561.





c) Computed Normal Load Factor Time History - Filtered.

Figure 68. Concluded.

The filtered results show that the aircraft reaches a maximum normal load factor of about 1.7g, while the test data show a maximum mean normal load factor of about 1.95g.

The normal load factor is a function of several variables, as seen by rewriting Equation (4.12.1.b) from page 116 of Etkin (Reference 9),

$$\begin{aligned} \text{Normal Load Factor} &= \frac{-Z}{m} & (28) \\ &= -(\dot{W} + pV - qU - g\cos\theta\cos\phi) \end{aligned}$$

where  $z$  is the total body-axis vertical force

$m$  is the aircraft mass

$\dot{W}$  is the body-axis vertical acceleration due to purely vertical motion

$p$  is the body-axis roll rate

$V$  is the body-axis lateral velocity

$q$  is the body-axis pitch rate

$U$  is the body-axis longitudinal velocity

$g$  is the acceleration due to gravity

$\theta$  is the Euler pitch attitude

$\phi$  is the Euler roll attitude

Although the roll rate,  $p$ , is large for this maneuver, the lateral velocity is small, so the  $pV$  term is small. The pitch rate and longitudinal velocities are both large during the peak-g portion of the maneuver, so their product,  $qU$ , is a primary term in Equation 28. At five seconds into the maneuver, the measured and computed pitch rates and airspeeds are about the same, so the  $qU$  terms should be similar. The measured and computed roll and pitch attitudes are also very similar at five seconds maneuver time, so the  $g\cos\theta\cos\phi$  terms are similar between the test and the simulation. The only term in Equation 28 that could be different between the

flight test and the simulation is  $\dot{W}$ . This quantity was not measured and cannot be accurately deduced from the available test data, so the source of the difference between the measured and computed load factor can only be suspected to be the  $\dot{W}$  term.

The measured and computed normal load factor time histories for the symmetric pullup maneuver of counter 562 are compared in Figure 69. The unfiltered time history produced by C81 is in reasonable agreement with the experimental data, although the simulation experiences a more oscillatory normal load factor early in the maneuver, while the test data show an increase in oscillatory load later in the maneuver. The filtered time history shows that the simulation achieves a peak normal load factor near 1.6g, while the peak mean value of the experimental data is about 1.7g.

The  $\dot{W}$  term must again be suspected as the cause for the difference between the maximum measured and computed normal load factors, as the measured and computed time histories for  $q$ ,  $\theta$  and  $\phi$  are quite similar. (The measured and computed roll rate time histories are not similar, but the lateral velocity is negligible, so the  $pV$  term is very small in comparison to the other terms in Equation 28.)

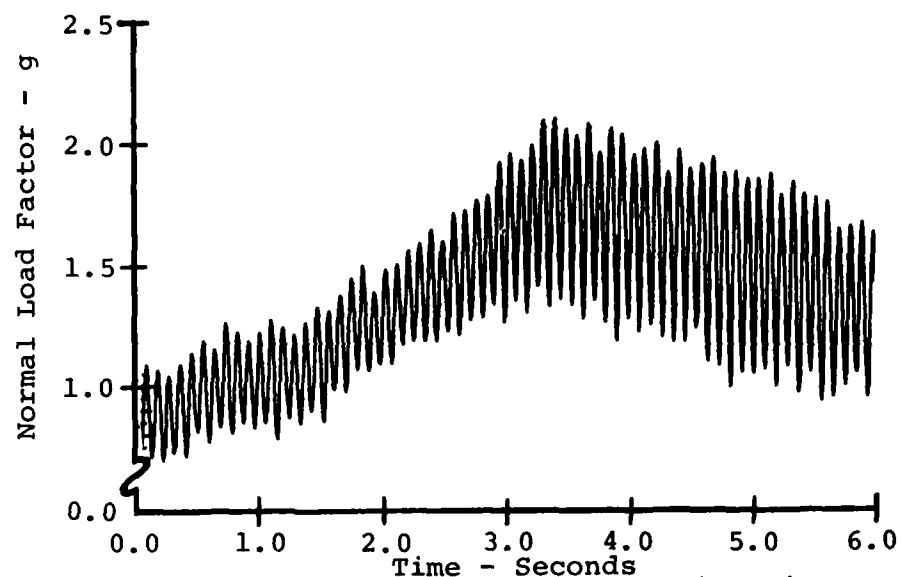
#### 7.2.3 Comparison of Measured and Computed Fuselage Euler Attitudes

The attitude instrumentation installed in the OLS test vehicle measured the Euler angles of the aircraft with respect to the earth.

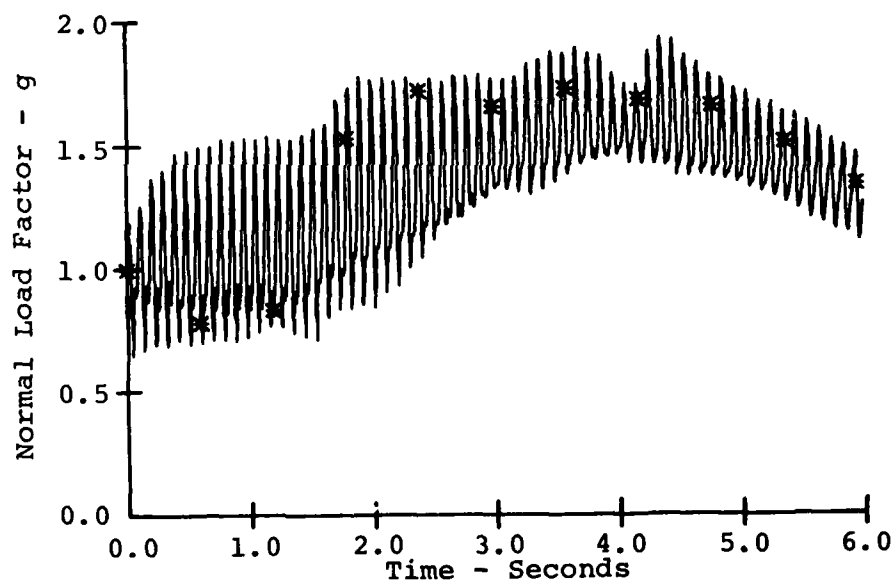
The roll attitude time histories measured in flight and computed in the simulation of the right-rolling pullout maneuver of counter 561 are compared in Figure 70. The two traces are almost identical, starting at -2.5 degrees at zero time. The roll attitude time history in the simulation passes through zero about 0.3 second later than the measured time history. The maximum roll angle achieved in the simulation is about 38 degrees, while the maximum measured roll angle was about 50 degrees.

The pitch attitude time histories for this maneuver are compared in Figure 71. The two time histories are remarkably similar. The simulated aircraft trims about one degree more nose down than the test aircraft, and the pitch attitude remained approximately constant for the first 3 seconds of the simulated maneuver and for the first 4 seconds during the actual maneuver. The pitch attitude time history goes through zero in the simulation about 0.2 second later than in the flight test and reaches a maximum value of about nine degrees, while the maximum experimental value was about five degrees.

The measured and computed yaw attitude time histories for the right-rolling pullout maneuver of counter 561 are plotted in Figure 72. The yaw gyro installed in the OLS aircraft did

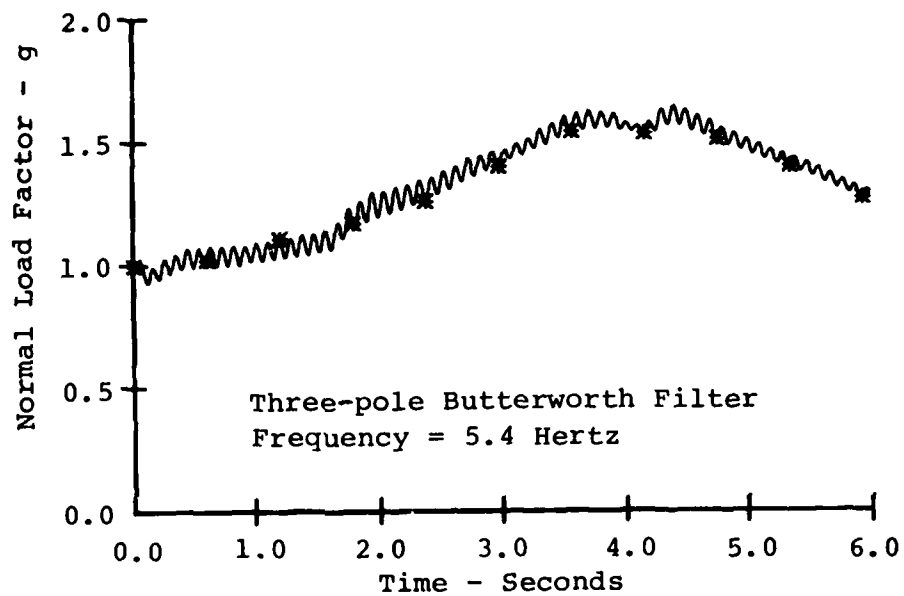


a) Measured Normal Load Factor Time History.



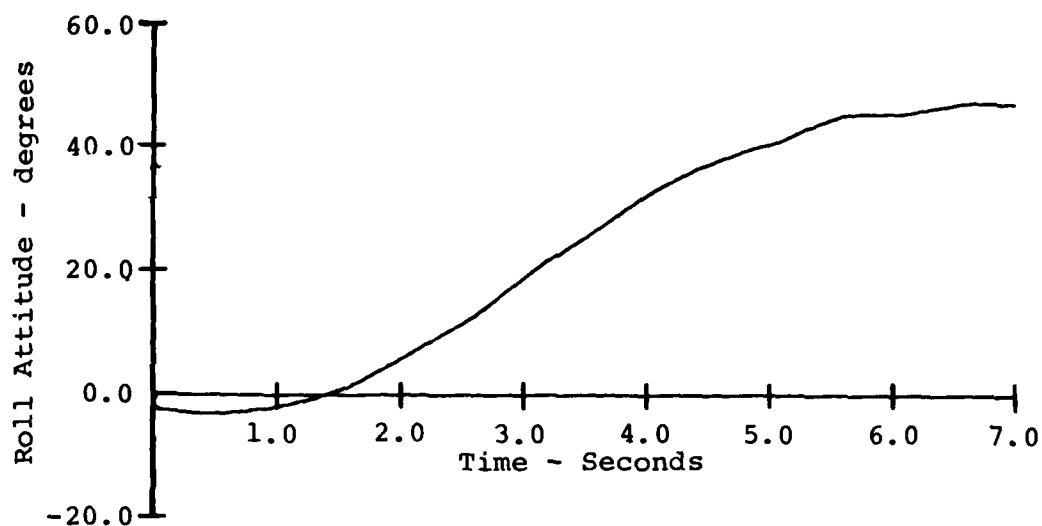
b) Computed Normal Load Factor Time History - Unfiltered.

Figure 69. Comparison of Measured and Computed Normal Load Factor Time Histories for the Symmetric Pullup Maneuver of Counter 562.

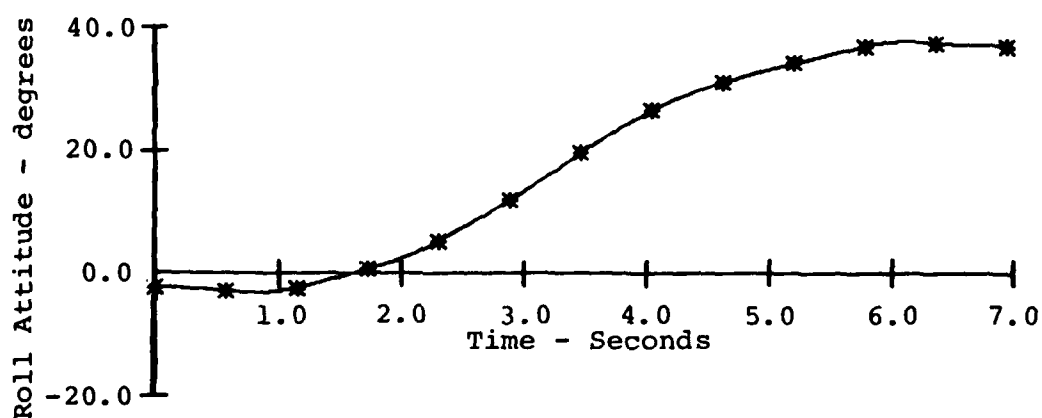


c) Computed Normal Load Factor Time History - Filtered.

Figure 69. Concluded.

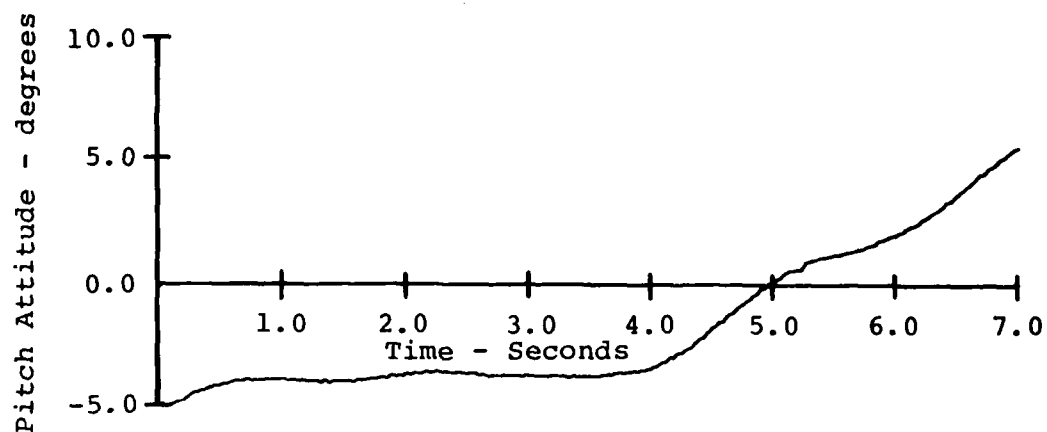


a) Measured Roll Attitude Time History.

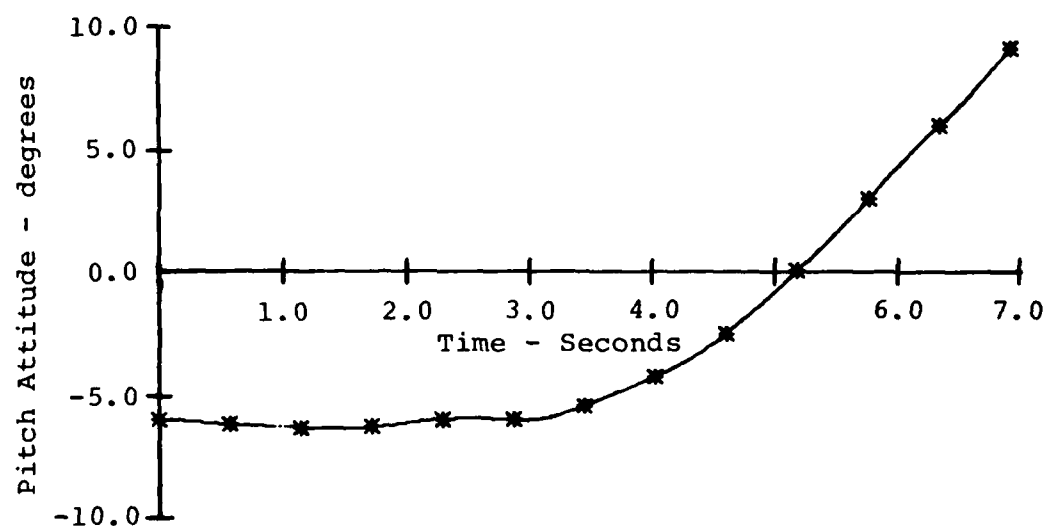


b) Computed Roll Attitude Time History.

Figure 70. Comparison of Measured and Computed Airframe Roll Attitude Time Histories for the Right Rolling Pullout Maneuver of Counter 561.

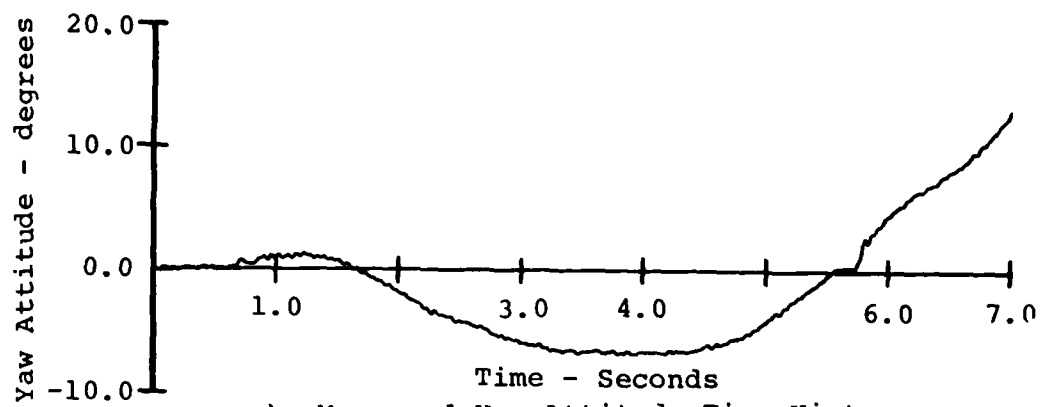


a) Measured Pitch Attitude Time History.

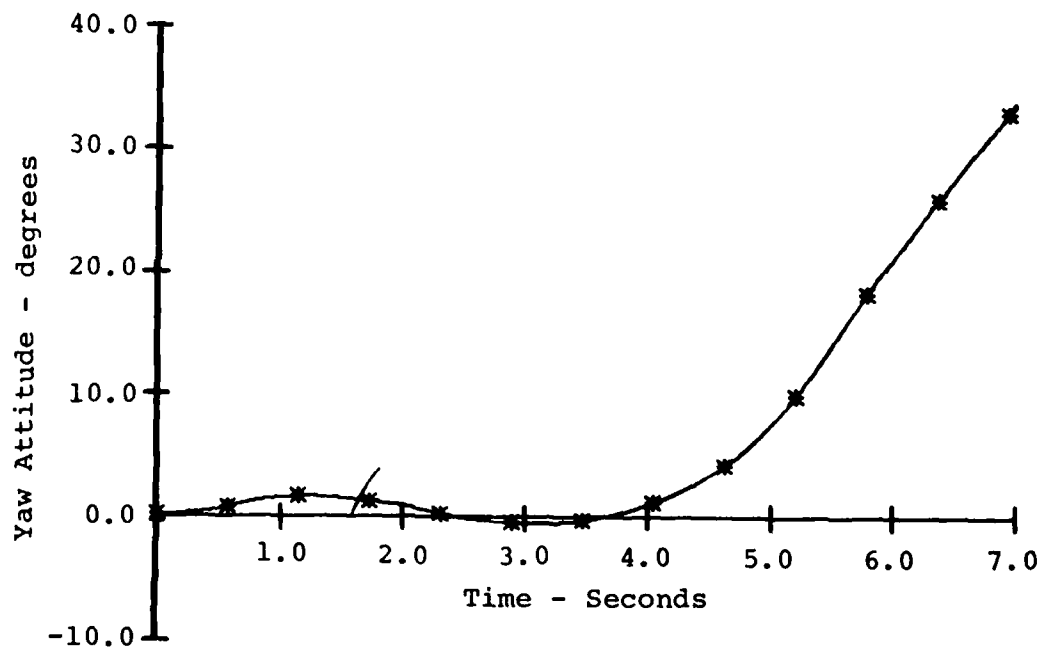


b) Computed Pitch Attitude Time History.

Figure 71. Comparison of Measured and Computed Airframe Pitch Attitude Time Histories for the Right Rolling Pullout Maneuver of Counter 561.



a) Measured Yaw Attitude Time History.



b) Computed Yaw Attitude Time History.

Figure 72. Comparison of Measured and Computed Airframe Yaw Attitude Time Histories for the Right Rolling Pullout Maneuver of Counter 561.



not measure heading angle. It remained caged until the prime data button was activated, beginning recording of the test data. Therefore, the yaw gyro measured yaw deviation from the yaw attitude at the beginning of the maneuver. The two yaw attitude time histories do not agree as well as the roll or pitch time histories, with the simulated aircraft yawing significantly more than the test vehicle. This discrepancy is difficult to understand in view of the excellent correspondence between the measured and computed yaw rate time histories.

The roll attitude time histories for the symmetric pullup maneuver of counter 562 are compared in Figure 73. The measured and computed traces are not in very good agreement, but the roll rate time history in the simulation did not agree with the measured roll rate time history (see Figure 65).

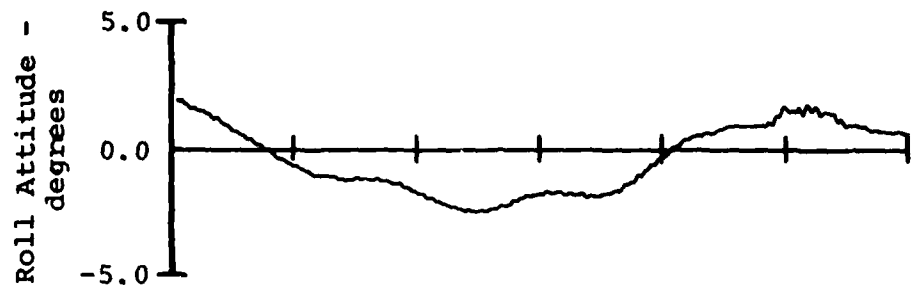
The pitch attitude time history resulting from the simulation of the symmetric pullup is compared with the measured time history in Figure 74. The two curves are in very close agreement, with the aircraft starting the maneuver at a slightly more nose-up pitch attitude in the simulation than in the test. Both time histories cross zero at about the same time, and reach almost the same maximum value at six seconds maneuver time.

The measured and computed yaw attitude time histories are compared in Figure 75. The aircraft trimmed at about  $-5.0$  degrees yaw in the simulation, and the yaw angle remained essentially constant throughout the maneuver. The yaw gyro was uncaged at the beginning of the test record and a small nose-right yaw deviation occurred at about 3.5 seconds in the maneuver, reaching a maximum value of about four degrees.

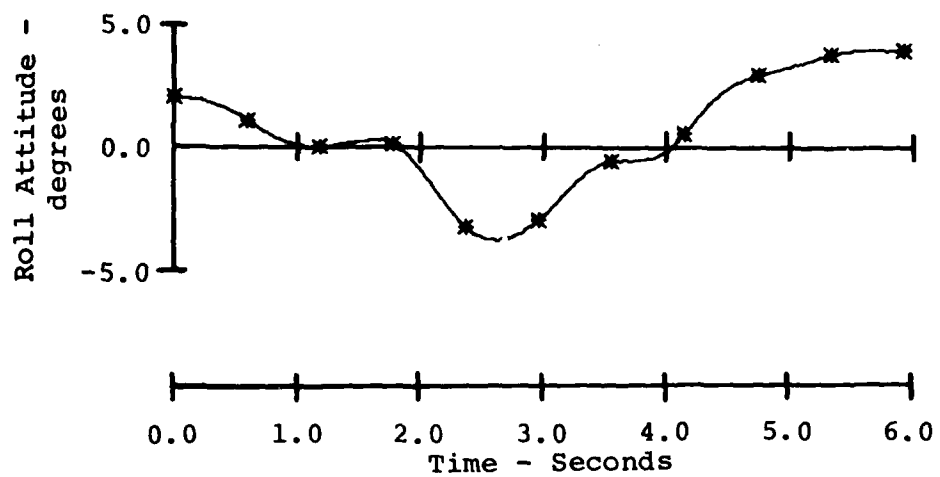
#### 7.2.4 Comparison of Measured and Computed Airframe Aerodynamic Angles

The airspeed-boom-measured aircraft angle of attack and sideslip angle time histories have been compared with those of the simulation for both the right-rolling pullout and the symmetric pullup. Since both maneuvers were entered at high forward speed, the effects of rotor downwash on the measured angle of attack should be minimal.

The airframe angle-of-attack time history in the simulation of the rolling pullout maneuver is almost identical to that measured in flight (Figure 76). The measured and computed sideslip time histories are not in as good agreement for this maneuver, though, as shown in Figure 77.

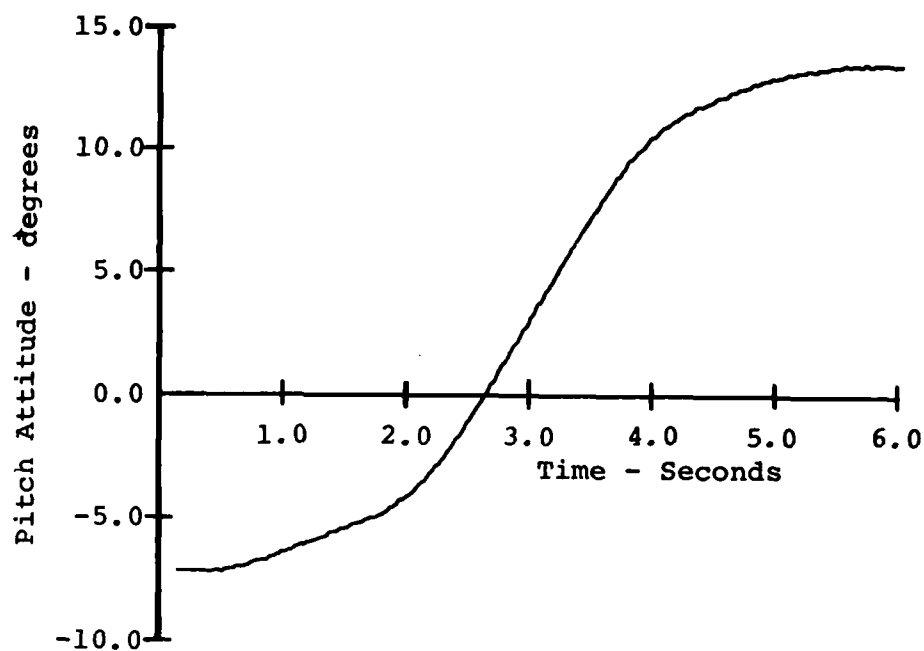


a) Measured Roll Attitude Time History.

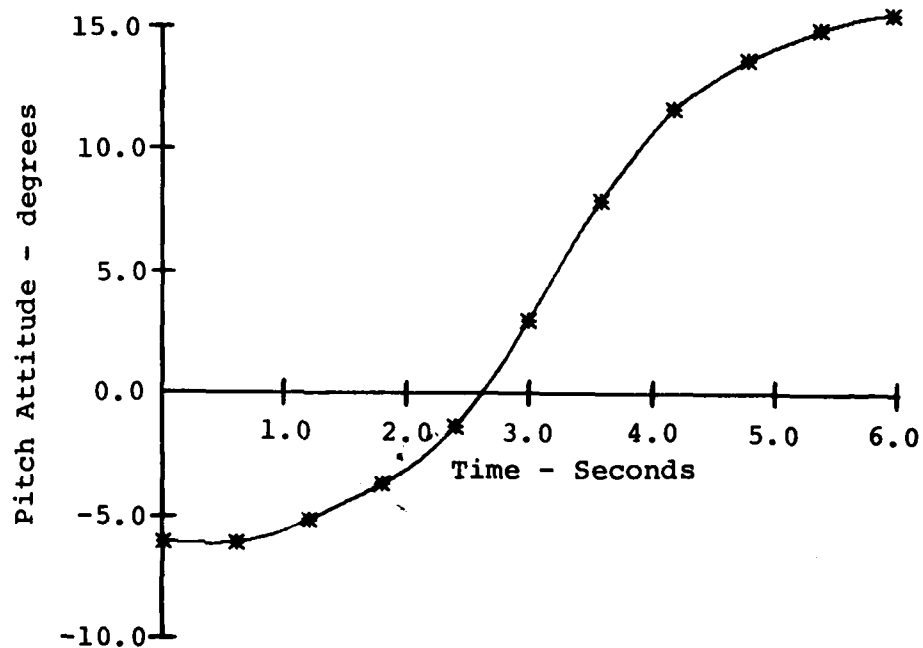


b) Computed Roll Attitude Time History.

Figure 73. Comparison of Measured and Computed Airframe Roll Attitude Time Histories for the Symmetric Pullup Maneuver of Counter 562.

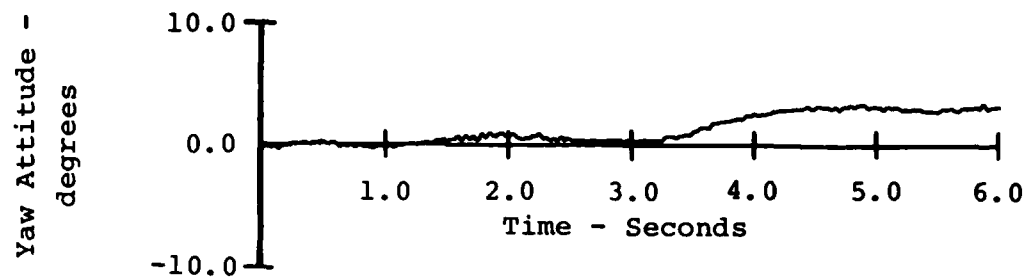


a) Measured Pitch Attitude Time History.

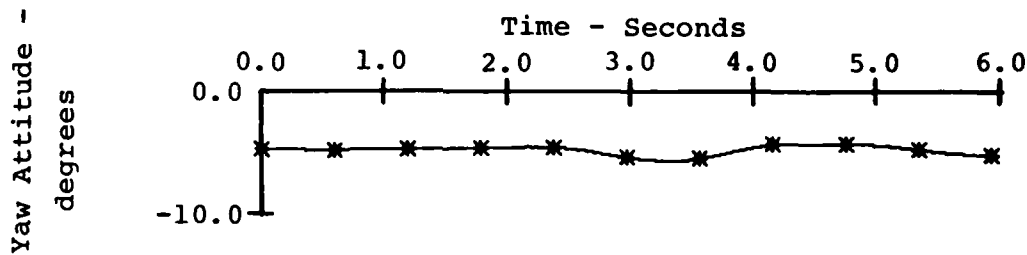


b) Computed Pitch Attitude Time History.

Figure 74. Comparison of Measured and Computed Airframe Pitch Attitude Time Histories for the Symmetric Pullup Maneuver of Counter 562.

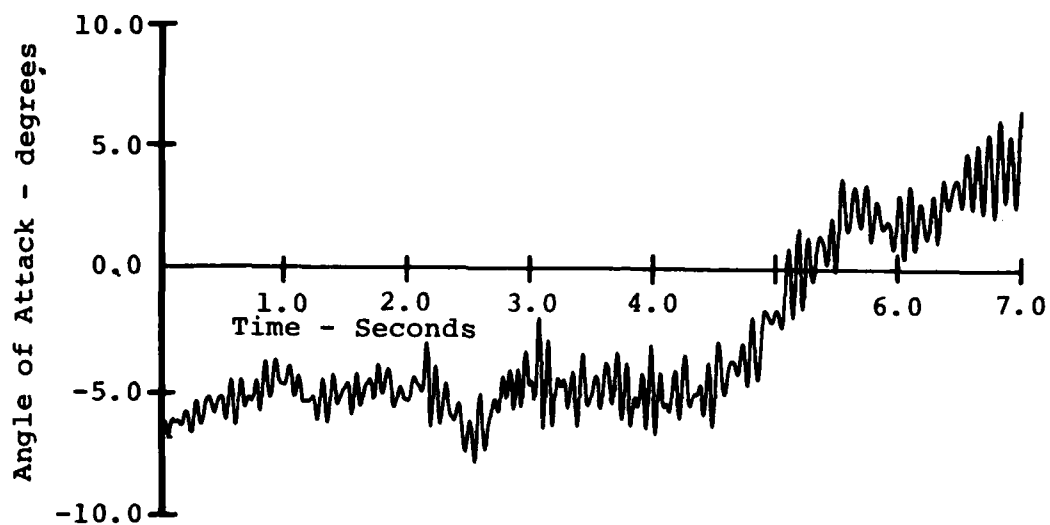


a) Measured Yaw Attitude Time History.

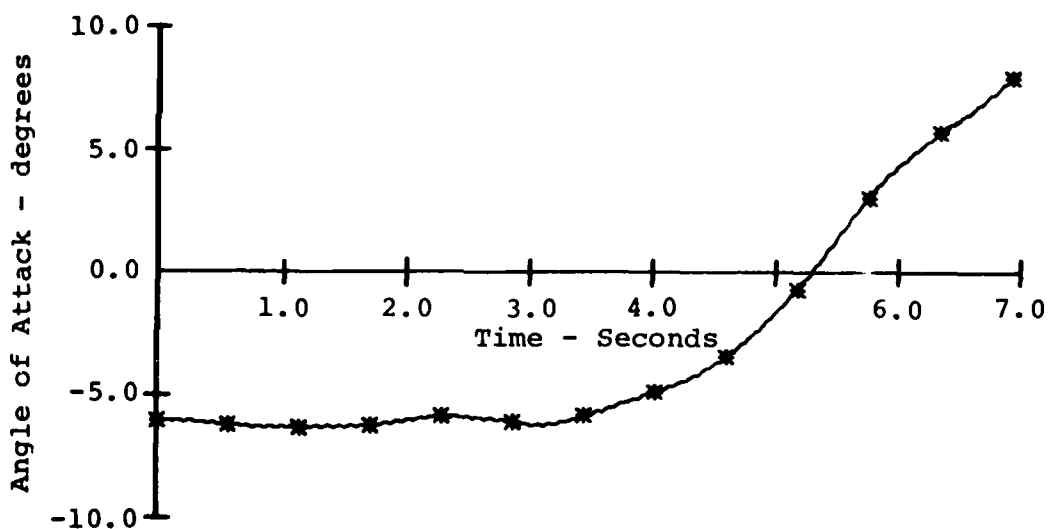


b) Computed Yaw Attitude Time History.

Figure 75. Comparison of Measured and Computed Airframe Yaw Attitude Time Histories for the Symmetric Pullup Maneuver of Counter 562.

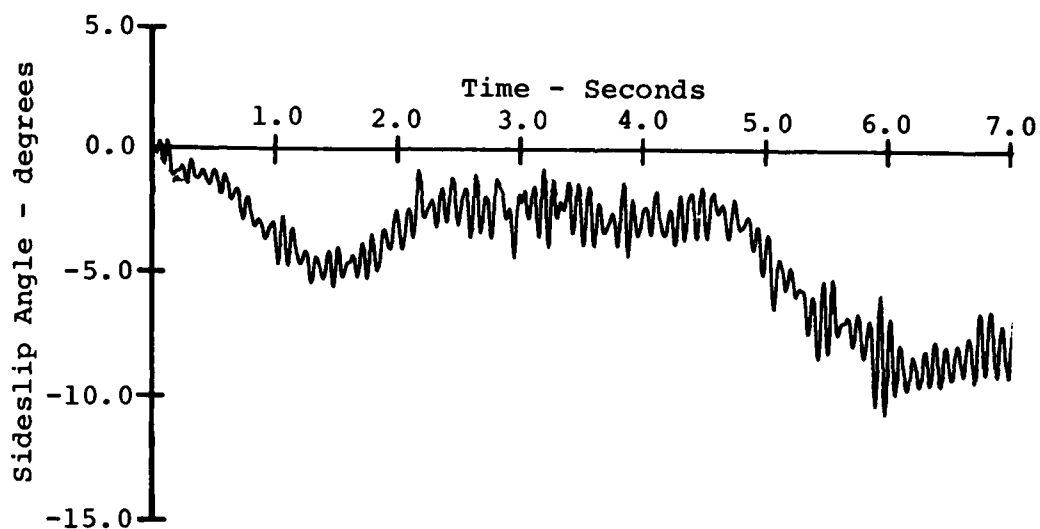


a) Measured Angle-of-Attack Time History.

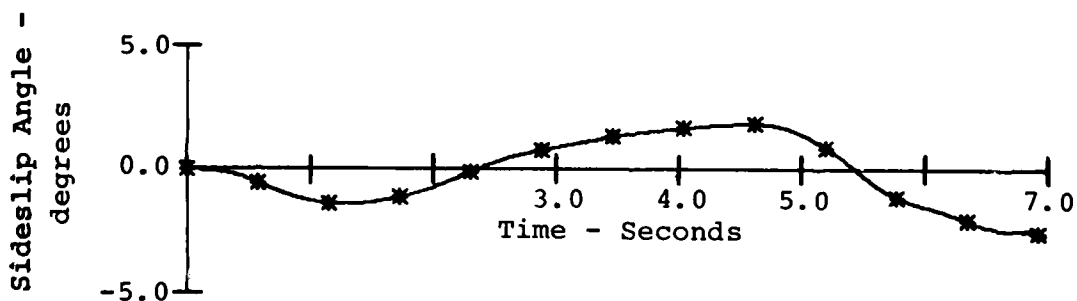


b) Computed Angle-of-Attack Time History.

Figure 76. Comparison of Measured and Computed Airspeed/ Boom Angle-of-Attack Time Histories for the Right Rolling Pullout Maneuver of Counter 561.



a) Measured Sideslip Angle Time History.



b) Computed Sideslip Angle Time History.

Figure 77. Comparison of Measured and Computed Airspeed/ Boom Sideslip Angle Time History for the Right Rolling Pullout Maneuver of Counter 561.

The computed and measured aircraft angle-of-attack time histories for the symmetric pullup maneuver are presented in Figure 78, with excellent agreement between the two traces. The measured sideslip angle time history is quite different from that computed in the simulation (Figure 79), due, in part, to a large difference between the measured and computed trimmed sideslip angles at the beginning of the maneuver.

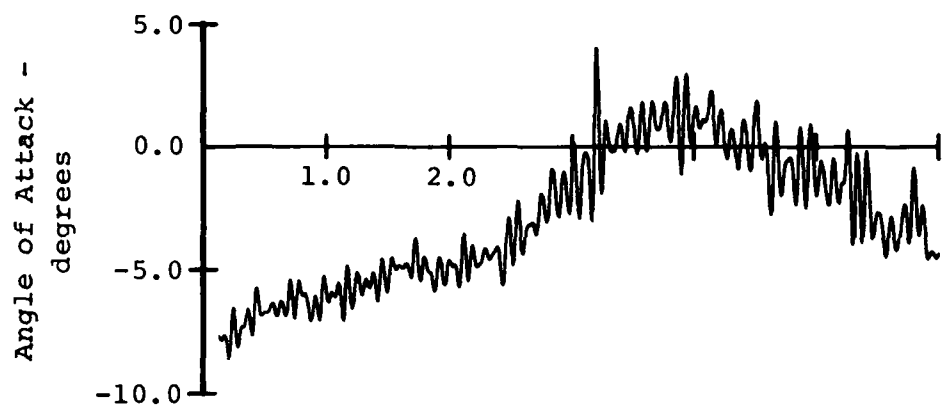
#### 7.2.5 Comparison of Measured and Computed Main-Rotor and Tail-Rotor Torque and Engine RPM

The time histories of the measured and computed main-rotor torque are plotted in Figure 80. The measured torque-required curve shows very little oscillatory loading, and the mean torque declines steadily, due to the beneficial effects of pitch rate. The required torque time history for the simulated main rotor contains a good deal of two-per-rev loading, and the mean value, which starts at a slightly lower value than the measured mean torque, remains reasonably constant for the first 4 seconds of the maneuver. The torque-required then rises to a peak at about 5.3 seconds and decreases for the remainder of the maneuver. The large two-per-rev content and the constant or increasing torque-required behavior both indicate a large amount of retreating blade stall.

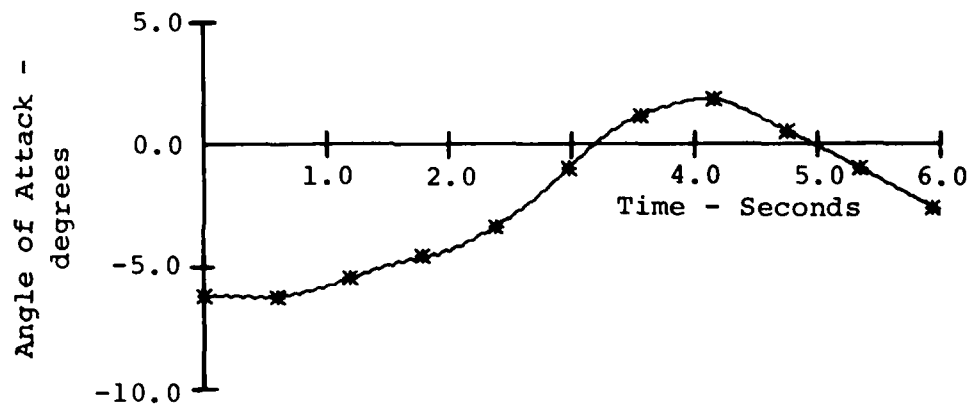
It should be noted that rotor torque is computed in C81 by summing the moment about the shaft of the inplane airloads only; inplane inertia loads are not included in the shaft torque calculations. Further, the mast torsional degree of freedom was not included in the model. The absence of a large two-per-rev component in the measured mast torque could be due to the possible reduction of inplane loads transmitted to the mast resulting from inertia relief or from mast flexibility.

The measured and computed tail-rotor mast torque time histories for the right-rolling pullout maneuver are compared in Figure 81. The simulated tail rotor requires slightly more torque at the beginning of the maneuver than did the test article, and exhibits less oscillatory torque throughout the maneuver. The mean measured and computed mast torques are in reasonable agreement for the entire maneuver.

Figure 82 contains the time histories of the engine RPM for the right-rolling pullout maneuver. The measured engine RPM increases steadily during the course of the maneuver, due to the decrease in required torque for the main and tail rotors. The computed engine RPM decreases steadily due to the increased torque demanded by the main rotor. The measured and computed RPM time histories do not agree because the rotors



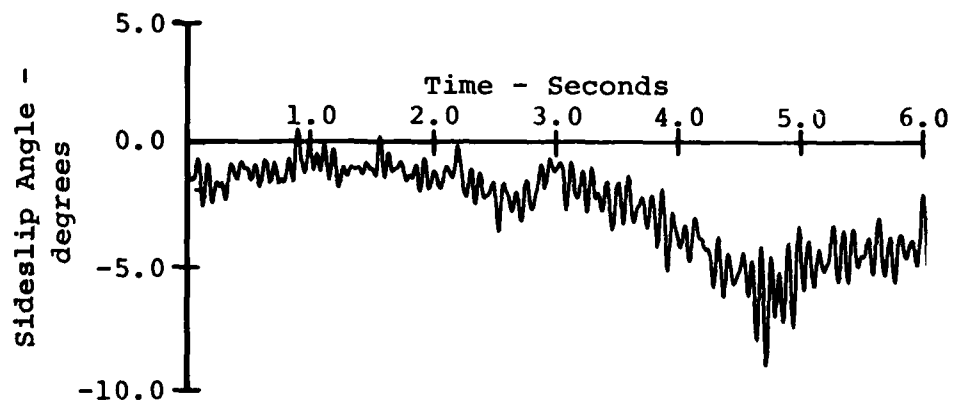
a) Measured Angle-of-Attack Time History.



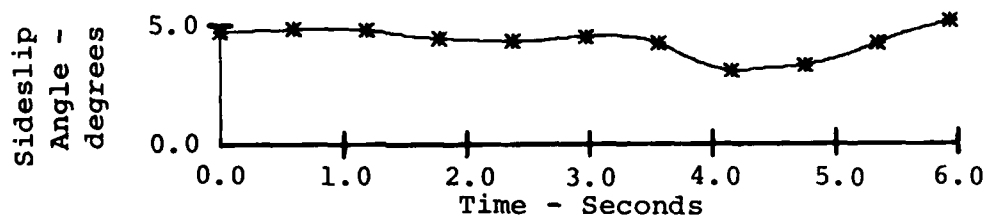
b) Computed Angle-of-Attack Time History.

Figure 78. Comparison of Measured and Computed Airspeed/Boom Angle of Attack Time Histories for the Symmetric Pullup Maneuver of Counter 562.



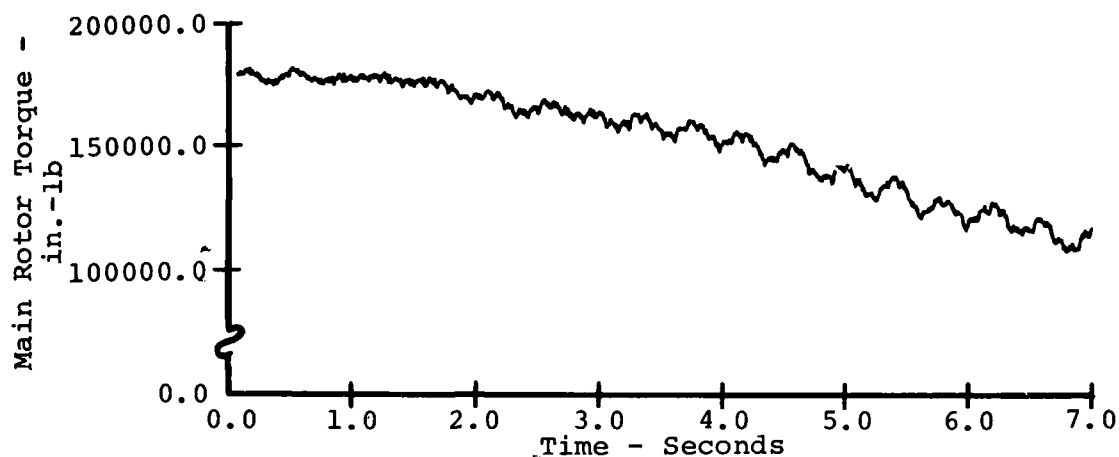


a) Measured Sideslip Angle Time History.

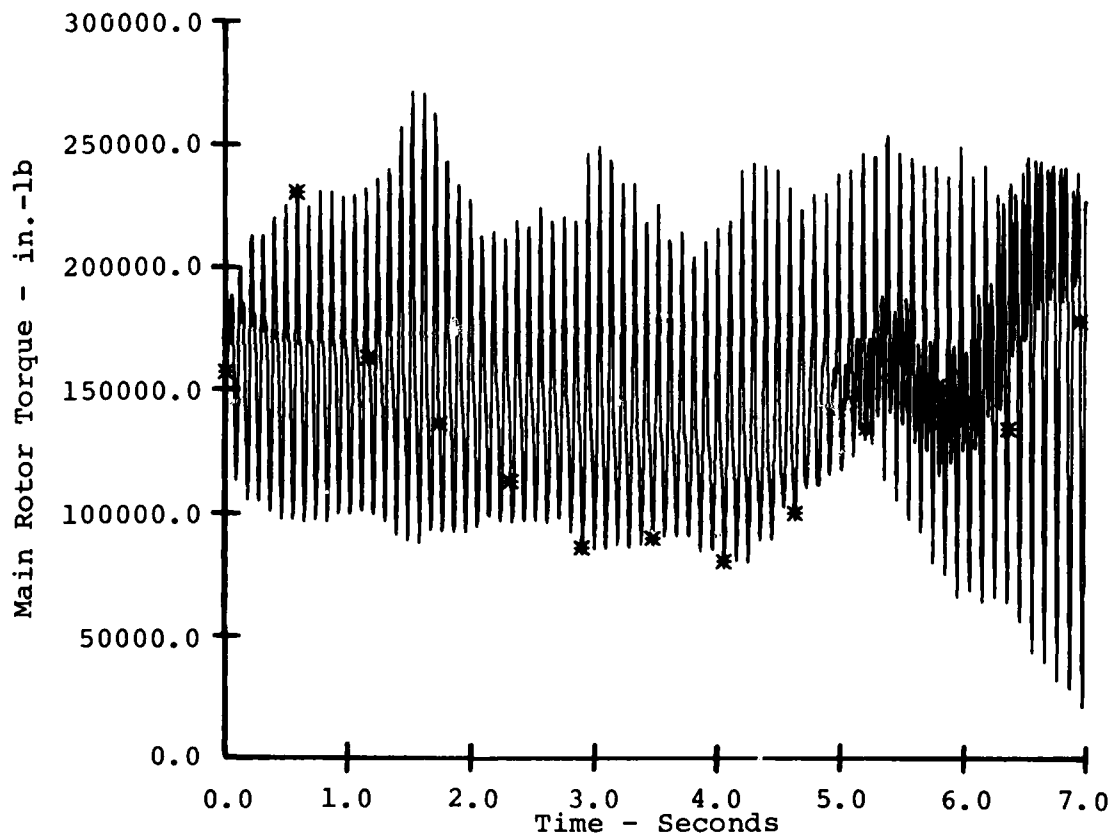


b) Computed Sideslip Angle Time History.

Figure 79. Comparison of Measured and Computed Airspeed/Boom Sideslip Angle Time Histories for the Symmetric Pullup Maneuver of Counter 562.



a) Measured Main Rotor Torque Time History.



b) Computed Main Rotor Torque Time History.

Figure 80. Comparison of Measured and Computed Main Rotor Torque Time Histories for the Right Rolling Pullout Maneuver of Counter 561.

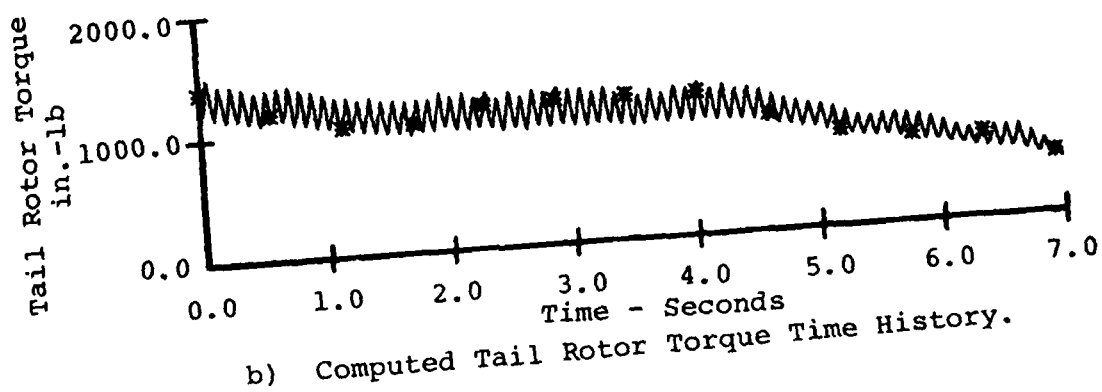
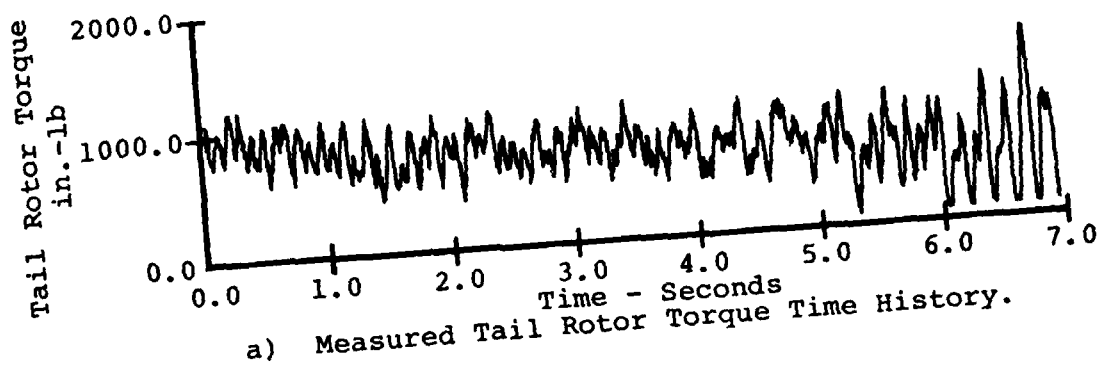
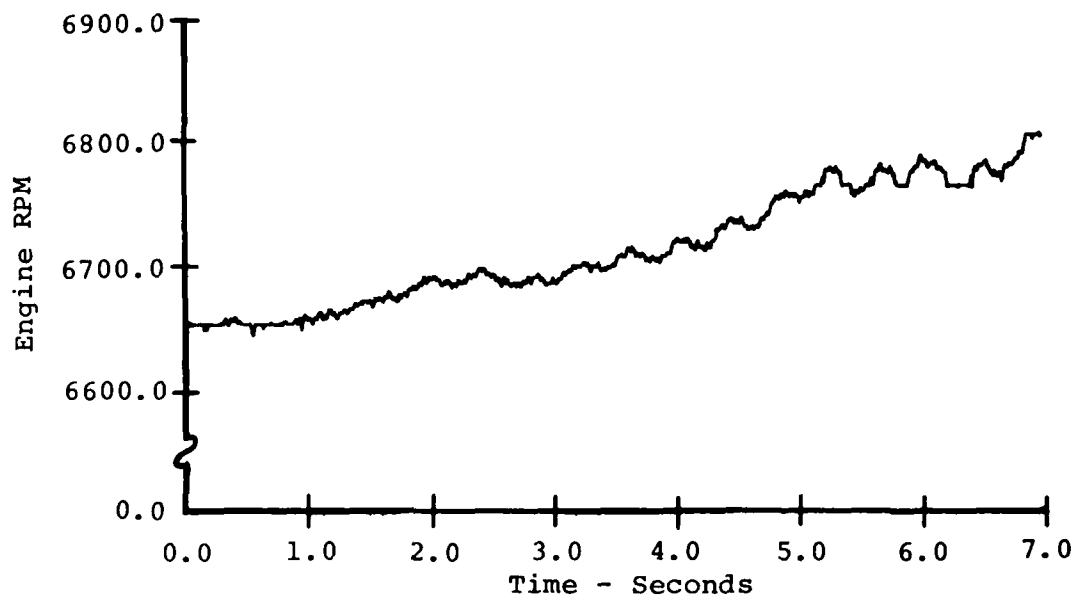
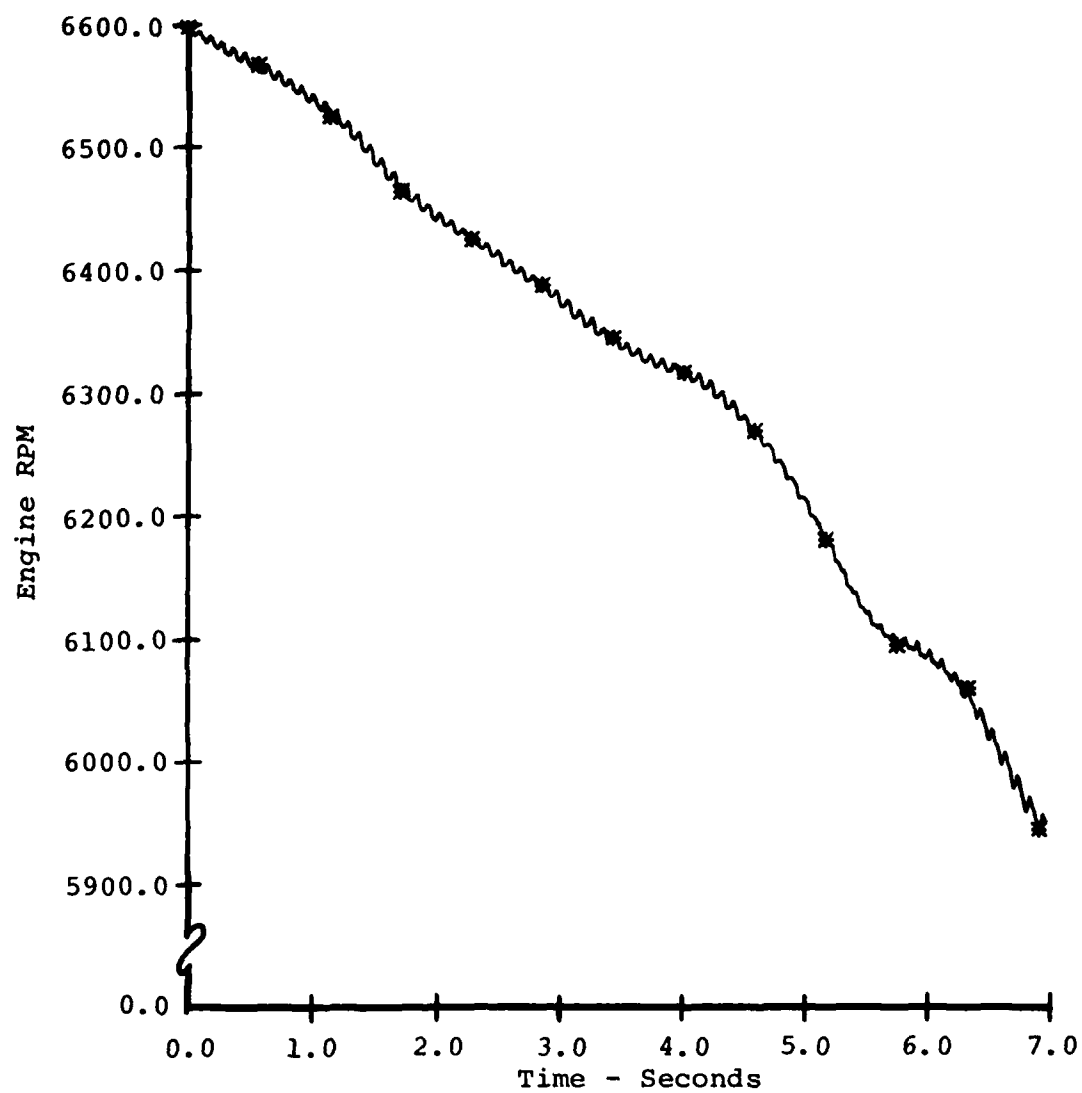


Figure 81. Comparison of Measured and Computed Tail Rotor Torque Time Histories for the Right Rolling Pullout Maneuver of Counter 561.



a) Measured Engine RPM Time History.

Figure 82. Comparison of Measured and Computed Engine RPM Time Histories for the Right Rolling Pullout Maneuver of Counter 561.



b) Computed Engine RPM Time History.

Figure 82. Concluded.

remained essentially unstalled during the test flight while the main rotor experiences some stall in the simulated maneuver.

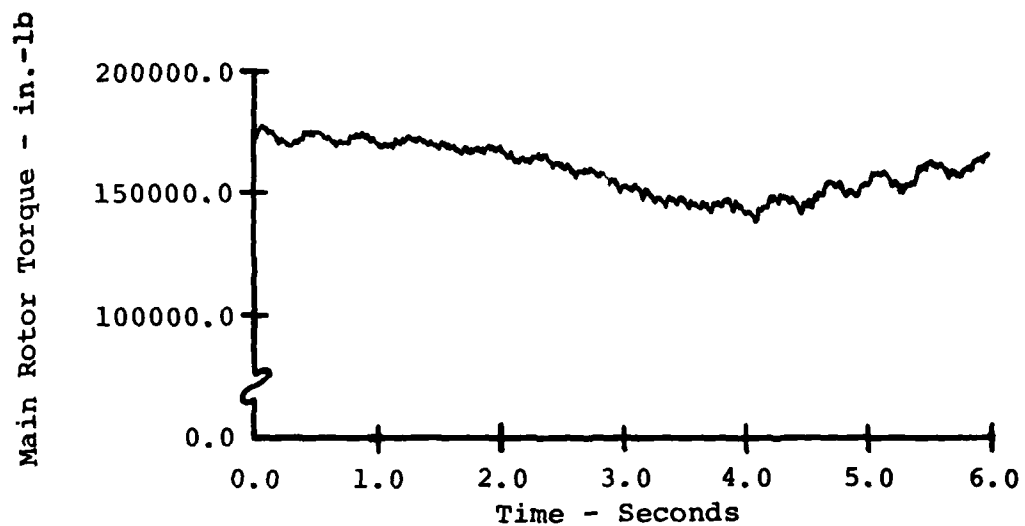
The main rotor shaft torque time histories for the symmetric pullup maneuver of counter 562 are compared in Figure 83. The simulated aircraft trims with lower mean torque required for the main rotor than the OLS test aircraft, but the mean torque required increases almost immediately, reaching a peak at approximately 2 seconds. The measured main rotor torque-required decreases slightly until 4 seconds and then begins to increase. The computed main rotor torque-required time history demonstrates a good deal of two-per-rev content (due to the use of just the airloads in its calculation) and rotor stall is indicated.

The computed mean tail rotor torque is approximately 1900 inch-pounds at the beginning of the symmetric pullup maneuver (Figure 84) while the measured mean tail rotor torque was about 900 inch-pounds. This discrepancy results from the difference in trimmed sideslip angles (Figure 79), as the tail rotor in the simulation is holding the aircraft more than 6 degrees more nose-left than the test aircraft. This requires more right side force from the tail rotor, which would require more tail rotor torque. The measured and computed tail rotor torque time histories have similar variations through the course of the maneuver.

The engine RPM time histories for the symmetric pullup are compared in Figure 85. The measured engine speed increases between 2.0 and 3.5 seconds and then returns to its trim value in response to the variations in torque required. The engine RPM in the simulation decreases steadily for the first 3 seconds, due to the increasing mean main-rotor torque at the beginning of the maneuver. The engine speed is almost constant for the last 3 seconds of the maneuver as a result of the decreasing main rotor torque during the latter portion of the maneuver.

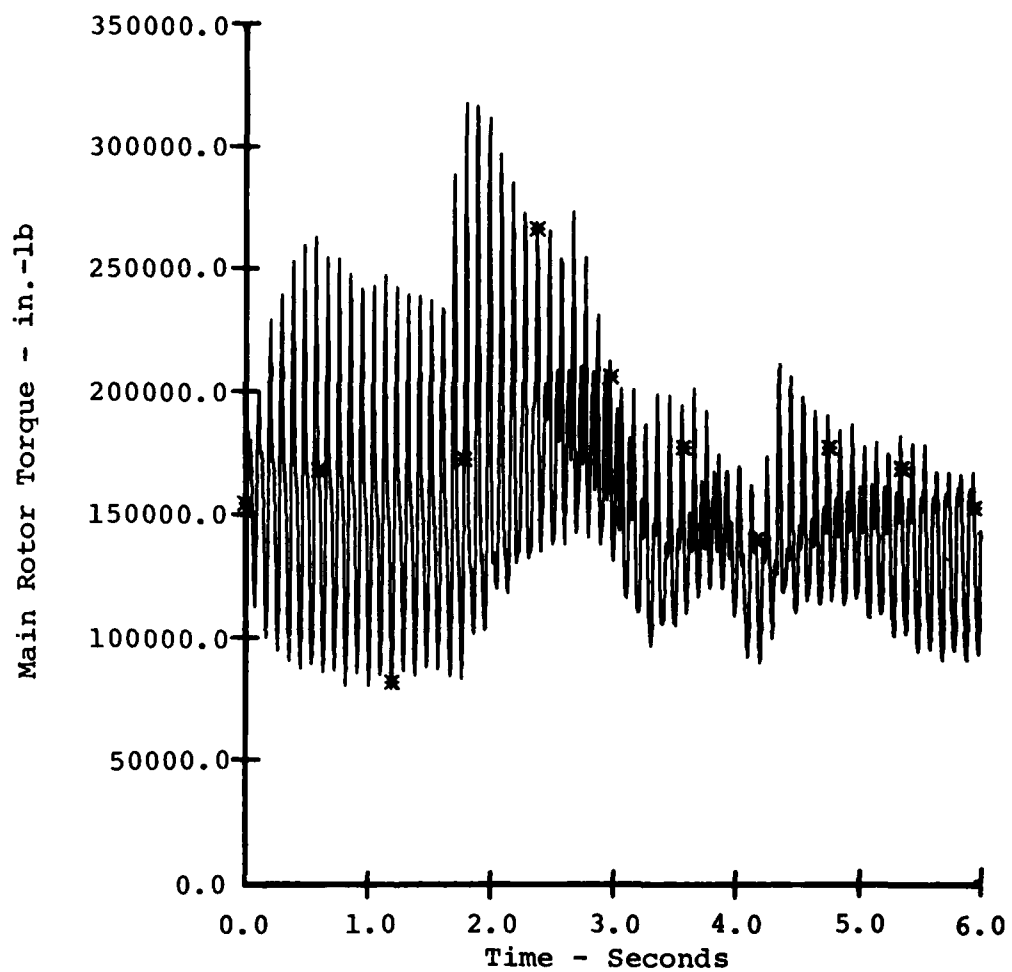
#### 7.2.6 Comparison of Measured and Computed Main-Rotor Hub Flapping Angles

The measured and computed main rotor hub flapping angle time histories for both maneuvers simulated are plotted in Figures 86 and 87. The measured main rotor hub flapping time histories have a pronounced zero-shift. There is little agreement between the flapping recorded during the test flights and that computed by the program, which is surprising in view of the excellent correspondence between the measured and computed aircraft motion. The maximum oscillatory flapping computed



a) Measured Main Rotor Torque Time History.

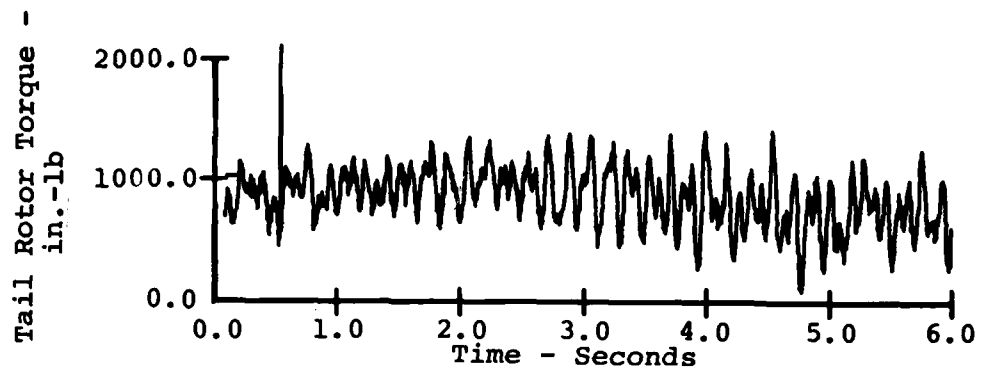
Figure 83. Comparison of Measured and Computed Main Rotor Torque Time Histories for the Symmetric Pullup Maneuver of Counter 562.



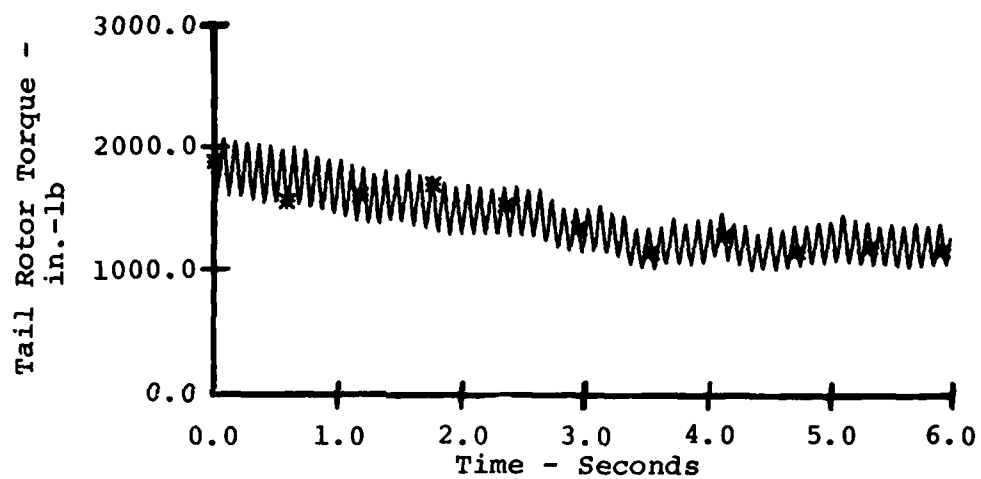
b) Computed Main Rotor Torque Time History.

Figure 83. Concluded.



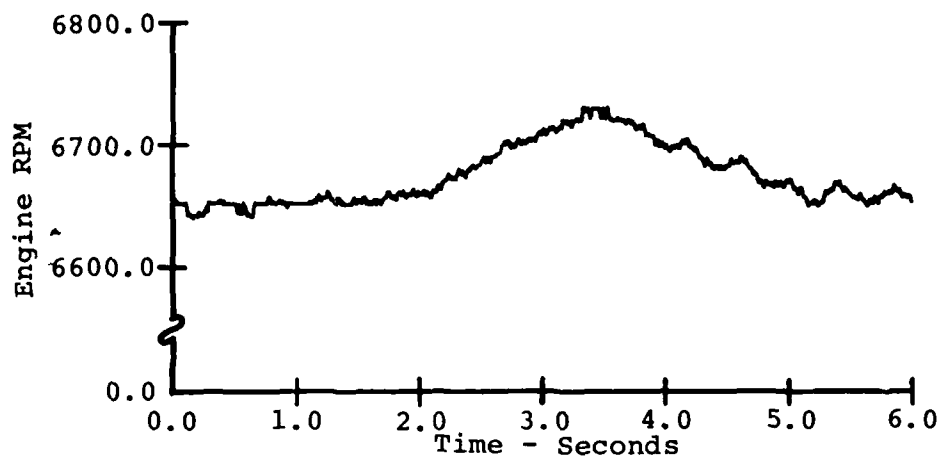


a) Measured Tail Rotor Torque Time History.

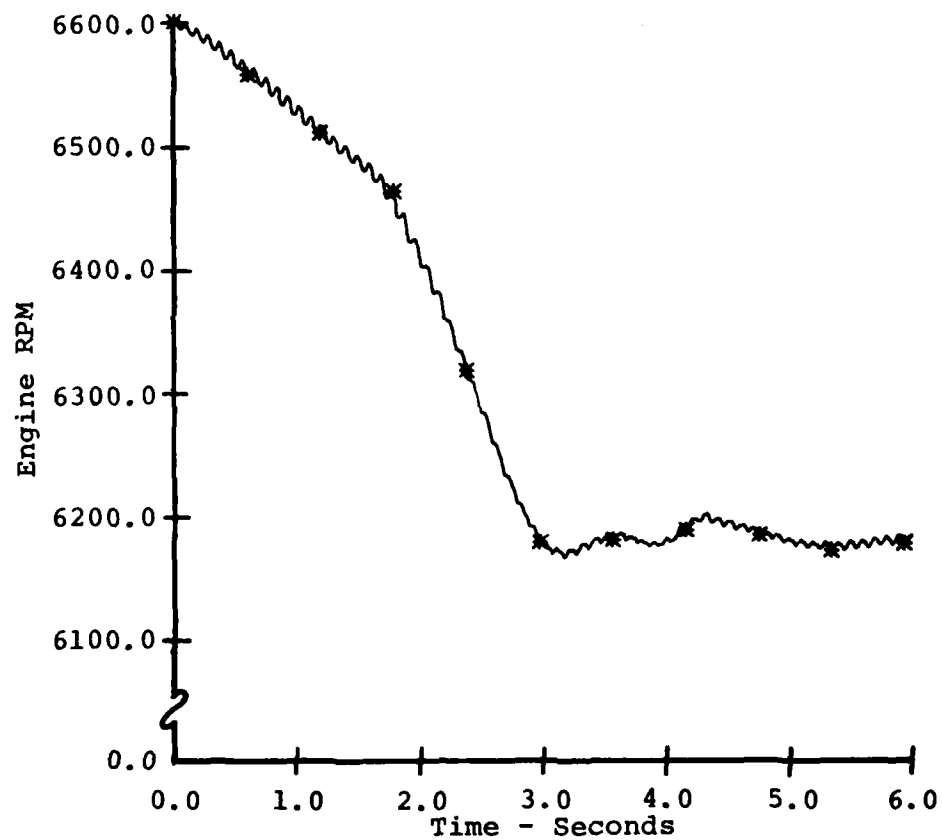


b) Computed Tail Rotor Torque Time History.

Figure 84. Comparison of Measured and Computed Tail Rotor Torque Time Histories for the Symmetric Pullup Maneuver of Counter 562.



a) Measured Engine RPM Time History.



b) Computed Engine RPM Time History.

Figure 85. Comparison of Measured and Computed Engine RPM Time Histories for the Symmetric Pullup Maneuver of Counter 562.

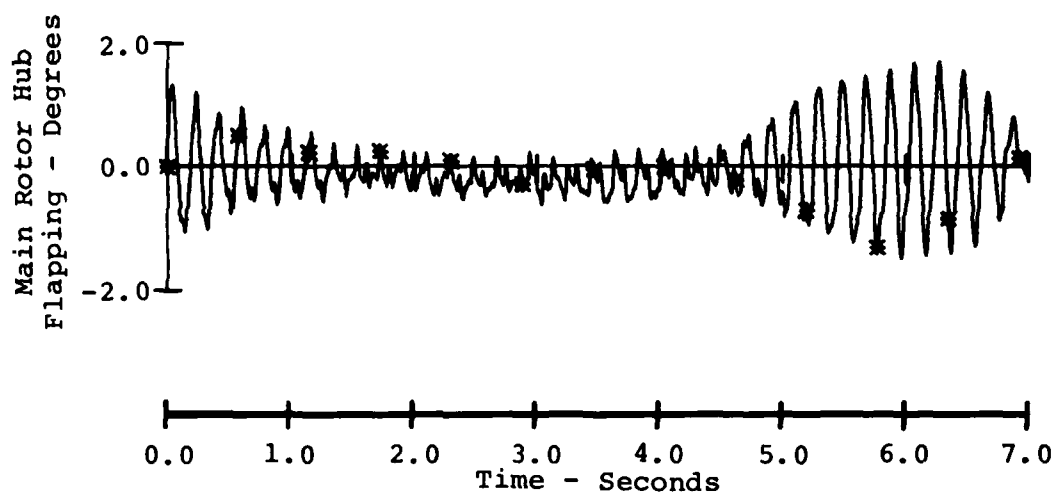
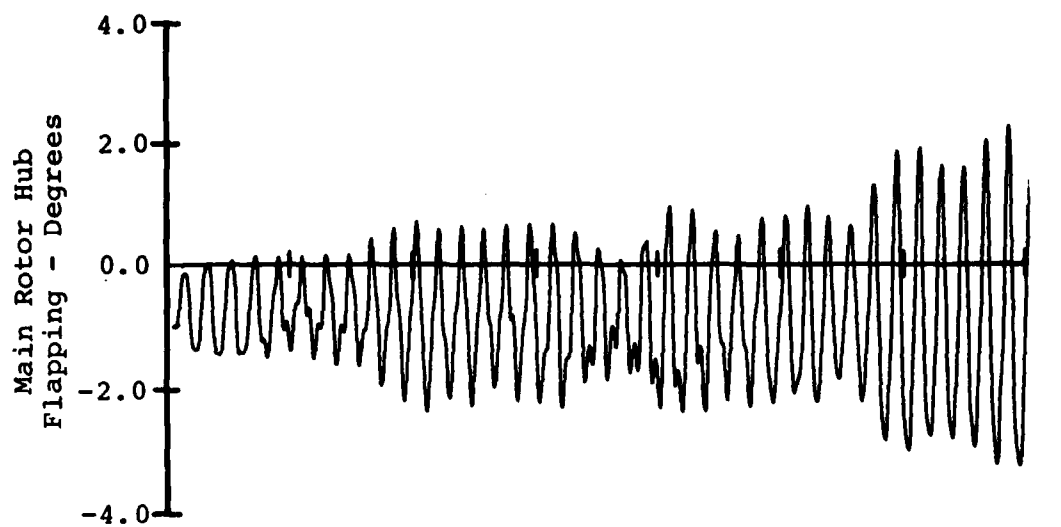
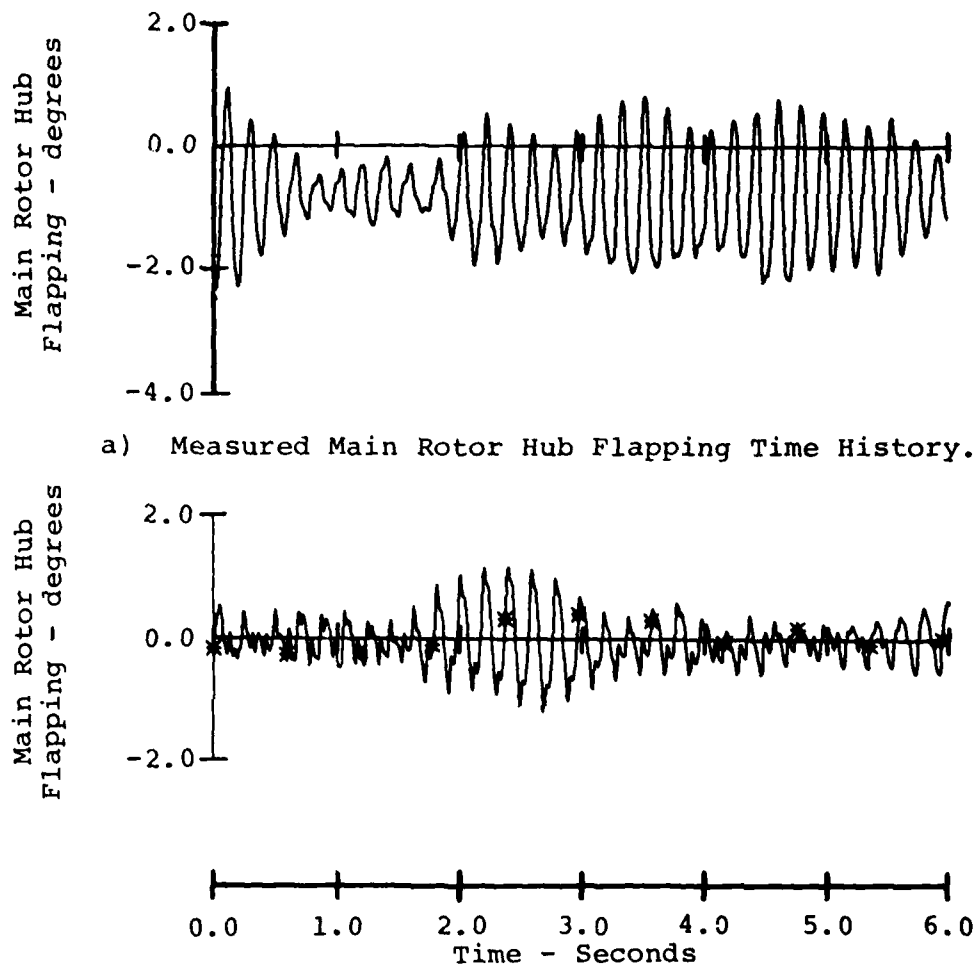


Figure 86. Comparison of Measured and Computed Main Rotor Hub Flapping Time Histories for the Right Rolling Pullout Maneuver of Counter 561.



a) Measured Main Rotor Hub Flapping Time History.

b) Computed Main Rotor Hub Flapping Time History.

Figure 87. Comparison of Measured and Computed Main Rotor Hub Flapping Time Histories for the Symmetric Pullup Maneuver of Counter 562.

for the pullup is approximately two-thirds of that measured, while the maximum oscillatory flapping computed for the symmetric pullup is about 80 percent of the measured maximum oscillatory flapping.

#### 7.2.7 Summary of the Comparison of Experimental and Simulated Maneuver Performance Data

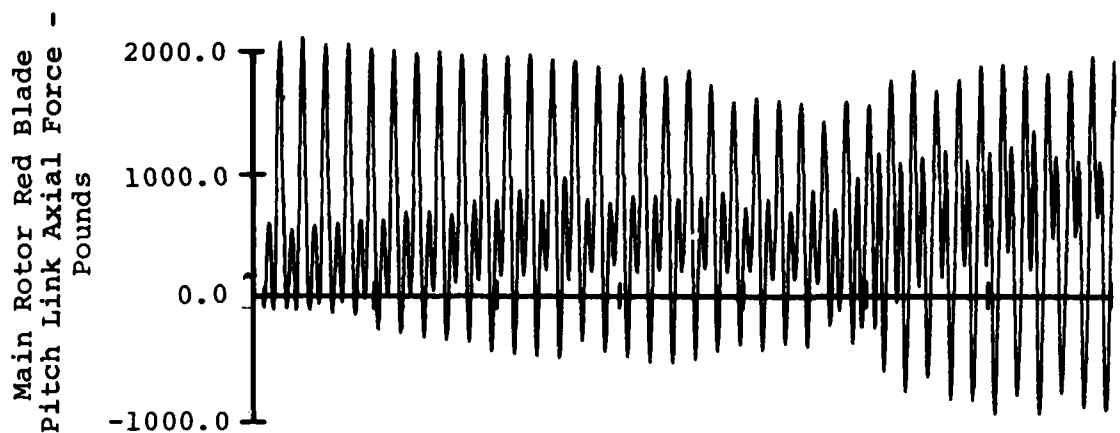
The data contained in Figures 62 through 75 demonstrate that the analyst can reproduce aircraft maneuver flight-path motion with a high degree of accuracy in C81. This indicates that the forces imposed on the aircraft by the rotor in the simulation are similar to the rotor forces generated in flight. The rotor torque, engine RPM, and rotor hub flapping traces (Figures 80 through 87) show that the rotor response in the simulation differs from that experienced during the flight test. The large two-per-rev aerodynamic loading observed in the computed rotor torque traces and the differences between the measured and computed main rotor hub flapping imply that the calculated rotor aerodynamics are not the same as those experienced in flight. These aerodynamic differences may be due to the absence of rotor wake or unsteady aerodynamic effects in the model. Further study of these two maneuvers is indicated.

#### 7.3 COMPARISON OF MAIN ROTOR LOADS AND ACCELERATIONS

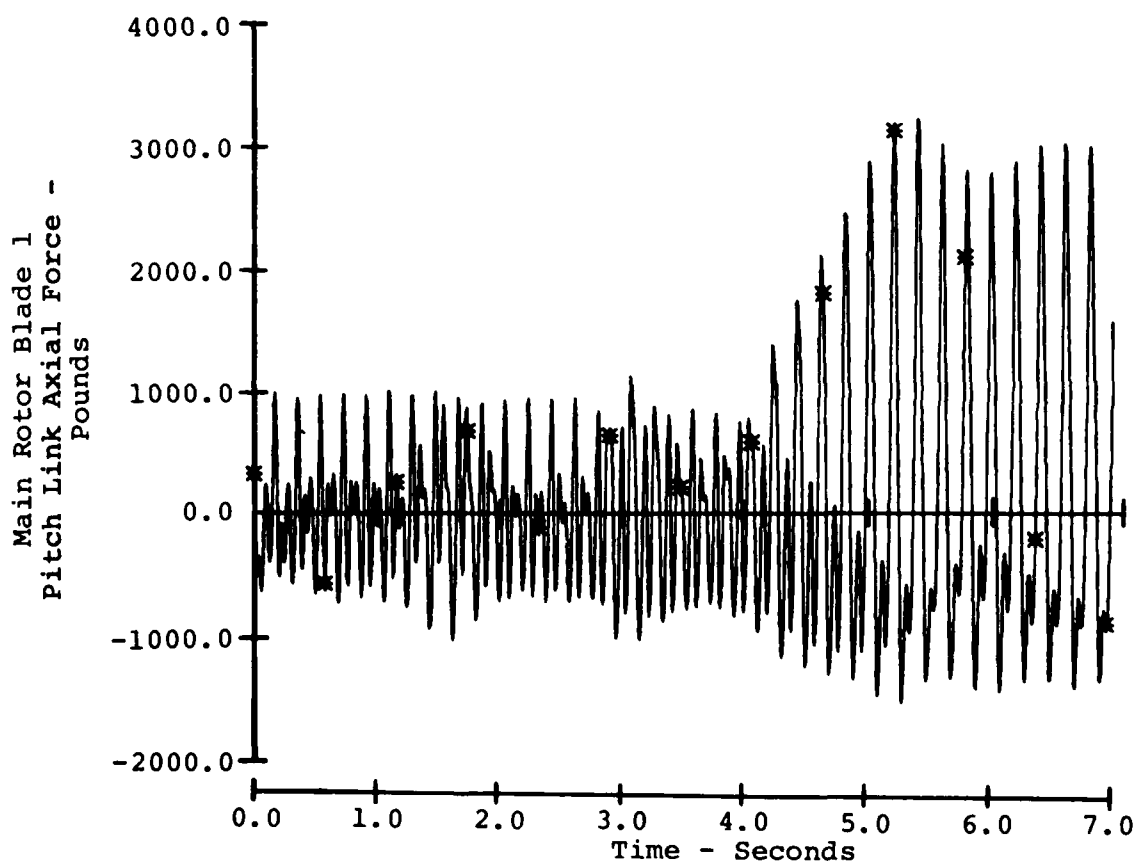
Time histories of the C81-computed main rotor pitch link loads, beam, chord, and torsional moments at four radial stations, and beam and chord accelerations at four radial stations have been compared with measured data for the two maneuvers simulated. Typical results of these comparisons are discussed in this section.

##### 7.3.1 Comparison of Measured and Computed Main Rotor Pitch Link Loads

Figure 88 contains the time history plots of the main rotor pitch link load for the right-rolling pullout maneuver of counter 561. Both the measured and computed loads are for the reference blade, i.e., the blade that is over the tailboom when the main rotor azimuth equals zero. The computed pitch link load time history has a mean value of about 200 pounds at the beginning of the maneuver and the measured mean pitch link load is about 1000 pounds. This discrepancy was not unanticipated, as the comparisons of pitch link loads in level flight (Section 6.2) documented a difference between measured and computed steady pitch link loads. The computed oscillatory pitch link load is approximately three-quarters the value measured at the beginning of the maneuver.



a) Measured Main Rotor Red Blade Pitch Link Axial Force Time History.



b) Computed Main Rotor Blade 1 Pitch Link Axial Force Time History.

Figure 88. Comparison of Measured and Computed Main Rotor Pitch Link Load Time Histories for the Right Rolling Pullout Maneuver of Counter 561.

The two time histories demonstrate similar behavior for the first 4 seconds of the maneuver, showing a strong, reasonably constant one-per-rev content and a slightly decreasing mean. The measured oscillatory pitch link load increases somewhat after the fourth second of the maneuver, and the computed oscillatory pitch link load more than doubles. This increase in the computed pitch link load corresponds with the simultaneous increase in flapping, as seen in Figure 86. The increased flapping causes an increase in inertial and aerodynamic loading, resulting in the increased pitch link loads.

The measured and computed main rotor pitch link load time histories for the symmetric pullup maneuver (counter 562) are plotted in Figure 89. The measured and computed mean and oscillatory pitch link loads at the beginning of this maneuver are quite similar to those observed for the right-rolling pullout (Figure 88), as they should be, since the entry conditions to both maneuvers are similar. The flight-test pitch link load time history shows moderate growth during the maneuver, with peak loading occurring between 3 and 4 seconds. The pitch link load time history calculated during the simulation has a large increase in the pitch link load between 2 and 3 seconds, which corresponds to the increase in hub flapping, as seen in Figure 87. The increased aerodynamic and dynamic loading imposed by the increased computed flapping must be considered as the cause of the increase in the calculated pitch link load.

#### 7.3.2 Comparison of Measured and Computed Main-Rotor Beam Bending Moments

Time histories of the measured and computed main-rotor beam bending moment at station 37.5 are plotted in Figure 90 for the right rolling pullout maneuver of counter 561. The measured and computed oscillatory bending moment at the beginning of the maneuver are very close in amplitude. The measured mean beam bending moment is approximately 50,000 in.-lbs at the beginning of the maneuver, while the computed time history has a small negative mean value. It is suspected that the measured mean beam bending moment at this station is in error, as was described in the discussion of the level flight rotor beam bending moments, Section 6.3. At the beginning of the maneuver, the test data have a predominant one-per-rev character while the time history computed by C81 shows more higher harmonic content. The measured and computed time histories are quite similar for the first 4 seconds of the maneuver, at which point the computed beam bending moment begins to increase, doubling in value by 5 seconds. This load growth occurs just before the large increase in the computed hub flapping.

BELL HELICOPTER TEXTRON FORT WORTH TX

VALIDATION OF THE ROTORCRAFT FLIGHT SIMULATION PROGRAM (C81) US--ETC(U)

JUL 80 J R VAN GAASBEEK

DAAJ02-77-C-0003

BHT-699-099-006

USAAVRADCOM-TR-80-D-4

NL

$\Delta_{\text{H}}^{\circ}$

■

END

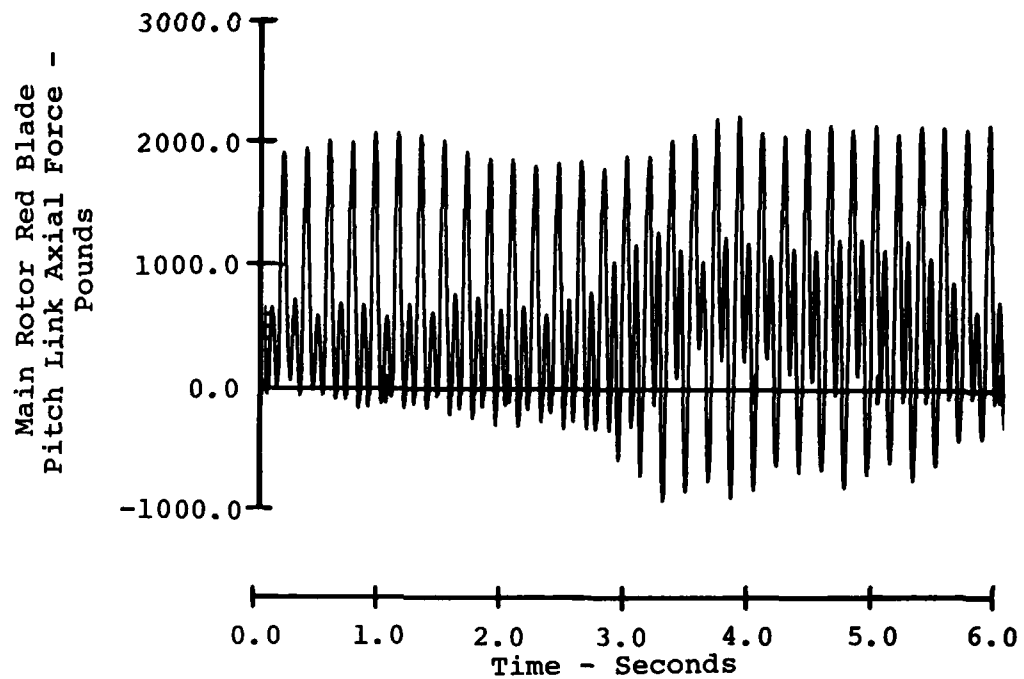
DATE \_\_\_\_\_

14. MFC

10 80

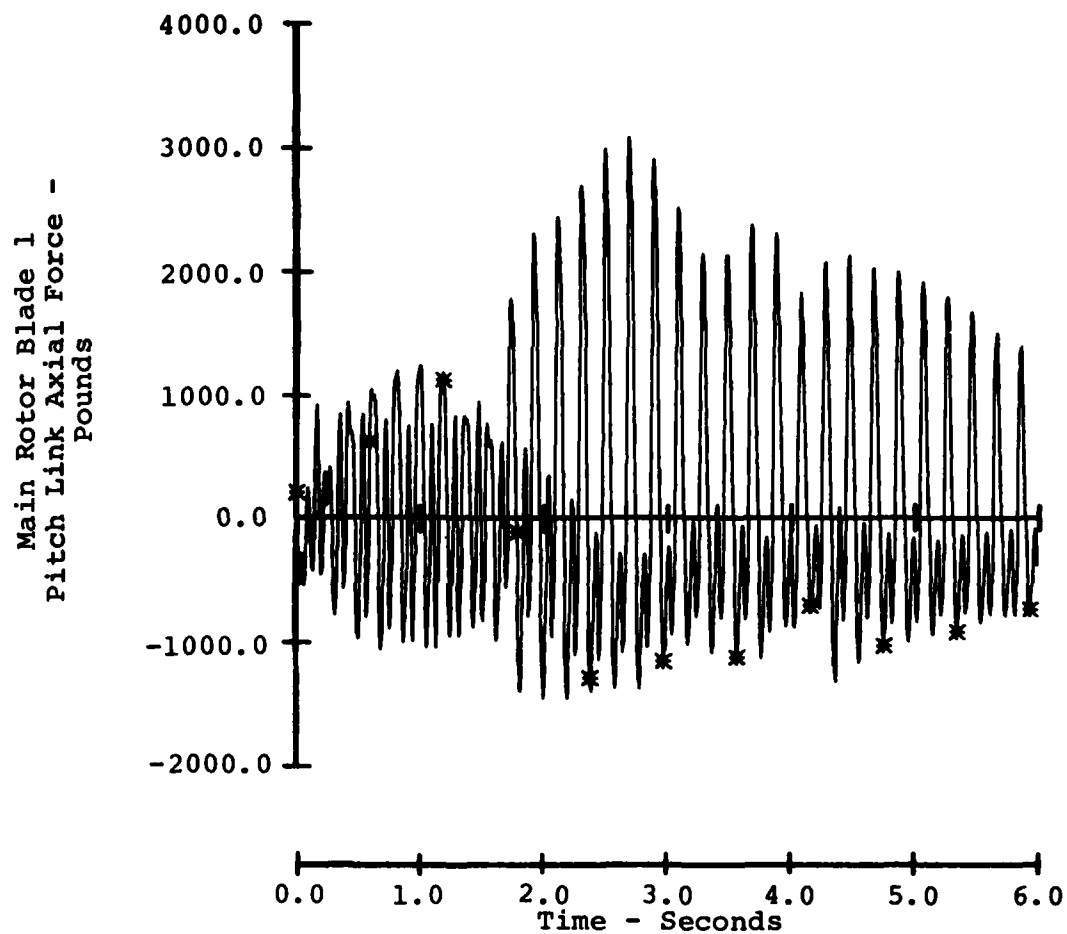
DTIC





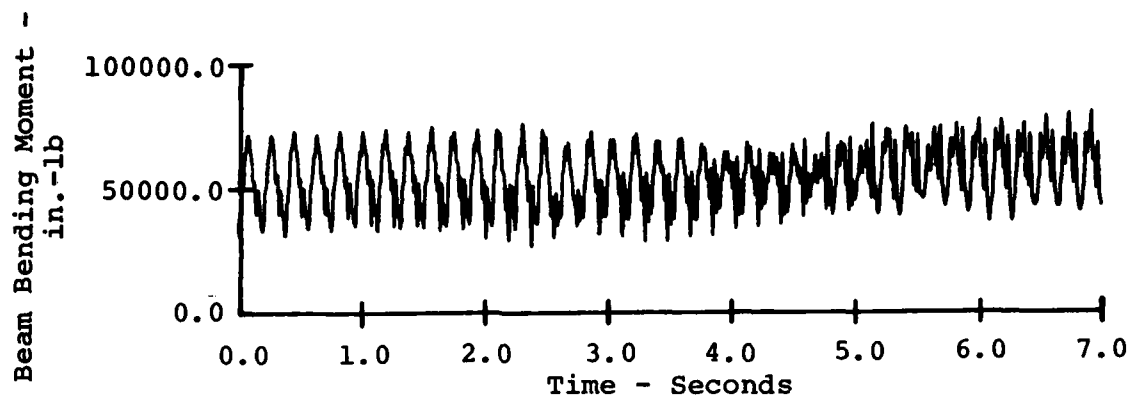
a) Measured Main Rotor Red Blade Pitch Link Axial Force Time History.

Figure 89. Comparison of Measured and Computed Main Rotor Pitch Link Load Time Histories for the Symmetric Pullup Maneuver of Counter 562.

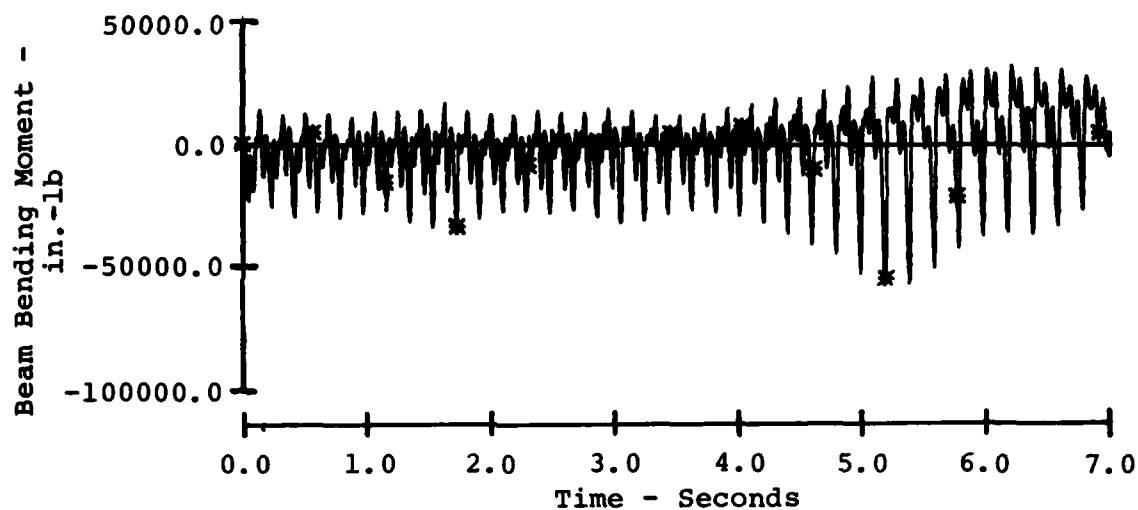


b) Computed Main Rotor Blade 1 Pitch Link Axial Force Time History.

Figure 89. Concluded.



a) Measured Main Rotor Beam Bending Moment Time History, Station 37.5.



b) Computed Main Rotor Beam Bending Moment Time History, Station 37.5.

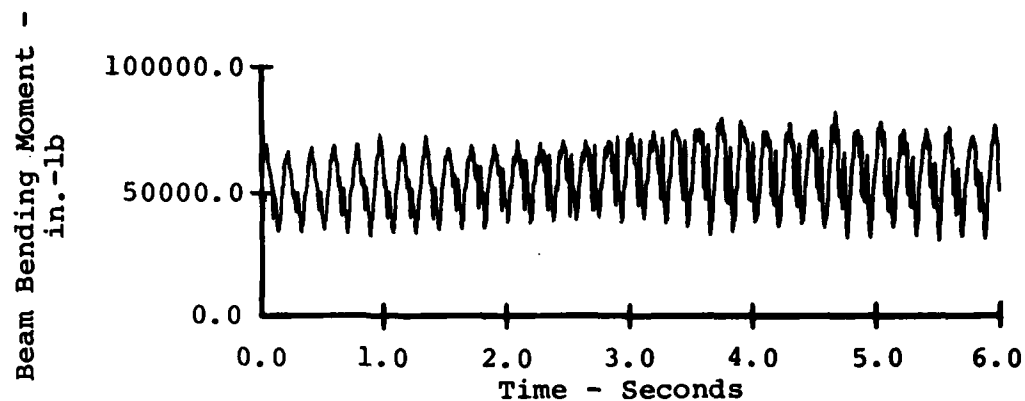
Figure 90. Comparison of Measured and Computed Main Rotor Beam Bending Moment (Station 37.5) Time Histories for the Right Rolling Pullout Maneuver of Counter 561.

Figure 91 contains the time history plots of the station 37.5 main-rotor beam bending moments for the symmetric pullup maneuver (counter 562). Again, the measured mean beam bending moment is significantly larger than that computed by C81. The oscillatory beam bending moment computed at the beginning of the maneuver is approximately the same as that measured, but increases by about 20 percent after 0.4 second. The experimental time history is predominantly one-per-rev in content, with the three-per-rev component increasing after 2.0 seconds. The computed beam bending moment time history has more higher harmonic content. The overall measured oscillatory beam bending moment does not increase a great deal over the course of the maneuver, but the C81-calculated beam bending moment is more than doubled in value in the period between 2 and 3 seconds. This load growth coincides with the increased flapping in the same time period.

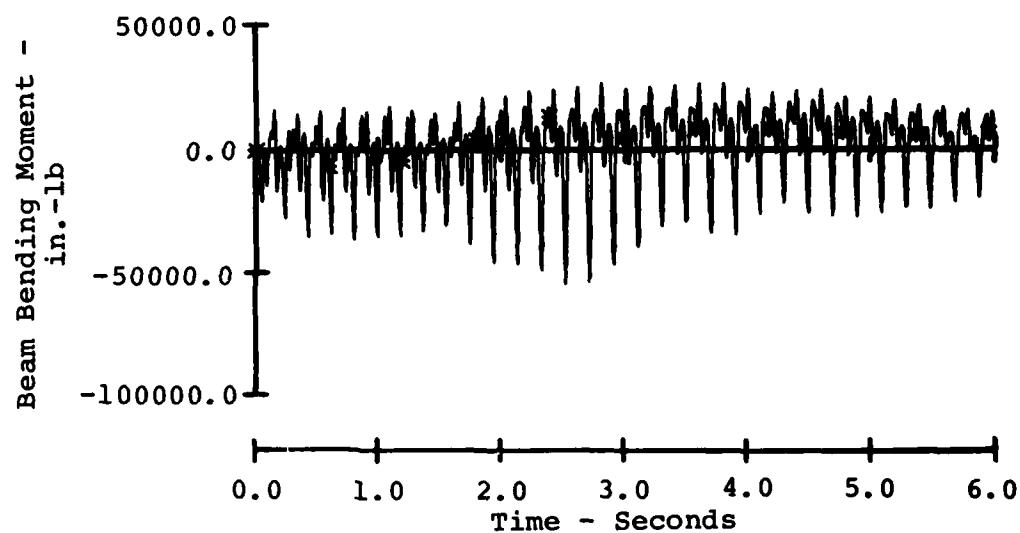
#### 7.3.3 Comparison of Measured and Computed Main-Rotor Chord Bending Moments

The time histories of the main-rotor chordwise bending moment at station 132 are plotted for the right-rolling pullout maneuver in Figure 92. The computed mean chord bending moment does not agree with the measured mean value. This discrepancy was also observed during the comparisons of level flight chord bending moments (see Section 6.4). The oscillatory chordwise bending moment computed at the beginning of the maneuver is comparable in magnitude to the measured value, but the computed chord bending moment increases in value by a factor of more than three, reaching its peak value just after 5 seconds. This is shortly before the maximum hub flapping occurs in the simulation, and it is interesting to note that the chord bending moment time history is almost pure one-per-rev in character during the peak load period, losing all the higher harmonic content observed near the beginning of the maneuver. Since the growth in the chordwise bending moment begins two-to-three rotor revolutions before the growth in the flapping response, the former phenomenon cannot be caused by the latter. The two events do result from the same, as yet unidentified, causative factor.

Figure 93 contains the time histories of the main-rotor chordwise bending moment at station 132 for the symmetric pullup maneuver. (The vertical stroke across the measured time history at about 0.5 second is part of the test data.)

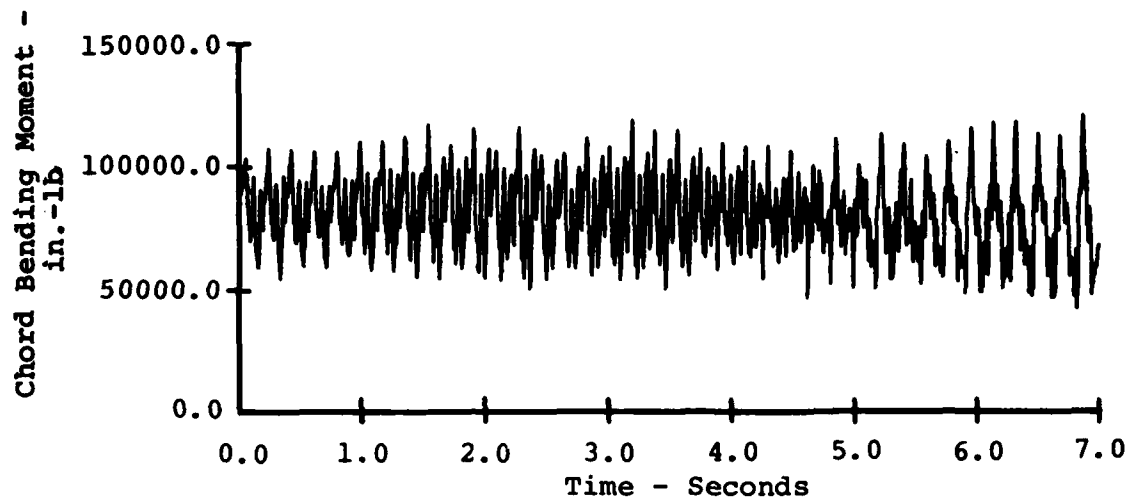


a) Measured Main Rotor Beam Bending Moment Time History, Station 37.5.

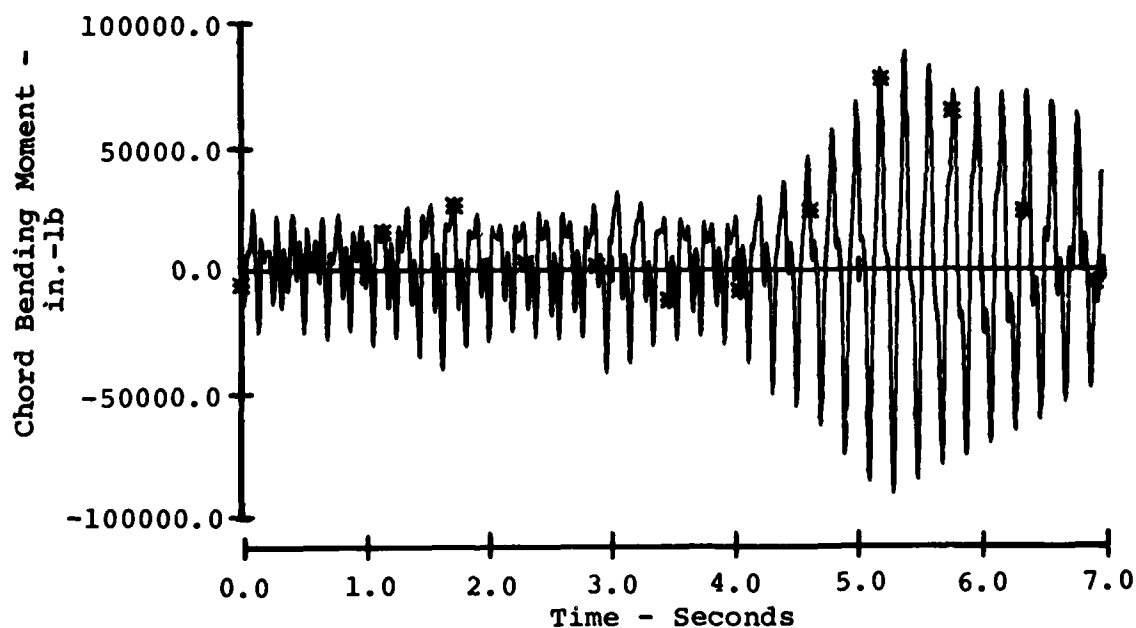


b) Computed Main Rotor Beam Bending Moment Time History, Station 37.5.

Figure 91. Comparison of Measured and Computed Main Rotor Beam Bending Moment (Station 37.5) Time Histories for the Symmetric Pullup Maneuver of Counter 562.

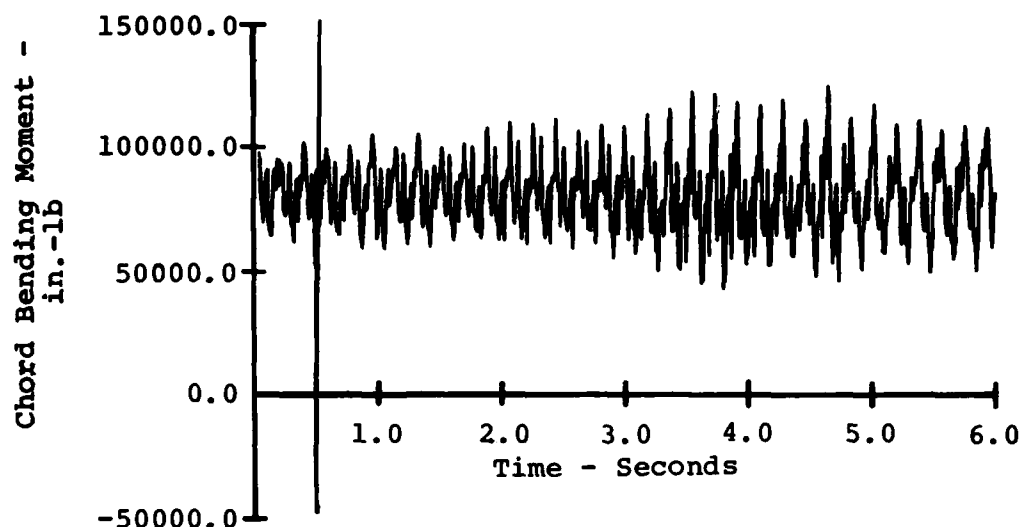


a) Measured Main Rotor Chord Bending Moment Time History, Station 132.0.

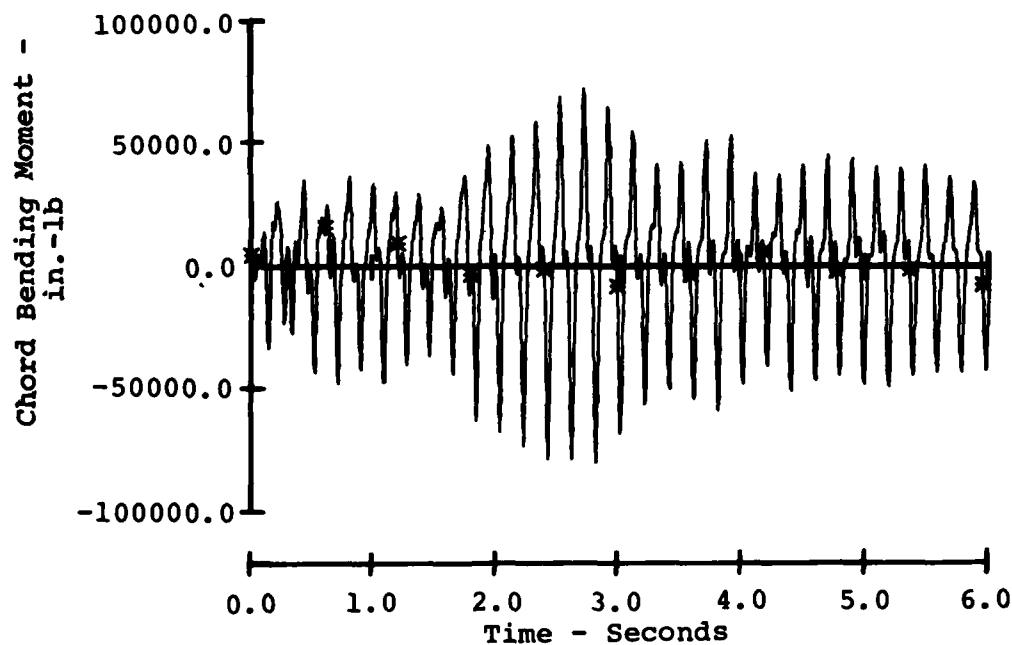


b) Computed Main Rotor Chord Bending Moment Time History, Station 132.0.

Figure 92. Comparison of Measured and Computed Main Rotor Chord Bending Moment (Station 132.0) Time Histories for the Right Rolling Pullout Maneuver of Counter 561.



a) Measured Main Rotor Chord Bending Moment Time History, Station 132.0.



b) Computed Main Rotor Chord Bending Moment Time History, Station 132.0.

Figure 93. Comparison of Measured and Computed Main Rotor Chord Bending Moment (Station 132.0) Time Histories for the Symmetric Pullup Maneuver of Counter 562.

The mean value of the computed time history is near zero and the mean value of the measured time history is about 80,000 inch-pounds. The difference between measured and computed mean chord bending moments has been observed for all the test points simulated. At the beginning of the maneuver, the computed oscillatory bending moment is larger than that measured. It should also be noted that the measured oscillatory chord bending moment at the beginning of the right rolling pullout maneuver (Figure 92) is about 20 percent larger than that for the beginning of the symmetric pullup (Figure 93), even though the entry conditions are similar.

The measured time history for the chord bending moment displays significant higher harmonic content throughout the maneuver, with moderate load growth between three and five seconds. The computed time history is essentially one-per-rev in nature for the entire maneuver, and reaches its peak load just before 3 seconds, coinciding with the maximum hub flapping response (Figure 87).

#### 7.3.4 Comparison of Measured and Computed Main-Rotor Torsional Moments

The measured and computed main rotor torsional moments at station 184.8 for the right-rolling pullout maneuver (counter 561) are compared in Figure 94 in time-history form. The mean value of the two time histories are not the same, but remain almost constant during the maneuver. The oscillatory computed torsional bending moment at the beginning of the maneuver is less than that measured, and both time histories are one- and three-per-rev in content. The computed torsional moment experiences load growth starting at about four seconds, just two or three rotor revolutions before the beginning of the increased flapping response (Figure 86). The measured torsional moment time history shows only small changes in the values measured during the maneuver.

The time history of the main-rotor torsional moment at station 184.8 measured during the symmetric pullup maneuver of counter 562 is compared with the time history produced by the C81 simulation in Figure 95. The measured and computed mean values of the torsional moment are different at the beginning of the maneuver, and the quantities remain essentially unchanged throughout the maneuver. The oscillatory torsional moment calculated at the end of the trim in the simulation is less than that measured at the start of the maneuver, and the computed values begin a substantial increase at about 1.8 seconds, just after the flapping begins to increase (Figure 87).



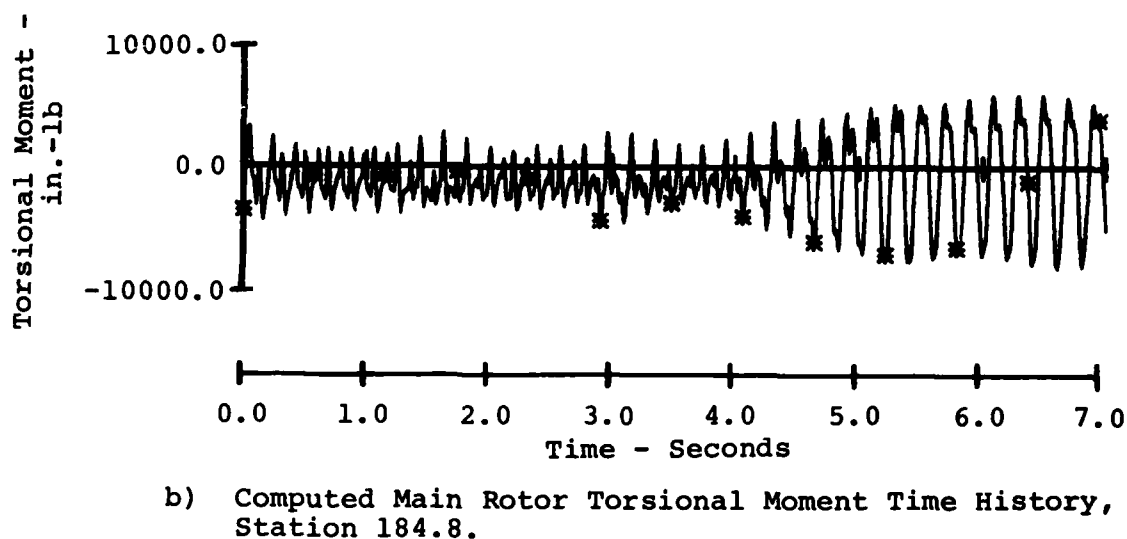
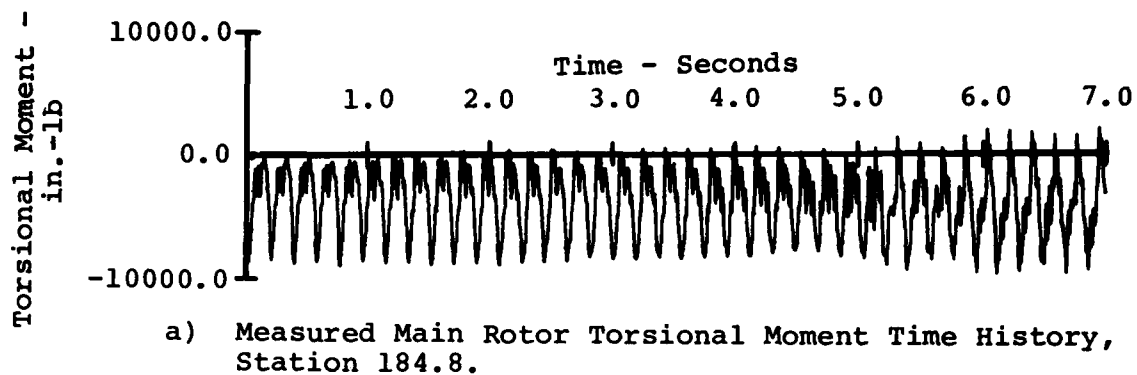
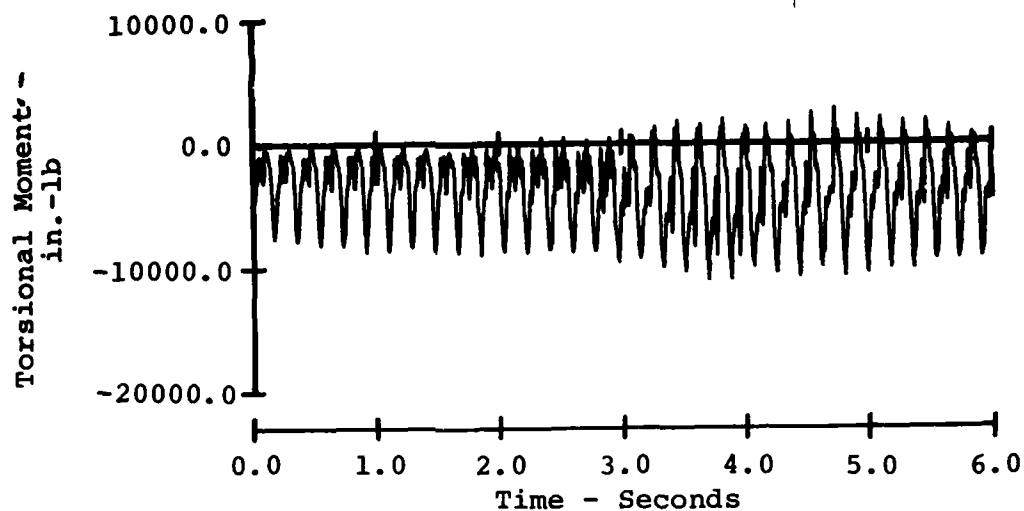
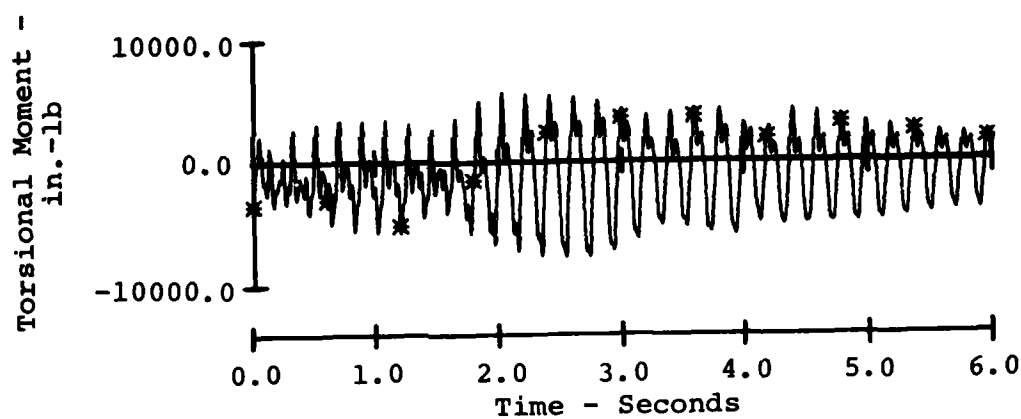


Figure 94. Comparison of Measured and Computed Main Rotor Torsional Moment (Station 184.8) Time Histories for the Right-Rolling Pullout Maneuver of Counter 561.



a) Measured Main Rotor Torsional Moment Time History, Station 184.8.



b) Computed Main Rotor Torsional Moment Time History, Station 184.8.

Figure 95. Comparison of Measured and Computed Main Rotor Torsional Moment (Station 184.8) Time Histories for the Symmetric Pullup Maneuver of Counter 562.

### 7.3.5 Summary of the Main Rotor Bending Moment Comparisons

The main rotor load comparisons described in the preceding sections are typical of the results obtained during the maneuver simulations. The program computed peak bending moments in excess of those measured in flight at every radial station examined. The peak loads were calculated in the simulation within one-to-two rotor revolutions of the time at which the peak hub flapping was computed. Since the peak loads computed by C81 were larger than those measured, the program would be conservative in the prediction of blade loads for fatigue life or failure analyses.

### 7.3.6 Comparison of Measured and Computed Main Rotor Beamwise Accelerations

The time history of the beamwise acceleration measured at station 132.0 during the right rolling pullout maneuver of counter 561 is plotted in Figure 96, which also contains the station 132.0 beam acceleration time history computed by C81 in the simulation of this maneuver. The details of the time histories are obscured by the large higher harmonic content in both waveforms. The mean value of the computed acceleration at the beginning of the maneuver is about twice that of the measured acceleration, and the oscillatory acceleration in the simulation is also about double the measured oscillatory beamwise acceleration. Both the measured and computed oscillatory beamwise accelerations increase as the maneuver progresses, reaching their maximum values at about 5 seconds. The mean value of both the measured and computed time histories is approximately 10 g higher at the end of the maneuver than at the beginning, and the measured and oscillatory beamwise accelerations are almost identical.

The time histories of the measured and computed beamwise acceleration at station 155.8 are plotted for the symmetric pullup maneuver (counter 562) in Figure 97. The measured beamwise acceleration time history does not demonstrate as much higher harmonic content as that observed during the right-rolling pullout (Figure 96), but the computed beamwise acceleration contains significant higher harmonic response. The mean beamwise acceleration measured at the beginning of the maneuver is slightly more than half of the computed value. The measured mean acceleration increases for the first 3 seconds of the maneuver and decreases for the remainder of the maneuver, almost returning to its starting value. The computed oscillatory beamwise acceleration is larger than the measured value at the beginning of the maneuver, increases slightly and begins to decrease at 2 seconds. The measured oscillatory beamwise acceleration increases until 3.5 seconds, decreases and then increases again until 5.5 seconds.

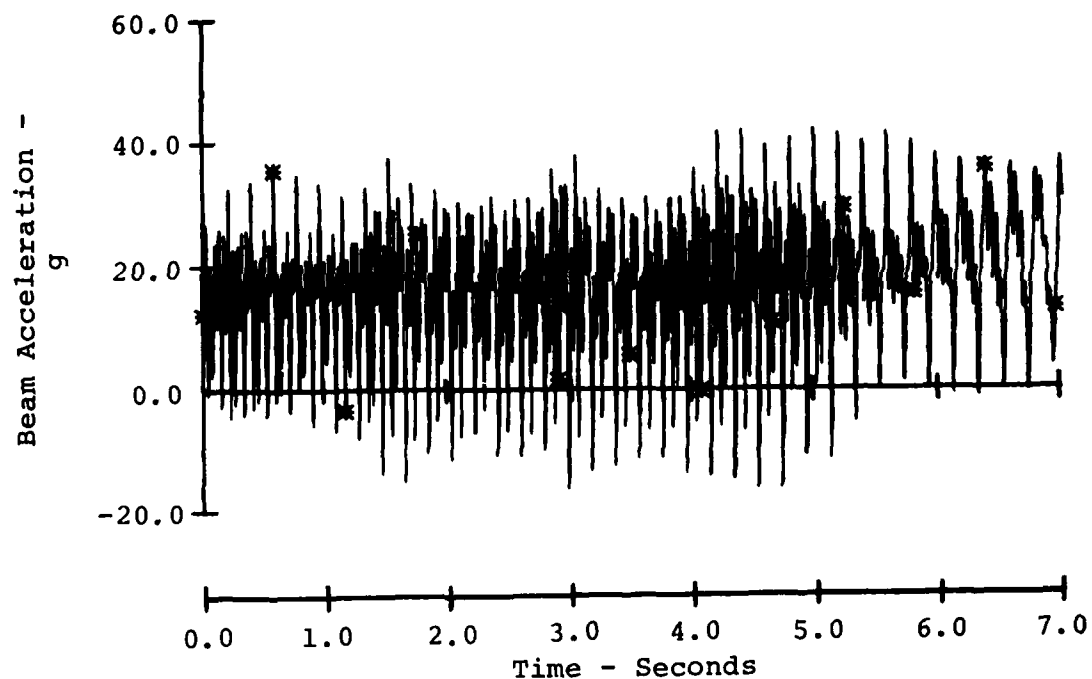
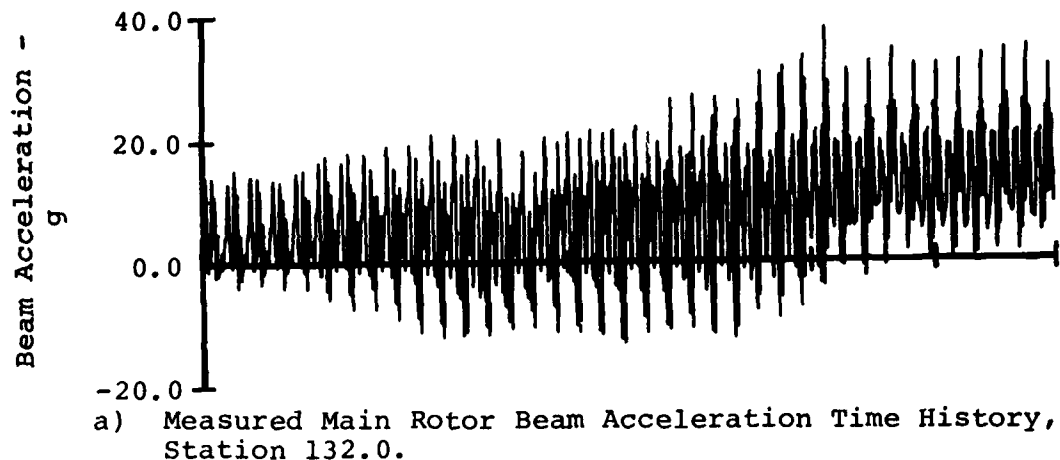
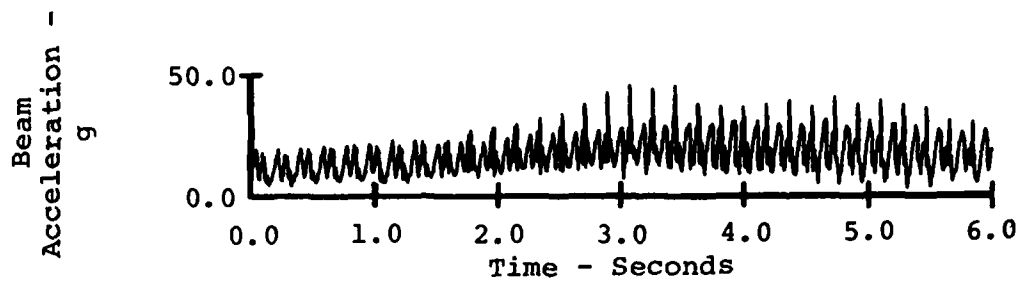
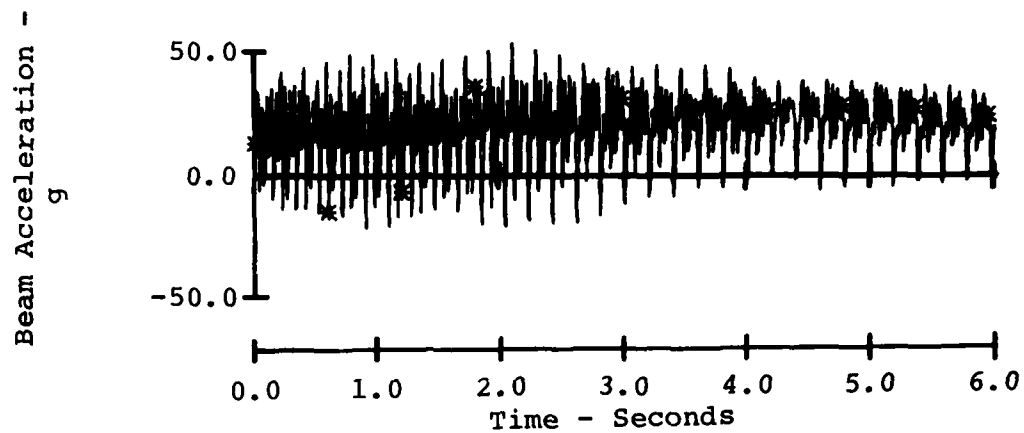


Figure 96. Comparison of Measured and Computed Main Rotor Beam Acceleration (Station 132.0) Time Histories for the Right-Rolling Pullout Maneuver of Counter 561.



a) Measured Main Rotor Beam Acceleration Time History, Station 155.8.



b) Computed Main Rotor Beam Acceleration Time History, Station 155.8.

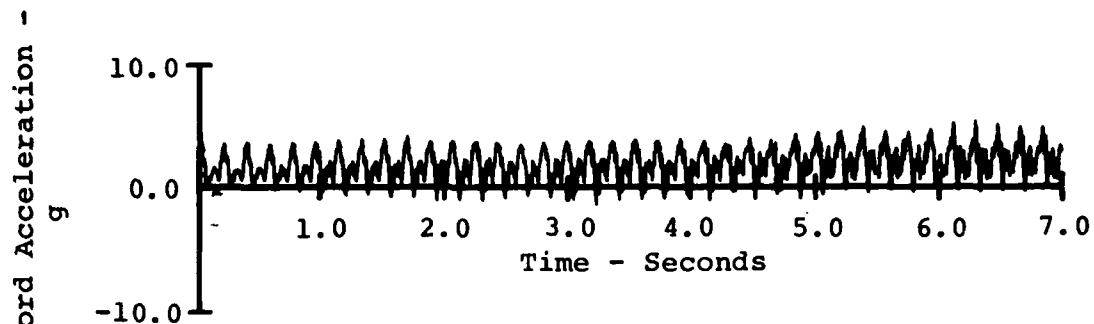
Figure 97. Comparison of Measured and Computed Main Rotor Beam Acceleration (Station 155.8) Time Histories for the Symmetric Pullup Maneuvers of Counter 562.

### 7.3.7 Comparison of Measured and Computed Main Rotor Chordwise Accelerations

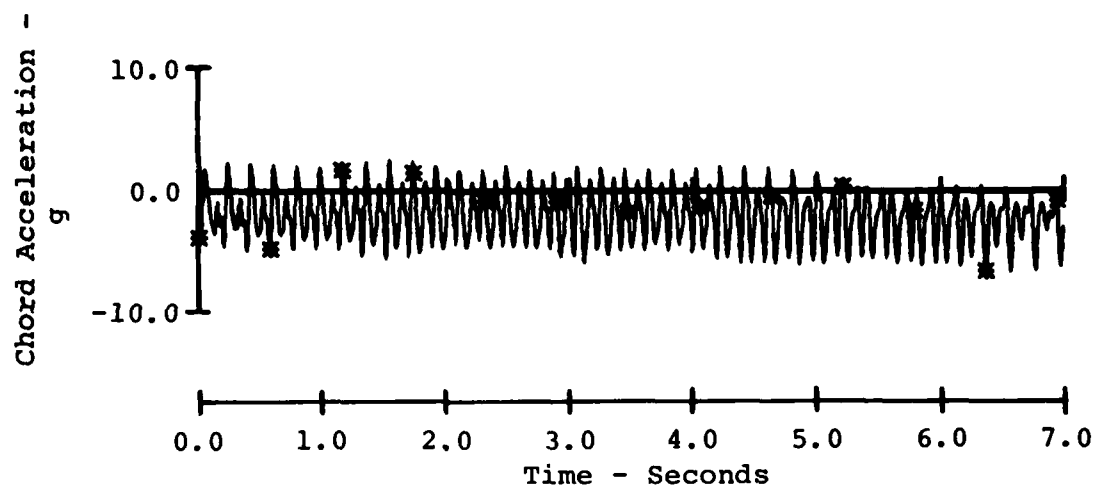
The measured and computed chordwise acceleration time histories for blade radial station 81.5 are compared in Figure 98 for the right-rolling pullout maneuver of counter 561. At the beginning of the maneuver, both waveforms are primarily one- and three-per-rev in character. The measured time history has an increase in higher harmonic content as the maneuver progresses, while the computed time history develops into a predominantly two-per-rev signal between 2 and 6 seconds. The measured oscillatory chordwise acceleration is about half of the computed oscillatory throughout the maneuver. The mean value of the measured time history at the beginning of the maneuver is about 1.5, and remains reasonably constant during the maneuver. The mean value of the computed time history starts at about -1.0 and decreases to a value of about -2.5 at the end of the maneuver.

Figure 99 contains the measured and computed time histories of the chordwise acceleration at station 37.5 for the symmetric pullup maneuver (counter 562). Both time histories have a mean value that has little variation throughout the maneuver, with the mean value of the measured data being about -7.0g and that of the computed time history being about -1.0g. The computed oscillatory chord acceleration reaches a peak value of approximately 3.0g at 2.5 seconds while the peak measured oscillatory, also about 3.0g, occurs at 3.7 seconds.

The two time histories are similar in harmonic content near the beginning of the maneuver, and more higher harmonic content is observed in the measured data than in the computed data as the maneuver progresses.

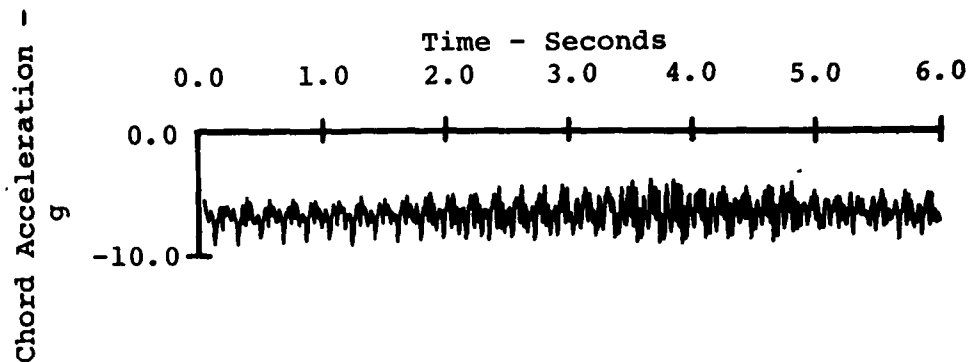


a) Measured Main Rotor Chord Acceleration Time History, Station 81.5.

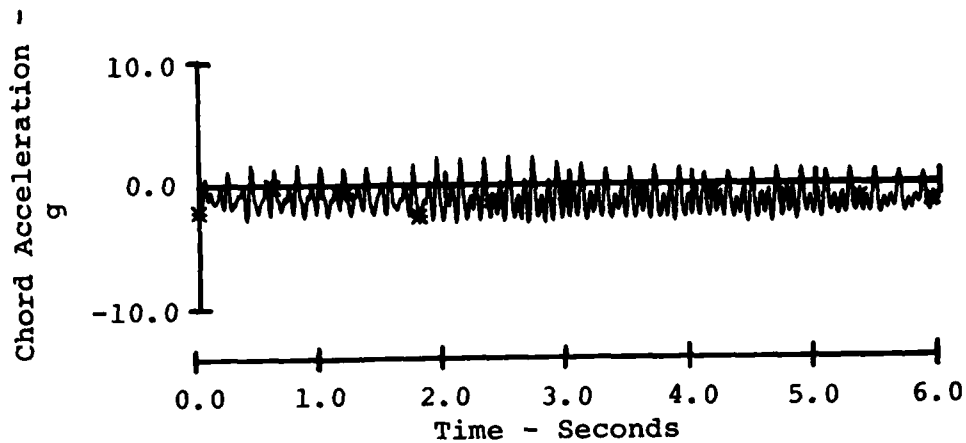


b) Computed Main Rotor Chord Acceleration Time History, Station 81.5.

Figure 98. Comparison of Measured and Computed Main Rotor Chord Acceleration (Station 81.5) Time Histories for the Right-Rolling Pullout Maneuver of Counter 561.



a) Measured Main Rotor Chord Acceleration Time History, Station 37.5.



b) Computed Main Rotor Chord Acceleration Time History, Station 37.5.

Figure 99. Comparison of Measured and Computed Main Rotor Chord Acceleration (Station 37.5) Time Histories for the Symmetric Pullup Maneuver of Counter 562.



## 8. REVIEW OF THE OLS FLIGHT TEST PROGRAM

As an additional task in this effort, the OLS flight test program and the resulting data base, were examined to assess their value in providing a tool for validating rotorcraft flight simulation programs. Overall, the test program and data base proved to be ideally suited to this need, with few deficiencies or omissions. The test program has provided a large, publicly available, reasonably well documented data base in which most data items are available over a wide range of well-defined test conditions. The few weak points in the test program and data management are outlined below, with recommendations for improvements in future such test programs.

### 8.1 INSTRUMENTATION

#### 8.1.1 General

One of the primary goals of the OLS test program was to collect data which could be used to define the main rotor aerodynamic environment. Two major weak points in the test program diminish the analyst's ability to perform this task: the lack of experimental calibration of the hot wire anemometers and the failure to detect the malfunction of an absolute pressure transducer and replace it.

Although main rotor angle-of-attack data were extracted from the flight test data, using the analytical calibration curves of Figure 3, the resulting contour plots (Section 5.5 and Appendix A) demonstrate sufficient anomalies as to suggest deficiencies either in the test data or the calibration curves. The availability of experimental calibration data could have eliminated some areas of suspicion. It is recommended that a wind-tunnel test program be conducted to acquire the calibration data for addition to the data base.

The absolute pressure transducer nearest the leading edge on the upper surface of the airfoil at the 60-percent radial station was apparently malfunctioning throughout the test program. This sensor would have been measuring the absolute pressure in the leading edge suction peak. Since the measured data are suspect and cannot be accurately replaced by extrapolation from data recorded by the other pressure taps at this radial station, it is not possible to compute the aerodynamic characteristics of the rotor at 60 percent radius. It is unfortunate that this instrumentation malfunction was not detected early in the program and the transducer replaced, as the remainder of the pressure data at the 60-percent radius are of little value in the absence of this particular data item.

Other instrumentation failures during the test program were not critical.

The inability to record all data items simultaneously was another deficiency in the test program, although not a serious one, as a great deal of information is available for every counter.

#### 8.1.2 Amount of Instrumentation

Inclusion of the following data items could have enhanced the data base for use in computer program validation:

- Several spanwise bending moment gauges on wing and stabilizing surfaces (used to determine aerodynamic loads)
- Elevator incidence angle
- Longitudinal and lateral accelerometers at the aircraft center of gravity
- Hot wire anemometers on the wing and stabilizing surfaces
- SCAS actuator positions
- Rate-of-climb
- Torsional acceleration instrumentation on the rotor

#### 8.1.3 Types of Instrumentation

In all cases, the type of instrument installed to measure a particular quantity was adequate to the need. The only instrumentation that might have been improved is the boom flight path instrumentation. The signals from the angle-of-attack, sideslip, and airspeed sensors all show a large high-frequency content, due to vibration of the boom. This high-frequency content does not significantly affect the steady component of the signal, as it can be filtered out.

Additionally, the angle-of-attack and sideslip instrumentation, being in front of the fuselage, measure the overall aerodynamic angles of the airframe relative to the freestream. They do not measure the effective aerodynamic angles at the fuselage center of pressure. There apparently is no way to avoid this problem.

The airspeed instrumentation, conversely, could be improved by the use of one of the sensitive, accurate, cup-anemometer type of airspeed sensors that have recently been developed.

#### 8.1.4 Location of Instrumentation

The location of the instrumentation on the OLS aircraft was very good.\* Four changes might be considered for future test programs of this nature to enhance their use for the validation of simulation programs:

- Remove the airspeed sensor from the boom and use a cup-anemometer instrument
- Locate the blade accelerometers so as to measure accelerations at the local blade element center of mass, as well as on the pitch change axis.
- Include more bending moment instrumentation in the multiple-load-path region of the hub and on the pitch horn.
- Install hot-wire anemometers over a larger range chordwise to avoid the stagnation point moving outside the range of wires.

#### 8.2 DETERMINATION OF TEST AIRCRAFT PHYSICAL CHARACTERISTICS

The physical characteristics of the OLS test vehicle were not documented to the level of detail required for creating the input data for a sophisticated, general-purpose rotorcraft flight simulation program. Although six formal reports were generated for the test program (References 10, 19 and 31 through 34), many of the C81 inputs had to be derived from unpublished data or reports or drawings not publicly available. It is recommended that all future test programs include a

<sup>31</sup>Cox, C. R., INSTRUMENTATION TEST PLAN FOR AH-1G OPERATIONAL LOADS SURVEY, Technical Report 299-099-666, Bell Helicopter Textron, Fort Worth, Texas, 1973.

<sup>32</sup>Shockey, G., COMPONENT TEST PLAN FOR AH-1G OPERATIONAL LOADS SURVEY, Technical Report 299-099-701, Bell Helicopter Textron, Fort Worth, Texas, 1975.

<sup>33</sup>Shockey, G., FLIGHT TEST PLAN FOR AH-1G OPERATIONAL LOADS SURVEY, Technical Report 299-099-746, Bell Helicopter Textron, Fort Worth, Texas, 1975.

<sup>34</sup>Shockey, G., FLIGHT SAFETY DATA FOR AH-1G OPERATIONAL LOADS SURVEY, Technical Report 299-099-752, Bell Helicopter Textron, Fort Worth, Texas, 1975.

document at least as detailed as ADS-10<sup>35</sup> including:

- a comprehensive weight breakdown for the test vehicle
- a complete description of the rotor geometric, structural and aerodynamic properties
- a complete description of the airframe geometric, structural and aerodynamic properties; the structural and weight data could be submitted in the form of a NASTRAN deck
- a complete description of all control linkages

Two minor deficiencies were discovered in the available documentation. The radial location of all rotor instrumentation was given but the chordwise location of the accelerometers, which is important information, was not given. Also, the sign conventions for positive bending and positive accelerations were not documented. These two oversights should be avoided in future test programs.

### 8.3 TYPES OF TESTING PERFORMED

Data were recorded for a wide range of flight conditions during the OLS test program, providing an adequate set of experimental points for use in validating simulation programs. The value of the data base could have been improved if hover cases had been run for all gross-weight/center-of-gravity configurations. Additionally, the hover tests could be improved by hovering with respect to the air, instead of with respect to a fixed point on the ground, as the pure hover condition would provide valuable data for validating both the aerodynamic and dynamic analysis.

### 8.4 DATA STORAGE METHODS

The digital tapes generated from the test program are a good medium for data storage, as they provide easy access to the data and assure transportability. There are three small problems with the data storage that should be avoided in future test programs.

<sup>35</sup>AIR VEHICLE TECHNICAL DESCRIPTION DATA, U.S. Army Aeronautical Design Standard, ADS-10, U.S. Army Aviation Research and Development Command, St. Louis, Missouri.

A small misalignment occurred in the digitization process, i.e., the time corresponding to the beginning of a record varied by a small amount from data item to data item within the record. This deficiency has been documented, the offsets recorded, and the DATAMAP<sup>12</sup> program can compensate for the misalignment, but it should be avoided if at all possible.

In some instances, data items were not grouped on the digital tapes in a logical manner. The absolute pressure data for Counter 1078 is stored on 16 separate tapes while the same data items for Counters 610 through 615 are recorded on only five digital tapes. Additionally, similar items were digitized at different rates and stored on separate tapes. It is recommended that the data recorded in future test programs be assembled in groups by type (i.e., performance data, beam bending moments, chord accelerations, etc.) and that all the data items within a group be stored on the same tape wherever possible.

The only currently available catalog of data items is the listing setup sheets in Reference 10. Although these are adequate, the data retrieval process would be improved if a listing were generated in which the data items were grouped by type (instead of by channel and track) so that the data item identification numbers could be easily located.

#### 8.5 REPORTING METHODS

The reports generated to document the test program (References 10, 19, and 31 through 34) described the flight tests adequately. They did not provide sufficient information to simulate the tests. This shortcoming can be overcome in the future by avoiding the omissions discussed in previous portions of this section through a strict attention to detail. Also, two additional reports should be generated in future efforts to further document the data base. The first would contain a complete physical description of the test article, while the second would give a comprehensive description of the instrumentation, including a listing of the data items recorded (by type) and, for each data item, the tape on which it was recorded for each counter, the digitization rate and the record length.

#### 8.6 PILOT TECHNIQUE AND TEST METHODOLOGY

The pilot technique used throughout the test program was excellent. The only improvements that can be suggested are:

- record pressure altitude and outside air temperature on the pilot card in addition to density altitude.
- begin recording data for maneuvers in level flight to firmly establish the initial conditions.

The test methodology was also very good, with the only fault being the major failure to detect the malfunctioning pressure tap at 60 percent radius. Other instrumentation problems were found during the daily instrumentation checks and resolved, which indicates that the pressure data recorded for this sensor appeared to be correct in strip-out form. The only way to identify this type of instrumentation problem would be to fully reduce all the data for a recent record on a periodic basis and subject that data to an intensive examination. This large a level of effort was not supported within the manpower and funding constraints of the OLS flight test program.

#### 8.7 SUMMARY

The OLS flight test program was well planned and well executed. The deficiencies discussed in this section of the report do not severely reduce the value of the data base generated by the test program. Test programs designed to provide data for the validation of rotorcraft flight simulation programs require a rigorous attention to detail, a great deal of care in execution, and a vast amount of supporting documentation.

The OLS test program set a high standard for this application. The modifications or additions discussed in this section of the report are recommended to improve on that standard.

## 9. CONCLUSIONS AND RECOMMENDATIONS

The data retrieval and simulation effort accomplished during this study was one of the first attempts to use the AH-1G Operational Loads Survey flight test data for the validation of a rotorcraft flight simulation program. More such comprehensive flight test programs should be conducted to acquire high-quality data for rotorcraft with other types of rotors. Validation efforts similar to the one reported herein should be conducted, using C81 and other general-purpose rotorcraft simulation programs. The data acquired in the test programs and the experience gained in the validation efforts will provide valuable assistance in improving rotary-wing analytical techniques as they are developed in the future. The conclusions and recommendations provided here are intended to extend the AH-1G OLS data base, suggest improved methodology for future test programs, and outline areas for future modification to C81.

### 9.1 OLS TEST PROGRAM CONCLUSIONS

The AH-1G OLS test program was conducted in a very professional manner and has provided an extensive library of high-quality test data. The data retrieval process has been greatly facilitated by the development of the DATAMAP computer programs, which can be applied to experimental data acquired under any flight test or wind-tunnel test program.

The OLS test program has been examined for its utility in providing a data base for the validation of rotorcraft flight simulation programs. The findings of that investigation may be found in Section 8 of this report. The few shortcomings discovered during this contracted effort were some deficiencies in the test documentation, minor (and normal) instrumentation difficulties, some inadequate instrumentation, and an easily-rectified problem with pilot technique.

### 9.2 RECOMMENDATIONS FOR THE OLS AND FUTURE TEST PROGRAMS

It is recommended that two additional reports be generated to supplement the OLS test program documentation. The information to be included in these reports is still available in project notebooks at BHT. The extra reports are:

- a. A supplement to Reference 31 containing all instrumentation locations (three coordinates), orientations, sign conventions and sensitivities. Where possible, the transfer function of the instruments should be documented. This report should also discuss

the overall transfer function (amplitude and phase) of the instrumentation, recording system, digitization procedure and data reduction analyses. Finally, the report should include a list of each data item, sorted by type, with the data item code, and, for each record, the record length, digitization rate and tape number.

- b. A supplement to Reference 10 which will provide a complete physical description of the aircraft, including the data given in Section 3 of this report, and a correlated NASTRAN model for the airframe.

The additional data included in these two supplemental reports should be included in the documentation of all future comprehensive test programs.

The quality of the OLS data base could be improved by performing static and dynamic wind-tunnel tests to provide calibration data for the rotor hot-wire anemometers. Two-dimensional wind-tunnel force-and-moment tests of the OLS airfoil could provide useful additional information. All future flight test programs should include two-dimensional airfoil tests, as necessary, to establish the rotor aerodynamic characteristics.

Future flight test programs should also utilize improved air-data instrumentation for determining airframe airspeed, angle of attack, sideslip angle and rate of climb. It would also be useful to have hot-wire anemometers installed on wings, elevators and fins to determine their angle of attack. (Calibration data for such hot-wire installations should be published in the flight test documentation.)

Test data should be recorded for an IGE and OGE hover-with-respect-to-the-air test point for each aircraft configuration flown. Main rotor, tail rotor, and engine power should be recorded during flat-pitch ground run-up to provide data to determine accessory horsepower and drivetrain efficiencies. Lastly, the data recording system should be turned on during the stabilized, steady-state flight preceding a maneuver to clearly define the entry condition.

### 9.3 CONCLUSIONS WITH RESPECT TO THE C81 SIMULATIONS

The Rotorcraft Flight Simulation Program C81 has computed level flight performance characteristics that are generally in good agreement with the data measured during the OLS test program. The maneuver simulations were quite successful in matching measured fuselage angular rates, but the rotor appears



to have suffered severe stall in the analysis that was not observed in the test data.

The rotor oscillatory loads computed by the program were in reasonable agreement with the test data for level flight, aft center-of-gravity flight conditions. The computed steady loads were seldom close to the measured values. The computed main rotor chordwise bending moments are more sensitive to main rotor flapping than the measured loads. The rotor flapping response computed in the simulation of the maneuvers is different from that measured, and the computed rotor loads vary from those measured. Further study is indicated in these areas to determine the causes of the problems and improve the analysis.

#### 9.4 RECOMMENDATIONS FOR FUTURE MODIFICATION TO C81

The future of the Rotorcraft Flight Simulation Program C81 is not well defined due to the imminent start of work on the Second-Generation Comprehensive Helicopter Analysis System. Program C81 can be used as a vehicle for testing certain analytical models, numerical techniques or validation concepts before the SGCHAS is released. To that end, several items are recommended to improve, correct or extend the program. It is suggested that errors or deficiencies discovered during this project be studied and corrected, and that improvements be made in the program logic or numerical analysis to facilitate use of the program.

Efforts directed towards correcting analytical deficiencies are:

- a. Examine the rotor aerodynamics in detail to determine the source of the rotor stall during the maneuver simulations.
- b. Determine the source of the sensitivity of the chord loads with rotor flapping. Determine the cause of the discrepancy between measured and computed flapping response during the maneuvers.
- c. Investigate the use of a force-integration scheme for the calculation of rotor bending moments. This would particularly help in the calculation of steady bending moments.
- d. Examine the DNAM06 inputs for the OLS rotor to determine the cause of the incorrect calculation of the cyclic torsion and "S-ing" mode frequencies,

with particular attention to the hub model. A non-rotating shake test of the rotor might provide valuable additional data for this effort. Since excellent frequency correlation is achieved when DNAM06 is used to analyze other rotors, the analysis incorporated in the program need not be investigated.

The remaining recommendations suggest improvements to the analytical model.

- e. Add feed-forward to the maneuver autopilot to minimize lag.
- f. Permit the program to trim with user-specified angular rates or accelerations.
- g. Update the partial derivatives used by the maneuver autopilot periodically during the maneuver.
- h. Allow the fuselage aerodynamics to be described by tables or by equations.
- i. Modify the RWAS tables to have advance ratio and rotor wake-plane angle of attack as independent variables.

The simulation effort should be repeated after these improvements have been implemented. A better rotor wake analysis, such as those of References 36 and 37, should be used in that study, both for RIVD and RWAS tables, and the unsteady aerodynamics models should also be used.

<sup>36</sup>Landgrebe, A. J., and Egolf, T. A., ROTORCRAFT WAKE ANALYSIS FOR THE PREDICTION OF INDUCED VELOCITIES, United Technologies Research Center, USAAMRDL TR 75-45, U.S. Army Air Mobility Research and Development Laboratory, Fort Eustis, Virginia, January 1976, AD A021202.

<sup>37</sup>Sadler, S. G., DEVELOPMENT AND APPLICATION OF A METHOD FOR PREDICTING ROTOR FREE WAKE POSITIONS AND RESULTING ROTOR BLADE LOADS, Volume I - Model and Results, CR-1911. National Aeronautics and Space Administration, Washington, D.C., 1971.

## 10. REFERENCES

1. Anderson, W. D., Conner, F., Kretsinger, P., and Reaser, J. S., REXOR ROTORCRAFT SIMULATION, VOLUME I, ENGINEERING DOCUMENTATION, Lockheed California Co., USAAMRDL TR 76-28A, U. S. Army Air Mobility Research and Development Laboratory, Fort Eustis, Virginia, July 1976, AD A028314.
2. Bergquist, R. R., and Thomas, G. C., TECHNICAL MANUAL NORMAL MODES ROTOR AEROELASTIC ANALYSIS COMPUTER PROGRAM, unpublished report, U. S. Army Air Mobility Research and Development Laboratory, Fort Eustis, Virginia.
3. Van Gaasbeek, J. R., McLarty, T. T., and Hsieh, P. Y., ROTORCRAFT FLIGHT SIMULATION, COMPUTER PROGRAM C81, Bell Helicopter Textron, USARTL TR 77-54A, -54B, and -54C, Applied Technology Laboratory, U. S. Army Research and Technology Laboratories, Fort Eustis, Virginia, October 1979, AD A079631, A079632, and A077345.
4. Ormiston, R. A., COMPARISON OF SEVERAL METHODS FOR PREDICTING LOADS ON A HYPOTHETICAL HELICOPTER ROTOR, Journal of the American Helicopter Society, 19, No. 4, October, 1974.
5. Freeman, F. D., and Bennett, R. L., APPLICATION OF ROTORCRAFT FLIGHT SIMULATION PROGRAM (C81) TO PREDICT ROTOR PERFORMANCE AND BENDING MOMENTS FOR A MODEL FOUR-BLADED ARTICULATED ROTOR SYSTEM, USAAMRDL TR 74-70, Bell Helicopter Textron, U.S. Army Air Mobility Research and Development Laboratory, Fort Eustis, Virginia, November 1974, AD A004015.
6. Briczinski, S. J., VALIDATION OF THE ROTORCRAFT FLIGHT SIMULATION PROGRAM (C81) FOR ARTICULATED ROTOR HELICOPTERS THROUGH CORRELATION WITH FLIGHT DATA, Sikorsky Aircraft Div., United Technologies Corp., USAAMRDL TR 76-4, U. S. Army Air Mobility Research and Development Laboratory, Fort Eustis, Virginia, May 1976, AD A025934.
7. Staley, J. A., VALIDATION OF ROTORCRAFT FLIGHT SIMULATION PROGRAM THROUGH CORRELATION WITH FLIGHT DATA FOR SOFT-IN-PLANE HINGELESS ROTORS, Boeing Vertol Co., USAAMRDL TR 75-50, U. S. Army Air Mobility Research and Development Laboratory, Fort Eustis, Virginia, January 1976, AD A021176.
8. McLarty, T. T., Van Gaasbeek, J. R., and Hsieh, P. Y., ROTORCRAFT FLIGHT SIMULATION WITH COUPLED ROTOR AERO-ELASTIC STABILITY ANALYSIS, Bell Helicopter Textron,

#### REFERENCES (Continued)

- USAAMRDL TR 76-41A, -41B, -41C, U. S. Army Air Mobility Research and Development Laboratory, Fort Eustis, Virginia, May 1977, AD A042462, A042908, and A042907.
9. Etkin, G., DYNAMICS OF FLIGHT, John Wiley and Sons, Inc., New York, 1959.
  10. Shockey, G. A., Cox, C. R., and Williamson, J. W., AH-1G HELICOPTER AERODYNAMIC AND STRUCTURAL LOADS SURVEY, USAAMRDL TR 76-39, Bell Helicopter Textron, U. S. Army Air Mobility Research and Development Laboratory, Fort Eustis, Virginia, February 1977, AD A036910.
  11. Philbrick, R. B., and Eubanks, A. L., OPERATIONAL LOADS SURVEY - DATA MANAGEMENT SYSTEM, VOLUMES I AND II, Bell Helicopter Textron, USARTL TR 78-52A, -52B, Applied Technology Laboratory, U. S. Army Research and Technology Laboratories, Fort Eustis, Virginia, January 1979, AD A065129 and A065270.
  12. Smetana, F. O., Summey, D. C., Smith, N. S., and Carden, R. K., LIGHT AIRCRAFT LIFT, DRAG AND MOMENT PREDICTION, A REVIEW AND ANALYSIS, NASA CR 2523, National Aeronautics and Space Administration, Washington, D.C., 1975.
  13. Critzos, C. C., Heyson, H. H., and Boswinkle, R. W., Jr. AERODYNAMIC CHARACTERISTICS OF NACA 0012 AIRFOIL SECTION AT ANGLE OF ATTACK FROM 0° to 180°, NACA TN 3361, National Advisory Council for Aeronautics, Washington, D.C., 1955.
  14. Shivers, J. P., and Carpenter, P. J., EFFECT OF COMPRESSIBILITY ON ROTOR HOVERING PERFORMANCE AND SYNTHESIZED BLADE-SECTION CHARACTERISTICS DERIVED FROM MEASURED ROTOR PERFORMANCE OF BLADES HAVING NACA 0015 AIRFOIL TIP SECTIONS, NACA TN 4356, National Advisory Council for Aeronautics, Washington, D.C., 1958.
  15. Graham, J., Nitzberg, E., and Olson, N., A SYSTEMATIC INVESTIGATION OF PRESSURE DISTRIBUTIONS AT HIGH SPEEDS OVER FIVE REPRESENTATIVE NACA LOW-DRAG AND CONVENTIONAL AIRFOIL SECTIONS, NACA TR 832, National Advisory Council for Aeronautics, Washington, D.C., 1949.
  16. Dooley, L. W. and Van Gaasbeek, J. R., FLAPPING LOAD PREDICTION AND NONLINEAR HUB SPRING DESIGN-INTERIM REPORT OF TASKS I AND II, Technical Report 699-099-091, Bell Helicopter Textron, Fort Worth, Texas, 1978.

#### REFERENCES (Continued)

17. McCormick, B. W., AERODYNAMICS OF V/STOL FLIGHT, Academic Press, New York, 1967.
18. Cronkhite, J. D., Berry, V. L., and Brunken, J. E., A NASTRAN VIBRATION MODEL OF THE AH-1G HELICOPTER AIRFRAME, TR 74-045, U.S. Army Rock Island Arsenal, Rock Island, Illinois, 1974.
219. White, J. A., MODEL AH-1G AIRFRAME AND CONTROL SYSTEM GROUND VIBRATION TEST RESULTS, Technical Report 299-099-819, Bell Helicopter Company, Fort Worth, Texas, 1976.
20. Van Gaasbeek, J. R., AN INVESTIGATION OF HIGH-G MANEUVERS OF THE AH-1G HELICOPTER, USAAMRDL TR 75-18, U.S. Army Air Mobility Research and Development Laboratory, Fort Eustis, Virginia, 1975.
21. Tisdale, P. R., COMPUTER PROGRAMS FOR ROTOR LOADS AND STRESS ANALYSIS, Technical Report 299-099-749, Bell Helicopter Company, Fort Worth, Texas, 1975.
22. Hoerner, Signard, FLUID DYNAMIC DRAG, published by the author, Brick Town, New Jersey, 1965.
23. Dommasch, D. O., Sherby, S. S., and Connally, T. F., AIRPLANE AERODYNAMICS, Fourth Edition, Pitman Publishing Corporation, New York, 1967.
24. Abbott, I. H. and von Doenhoff, A. D., THEORY OF WING SECTIONS, Dover Publications, New York, 1959.
25. Oldenbottle, R. H., White, R. M., and Cooksey, J. M., A LOW SPEED WIND TUNNEL TEST OF THE BELL HELICOPTER COMPANY 0.200 SCALE AH-1G/AH-1S MODEL INVESTIGATING AERODYNAMIC CHARACTERISTICS, Vought Systems Division Report LSWT 490, Vought Corporation, Dallas, Texas, 1975.
26. Finnestead, R. L., Laing, E., Connor, W. J., and Buss, M. W., ENGINEERING FLIGHT TEST AH-1G HELICOPTER (HUEY COBRA), PHASE D, PART 2, PERFORMANCE, FINAL REPORT, U.S. Army Aviation Systems Test Activity, Edwards Air Force Base, California, 1970.
27. Jacobs, E. A., and Abbott, I. H., AIRFOIL SECTION DATA OBTAINED IN THE N.A.C.A. VARIABLE DENSITY TUNNEL AS AFFECTED BY SUPPORT INTERFERENCE AND OTHER CORRECTIONS, NACA TR 669, National Advisory Committee for Aeronautics, Washington, D.C., 1939.

#### REFERENCES (Concluded)

28. Pinkerton, R. M., and Greenberg, H., AERODYNAMIC CHARACTERISTICS OF A LARGE NUMBER OF AIRFOILS TESTED IN THE VARIABLE-DENSITY WIND TUNNEL, NACA TR 628, National Advisory Committee for Aeronautics, Washington, D.C., 1938.
29. Davis, J. M., STABILITY AND CONTROL DATA SUMMARIES FOR THE AH-1G AND UH-1H HELICOPTERS, Technical Report 699-099-012, Bell Helicopter Company, Fort Worth, Texas, 1976.
30. Smith, R. P., AH-1G AERODYNAMIC SUBSTANTIATING DATA REPORT FOR STANDARD AIRCRAFT CHARACTERISTICS CHARTS AND FLIGHT MANUAL BASED ON ARMY PHASE D FLIGHT TEST RESULTS, Technical Report 209-099-274, Bell Helicopter Company, Fort Worth, Texas, 1971.
31. Cox, C. R., INSTRUMENTATION TEST PLAN FOR AH-1G OPERATIONAL LOADS SURVEY, Technical Report 299-099-666, Bell Helicopter Company, Fort Worth, Texas, 1973.
32. Shockey, G., COMPONENT TEST PLAN FOR AH-1G OPERATIONAL LOADS SURVEY, Technical Report 299-099-701, Bell Helicopter Company, Fort Worth, Texas, 1975.
33. Shockey, G., FLIGHT TEST PLAN FOR AH-1G OPERATIONAL LOADS SURVEY, Technical Report 299-099-746, Bell Helicopter Company, Fort Worth, Texas, 1975.
34. Shockey, G., FLIGHT SAFETY DATA FOR AH-1G OPERATIONAL LOADS SURVEY, Technical Report 299-099-752, Bell Helicopter Company, Fort Worth, Texas, 1975.
35. AIR VEHICLE TECHNICAL DESCRIPTION DATA, U.S. Army Aeronautical Design Standard, ADS-10, U.S. Army Aviation Research and Development Command, St. Louis, Missouri.
36. Landgrebe, A. J., and Egolf, T. A., ROTORCRAFT WAKE ANALYSIS FOR THE PREDICTION OF INDUCED VELOCITIES, USAAMRDL TR 75-45, United States Army Air Mobility Research and Development Laboratory, Fort Eustis, Virginia, 1976.
37. Sadler, S. G., DEVELOPMENT AND APPLICATION OF A METHOD FOR PREDICTING ROTOR FREE WAKE POSITIONS AND RESULTING ROTOR BLADE LOADS, Volume I - Model and Results, CR-1911, National Aeronautics and Space Administration, Washington, D.C., 1971.

APPENDIX A. CONTOUR PLOTS OF MAIN ROTOR AERODYNAMIC  
QUANTITIES DERIVED FROM MEASURED DATA FOR  
FOUR LEVEL FLIGHT TEST CONDITIONS

Section 5.5 contains comparisons between contour plots of test-derived and C81-generated main rotor normal force coefficient, pitching moment coefficient, and blade-element angle of attack for two level-flight test conditions. Contour plots derived from test data for four other straight-and-level flight conditions are included and discussed in this appendix to expand the body of data available for interpretation. The four flight conditions are:

Counter 1078 - 8289 pounds gross weight, mid center of gravity, clean wing, 10 KTAS.

Counter 612 - 8319 pounds gross weight, aft center of gravity, clean wing, 85 KTAS.

Counter 614 - 8319 pounds gross weight, aft center of gravity, clean wing, 116 KTAS.

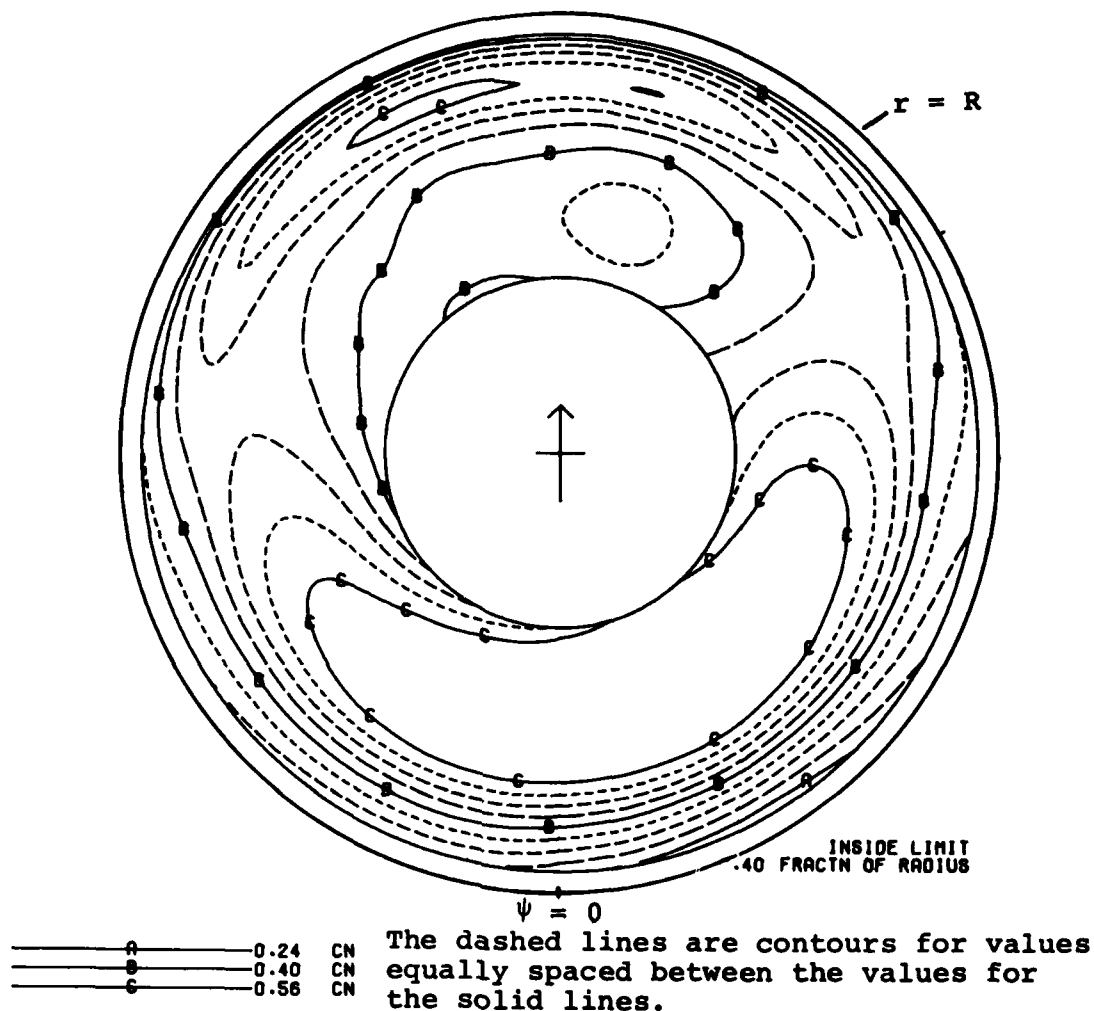
Counter 615 - 8319 pounds gross weight, aft center of gravity, clean wing, 129 KTAS.

A.1 Main Rotor Contour Plots for Counter 1078

The  $c_N$ ,  $c_M$  and  $\alpha$  contour plots for the 10 KTAS flight condition are given in Figure A-1. The pilot card states that this is a flight condition in which the aircraft hovered, with respect to the ground, at a heading angle of 180 degrees in a 10-KTAS south wind. The normal-force-coefficient contour plot, Figure A-1a, shows a small variation of  $c_N$  across the disc, with the regions of highest  $c_N$ , 0.56, centered along a 20-degree to 200-degree azimuth line. This distribution tends to indicate that the aircraft was actually in sideward flight with a sideslip angle of as much as 70 degrees.

The pitching moment coefficient plot (Figure A-1b) also shows a small variation in value across the disk, with the region of largest negative values being centered on the 200 degree azimuth line, further indicating a large sideslip angle. The region of highest angles of attack were experienced at an azimuth of about 225 degrees, implying a sideslip angle of approximately 45 degrees (Figure A-1c).

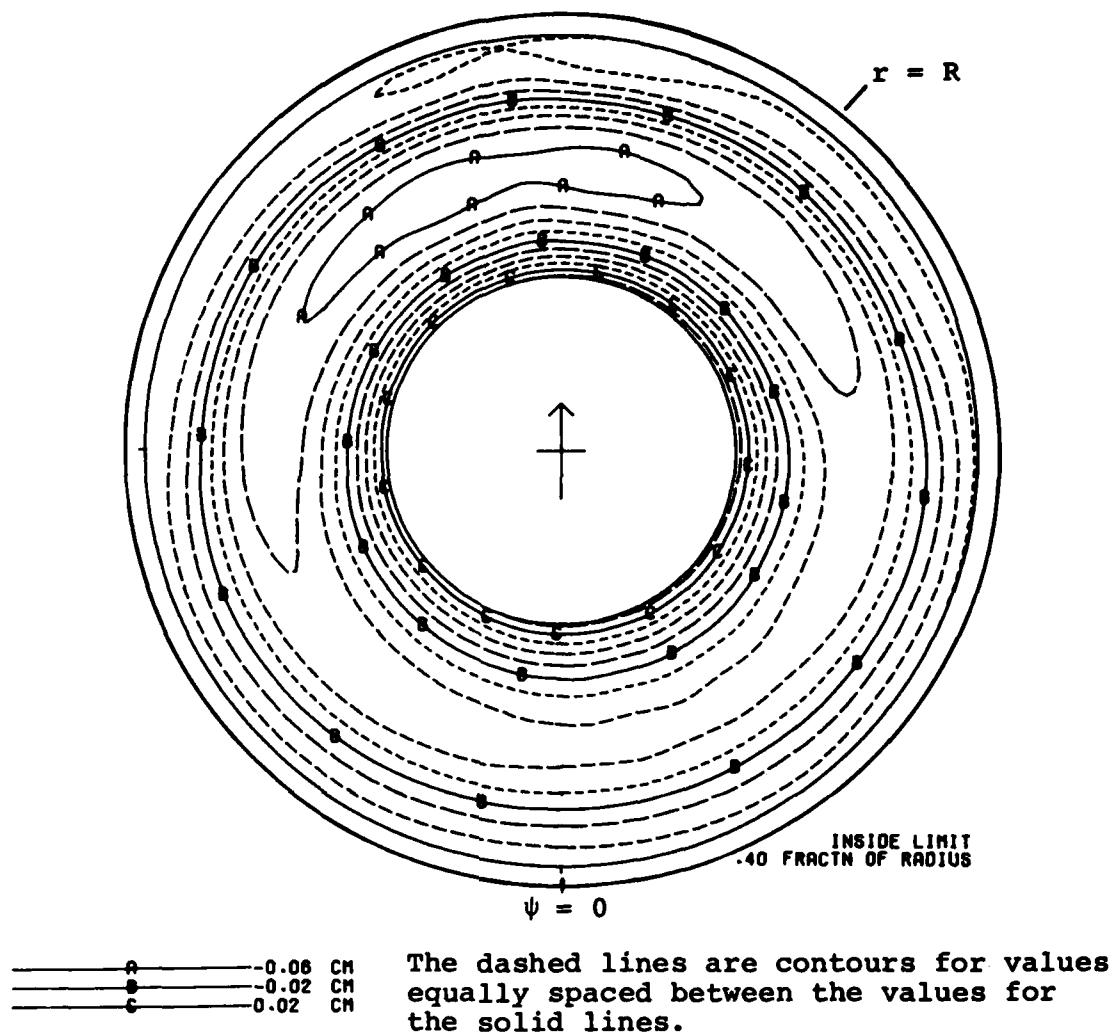
All three contour plots for the 10-KTAS case are in reasonable agreement and the data demonstrate that the test point was flown with a good deal of sideslip.



a) Normal Force Coefficient Contour Plot.

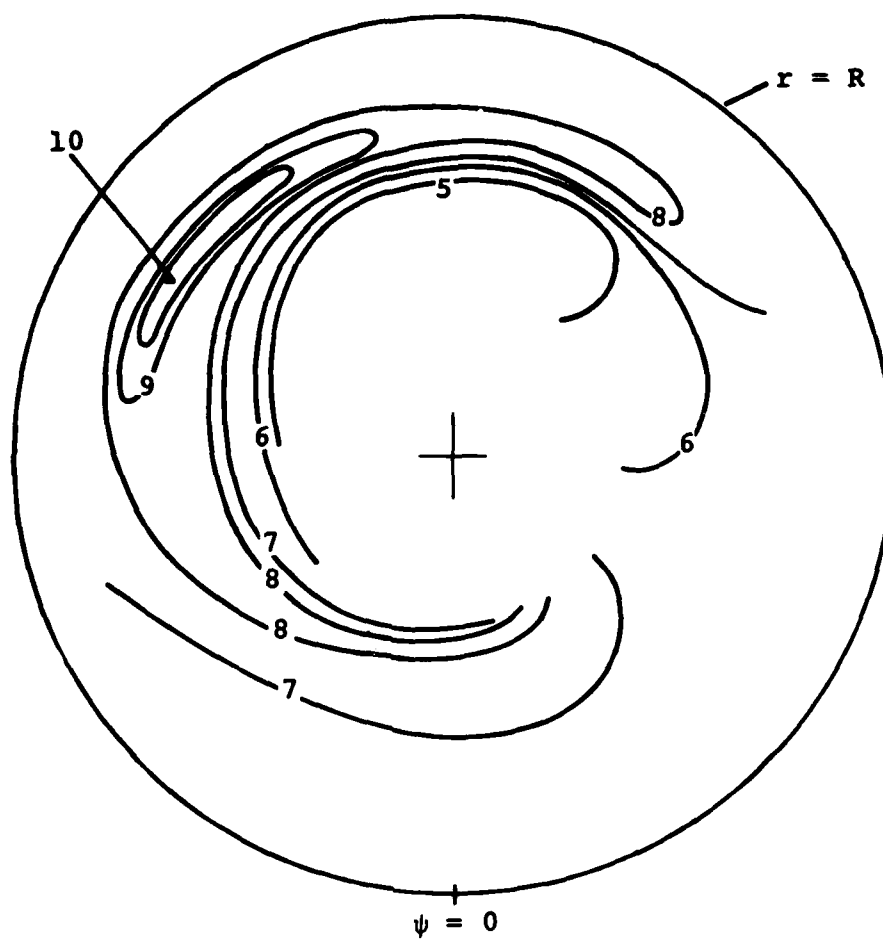
Figure A-1. Main Rotor Contour Plots Derived From Test Data for Flight 45B, Counter 1078 (8289 Pounds Gross Weight, Mid CG, Clean Wing, 10 KTAS).





b) Pitching Moment Coefficient Contour Plot.

Figure A-1. Continued.



Angle-of-attack contours in degrees.

c) Angle-of-Attack Contour Plot.

Figure A-1. Concluded.

### A.2 Main Rotor Contour Plots for Counter 612

Figure A-2 contains the normal force coefficient, pitching moment coefficient, and angle-of-attack contour plots for the 85-KTAS case of counter 612. All three plots show the typical dissymmetry in properties across the disc that is experienced in forward flight. The  $c_N$  plot (Figure A-2a) has a region of large values between 40- and 75-percent radius between the 180- and 300-degree azimuth location, indicating some stall, or at least large angles of attack. The "D" contour, between 210- and 240-degree azimuths delineates a region of severe stall, with very large positive angles of attack.

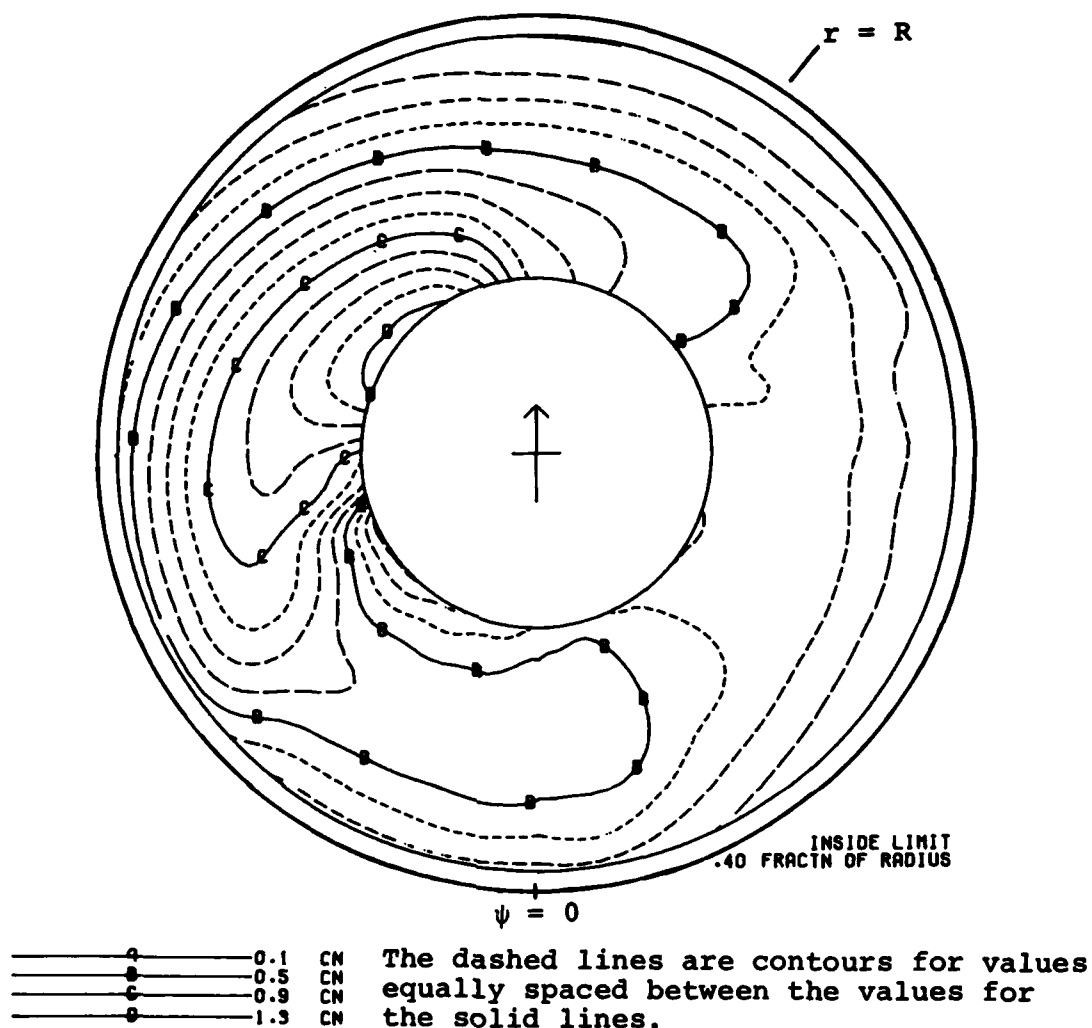
The pitching moment coefficient contour plot of Figure A-2b has a region of positive values on the inboard portion of the blade over the entire azimuth range. This would be a region of negative angle-of-attack stall, in direct disagreement with the  $c_N$  plot shown previously. The small "D" contour between 40- to 45-percent radius at 270-degrees azimuth describes a region in which the pitching moment coefficient is greater than, or equal to, 0.22. If it is assumed that the CLCD5474 table of Figure 5 is a reasonably accurate reflection of the OLS airfoil, then the angles of attack in this region must be more negative than -30 degrees. Such large negative values of  $\alpha$  are not in evidence on the angle-of-attack contour plot of Figure A-2c. The ridge-and-valley angle-of-attack anomaly observed in the 66- and 142-KTAS plots, Figures 37a and 40a, is also prominent for the 88-KTAS case.

### A.3 Main Rotor Contour Plots For Counter 614

The contour plots for the 116-KTAS case are presented in Figure A-3a. They demonstrate characteristics similar to those already seen, with a region of very high  $c_N$ 's inboard on the retreating blade simultaneously with large positive  $c_M$ 's. The ridge-and-valley anomaly at about 70 percent radius is also seen on the angle-of-attack contour plot, Figure A-3c.

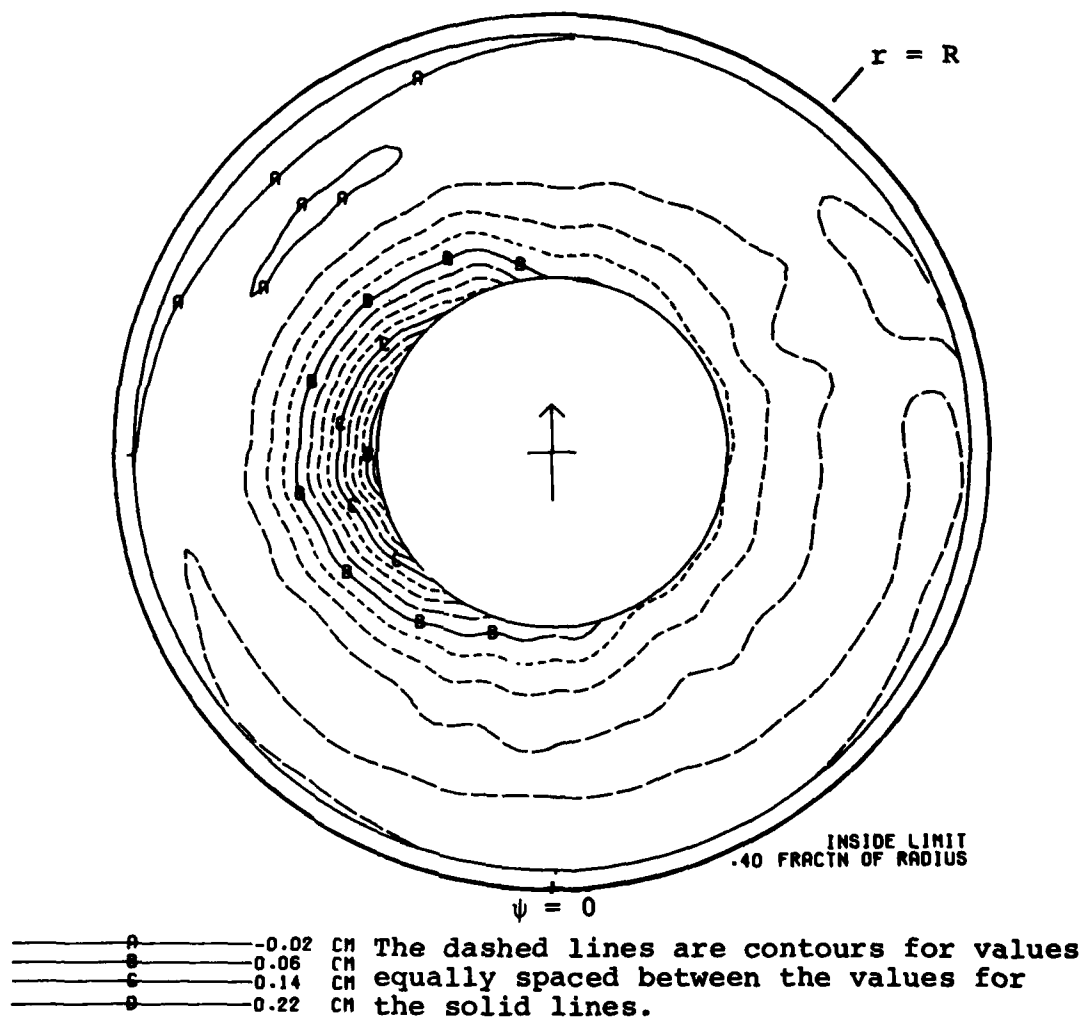
### A.4 Main Rotor Contour Plots for Counter 615

The  $c_N$ ,  $c_M$  and  $\alpha$  contour plots for the 129-KTAS forward flight case are given in Figure A-4, with essentially the same qualitative characteristics as observed for the other cases.



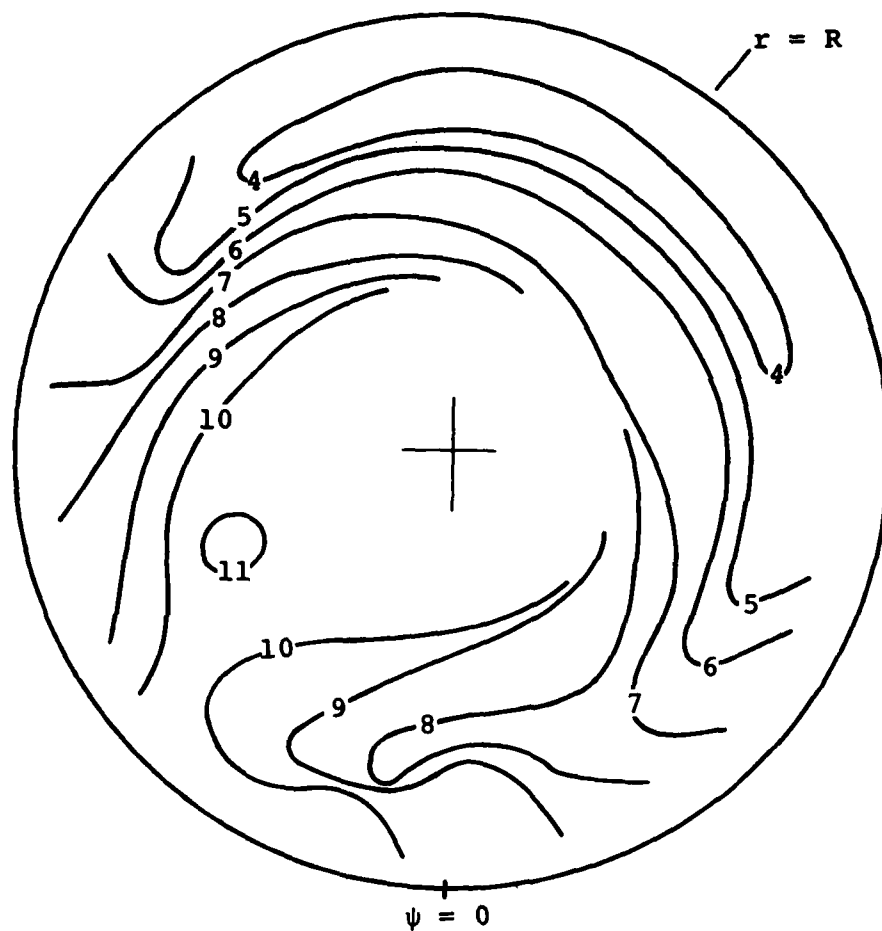
a) Normal Force Coefficient Contour Plot.

Figure A-2. Main Rotor Contour Plots Derived From Test Data for Flight 35A, Counter 612 (8319 Pounds Gross Weight, Aft CG, Clean Wing, 85 KTAS).



b) Pitching Moment Coefficient Contour Plot.

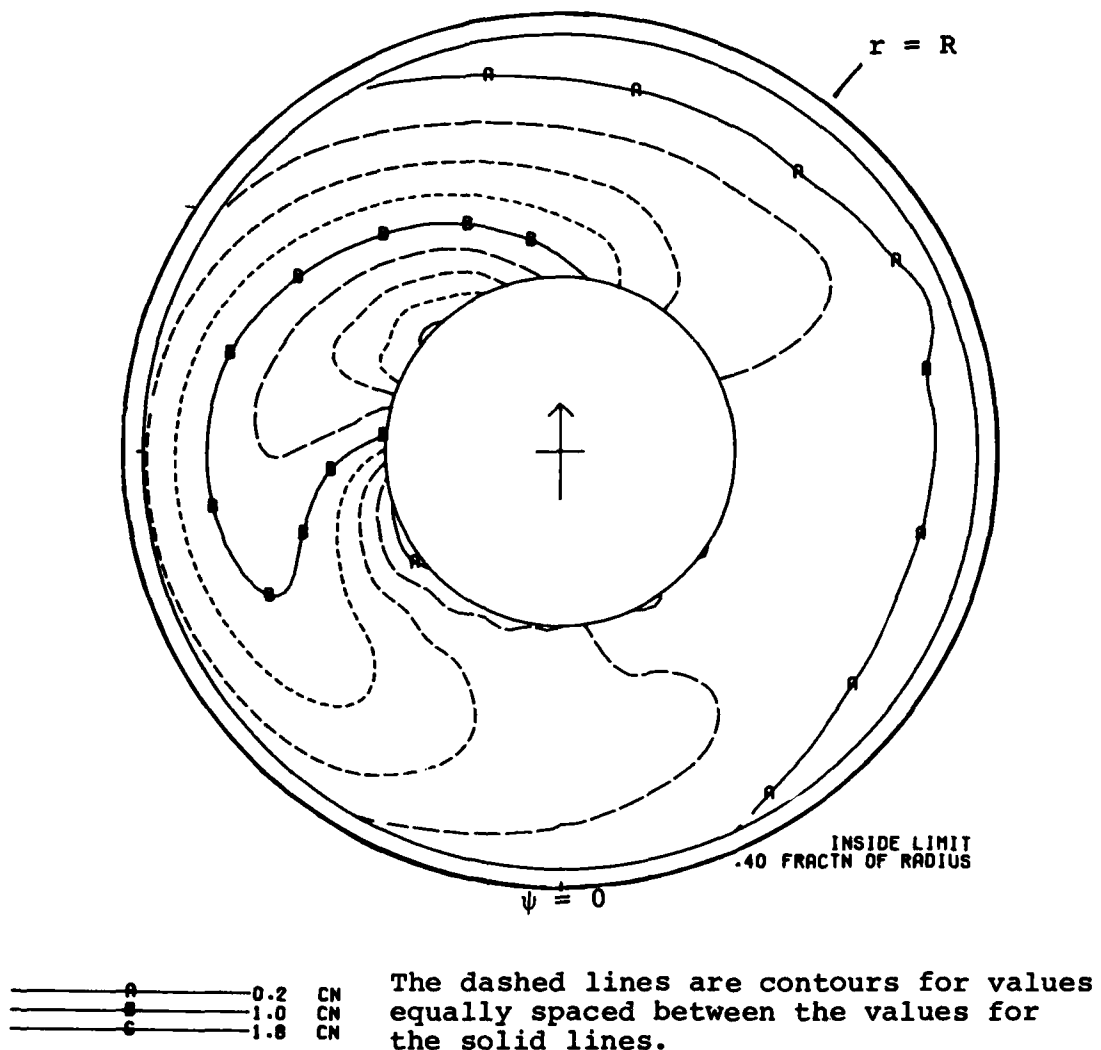
Figure A-2. Continued.



Angle-of-attack contours in degrees.

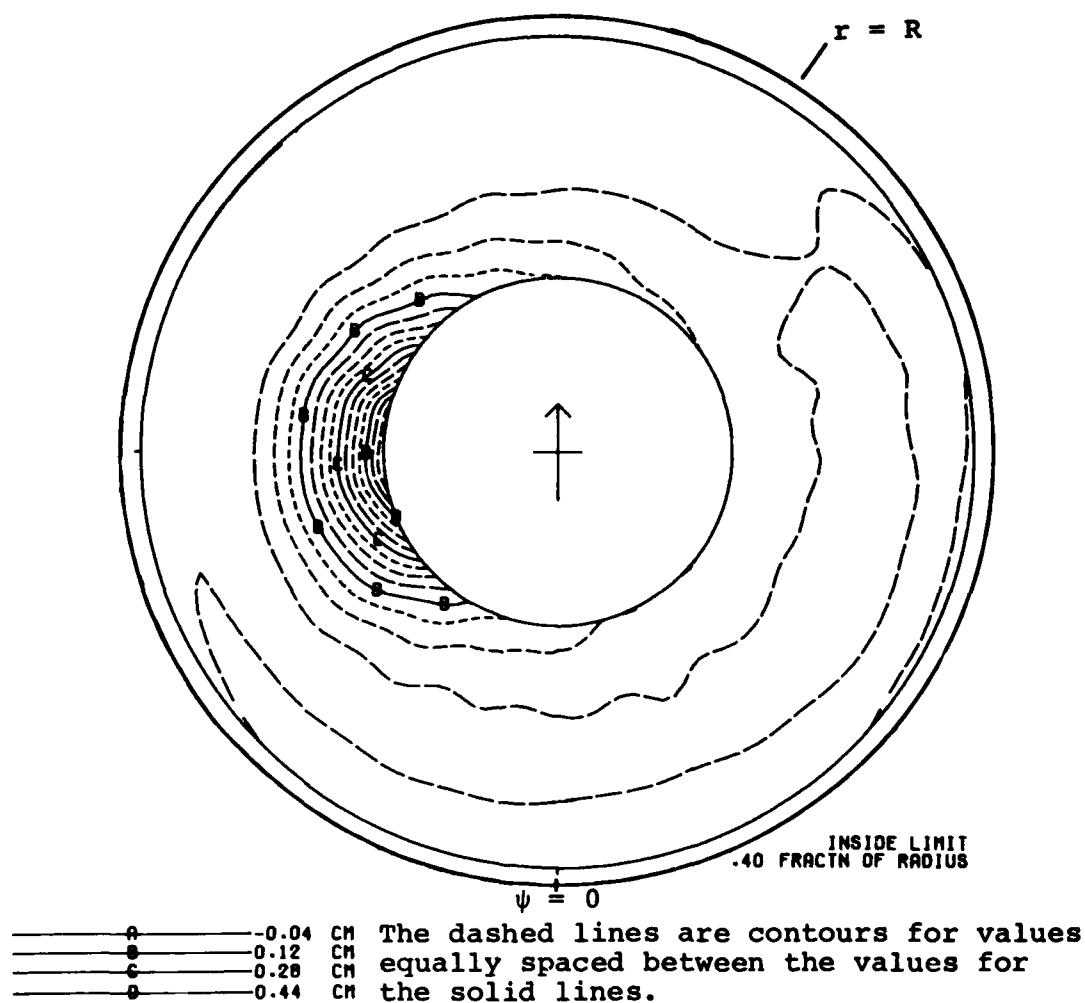
c) Angle-of-Attack Contour Plot.

Figure A-2. Concluded.



a) Normal Force Coefficient Contour Plot.

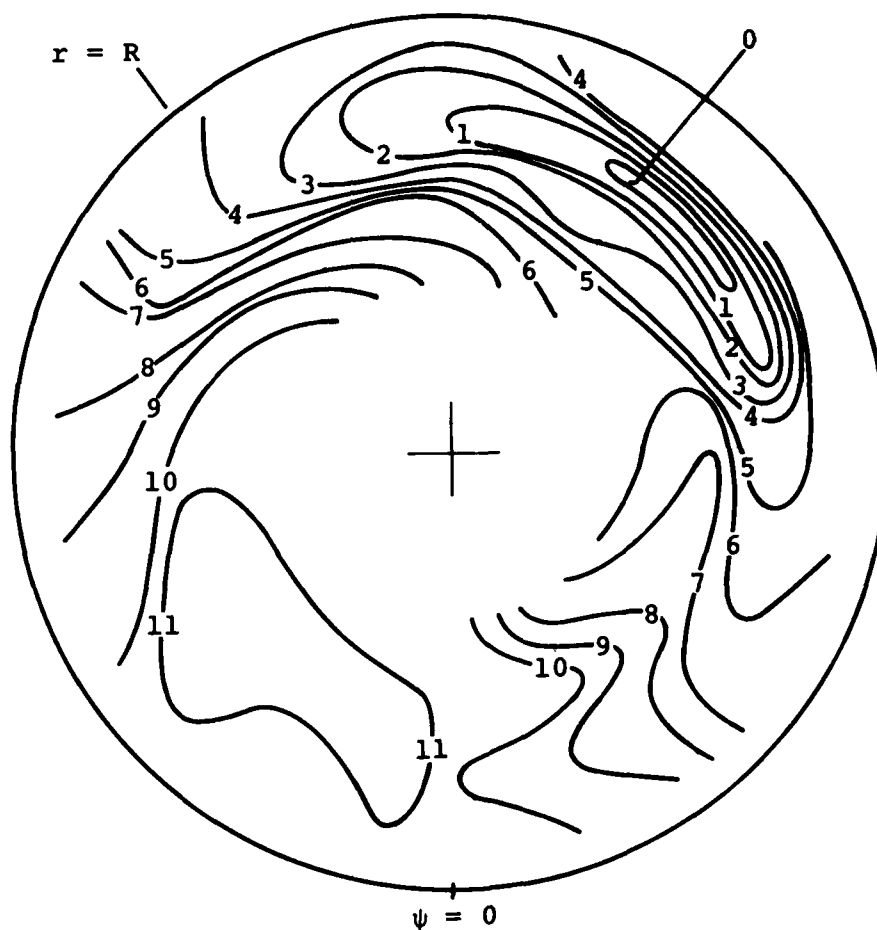
Figure A-3. Main Rotor Contour Plots Derived From Test Data for Flight 35A, Counter 614 (8319 Pounds Gross Weight, Aft CG, Clean Wing, 116 KTAS).



b) Pitching Moment Coefficient Contour Plot.

Figure A-3. Continued.

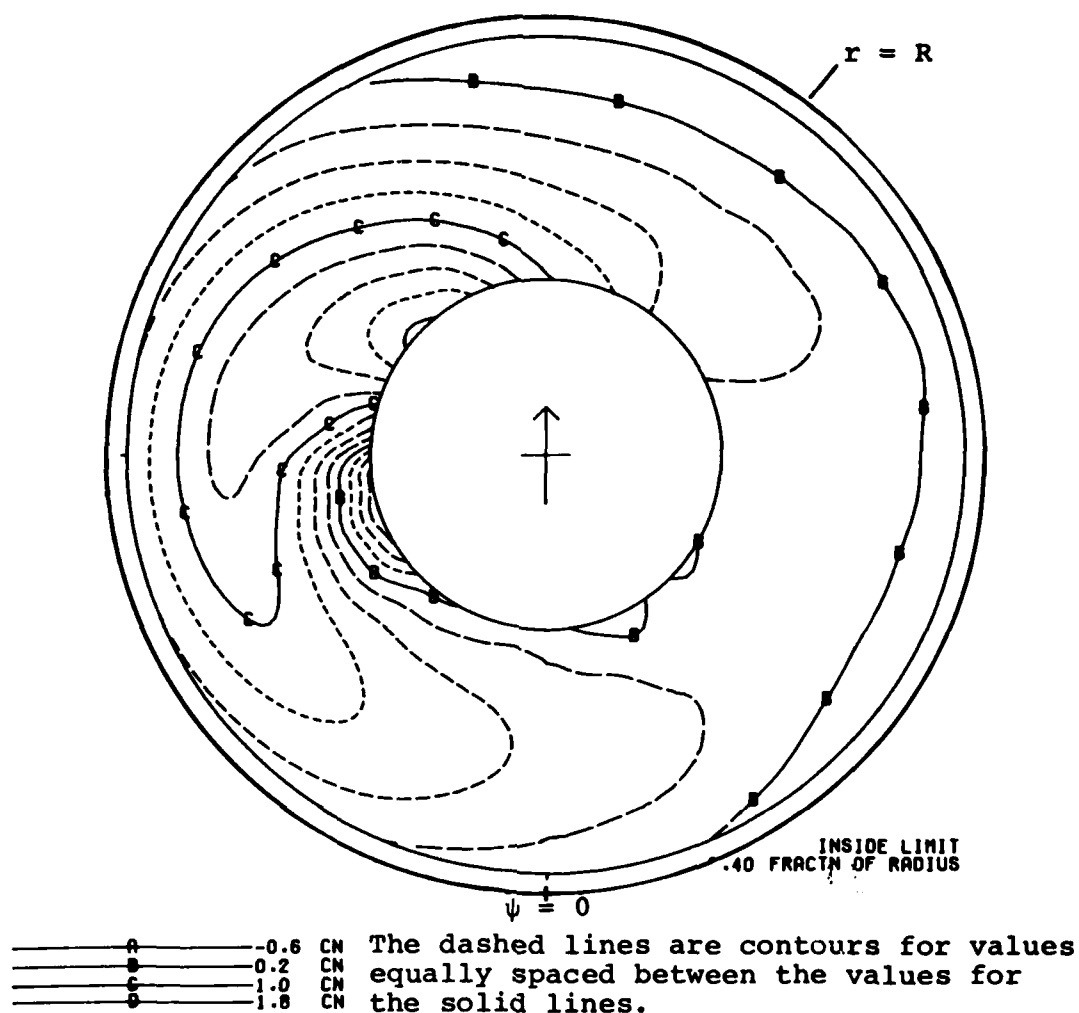




Angle-of-attack contours in degrees.

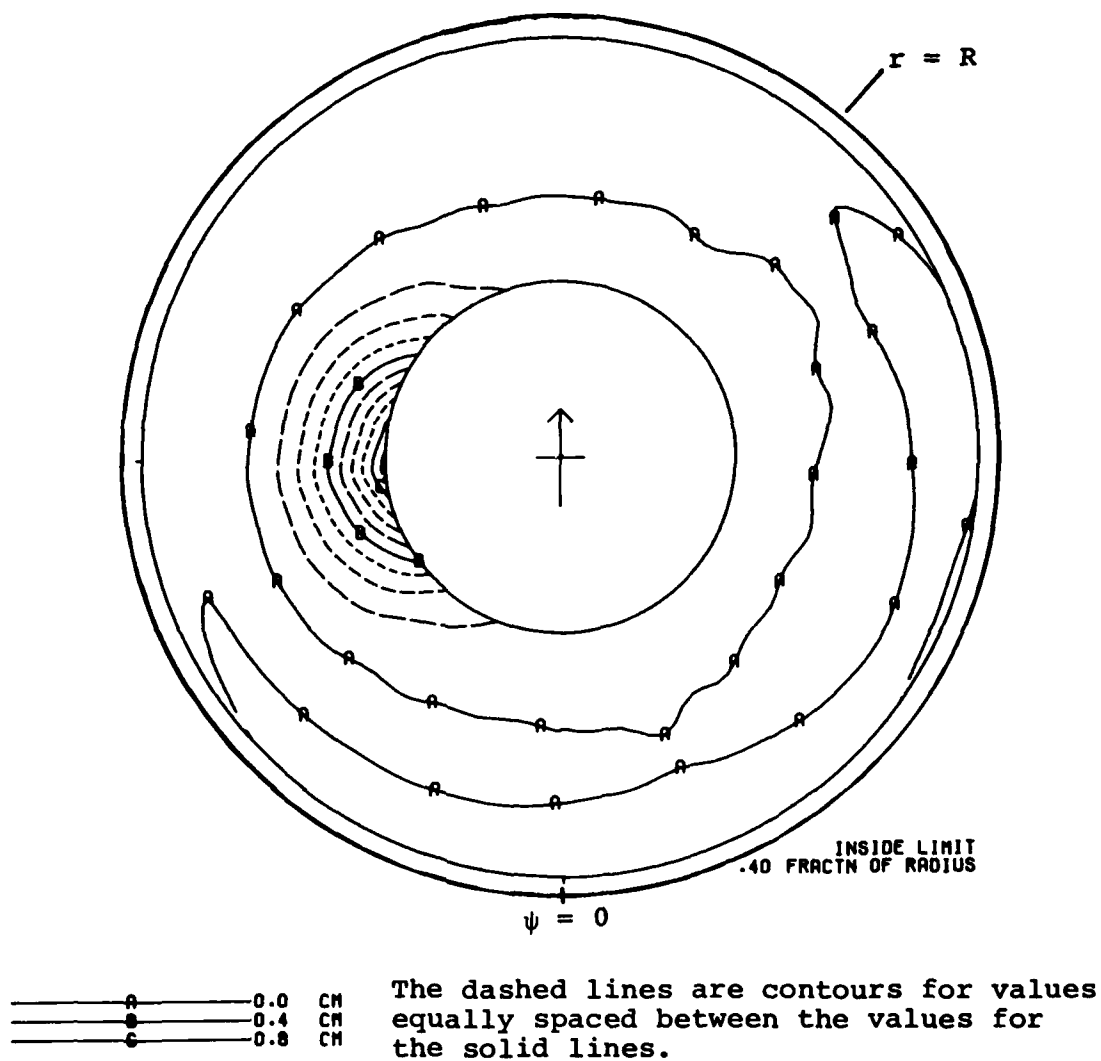
c) Angle-of-Attack Contour Plot.

Figure A-3. Concluded.



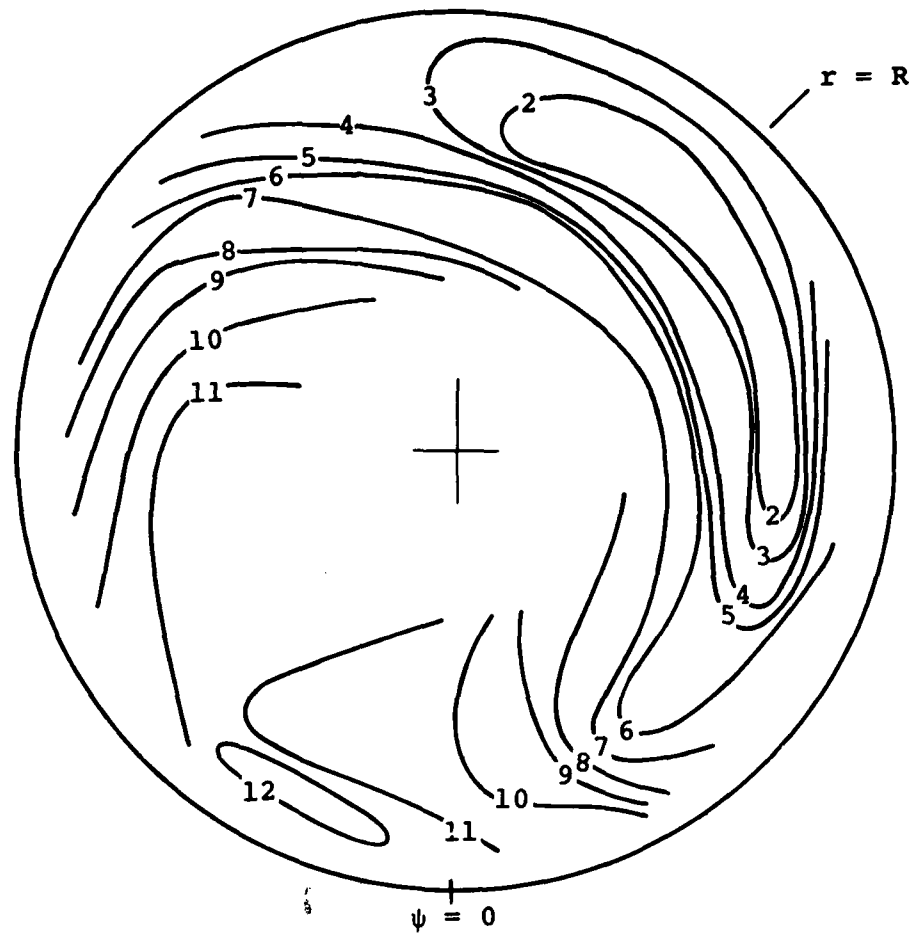
a) Normal Force Coefficient Contour Plot.

Figure A-4. Main Rotor Contour Plots Derived From Test Data for Flight 35A, Counter 615 (8319 Pounds Gross Weight, Aft CG, Clean Wing, 129 KTAS).



b) Pitching Moment Coefficient Contour Plot.

Figure A-4. Continued.



Angle-of-attack contours in degrees.

c) Angle-of-Attack Contour Plot.

Figure A-4. Concluded.

#### A.5 Summary

The anomolous characteristics demonstrated in the test data, and the contradictions between the  $c_M$  plots and the  $c_N$  and  $\alpha$  plots require further examination. Main rotor aerodynamic data should be reduced for other forward flight test conditions to determine if the phenomenon observed in the plots presented here were experienced in other flight conditions.